Layer-Controlled CVD Growth of 2D Tungsten Disulfide and Its Lateral Heterostructure with Molybdenum Disulfide for Optoelectronic and Biosensing Applications

A Thesis Submitted to
Indian Institute of Technology Guwahati
For the Degree of

Doctor of Philosophy

By

Abdul Kaium Mia

Centre for Nanotechnology
Indian Institute of Technology Guwahati
Guwahati-781039, India
May 2025

Dedicated

To all my family members, especially to my parents,
who have always believed in me.

Centre for Nanotechnology
Indian Institute of Technology Guwahati
Guwahati-781039, India

STATEMENT

The work contained in the thesis entitled "**Layer-Controlled CVD Growth of 2D Tungsten Disulfide and Its Lateral Heterostructure with Molybdenum Disulfide for Optoelectronic and Biosensing Applications**" has been carried out by me at Indian Institute of Technology Guwahati under the supervision of **Prof. P. K. Giri**, Professor, Department of Physics and Centre for Nanotechnology, Indian Institute of Technology Guwahati. This work has not been submitted elsewhere for any degree award.

Abdul Kaium Mia
Roll No. - 196153001
Senior Research Fellow
Centre for Nanotechnology
Indian Institute of Technology Guwahati
Guwahati-781039, India

Prof. P. K. Giri
Professor *Department of Physics*
and Centre for Nanotechnology
Indian Institute of Technology Guwahati
Guwahati-781039, India
Phone: ***+91 361 2582703***,
Fax: ***+91 361 2690762***
Email: ***giri@iitg.ac.in***

CERTIFICATE

This is to certify that the work contained in the thesis entitled "**Layer-Controlled CVD Growth of 2D Tungsten Disulfide and Its Lateral Heterostructure with Molybdenum Disulfide for Optoelectronic and Biosensing Applications**" has been carried out by **Mr. Abdul Kaium Mia** at the Indian Institute of Technology Guwahati under my supervision. This work has not been submitted elsewhere for any degree award.

Prof. P. K. Giri
Thesis supervisor

ACKNOWLEDGEMENT

I would like to express my heartfelt gratitude to everyone who has contributed to my journey towards the completion of my Ph.D. thesis.

First and foremost, I extend my deepest appreciation to my supervisor, Professor **P. K. Giri**, for providing me with the invaluable opportunity to work under his guidance. His profound knowledge and boundless passion for science have deeply inspired me and significantly shaped my approach to scientific research. His exceptional technical expertise and practical skills in semiconductor material synthesis and device fabrication were instrumental throughout my research. I am immensely grateful for his continuous support, the necessary resources, laboratory facilities, and, above all, the freedom he allowed me to conduct my research, which enabled me to achieve my objectives.

I would also like to extend my sincere thanks to the members of my Doctoral Committee, Prof. **H. B. Nemade**, Prof. **Biman B. Mandal**, and Prof. **Nageswara Rao Peela**, for their unwavering encouragement, insightful feedback, and constructive criticism throughout the course of my research. My deep appreciation goes to the Head of the Centre for Nanotechnology, along with other faculty members, for their constant support and guidance, which played a crucial role in the completion of my Ph.D. research work.

I am especially grateful to the Centre for Nanotechnology and the Central Instrumentation Facility for providing a conducive research environment equipped with state-of-the-art cleanroom-based fabrication and characterization facilities. I would also like to acknowledge the Indian Institute of Technology Guwahati for their financial assistance, a safe and supportive working environment, and comfortable accommodation throughout my stay.

I extend my gratitude to my collaborators: Dr. **Swapnil Sinha** (CEO of Bio-NEST, IIT Guwahati), Professor **Meyya Meyyappan** (Former Head of NASA Ames Research Centre, USA), and Professor **Saptarshi Das (**The Pennsylvania State University, USA), for their invaluable support and contributions to my thesis work. I am profoundly thankful to Dr. Swapnil Sinha, who meticulously carried out all bio-related activities in her laboratory under her expert supervision, including aptamer selection, bacterial selection, and culture. Her guidance was instrumental in the success of these experiments. I am equally grateful to Professor Meyya Meyyappan for his extensive knowledge of semiconductor devices and his constructive suggestions, which significantly enhanced both the scientific understanding and quality of the manuscript. A special acknowledgment goes to Professor Saptarshi Das for his

exceptional guidance in addressing the critical issue of gate leakage current during device fabrication. His insightful advice was key to identifying and resolving this challenge. Additionally, the wafers he generously provided were pivotal in overcoming the leakage current issue, ultimately enabling the fabrication of high-quality devices. This achievement would not have been possible without his expertise and unwavering support.

The successful completion of this work is a testament to the unwavering encouragement and intellectual support I received from my seniors and junior colleague. I am deeply grateful to Dr. **Abhilasha Bora**, Dr. **Larionette P. L. Mawlong**, Dr. **N. Somorjit Singh**, Dr. **Md Tarik**, **Ravinder, Koushik, Tadasha, Sirshendu, Sanju, Subhankar, Debabrata, Sanjoy, Shipra, Sourav, Garima,** and **Shantanu** for their invaluable contributions to both the personal and professional dimensions of my research journey. Their presence made this endeavor not only fruitful but also profoundly enjoyable and intellectually rewarding.

Finally, I wish to express my heartfelt gratitude to my extended family members, whose constant support I deeply value. I am profoundly thankful to my parents, whose unwavering belief in me and sacrifices, despite our financial struggles, have been the cornerstone of my academic journey. I am eternally grateful to the late **Sushanta Kr Basak** and **Babli Basak** from Gangarampur for the life-changing kindness of offering me accommodation at their home that pivotal night. His generosity provided me with the environment I needed to focus on my studies, a gesture that transformed the course of my life. I extend my deepest thanks to my Physics teacher, **Bhaskar Roy**, and my Chemistry teacher, Dr. **Sujan Kumar Paul**, for their selfless guidance and encouragement, which went far beyond the tuition. Their support instilled in me the confidence to pursue my dreams. I am also deeply indebted to the **Foundation for Academic Excellence and Access**, whose financial assistance supported my education from my B.Sc. to my M.Sc., enabling me to pursue my aspirations without burdening my family. Lastly, I want to thank Professor **Anushree Roy** from IIT Kharagpur for helping me during one of the toughest times of my life. I am extremely thankful to her. This journey would not have been possible without the boundless love, support, and encouragement of my entire family, the remarkable individuals mentioned above, and other individuals I missed. To each of you, I am forever grateful

Abdul Kaium Mia
IIT Guwahati

Contents

Synopsis

Atomically thin two-dimensional (2D) transition metal dichalcogenides (TMDs) are increasingly gaining interest because of their exceptional structural, optical, and electronic properties, making them a promising candidate for a wide range of applications. Among 2D TMDs, semiconducting MoS_2 and WS_2 have garnered significant attention due to their natural abundance, tunable optical band gap, high chemical stability, remarkable mechanical properties, efficient carrier generation, and separation. In TMDs, weak van der Waals forces bind individual covalently bonded X–M–X layers (where M is the transition metal and X is the chalcogen), making layer-controlled synthesis and exploration of layer-dependent properties. Unlike graphene, MoS_2 and WS_2 have semiconducting electrical properties and have been studied extensively for their application in future integrated electronic circuits. Unique optoelectronic properties arise when multilayer TMDs are reduced to monolayers (1L), and the electronic band structure becomes direct from indirect, along with strong photoluminescence (PL) and large exciton binding energy. The bandgap difference of 1L-WS_2 and MoS_2 from their bulk counterpart is quite high, and hence, this vast difference in the electronic structure of the bulk to 1L offers a great opportunity for diverse applications such as in photodetectors, light-emitting devices, phototransistors, sensors, etc. However, these versatile applications demand large-scale, layer-controlled, high-quality growth. Usually, 1L-TMDs are obtained through a top-down approach, such as mechanical exfoliation or liquid exfoliation. However, these approaches are challenging to use in the fabrication of large-scale devices because they produce randomly distributed flakes and provide limited control over the number of layers. A more promising technique for the growth of large area WS_2, MoS_2, and other 2D materials is by one-step chemical vapour deposition (CVD). Additionally, this method demonstrates the synthesis of high-quality films with high crystallinity, which is favorable for the fabrication of high-quality optoelectronic devices and circuits. The 1L-WS_2 exhibits intense PL emission at room temperature, which decreases significantly by 99% when transitioning to 2L and beyond. Therefore, this intense PL emission has many potential applications. Conversely, 2L-WS_2 has better electronic mobility and light absorption, making it suitable for high-performance electronic applications. There are still challenges in controlled doping mechanisms in TMDs, and they require more intense studies for future generation applications in electronic chips to flexible robotics.

This thesis presents a systematic study on the controlled growth of 1L and 2L-WS_2, MoS_2, and in-situ WS_2-MoS_2 lateral HS by CVD technique and their applications in biosensing, broadband photodetection, high-performance FETs, and flexible electronics. We believe that these studies are very significant in addressing the current challenges of optoelectronic applications. Here, the complete thesis work has been organized into eight chapters, as detailed below:

Chapter 1 provides a concise introduction to the key properties and growth techniques of WS_2, emphasizing its potential applications in fields such as healthcare monitoring (e.g., biosensors), photodetectors, memristors, artificial synapses, and field-effect transistors (FETs), among others. Additionally, the chapter explores the critical properties of WS_2-based heterostructures (HSs) formed with other 2D materials like MoS_2 and WSe_2. The formation of these HSs, either through transfer techniques or in-situ growth, unlocks novel properties that significantly enhance device performance. A brief overview of advancements in experimental techniques for synthesizing high-quality, wafer-scale WS_2 is also presented. The chapter concludes with a discussion of current challenges in producing large-area, high-quality WS_2, and its in-situ lateral heterostructures. Finally, the focus of this thesis is outlined, concluding with the motivation behind the present work.

Chapter 2 presents a systematic study for understanding the nucleation and growth mechanism for CVD growth of WS_2. Here, we discuss the optimization process for large-area growth of 1L and 2L WS_2 by precisely controlling the growth parameters. Our findings highlight the critical role of growth temperature, carrier gas flow, growth pressure, and precursor quantities in achieving uniform layer control over a large area. Tungsten oxide and sulfur powders were used as precursors for the complete vapor-phase CVD growth of 2D WS_2 on SiO_2/Si substrate. We observed multilayer, rod-like, defective WS_2 growth at a growth temperature of 850°C and pressure of 10 mbar. Increasing the temperature to 1000°C, a notable enhancement in lateral growth occurred. Through careful adjustment of growth pressure and duration, we successfully achieved uniform 1L and 2L WS_2 growth at 1000°C. Moreover, the addition of salt catalysts like NaCl significantly enhanced lateral growth, extending it to the millimeter scale.

Chapter 3 discusses a simple and powerful strategy to achieve simultaneous asymmetric doping in CVD-grown 2L-WS_2 via contact engineering and its application toward high-performance photodetection. The 1L and 2L-WS_2 grown by the CVD technique are excellent candidates for high-performance optoelectronics due to their high carrier mobility, air stability,

and strong optical absorption. However, photodetectors made with 1L-WS_2 often exhibit high dark current with instability for a longer duration, and thus, there is a scope for further improvement. Compared to conventional symmetric contact electrodes, utilizing metal electrodes with higher and lower work functions relative to 2L-WS_2 aids in achieving asymmetric lateral doping in the WS_2 flakes. This doping asymmetry was confirmed through photoluminescence spectral profile and Raman mapping analysis. With the asymmetric contacts on 2L-WS_2, we find evidence of selective doping of electrons and holes near the Ti and Au contacts, respectively, while the WS_2 region away from the contacts remains intrinsic. When compared to the symmetric contacts case, the WS_2 photodetector with asymmetric (Au, Ti) contacts decreased the dark current by an order of magnitude under reverse bias and increased the photocurrent, resulting in an excellent on/off ratio of ~10^5 and overall improved device performance under identical illumination conditions. We explain this improved performance based on the energy band alignment showing unidirectional charge flow under light illumination. Our results indicate that the planar device structure and compatibility with current nanofabrication technologies can facilitate its integration into advanced chips for futuristic low-power optoelectronic and nanophotonic applications.

Chapter 4 investigated the potential application of Bi_2Se_3 as a contact material for monolayer (1L-MoS_2) in the development of high-performance field-effect transistors and flexible photodetectors. The metal-semiconductor interface is crucial in determining the performance of optoelectronic devices. Deposition of conventional metal contacts on an ultrathin layer often introduces defects in the semiconductor due to the high mass and kinetic energy of the metals, adversely affecting device performance. Using topologically insulating Bi_2Se_3 as a contact material for 1L-MoS_2 results in a better Bi_2Se_3-MoS_2 interface, which improves electron mobility and field control. Enhanced field control leads to a reduction in off-state current and an increase in on-state current, resulting in an improved peak on-off current ratio of approximately 10^8. The application of Bi_2Se_3 contacts also significantly reduces subthreshold swing compared to conventional Cr/Au contacts, indicating fewer interface defects. Furthermore, the Bi_2Se_3-contacted 1L-MoS_2 was explored as a flexible photodetector, achieving an impressive current on-off ratio of ~10^3, which is double that of devices with traditional Cr/Au metal contacts. The key performance metrics for the Bi_2Se_3-contacted 1L-MoS_2 flexible photodetector show significant improvement. This combination of 2D TMDs, along with the highly stable and cost-effective Bi_2Se_3 contact material, demonstrates its great potential for future flexible electronics.

Chapter 5 demonstrates the controlled growth of WS_2-MoS_2 in-situ lateral HS using a novel single-step CVD and its application as FET. There has been extensive focus on 2D TMDs in the last decade for optoelectronic applications. However, relatively little attention has been given to their lateral HSs, particularly their in-situ growth. This in-situ HS growth ensures a clean interface between WS_2-MoS_2, enabling faster charge transfer. The Raman and Auger spatial mapping on the CVD-grown WS_2-MoS_2 lateral HS shows uniform intensity distributions of WS_2 and MoS_2 in a single lateral HS flake with a diffuse $W_{(1-x)}Mo_xS_2$ alloy interface. Spatially resolved PL spectra and PL mapping reveal a strongly enhanced (more than one order of magnitude) PL intensity in the HS interface, attributed to the strain-induced bandstructure modification in the alloyed interface. Interestingly, the alloyed interface in the lateral HS also dramatically improves the electronic properties, resulting in an on-off ratio of 10^8 in the fabricated field effect transistor, which is two orders of magnitude higher than their individual counterpart. These results on lateral HS are significant, and they pave the way to synthesize other different HSs for future electronic devices and integrated circuits.

Chapter 6 explores the potential application of CVD-grown 1L-WS_2 as biosensors using its excellent PL emission at room temperature. The extraordinary PL emission at room temperature from CVD-grown 1L-WS_2 was utilized as a recognition tool for detecting *S. aureus* bacteria with high sensitivity and selectivity. The 1L-WS_2 possesses sulfur vacancy and is utilized for ssDNA aptamer immobilization to the sulfur vacancy sites of 1L-WS_2 via the thiol functional group. The small-sized, highly selective ssDNA aptamers identify and selectively interact with targeted *S. aureus*, enabling selective detection. Interestingly, external charge doping strongly influences the PL emission of 1L-WS2. The shape of the PL emission peak for 1L-WS_2 undergoes significant changes in the presence of targeted *S. aureus* as a result of charge transfer originating from selective interactions of the ssDNA aptamer with *S. aureus*, while it remains unaffected for non-targeted *Escherichia coli*. The ratio of the integrated intensities of trion to neutral exciton peak was used as a calibration parameter for the quantification of *S. aureus* concentrations. The PL analysis of 1L-WS_2 with increasing concentration of *S. aureus* exhibits a linear response over 10^2 CFU/mL to 10^7 CFU/mL with a lower detection limit of 2.0 CFU/mL. The proposed sensing system can identify an unknown concentration of *S. aureus* in human urine. These results demonstrate the potential future-generation application of 1L-WS_2 in the optical biosensing of pathogenic species using suitable receptors.

Chapter 7 presents a simple method for the detection of *S. aureus*, a harmful gram-positive human pathogenic bacterium using strong PL emission of WS_2 quantum dots (QDs). The WS_2 QDs of a mean diameter of 2.5 nm were synthesized by liquid exfoliation of bulk WS_2. Due to the quantum confinement effect, WS_2 QDs exhibit high PL emission under UV excitation. The addition of Bi_2O_2Se NSs resulted in the adsorption of WS_2 QDs on their surface, resulting in quenching of its PL emission through static quenching complex formation among WS_2 QDs and Bi_2O_2Se NSs. A specific sequencing ssDNA aptamer, which identifies and explicitly binds with *S. aureus*, was attached to the defect sites of WS_2 QDs for selective detection. The thiol-modified ssDNA aptamers attach covalently to the WS_2 QDs defect sites, which was confirmed by Raman and XPS. The interaction of *S. aureus* with aptamer functionalized WS_2 QDs weakens the van der Waals interaction between WS_2 QDs and Bi_2O_2Se nanosheets, which results in the detachment of WS_2 QDs from the Bi_2O_2Se nanosheet surface and restores PL intensity of WS_2 QDs. Similar measurements with non-targeted bacteria show that the system is selective towards *S. aureus.* Our PL-based biosensor has a linear response in the range 10^3-10^7 CFU/mL with a detection limit of 580 CFU/mL. We have observed a first response time of 15 minutes for sensing, which is much faster than the previous reports. This proposed system was tested in human urine and can detect *S. aureus* in human urine samples selectively, proving its potential in real-life applications. The reported approach is versatile enough to sense other biomolecules and metal ions by choosing suitable receptors.

Chapter 8 presents the summary and highlights of the contributions of the present thesis. The future scope of work on WS_2, MoS_2, and their HSs for advanced optoelectronic applications is presented at the end.

List of Publications:

A. In Peer-Reviewed Journals:

1. **Abdul, Kaim Mia,** Dey, S., & Giri, P. K. In-situ CVD Grown WS_2-MoS_2 Lateral Heterostructure with Alloyed Interface: Strong Photoluminescence Enhancement and High On-Off Ratio Field Effect Transistors (Accepted, Materials Today Nano).

2. **Abdul, Kaim Mia,** Debnath, S., & Giri, P. K. Non-metal contact Engineering on Monolayer MoS_2 for High-Performance Field Effect Transistor and Flexible Photodetector (***Under Review***).

3. **Abdul, Kaim Mia,** Meyyappan, M. & Giri, P. K. Two-dimensional transition metal dichalcogenide based biosensors: from fundamentals to healthcare applications. *Biosensors 13, 169 (2023).*

4. **Abdul, Kaim Mia,** Sinha, S. & Giri, P. K. Highly sensitive and selective optical detection of Staphylococcus aureus using thiol functionalized monolayer tungsten disulfide grown by chemical vapor deposition. *Sensors and Actuators Reports 8, 100214 (2024).*

5. **Abdul, Kaim Mia,** Meyyappan, M. & Giri, P. K. Asymmetric contact-induced selective doping of CVD-grown bilayer WS2 and its application in high-performance photodetection with an ultralow dark current. *Nanoscale 16, 8583–8596 (2024).*

6. **Abdul, Kaim Mia,** Bora, A., Hossain, M. T., Sinha, S. & Giri, P. K. Fast detection of Staphylococcus aureus using thiol-functionalized WS2 quantum dots and Bi2O2Se nanosheets hybrid through a fluorescence recovery mechanism. *J. Mater. Chem. B 11, 10206–10217 (2023).*

7. **Abdul, Kaim Mia,** Bora, A., & Giri, P. K. Aptamer Functionalized CVD Grown Monolayer WS2 Based FETs for Real-Time Detection of E. coli. *The Physics of Semiconductor Devices (eds. Singh, R., Singh, M. & Kapoor, A.) 285–291 (Springer Nature, Singapore, 2024).*

8. Dey, S., **Abdul, Kaim Mia,** Giri, P.K. Printed Optoelectronic Synapse based on CVD-grown Monolayer MoS2 with Ultralow Power Consumption and High Photoresponsivity. (***under review***)

9. Paul, S., Hossain, M. T., **Abdul, Kaim Mia,** & Giri, P. K. Ultrabroadband Absorption and High-Performance Photodetection in Europium-Doped 2D Topological Insulator Bi 2 Se 3 Nanosheets. *ACS Appl. Nano Mater. 4, 12527–12540 (2021).*

10. Bora, A., Mawlong, L. P. L., **Abdul, Kaim Mia,** & Giri, P. K. Manipulating Trion and Biexciton Emissions in Monolayer WS2 by Sandwiching with Ultrathin ZnO Layers for Excitonic Light Emission Applications. *ACS Appl. Nano Mater. 7, 8612–8623 (2024).*

11. Marappan, G., **Abdul, Kaim Mia,** K. Puspharaj, S. Vaidyanathan, Yoshiyuki Kawazoe, Yuvaraj Sivalingam, & Velappa Jayaraman Surya. Response to VOCs stimuli by triphenylamine derivatives functionalized zinc oxide nanorods: A promising material for food freshness monitoring. *Surfaces and Interfaces 44, 103648 (2024).*

12. Somorjit Singh, N., **Abdul, Kaim Mia,** & K. Giri, P. Role of oxygen functional groups and attachment of Au nanoparticles on graphene oxide sheets for improved photodetection performance. *Nanoscale Advances 6, 2136–2148 (2024).*

13. Chahal, R., **Abdul, Kaim Mia,** Bora, A. & K. Giri, P. Facile in situ synthesis of double perovskite Cs2AgBiBr6 /WS2 heterostructure and interfacial charge transfer mediated high-performance ultraviolet photodetection. *J. Mater. Chem. C, 2024,12, 12835-12846*

B. Conference Papers Presented:

1. ***Abdul, Kaim Mia***, Abhilasha Bora and P. K. Giri; Poster presentation on "*Aptamer Functionalized CVD Grown WS_2 Monolayer FET for Real-time Detection of E.Coli*" at The XXI st International Workshop on the Physics of Semiconductor Devices (IWPSD 2021), IIT Delhi, 14-17 December 2021.
2. ***Abdul Kaium Mia,*** and P. K. Giri; Poster presentation on "CVD Growth of Monolayer WS_2 and its Application Toward Bacteria Detection" Indian Nanoelectronics Users Program - Idea to Innovation **(INUP i2i-2022),** *IIT Guwahati, 4-6 April 2022.* ***(Best Poster Award).***
3. ***Abdul Kaium Mia***, Abhilasha Bora and P. K. Giri; Poster presentation on "*Functionalization of CVD Grown Monolayer WS_2 for Molecular Sensing via Defect Engineering*", at International Symposium on Semiconductor Materials and Devices-2022 **(ISSMD-2022)**, KIIT Bhubaneswar, 16-18 December 2022.
4. ***Abdul Kaium Mia,*** Swapnil Singha and P. K. Giri; Poster presentation on "*Real-time Detection of S. aureus Bacteria using Aptamer Functionalized Silicon Field Effect Transistor*", at Research and Industrial Conclave 2023 **(RIC-2023)**, IIT Guwahati, 14-16 May 2023.
5. ***Abdul Kaium Mia,*** and P. K. Giri; Oral presentation on "*Self-Powered Metal-Semiconductor-Metal 2D WS_2 Monolayer Photodetector with Asymmetric Contacts*" at Recent Progress in Graphene and 2D Materials Research **(RPGR-2023),** Bangalore, 20-23 November 2023.
6. ***Abdul Kaium Mia,*** Swapnil Singha and P. K. Giri; Oral presentation on "*Label-Free Detection of Staphylococcus Aureus using Aptamer Functionalized Monolayer WS_2 Grown by CVD*", at the 8th International Conference on Advanced Nanomaterials and Nanotechnology 2023 **(ICANN-2023)**, IIT Guwahati, 14-16 May 2023.

7. The 4th International Electronic Conference on Biosensors **(IECB-2024)**, Online mode, 20-22 May 2024.

C. Workshops Attended:

1. 5th DAE-BRNS National Workshop on Material chemistry (NWMC 2019), 08-09th November 2019.
2. IEEE Sensors Winter School 2023, IIT Guwahati, 05-06th December 2023.
3. SPARC Workshop on 2D Materials, IIT Kharagpur, 24-25 August 2024

List of Abbreviations

Abbreviation	***Description***
2D	Two-dimensional
3D	Three-dimensional
1L	Monolayer
2L	Bilayer
CVD	Chemical Vapor Deposition
EDS	Energy Dispersive X-ray Spectroscopy
FESEM	Field Emission Scanning Electron Microscopy
FETEM	Field Emission Transmission Electron Microscopy
FWHM	Full Width at Half Maxima
HER	Hydrogen Evolution Reaction
HRTEM	High Resolution Transmission Electron Microscopy
HS	Heterostructure
NC	Nanocrystal
NS	Nanostructure
NP	Nanoparticle
NR	Nanorod
NT	Nanotube

NW	Nanowire
O_V	Oxygen vacancy
PL	Photoluminescence
QC	Quantum Confinement
QD	Quantum Dot
RTA	Rapid Thermal Annealing
RIE	Reactive Ion Etching
SAED	Selected Area Electron Diffraction
SPR	Surface Plasmon Resonance
STEM	Scanning Transmission Electron Microscopy
TEM	Transmission Electron Microscopy
TRPL	Time-Resolved Photoluminescence
UV-Vis	Ultraviolet Visible
XPS	X-ray Photoelectron Spectroscopy

Chapter 1

Introduction

Since the discovery of graphene in 2004, there has been growing interest in graphene and other graphene-like two-dimensional (2D) materials among the scientific community. The zero-band gap of graphene and its conducting nature impose fundamental limitations in electronic applications as well as in sensitivity and detection limits for sensing applications[1]. The cutting-edge research on graphene and its underlying physics has paved the way for the identification of additional 2D layered materials. These 2D materials seek to address the limitations of graphene while broadening their applications across various domains. The other 2D materials include transition metal dichalcogenides (TMDs), hexagonal boron nitride (hBN), graphite carbon nitride (g-C_3N_4), bismuth oxy chalcogenides, black phosphorus (BP), etc. Among all 2D materials, the TMDs represent a category of 2D materials in which weak van der Waals (vdW) forces bind individual covalently bonded X–M–X layers (with M as the transition metal, such as Mo or W, and X as the chalcogen, namely S, Se, or Te), enabling the potential for layer-controlled synthesis[2]. These individual building blocks (monolayer TMDs) show a transition from indirect to direct band gaps and have fascinating optical and electronic properties[3]. Layer-dependent optoelectrical properties, along with the existence of finite band gaps, make 2D TMDs superior to graphene. This uniqueness opens up a range of applications, including electronic circuits, energy storage, biosensing, catalysis, and more, while also facilitating the exploration of two-dimensional physics and device applications[4]. Among the TMDs, Molybdenum disulfide (MoS_2) has been one of the most studied TMDs due to its unique optical and electrical properties during the transition from an indirect bandgap to a direct bandgap when scaled down from bulk to monolayer form. Tungsten disulfide (WS_2), another member of the TMD family, has garnered significant attention recently and is actively being investigated for potential applications in next-generation optoelectronics[5]. The layer-dependent tunability of its bandgap, along with optical absorptions and PL emissions, makes it a promising candidate for various applications such as photovoltaics cells[6,7], photodetectors,[8,9] p-n junction diodes[10,11], catalysis, [12,13] energy storage [14,15] phototransistors,[16,17] biosensing [18], and future generation electronic devices[19]. The weak van der Waals (vdW) forces among the individual monolayers result in weak bonding, facilitating easy isolation and stacking with other materials. This characteristic allows the formation of a diverse array of heterostructures

(HSs) without the constraint of lattice matching[20,21]. By introducing additional structural complexities in the formation of the HS, one can selectively tune its distinctive properties, including electrical, optical, and structural aspects[21,22]. This process results in a material that possesses unique and vastly superior properties. We can gain a comprehensive understanding of WS_2-based HSs by manipulating these innovative properties, positioning them as promising candidates for upcoming optoelectronic applications. In this chapter, we provide a brief overview of the key characteristics of 2D WS_2, examine recent methodologies for growing WS_2 nanostructures, and explore its emerging applications, including biosensors, photodetectors, memristors, artificial synapses, and others. Toward the end of the chapter, we present a perspective on the primary challenges in synthesizing 2D WS_2 and the fabrication of field-effect transistors (FETs) for optoelectronic applications.

1.1. Properties of WS_2

1.1.1 Crystal Structure of WS_2

WS_2 is a layered material described by the generalized common formula MX_2, where M represents the transition metal (W) and X represents the chalcogen (S). These have structures like sandwiches, with a single layer; W atoms are situated in a hexagonal plane between two planes of S atoms[23]. These three layers of atoms are bound together by strong covalent bonding, forming a single layer of WS_2. Each layer of WS_2 is connected to the others by weak van der Waals forces, as depicted

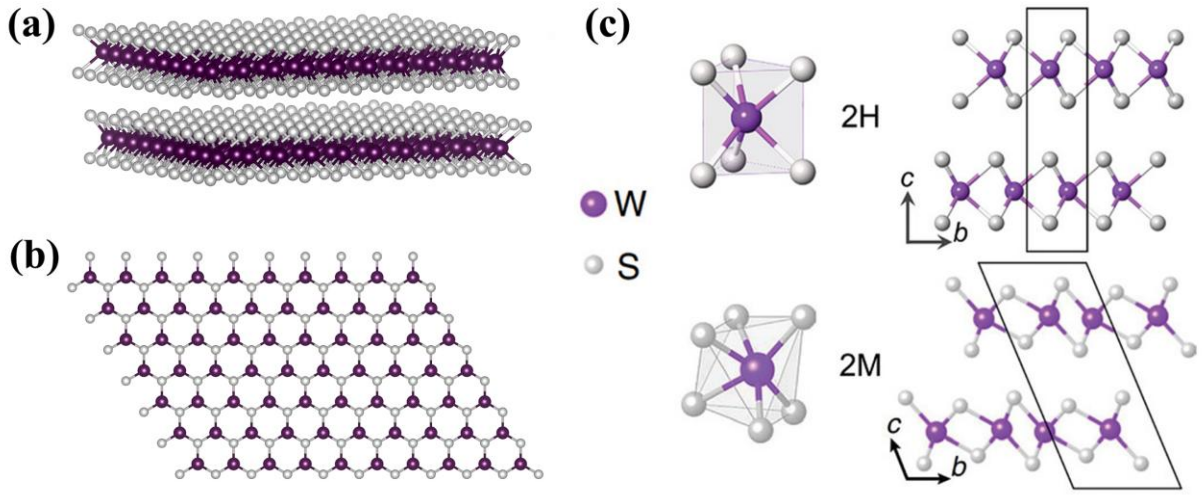

Figure 1.1: Schematic representation of WS_2 crystal structure showing: (a) cross-sectional view; (b) top view; (c) Crystal structure of highly stable 2H and metastable 2M phase of WS_2. Adapted from Ref.[24].

in **Fig. 1.1(a).** The top view of the 2D WS_2 plane is shown in **Fig. 1.1(b).** The strong bonding with--in the plane, and weaker interactions perpendicular to the plane in these 2D crystals facilitate their exfoliation into single layers. With the variation of layers stacking geometry, 2D WS_2 have well reported two phases, namely a trigonal prismatic phase (2H) or an octahedral phase (1T)[25]. Recently 2M phase of WS_2 has also been reported with superconducting properties, as shown in **Fig. 1.1(c)**[24]. Among all the phases, 2H semiconducting WS_2 is the most stable and dominant in nature compared to all other phases. The lattice structure corresponding to the 2H and 2M are shown in **Fig. 1.1(c).**

1.1.2. Electronic Band Structure of WS_2

WS_2 is a layered material and has exciting layer-dependent optoelectronic properties. The electronic band structure of WS_2 is highly influenced by layer number and exhibits an interesting transition from indirect to direct at monolayer[26]. The electronic band structure calculated using the ab initio method by using the projector augmented wave method is shown in **Fig. 1.2** from monolayer to quadallayer[26]. The bulk WS_2 has an indirect bandgap of 1.3 eV, and with the reducing

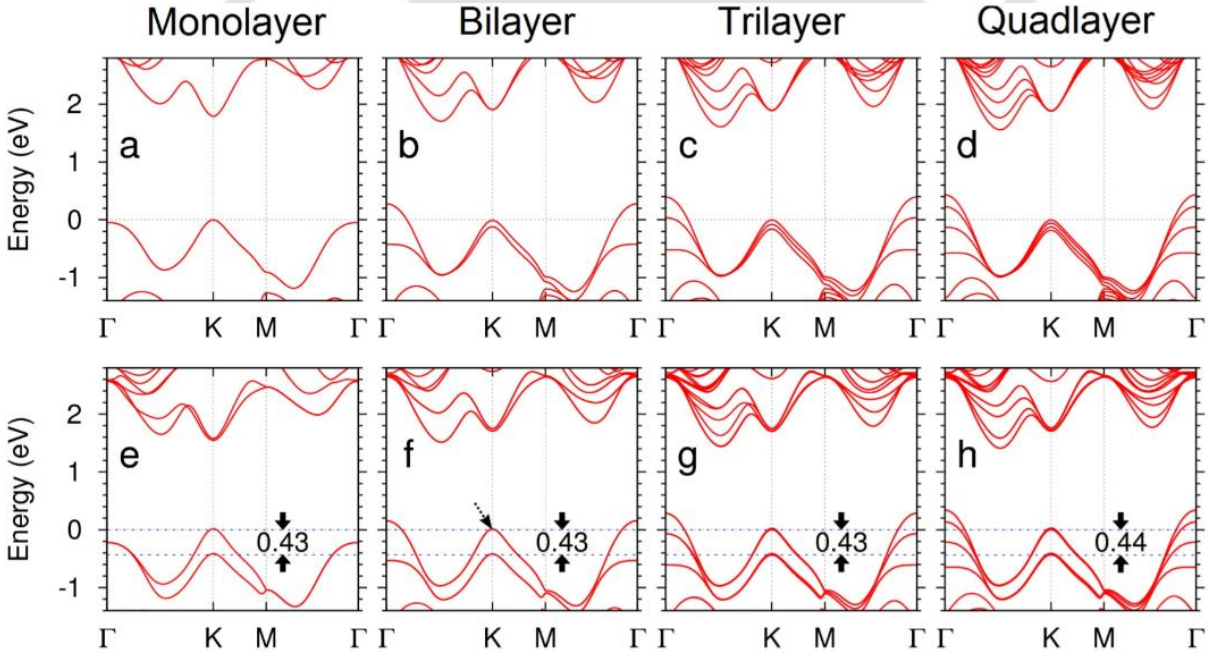

Figure 1.2: Band structures for WS_2 ultrathin films were calculated ab initio: (a–d) depict the structures without spin-orbit coupling; (e–h) illustrate those with spin-orbit coupling. The valence band splitting at the K point remains nearly constant, approximately 0.43 eV for mono, bi, tri, and quad-layers. Adopted from Ref.[26].

layer number, band edge separation increases and becomes a direct bandgap of 2.0 eV for monolayer WS_2[27], as shown in **Fig. 1.2**. For monolayer WS_2, the valence band maxima (VBM) and conduction band minima (CBM) coincide at the K point. As the layer number increases, the VBM aligns with the Γ point, while the CBM ranges between the K and Γ points, exhibiting a narrower indirect bandgap between them. Due to spin-orbit coupling, the valence band experiences splitting that remains unaffected by the layer number, thus disregarding interlayer interactions as shown in **Fig. 1.2**. Along with the band structure, the electron and hole mobility in 2D TMDs varies with layer number[28]. In general, WS_2 is n-type semiconducting and the monolayer has an electron mobility of approximately 140 $cm^2/(V.s)$ at low temperature (83K); the mobility increases more than two times for bilayer WS_2 ~ 300 $cm^2/(V.s)$ offering better performance possibilities for electronics applications. The monolayer WS_2 has an electron mobility of ~ 50 $cm^2/(V.s)$ at room temperature with an excellent on/off ratio of 10^8 in FET configuration. By using high K dielectric and top gate configuration, the performance of the 2D WS_2 was further enhanced in terms of electron mobility and on/off ratio[19]. The Excellent mobility of 2D WS_2 and a high on/off ratio make it a suitable replacement for traditional Si channels in FETs.

1.1.3. Optical properties of WS_2

A comprehensive understanding of the optical properties of WS_2 is essential for a wide range of applications in optoelectronics. The interesting layer-dependent optical properties determine suitable applications in optical devices. The optical properties are usually studied by ultraviolet-visible (UV-Vis) absorption spectroscopy, photoluminescence (PL) emission, and Raman spectroscopy. The excellent PL emission of monolayer WS_2, originating from its transition to a direct band structure from an indirect band structure corresponding to its bulk counterpart, is a distinct optical feature[29]. Optical images of mechanically exfoliated monolayer, bi-layer, tri-layer, and multilayer WS_2 flakes are shown in **Fig. 1.3(a)**[27]. The ultrathin layers of WS_2 are transparent in nature, but as the layer number increases, it becomes opaque, as seen in the optical image of **Fig. 1.3(a)**. The Raman spectra serve as fingerprints for 2D materials, each exhibiting unique spectra that vary according to the material and are influenced by the number of layers[30]. The Raman spectra of 2D WS_2 is highly influenced by the excitation wavelength as shown in **Fig. 1.3(b)** and **Fig. 1.3(c)**. The two fundamental Raman modes of 2D WS_2 are A_{1g} and E_{2g}, correspon-

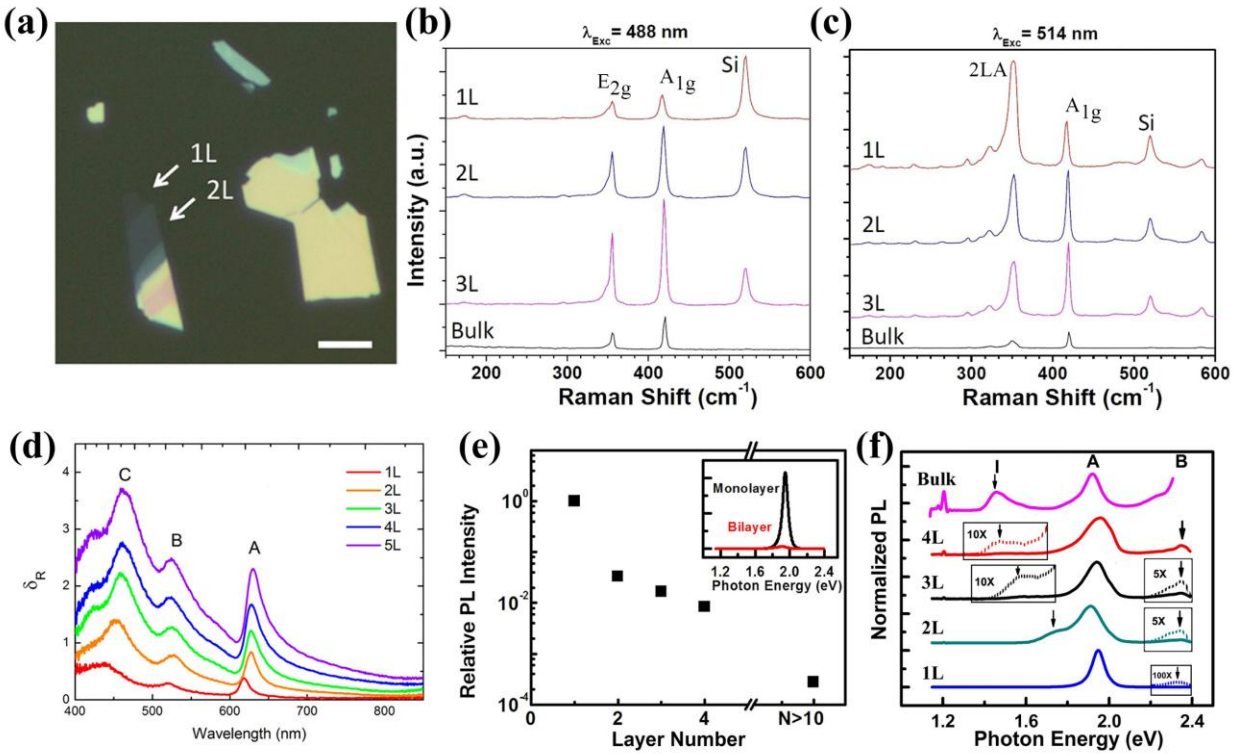

Figure 1.3: (a) Optical microscope images of mechanically exfoliated 1L, 2L, and bulk WS_2 on quartz substrates, adopted from ref.[27]; (b) and (c) Raman spectra of 1L, 2L, 3L, and bulk WS_2 under excitation wavelength of 488 nm and 514 nm, respectively, adopted from Ref.[30]; (d) UV-vis absorbance spectra of 1L, 2L, 3L, 4L and 5L WS_2 on quartz substrate, adopted from ref. [27]; (e) and (f) Relative PL emission intensity of WS_2 with layer numbers and normalized PL emission of 1L, 2L, 3L, 4L, and bulk 2D WS_2, adopted from ref. [26].

-ding to the out-of-plane and in-plane vibrations of the S and W atoms, respectively[31]. The out-of-plane mode, A_{1g}, is highly influenced by charge density and layer number, whereas the in-plane vibration mode E_{2g} is influenced by strain.[32] The separation of these fundamental phonon modes is characteristic of layer number and provides an indirect means of determining the layer number. When excited with 488 nm laser, the 2D WS_2 shows only two characteristic Raman modes (A_{1g} at 418 cm^{-1} and E_{2g} at 356 cm^{-1}) with a weaker 2LA phonon mode observed, as shown in **Fig. 1.3(b)**. However, when excited with 514 nm laser, in addition to fundamental modes, many second-order stronger modes are also observed, as displayed in **Fig. 1.3(c)**. For monolayer WS_2, the intensity of second order 2LA mode at 352 cm^{-1} is maximum, which decreases with increasing layer number,

whereas A_{1g} mode intensity increases with layer number. The stronger A_{1g} mode with increasing layer number is presumably due to stronger interlayer contributions to the electron-phonon coupling[30].

For atomically thin films, the differential reflectance provides an effective measure of absorbance. The differential reflectance spectra of mechanically exfoliated WS_2 with various layer numbers are displayed in **Fig. 1.3(d)**. For monolayer WS_2, the two strong absorption peaks A and B, originated from direct band-to-band transitions at K-K´ valley in the Brillouin zone around 615 and 533 nm, respectively.[33] With the increasing layer numbers, there is redshift in spectrum with A and B absorptions peaks at 625 nm and 550 nm, respectively for bulk WS_2.[27] The energy difference between A and B remains constant with layer number at 400 meV as a result of the splitting of VBM at K point. This is because of the spin-orbit coupling at the K point, which remains constant with layer number[26], as shown in **Fig. 1.2**. In addition to the direct band transition peaks, there is another peak labeled by C, originating from the optical transition between the density of states peak at the valence band and the conduction band. The relative PL emission intensities of WS_2 with layer number is shown in **Fig. 1.3(e)**. The monolayer WS_2 has a direct bandgap of 2.0 eV, giving rise to strong PL emission at room temperature.[34] The PL emission drastically quenches for bilayers and beyond, decreasing by approximately 99% for bilayer WS_2. The PL intensity is notably weak in bulk WS_2, consistent with its behavior as an indirect band-gap semiconductor in bulk form. The faint PL emission peak corresponding to the indirect bandgap transition shifts towards lower energy as the layer number increases and indicated by "I" in **Fig. 1.3(f).** These behaviors align perfectly with the calculated band structures.[26] In addition to the peaks originating from indirect transition and the prominent direct transition peak (A), a faint PL peak (B) is detected at a higher energy level. The origin of the B peak can be explained flowing way: The splitting between the A and B peaks is nearly identical, approximately 0.4 eV, across mono, bi, tri, and quad-layer samples. In 1L, the valence band edges at the K points exhibit spin splitting solely due to the strong spin-orbit coupling in the d-orbitals of the tungsten atom. In multilayers, however, both spin-orbit coupling and interlayer hopping contribute to the valence band splitting at the K points. Thus, the B peak is prominent at multilayer WS_2.

1.2. Synthesis of 2D WS_2

The growth/synthesis protocol of 2D WS_2 plays a significant role in their applications in optoelectronic, sensing, drug delivery, and so on. Top-down and bottom-up are two standard approaches for the synthesis of 2D nanomaterials. In the top-down method, nanomaterials are obtained by breaking down their bulk counterparts, whereas in the bottom-up method, atomic-range chemical or physical forces aid in the assembly of basic units in the formation of larger structures. Considerable efforts have been made to synthesize controllable, large-scale, high-quality monolayer to few-layer WS_2 using various top-down and bottom-up approaches, such as mechanical exfoliation, chemical exfoliation, hydrothermal methods, physical vapor deposition, atomic layer deposition (ALD), chemical vapor deposition (CVD), and others.

1.2.1. Mechanical exfoliation

The scotch-tape-aided mechanical exfoliation is a top-down method where thin layers of TMDs can be exfoliated from their bulk form.[35–37] Graphene was first obtained from graphite using scotch tape in 2004.[38] The mechanical exfoliation method provides WS_2 of exceptional quality and crystallinity, enabling the exploration of its pristine properties and subsequent device performances.[26,27,39–41] In this technique, a small quantity of high-quality natural bulk WS_2 crystal is affixed to a piece of adhesive tape, which is then repeatedly peeled off using sticky tape and pressed onto the substrate. Through this iterative process, WS_2 flakes of various shapes, sizes, and layer numbers are deposited onto the substrate. Despite its simplicity and cost-effectiveness, this method encounters challenges regarding repeatability and uniformity across large areas, rendering it impractical for real-world applications.

1.2.2. Chemical exfoliation

In addition to mechanical exfoliation, liquid phase exfoliation techniques such as ultrasonication and ion-intercalation are also utilized for the synthesis of 2D WS_2. These methods are highly straightforward and cost-effective and enable the synthesis of significant quantities of dispersed monolayer and few-layer WS_2 flakes. For the liquid phase exfoliation, high-quality bulk material is dispersed in polar organic solvents such as dimethylformamide (DMF), N-methylpyrrolidone (NMP), isopropyl alcohol (IPA) etc.[42] This solution undergoes sonication either via probe

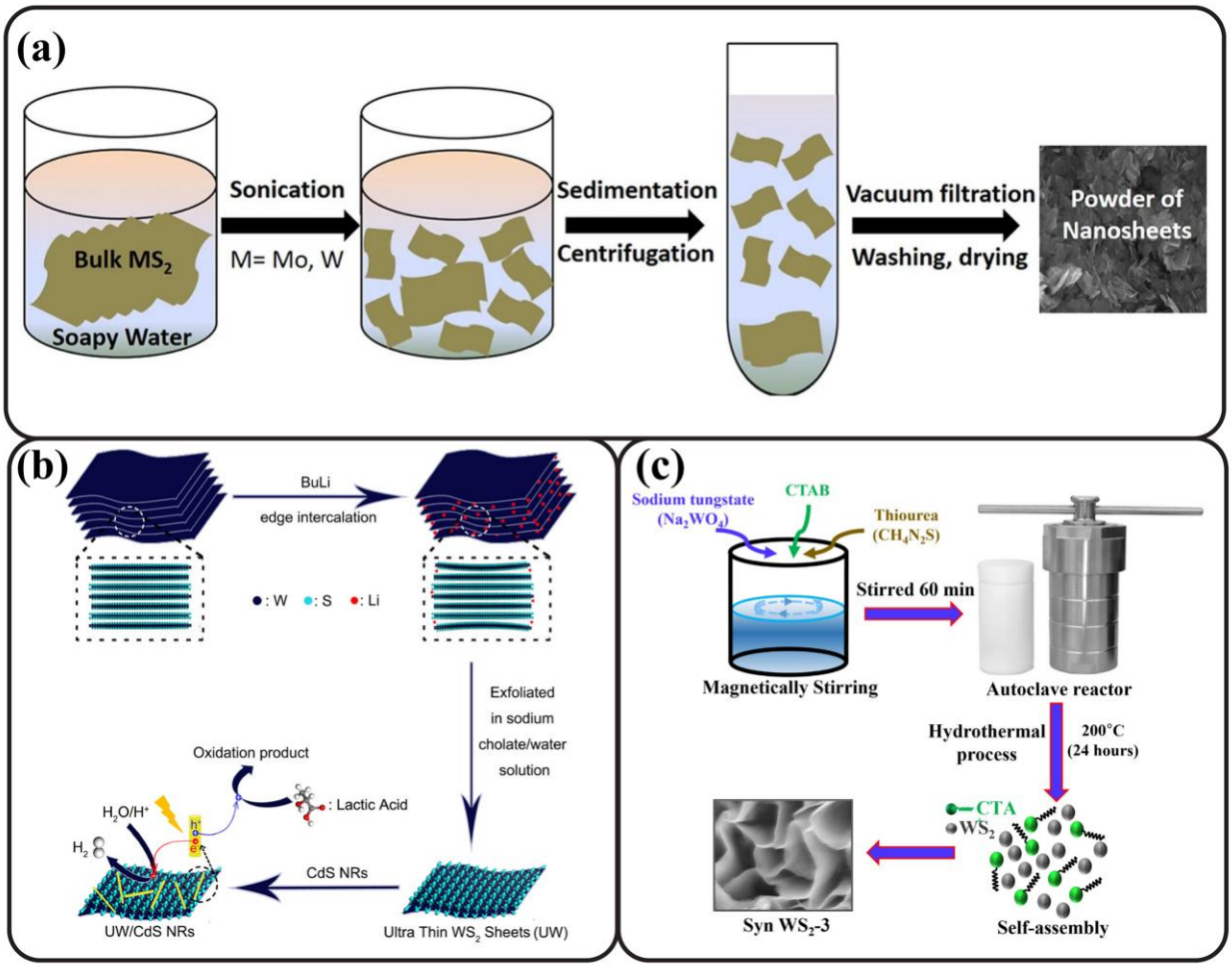

Figure 1.4: (a) Schematic representation of liquid exfoliation of a few layers WS_2 via solvent assistant sonication, Adopted from Ref.[42]; (b) Lithium-ion intercalation-assisted chemical exfoliation of monolayer WS_2 from bulk crystal, Adopted from Ref.[44]; (c) Schematics representation of the hydrothermal synthesis of WS_2 nanostructure. Adopted from Ref.[43]

sonication or bath ultrasonication followed by centrifugation to isolate the nanosheets, as illustrated in **Fig. 1.4(a)**. In this method of synthesis, there is limited control over the layer number and lateral size. Other chemical exfoliation techniques include ion intercalation-assisted exfoliation from bulk WS_2. In this method, metal ions such as lithium (Li) or sodium (Na) are introduced between the WS_2 layers, increasing the interlayer spacing and ultimately leading to layer separation, as illustrated in **Fig. 1.4(b)**. Mostly Li ions are used in this method. Alongside the top-down chemical route, hydrothermal synthesis is a prominent bottom-up approach for synthesizing WS_2. In this process, tungsten and sulfur sources are combined in an appropriate

solvent, which is then placed in an autoclave. The mixture is subjected to elevated temperatures in a hot air oven for 24 to 72 hours, allowing for the formation of WS_2[43]. A schematic representation of the hydrothermal synthesis process is shown in Fig. 1.4(c). There are advantages to employing chemical processes in synthesis, such as *in-situ* doping of 2D materials through s[45] as well as for functionalization with appropriate metal nanoparticles[46]. However, these techniques also come with some significant drawbacks, such as the potential loss of semiconducting properties with electrochemical intercalation. In addition, during the ultrasonication process, defects are introduced into the lattice of 2D WS_2, along with a reduction in flake size, which in turn limits the applicability of WS_2 in large-scale integrated circuits and optoelectronic devices.

1.2.3. Physical and chemical vapor deposition

The optoelectronic properties of 2D WS_2 strongly depend on the quality of the film. However, WS_2 layers obtained via chemical methods are not up to the standards required for optoelectronic devices. To overcome the limitations of chemical techniques, there have been many attempts to obtain high-quality 2D WS_2 films with controlled thickness and wafer-scale uniformity by various physical vapor deposition (PVD) techniques, such as sputtering,[47] pulsed laser deposition (PLD)[48], and molecular beam epitaxy (MBE)[49], as shown in **Fig.1.5.** These growth processes have been successful in achieving large-area growth of monolayer to few-layer WS_2 films. Nevertheless, these methods come with certain disadvantages. The films grown using those techniques have large area but exhibit sulfur vacancy sites, nonuniform film thickness, and poor crystallinity,[50] therefore resulting in performance variation among the devices and thus limiting their practicality in device applications. Other physical methods include sulfurization of tungsten film. In this process, a thin film of tungsten is deposited on sapphire substrate by e-beam evaporation of tungsten, and then annealing the film in the presence of sulfur vapour in order to transform the tungsten films into WS_2[51], as displayed in **Fig. 1.5(c)**. Till now, the primary challenge has been maintaining control over the wafer scale lateral dimensions and ensuring a consistent thickness of WS_2. In this regard, the CVD has attracted much attention because it is one of the most effective methods to synthesize high-quality large-area growth of atomically thin WS_2, which shows great potential toward device applications[52]. The high temperature-controlled chemical reactions between the tungsten and sulfur precursors form highest quality of WS_2 with minimum defects[30]. A schematic diagram for CVD growth of WS_2 is shown in **Fig. 15(d)**. This method has been shown

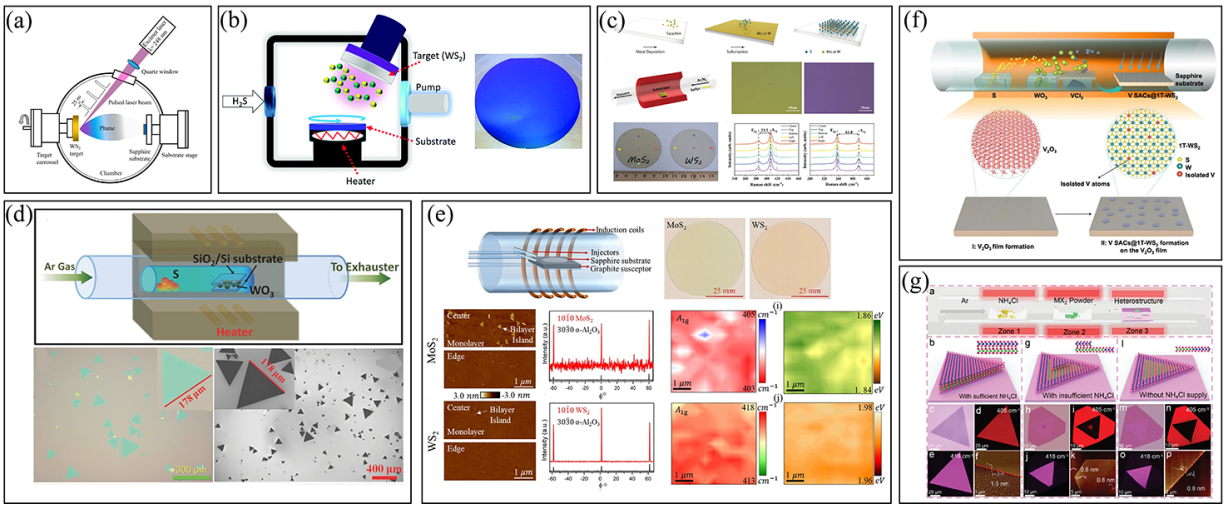

Figure 1.5: Schematics representation of: (a) Pulse laser deposition technique for large area WS_2, Adopted from Ref [50]; (b) RF sputtering method for depositing WS_2 film, Adopted from Ref[47]; (c) Wafer-scale synthesis of WS_2 films via sulfurization of tungsten film deposited by e beam evaporation technique, Adopted from Ref[51]; (d) Schematics representation of a thermal CVD for large area growth of WS_2 and corresponding images, Adopted from Ref [52]; (e) MOCVD growth of wafer-scale monolayer WS_2, Adopted from Ref[19]; (f) Schematic representation for the single step CVD growth of Vanadium doped WS_2 film, Adopted from Ref [53]; (g) Schematic representation for single-step CVD growth of WS_2-MoS_2 lateral HS, Adopted from Ref [55].

to be more feasible over other growth techniques because it could achieve large-area growth of WS_2 with precise chemical doping, leading to enhanced optoelectronic properties[53]. The doping possibility enables us to control the type of conductivity alongside resistivity similar to what is available for silicon technology[54], which one of the greatest milestones toward commercialization. In addition to the doping feasibility in the controlled growth, recent studies demonstrated the synthesis of lateral HS in single-step CVD, opening a topic for further exploration for applications in optoelectronic[21,22,55,56]. A schematic representation and optical images for single-step CVD growth of lateral HS are shown in **Fig 1.5(f)** and **Fig. 1.5 (g)**. Interestingly, the lateral HS exhibits excellent electronic properties such as high on-off ratio and mobility as compared to individual counterparts. Generally, the WS_2 grown by CVD is in the form of flakes having size in the order of mm to cm scale, but for practical device applications, we need wafer-scale uniformity. To overcome the lateral size limitation, MOCVD growth technique where one can grow wafer scale

WS_2 film[19], as displayed in **Fig. 1.5(e)**. Thus, there is a need for robust growth strategy for real-time commercial application of 2D TMDs.

1.3 Applications of WS_2

Given the widespread use of semiconducting devices in daily life, WS_2 holds significant potential for next-generation semiconductor technologies. One of the most distinct features of WS_2 is the widening bandgap as the number of layers decreases, transitioning from an indirect bandgap material in its 2L to the bulk counterpart to a direct bandgap in the 1L[57]. The finite bandgap in WS_2 makes it significantly superior for optoelectronic applications compared to the well-explored 2D material, graphene. Owing to unique properties such as a finite bandgap, excellent carrier mobility, thickness-dependent optical properties, transparency, flexibility, along biocompatibility, WS_2 has attracted considerable attention for a wide range of applications, from future-generation optoelectronics to healthcare[5,58]. Furthermore, the planar 2D structure facilitates the formation of HSs with other 2D materials. such as MoS_2, graphene, and WSe_2, without the need for precise lattice constant matching, thereby enhancing the overall properties. Lastly, the compatibility with the existing fabrication process makes it one of the most promising candidates for replacing conventional Si. In this section, we will discuss the promising applications of WS_2 and its HS systems in biosensing, photodetection, memristor, and artificial synapse applications and a brief summary of other future-generation applications.

1.3.1 Healthcare monitoring systems focused on biosensing

The sensing of bioanalytes and environmental pollutants is essential for continuous monitoring of public health in order to prevent a worldwide outbreak like SARS-CoV-2[59]. During the global COVID-19 pandemic, there was an immediate requirement for real-time mass screening of patients to curb the spreading of viral infections. Thus, we need a robust sensing system capable of detecting analytes in real time with high accuracy. The 2H hexagonal semiconducting 2D WS_2 possesses excellent optoelectronic properties suitable for use as a transducer in sensing systems. This makes it potentially valuable in creating healthcare devices for the real-time detection of bioanalytes. There are mainly three types of detection mechanisms: optical, electrochemical, and electrical.

The optical biosensors leverage the advanced and exceptional optical properties of 2D TMDs to detect bioanalytes. These biosensors are among the most sensitive, capable of detecting even a single analyte in real-time[60]. Common detection mechanisms in optical biosensors include Förster resonance energy transfer (FRET), surface-enhanced Raman spectroscopy (SERS), surface plasmon resonance (SPR), and fluorescence imaging. SERS detects changes in the Raman signal of samples before and after the adsorption of analytes on a SERS substrate. SPR is highly dependent on the refractive index, where analyte absorption causes local changes in the materials refractive index. FRET involves nonradiative energy transfer between two fluorophores via dipole-dipole coupling, and due to its sixth power law dependence, it is highly sensitive to distance changes between fluorophores. Consequently, fluorescence intensity modulation in the presence of a target analyte is widely used for detection. The high density of active sites in WS_2 helps in the sensitive detection of the biomarkers in the early stage of disease propagation[61]. 2D MoS_2 has been extensively studied for biosensing applications, while the potential of WS_2 has only recently begun to be explored[18,62]. The ability to quench the PL of a probe by WS_2 was utilized for ultralow detection of targeted DNA and other bioanalytes. In 2014, Xi et. al first showed the detection of microRNA-21 (miRNA-21), a breast cancer biomarker, using WS_2 NSs through duplex-specific nuclease signal amplification (DSNSA)[63]. The binding of highly fluorescent dye-labeled ssDNA onto the basal plane of WS_2 NSs quenches its FL intensity by almost 97%, via van der Waal interactions between ssDNA and WS_2 NSs. Binding with the targeted miRNA-21, the probe DNA formed a DNA/RNA heteroduplex, which detached from the WS_2, restoring its PL intensity and acted as the substrate for duplex-specific nuclease (DSN) cleavage. The DSN selectively cleaves the ssDNA from the heteroduplex, allowing the miR-21 to hybridize with another ssDNA. Later this PL quenching ability of WS_2 was used to detect other DNA and *E.coli*[64,65]. The schematic representation for *E. coli* sensing using highly fluorescent aptamers functionalized upconversion NPs and WS_2 NSs is displayed in **Fig. 1.6(a)**. The working mechanism for PL quenching-based optical biosensor using WS_2 as quencher is displayed in **Fig. 1.6(b)**[66]. Other than PL quenching, Dey et al. proposed a WS_2-based layer structure for SPR-based biosensing applications[67], and Wang et al. demonstrated a WS_2 layer-based SPR sensor with improved sensitivity of 2459.3 nm/RIU[68]. Shorie et at has selectively detected cardiac marker myoglobin using SERS active WS_2 NSs incorporated with AuNPs[69]. This SERS sensing system has a linear detection range over 10 fM to 0.1 μM with a lower detection limit of 0.5 aM. Thus, WS_2 is a promising

material for future generations applications in optical biosensing but there is a need for extensive study for real-time implementation of WS_2-based optical biosensors.

Electrochemical sensors are sensing platforms based on a three-electrode system, where redox (reduction-oxidation) reactions generate ions and charges, altering the electrochemical response. The three electrodes consist of the working electrode (WE), the reference electrode (RE), and the counter electrode (CE). All the potentials are measured relative to the reference electrode (RE), while the counter electrode (CE) completes the electrochemical cell connections. The WE is modified with nanomaterials for better electrochemical activity. The fundamental operating principle involves detecting Faraday currents through voltammetry or amperometry while modulating interfacial impedance using electrochemical impedance spectroscopy (EIS). The WE is modified with suitable biorecognition elements for detecting specific analytes via redox reaction,

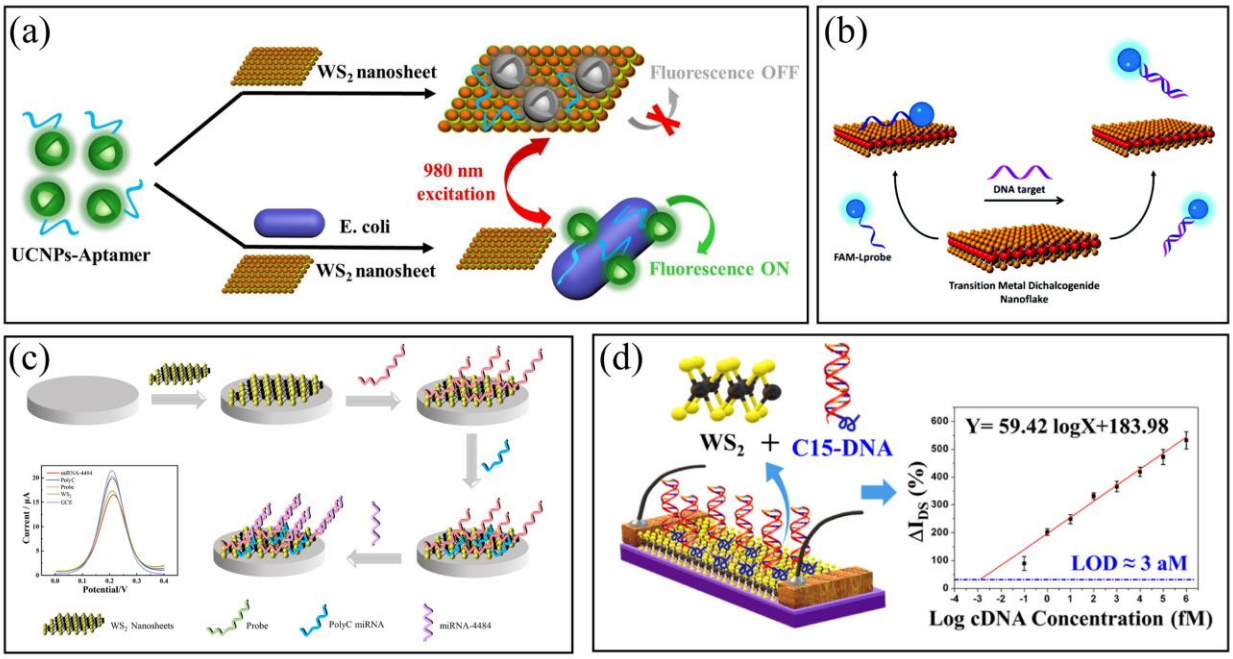

Figure 1.6: (a) Schematic representation for the detection of *E. coli* using aptamer and WS_2 NSs; The aptamer functionalized upconversion NPs adsorbed to WS_2 NSs, resulting in the quenching of PL intensity. Upon binding with targeted *E. coli* restored its PL, Adopted from Ref [65]; (b) Schematic representation of WS_2-based optical biosensors using its PL quenching ability, Adopted from Ref[66]; (c) Working principles of WS_2 based electrochemical biosensors for the detection of miRNA-4484, Adopted from Ref[71]; (d) Schematics representation of WS_2-based FETs biosensors for ultralow detection of DNA, Adopted from Ref [72].

which generate or suppress electrons or ions and change the current across the WE. In the case of EIS, analytes adsorbed onto the modified WE surface influence the electrochemical current or interfacial impedance. The sensing response is determined by quantitatively correlating changes in interfacial impedance or electrochemical current with the number of analytes present. The incorporation of TMDs in the electrochemical biosensors enhances its lower detection limits[18]. Among the TMD family members, WS_2 has demonstrated a promising ability to distinguish between ssDNA and dsDNA, driving the use of TMD nanosheets in biosensing applications[63]. Yang et al. have incorporated poly (indole-6-carboxylic acid) (PIn6COOH) with WS_2 nanosheets and modified the WE to create a sensing interface for developing an electrochemical DNA biosensor[70]. By mobilizing the probe DNA to the surface, the system was able to detect targeted DNA for a wide range of 10^{-17} to 10^{-11} mol/L, having a detection limit of 2.8×10^{-18} mol/L. Using the same technique, Li et al. developed an electrochemical biosensor that employs a self-assembled DNA aptamer on a WS_2 nanostructure for the detection of ATP[73]. In this case, the aptamers were modified with the thiol functional group in order to have covalent bonding with the WS_2, which eventually enhances the selectivity toward ATP. WS_2 has also been used for the electrochemical detection of miRNA using its high-stability[71]. The schematic representation for electrochemical detection of miRNA using WS_2 NSs is displayed in **Fig. 1.6(c)**. The electrochemical performance of WS_2 was improved by incorporating metal NPs such as Au, Ag, and Pt. Shuai et al. synthesized WS_2 NSs and modified them with AuNPs for highly sensitive electrochemical DNA detection[74]. The integration of AuNPs not only enhanced sensitivity but also enabled covalent bonding with thiol-modified aptamers, improving selectivity with a detection limit as low as 0.12 fM.

Electrical biosensors convert information about analytes into user-readable electrical signals, such as changes in current or resistance. The fundamental working principle of FETs is that the current flowing between the source and drain terminals is controlled by a third terminal, called the gate. FETs are critical components in modern electronic circuits with well-established fabrication technologies. As a result, electrical detection can potentially be integrated with various modern electronic devices for real-time bioanalyte detection. These biosensors consist of a semiconductor transducer and a bioreceptor connected to it. Bioanalytes interact with the semiconducting transducer through the receptor, altering the transducers electrical properties via charge transfer mechanisms. The binding of a bioanalyte to the semiconductor surface acts like applying a potential bias to the gate terminal, which leads to changes in the drain current. The key advantage

Table 1.1: Comparison of the performance parameters of reported biosensors based on 2D WS_2.

Sensing Materials	Sensing Method	Target analytes	Linear Range	Detection limit	Reference
WS_2 NSs	Fluorescence	miRNA-21	0.001-10 nM	300 fM	[63]
WS_2 NSs	Fluorescence	Peptide nucleic acid	1-20 nM	500 pM	[64]
WS_2 NSs	Fluorescence	E. coli	85-85×10^7 CFU/mL	17 CFU/mL	[65]
WS_2 NSs	Fluorescence	DNA	13.3-143 nM	NA	[66]
WS^2 NSs	Surface plasmon resonance	NA	NA	NA	[67]
WS_2 NSs	Surface plasmon resonance	NA	NA	NA	[68]
AuNPs-WS_2 NSs	Surface-enhanced Raman spectroscopy	myoglobin	10 fg/mL - 0.1 μg/mL	10 fg/mL	[69]
WS_2-NSs/PIn6COOH	Electrochemical	DNA	1×10^{-17}-1×10^{-11} mol/L	2.3×10^{-18} mol/L	[70]
WS_2 NSs	Electrochemical	miRNA4484	1 aM - 100 fM	1.61 aM	[71]
WS_2 NSs	Electrochemical	ATP and Hg^{2+}	0.1 μM-5 mM and 0.1 nM-500nM	1.5 nM and 0.5pM	[73]
1L-WS_2	Electrical	DNA	10^{-16}-10^{-9} M	2 aM	[72]
WS_2-acetylene black	Electrochemical	DNA	0.001-100 pM	0.12 fM	[74]
1L-WS_2	Electrical	Ampicillin	10^{-12}-10^{-6} M	0.55 pM	[75]

of FET biosensors is their improved sensitivity and lower LoD[76]. As a semiconducting material, the WS_2 is an excellent choice of channel for FETs has a high on/off ratio of 10^8 and high mobility[19,77]. But WS_2-based FETs biosensors have not been explored yet exist only a few

reports[72,75]. Bahri et al. detected targeted DNA using WS_2 FETs with an extraordinary low detection limit of 3 aM with a wide linear range from 0.1 fM to 1 nM[72]. The schematic diagram of a WS_2-based FET biosensor for detecting DNA is displayed in **Fig. 1.6(d)**. Wei et al. used the same strategy for real-time ultrasensitive detection of ampicillin[75]. AuNPs were used to bind the aptamer probe with monolayer WS_2 for selective detection. Their sensing system showed a linear response from 10^{-12} M to 10^{-6} M with a detection limit of 0.556 pM. A detailed comparison of biosensing applications using 2D WS_2 is tabulated in **Table 1.1**. More specific research is needed in order to use the excellent optoelectronic properties of WS_2 for FET-based biosensors.

1.3.2. Photodetector

Photodetectors are electrical devices engineered to convert light signals into user-readable electrical signals, playing a crucial role in modern society across a wide range of practical applications from imaging, optical communications to sensing applications[78]. Owing to the exceptional optical and optoelectronic properties of 2D materials, they have the potential to surpass conventional silicon-based photodetectors[79]. Graphene, a well-known 2D material, has shown remarkable properties such as high carrier mobility, broadband response and rapid response time, making it a promising candidate for a wide range of photodetectors[80]. However, despite these excellent characteristics, its zero bandgap and low light absorption across the visible spectrum are drawbacks for achieving high-performance photodetectors. In this regard, WS_2 is one of the most suitable 2D materials because of its tunnelable bandgap from 1.2 to 2.0 eV with a high absorption coefficient, excellent mobility, and efficient electron-hole generation under photo illumination[58]. The schematic diagram of a WS_2 based photodetector is shown in **Fig. 1.7(a)**. There have been reports on WS_2-based photodetectors in the visible spectrum using monolayer, few layers and multilayer WS_2[9,82–87]. However, the performance of these devices is not up to the standards of typical commercial photodetectors. For instance, Perea-López et al. observed a low responsivity on the order of µA/W in multilayer WS_2 PD within the visible range.[82] By passivating the sulfur vacancy sites, the responsivity of few-layered WS_2 was enhanced to few mA/W to 5.7 A/W; however, the on/off ratio dropped by a few orders. This decrease was caused by the increase in dark current due to the electron doping effect.[83,88] The photoresponse was improved by several orders and reached o on/off rato of ~ 10^8 in a 3-terminal FET configuration, but it remains low in two terminal devices[9]. Power dependent I-V characteristics of a Si/WS_2 HS is displayed in **Fig.**

1.7(b). The photocurrent increases with increasing illumination intensity, which is attributed to a greater number of photoinduced generation with intensity. The photoinduced carrier generation strongly depends upon the bandgap of the semiconducting channel material and the wavelength of the incident illuminations. The variation of photoresponse with incident light wavelength is shown in **Fig. 1.7(c)**. The responsivity of monolayer WS_2 PD in two-terminal devices was enhanced by incorporating plasmonic nanoparticles[89]. The integration of plasmonic gold nanoparticles significantly boosts visible absorption, leading to improved responsivity and on/off ratios. Therefore, optimizing the doping levels can further enhance the performance of WS_2-based photodetectors. The formation of Schottky junction with WS_2 improves the performance in contrast to the Ohmic junctions[92] by reducing the dark current and facilitating charge separation due to the built-in potential.[93] The 2D WS_2 synthesized by CVD exhibits high stability with low defect density and high crystalline quality, and usually possesses good mobility at room temperature.[94] Interestingly, the carrier mobility in 2D WS_2 is layer-dependent. Specifically, 2L-

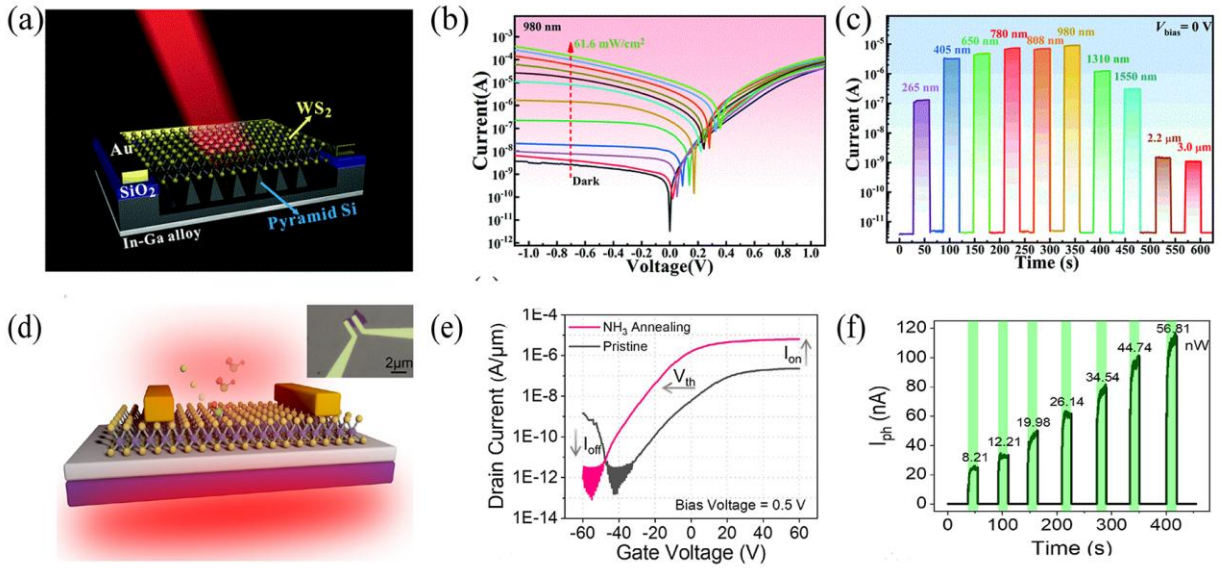

Figure 1.7: (a) Schematic diagram WS_2/Si HS-based photodetector; (b) I-V characteristics of the photodetector under different illumination intensities; (c) temporal photoresponse properties of the WS_2/pyramid Si heterojunction device under light illumination with different wavelengths; (d) Schematic illustration of few-layer WS_2 device with NH_3 atmosphere annealing. Inset is the optical microscopy image of the device; () Electrical transport characteristics on a logarithmic scale of WS_2 device before and after NH_3 annealing; (f) Time dependence of the photocurrent with varying laser powers. Image a-c are adopted from Ref. [81]; and image d-f are adopted from Ref[9].

Table 2.2: Comparison of the performance parameters of reported photodetectors based on 2D WS_2.

Material	**Wavelength (nm)**	**On/off ratio**	**Responsivity (A/W)**	**Detectivity (Jones)**	**Response time**	**Ref.**
WS_2 nanotubes	633	391	3.14	--	228 μs /330 μs	[90]
Few layer WS_2	514	--	92 $\times 10^{-6}$	--	5.3 ms	[82]
Multilayer WS_2	633	25	5.7	--	20 ms	[83]
Monolayer WS_2	405	10^3	290	52×10^{14}	0.2 s /0.07 s	[91]
Few layer WS_2	532	10^8	2.97	10^{10}	--	[9]
Multilayer WS_2	532	--	0.51	2.7×10^9	4.1 s/4.4 s	[85]
Multilayer WS_2	365	--	53.4	1.22×10^{11}	--	[86]
Bilayer WS_2	457	1.4×10^4	3×10^3	5×10^{12}	59μs/87 μs	[87]
Monolayer WS_2	532	8×10^3	5×10^{-3}	4.9×10^9	560 μs	[88]
Few layer WS_2	590	10^3	1050	--	100 ms/200 ms	[89]
Multilayer WS_2	405	10^4	3.45	4.94×10^{11}	7.8/ 37.3 ms	[92]
Bilayer WS_2	520 nm	--	2.5 $\times 10^{-3}$	3.55×10^8	2.6 ms/1.5 ms	[84]
Bilayer WS_2	405 nm	10^5	1.2	2.2×10^{12}	0.35 s/15 ms	[29]
Multilayer WS_2/Si HS	980 nm	2×10^4	0.29	2.6×10^{14}	5.2/22.3 μs	[81]

-WS_2 displays mobility that is twice that of the monolayer WS_2, and it possesses enhanced photo-absorption due to higher thickness, underscoring the significance of using bilayer WS_2 in photodetection applications[28]. Chemical doping on the WS_2 surface yields improved photodetection performance as a result of efficient charge transfer[9]. The schematic diagram and

optical image of NH_3 annealed WS_2 photodetector is displayed in **Fig. 1.7(d)**. From the transfer characteristics in Fig. 1.7(e) one can observe an enhanced on-off ratio by an order to 10^8 as a result of electron transfer from NH_3 to WS2 surface. The photocurrent increased progressively with increasing illumination, as shown in **Fig. 1.7 (f)**. A detailed comparison of WS_2 based photodetector reported in the literature is tabulated in **Table 1.2.**

1.3.3 Memristor and Artificial Synapse

The memristor, a term derived from "memory" and "resistor," has recently become a crucial component in brain-inspired neuromorphic computing. Neuromorphic computing, which emulates the brain's highly interconnected and energy-efficient neural networks, has garnered significant interest as an innovative approach[95]. It offers not only traditional data processing and storage solutions but also enhances capabilities for advanced tasks such as cognition, inference, and learning. These devices can adjust their resistance across multiple states by remembering previous electrical inputs, allowing them to emulate the function of biological synapses within neural networks. This emerging technology, capable of massive parallel processing, is expected to overcome the fundamental limitations of current von Neumann computing architectures, where the separation of processing and memory units leads to inefficiencies in digital computation[96]. To harness the advantages of the human brain, particularly its ability to perform complex tasks with minimal energy, systems must be designed to mimic biological neural networks, which consist of neurons and synapses. Biological synapses, which enable time-dependent transmission of signals between neurons, are essential for spiking neural networks (SNNs) that facilitate parallel computing[97]. In this context, artificial synapses replicating event-driven synaptic behaviors have been developed using technologies such CMOS transistors, emerging transistors with ferroelectric or electrochemical gate coupling, and memristors based on non-volatile memory[97]. Among these, memristors are particularly promising for neuromorphic computing applications due to their intrinsic ability to store historical information from electrical signals, even within a single unit. Among various materials used for memristors such as metal oxides, organic compounds, and low-dimensional nanomaterials, 2D layered materials have been extensively studied for their exceptional stability, electrical tunability, low power switching capabilities, and compatibility with existing fabrication processes. MoS_2 is one of the 2D materials being widely researched for

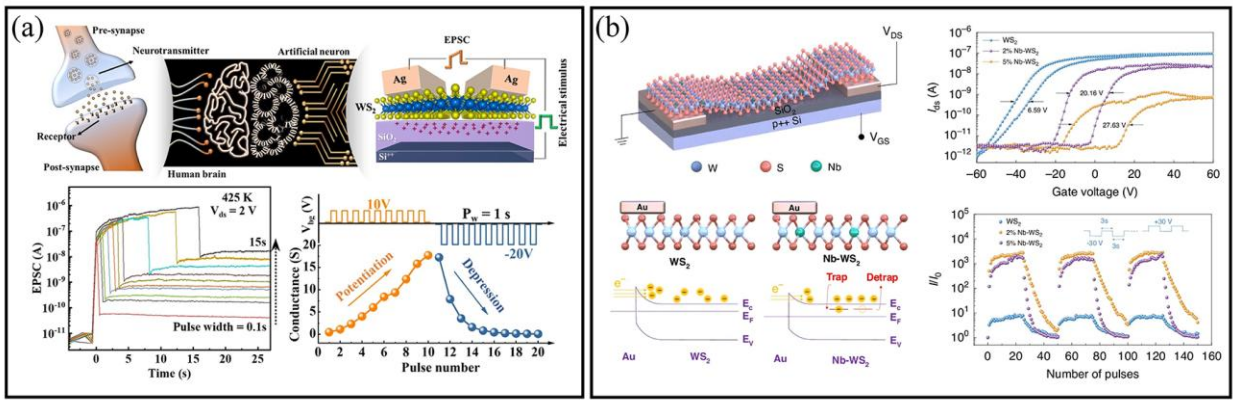

Figure 1.8: (a) A schematic representation of a WS_2-based artificial synapse with and its characteristics as synapse; Adopted from Ref.[101] (b) Memory and artificial synapse based on Nb-doped WS_2; Adopted from Ref [107].

neuromorphic computing applications using gate pulses or photo pulses[95,98–100]. The schematic representation along with synaptic characteristics of a WS_2 FETs-based artificial synapse is displayed in **Fig. 1.8(a)**[101]. Most of the synaptic behaviors were explained by sulfur vacancies or ion migrations caused by defect sites. Qiu et al. were the first to demonstrate potential applications of 2D WS_2 in non-volatile memory devices by stacking WS_2 between highly conductive graphene and insulating hBN, achieving a memory window of 20 V[102]. Later, Wang et al. utilized the high trap charge density of multilayer WS_2 to achieve a smaller memory window of 2.26 V under a gate bias of ±5 V[103]. However, these two-terminal memristors faced challenges with low sensitivity and reproducibility. To address this, an array of ZnO/WS_2-based two-terminal devices was integrated, significantly improving reproducibility and neuromorphic computing capabilities[104]. The non-uniform distribution of oxygen vacancies facilitates charge trapping and detrapping. In addition to the oxygen vacancy assisted memory, the generation of oxygen ions via plasma treatment in the WS_2 enhances the synaptic characteristics[105]. The oxygen vacancy based memristor has higher operating voltage and higher power consumption, but the power consumption was reduced by many fold using sulfur or tungsten vacancy based synapses[106]. Mallik et al. used the migration of Na^+ ions into WS_2 films at high temperature for synaptic application, Since the ion induced memory devices have higher response and endurance[101]. By using the gate tuneability, the response of the ionotropic memory devices using WS_2 demonstrate reverse hysteresis with memory windows exceeding 25 V and an extinction ratio greater than 10^6. The memristor exhibit stable retention and durability, enduring over 100 sweep cycles and 400 pulse cycles. Additionally, they

offer 6-bit pulse-programmable memory capabilities, spanning six orders of magnitude in current levels. In addition to ionic synapse, the doping of niobium (Nb) with WS_2 which replaces tungsten atoms uniformly through the flake, also exhibits synaptic behavior. Interestingly the transistor switching ratio improved by 10^3 times as compared to pristine WS_2[107]. The extraordinary PL emission of monolayer WS_2 was first utilized as a complete optical synapse[108]. Recently, HSs based on 2D materials also gained much attention for their applications as artificial synapse[109,110]. The schematic representation along with synaptic characteristics of a WS_2 FETs based artificial synapse is displayed in **Fig. 1.8(b)**. This HS enhances the ion or charge migration faster increasing the device speed. There is a need for robust studies for real time applications of WS_2 as artificial synapses to mimic the function of human synapses. The progress of WS_2 based memristor and synapse is tabulated in Table 1.2:

1.3.4 Other applications of WS_2

In addition to the above-mentioned applications, WS_2 and its HS are also being explored for many other applications such as hydrogen production[111], energy storage[14], gas sensors[112], heavy metal ion sensing[113] and so on. The rapid pace of human industrialization has led to significant challenges, including a global energy crisis and worsening global warming. Our excessive reliance on fossil fuels has also contributed to environmental pollution. Addressing the energy crisis requires urgent exploration of alternative energy sources, which has become a critical area of research. Among renewable energy options, hydrogen production is viewed as a clean and storable energy resource. In this context, WS_2 has attracted considerable attention as a promising photocatalyst for efficient hydrogen production through water splitting[114]. In addition to energy production, storage of energy remains a bigger challenge. An ideal, efficient energy storage system should be capable of delivering energy over an extended period without compromising its efficiency. Devices with a longer cycle life reduce the need for frequent replacements, thereby lowering replacement costs and minimizing the need for recycling used batteries or supercapacitors. As a result, cycle life has become an increasingly critical factor in the development of efficient energy storage systems. Among the available options, supercapacitors are currently one of the best energy storage devices for applications demanding long cycle life. In this regards WS_2 is one of the most suitable options for supercapacitor applications[115,116]. Thus,

WS_2 holds great potential for numerous next-generation applications and requires further research to meet real-world demands.

1.4. Challenges in the Fabrication of 2D WS_2 and its Heterostructures and Their Applications

Over the past decade, 2D WS_2 has garnered significant attention, leading to extensive research into its synthesis, property tuning, and potential applications. Many researchers have explored these aspects, yet several challenges remain for large-scale practical device applications. First, achieving reproducible growth of uniform, large-area, high-quality monolayer WS_2 on an industrial scale remains difficult. Additionally, the quality of WS_2 produced through various synthesis techniques has yet to match that of mechanically exfoliated WS_2 flakes. In chemical exfoliation methods, controlling layer number, flake size, purity, and phases of WS_2 continues to pose a major challenge. Advancements in the effective synthesis of stable, defect-free WS_2 and its alloys are still needed. Chemical doping, which can enhance charge transport and other properties, also remains difficult to control and requires further investigation. Second, integrating WS_2 with other materials to form hybrid HSs has revealed unique properties that are promising for optoelectronic devices. However, while such devices have been successfully fabricated for scientific research and need further robust understanding for commercialization. Third, WS_2-based HSs with other 2D materials have shown potential for various applications. In light-harvesting devices, however, poor interfacial contact often leads to low carrier mobility a significant drawback for electronic applications. A deeper understanding and optimization of these interfacial properties are necessary. Furthermore, band engineering in WS_2-based HSs could lead to hybrid materials with superior electrical performance and tunable band structures, enriching the field of HS research. Lastly, a comprehensive understanding of charge carrier dynamics, which are crucial for numerous applications, remains an important area for both experimental and theoretical research.

1.5. Focus of the Present Thesis

Although WS_2 has demonstrated considerable potential, several challenges still remain for the fabrication of well-controlled layer-dependent large-area WS_2 and its HSs for a wide range of applications in nanotechnology. In the present thesis, we have made an effort to control the

fabrication of large-area monolayer and bilayer WS_2 and their HSs with other semiconductors to achieve superior properties. The main objectives of the present thesis are as follows:

- Synthesis of large-area high-quality 1L and 2L-WS_2 by CVD method.
- Study the growth mechanism of 2D WS_2 by tuning the different growth parameters to obtain high-quality large-area controlled growth.
- Asymmetric contact-induced selective doping of CVD-grown 2L-WS_2 and its application in high-performance photodetection.
- Bi_2Se_3 Contact-Based High-Performance Field Effect Transistor using Monolayer MoS_2 and its Application as Flexible Photodetector.
- Controlled Synthesis of WS_2-MoS_2 Lateral HS Using CVD and Its Application in High-Performance Field Effect Transistor.
- Highly Sensitive and Selective Optical Detection of Staphylococcus aureus using Thiol Functionalized Monolayer WS_2 Grown by Chemical Vapor Deposition.
- Fast Detection of Staphylococcus aureus using thiol-functionalized WS_2 Quantum Dots and Bi_2O_2Se Nanosheets Hybrid Through Photoluminescence Recovery Mechanism.

1.6. Organization of the Thesis

The entire thesis is organized into eight chapters. **Chapter 1** provides a concise overview of the reported research on key properties, various growth techniques, and the potential applications of WS_2, ranging from healthcare sensing to optoelectronics. **Chapter 2** details the controlled growth of high-quality, large-area monolayer, bilayer WS_2 using CVD technique by optimizing growth parameters such as carrier gas, temperature, precursors, pressure, and duration. In **Chapter 3**, we examine the metal contact-induced asymmetric doping effect in CVD-grown monolayer and bilayer WS_2 and its impact on improved photodetection performance. **Chapter 4** focuses on enhancing the performance of monolayer MoS_2 FETs and their application in flexible photodetection using non-metal Bi_2Se_3 contacts. **Chapter 5** discusses the controlled single-step CVD growth of WS_2-MoS_2 lateral HSs and their application in high-performance FETs. **Chapter 6** explores the thiol functionalization of monolayer WS_2 for highly sensitive detection of *S. aureus* through strong PL emission. **Chapter 7** covers optical detection of *S. aureus* using highly

luminescent WS_2 QDs and $Bi_2O_2Se_3$ nanosheets. Finally, **Chapter 8** summarizes the key findings, draws important conclusions from the research, and outlines the future scope of the work.

References

(1) De, S.; Coleman, J. N. Are There Fundamental Limitations on the Sheet Resistance and Transmittance of Thin Graphene Films? *ACS Nano* **2010**, *4* (5), 2713–2720. https://doi.org/10.1021/nn100343f.

(2) Jiang, J.; Wen, Y.; Wang, H.; Yin, L.; Cheng, R.; Liu, C.; Feng, L.; He, J. Recent Advances in 2D Materials for Photodetectors. *Adv. Electron. Mater.* **2021**, *7* (7), 2001125. https://doi.org/10.1002/aelm.202001125.

(3) Mia, A. K.; Sinha, S.; Giri, P. K. Highly Sensitive and Selective Optical Detection of *Staphylococcus Aureus* Using Thiol Functionalized Monolayer Tungsten Disulfide Grown by Chemical Vapor Deposition. *Sens. Actuators Rep.* **2024**, *8*, 100214. https://doi.org/10.1016/j.snr.2024.100214.

(4) Choi, W.; Choudhary, N.; Han, G. H.; Park, J.; Akinwande, D.; Lee, Y. H. Recent Development of Two-Dimensional Transition Metal Dichalcogenides and Their Applications. *Mater. Today* **2017**, *20* (3), 116–130. https://doi.org/10.1016/j.mattod.2016.10.002.

(5) Uthappa, U. T.; Nehra, M.; Kumar, R.; Dilbaghi, N.; Marrazza, G.; Kaushik, A.; Kumar, S. Trends and Prospects of 2-D Tungsten Disulphide (WS_2) Hybrid Nanosystems for Environmental and Biomedical Applications. *Adv. Colloid Interface Sci.* **2023**, *322*, 103024. https://doi.org/10.1016/j.cis.2023.103024.

(6) Bin Rafiq, M. K. S.; Amin, N.; Alharbi, H. F.; Luqman, M.; Ayob, A.; Alharthi, Y. S.; Alharthi, N. H.; Bais, B.; Akhtaruzzaman, M. WS_2: A New Window Layer Material for Solar Cell Application. *Sci. Rep.* **2020**, *10* (1), 771. https://doi.org/10.1038/s41598-020-57596-5.

(7) Wang, Q.; Wee, A. T. S. Upconversion Photovoltaic Effect of WS_2/2D Perovskite Heterostructures by Two-Photon Absorption. *ACS Nano* **2021**, *15* (6), 10437–10443. https://doi.org/10.1021/acsnano.1c02782.

(8) Tan, H.; Fan, Y.; Zhou, Y.; Chen, Q.; Xu, W.; Warner, J. H. Ultrathin 2D Photodetectors Utilizing Chemical Vapor Deposition Grown WS_2 With Graphene Electrodes. *ACS Nano* **2016**, *10* (8), 7866–7873. https://doi.org/10.1021/acsnano.6b03722.

(9) Sun, J.; Lin, Z.; Jia, X.; Li, H.; Song, C.; Pan, F.; Fang, L.; Zhang, J.; Wang, Y. High-Performance 2D WS_2 Photodetector Enhanced by Charge-Transfer Doping through NH_3 Annealing. *Mater. Today Phys.* **2023**, *35*, 101133. https://doi.org/10.1016/j.mtphys.2023.101133.

(10) Kim, J.; Venkatesan, A.; Phan, N. A. N.; Kim, Y.; Kim, H.; Whang, D.; Kim, G.-H. Schottky Diode with Asymmetric Metal Contacts on WS_2. *Adv. Electron. Mater.* **2022**, *8* (3), 2100941. https://doi.org/10.1002/aelm.202100941.

(11) Jaffery, S. H. A.; Kim, J.; Dastgeer, G.; Hussain, M.; Ali, A.; Hussain, S.; Eom, J.; Hong, S.; Jung, J. Thickness-Dependent, Gate-Tunable Rectification and Highly Sensitive

Photovoltaic Behavior of Heterostructured GeSe/WS_2 p–n Diode. *Adv. Mater. Interfaces* **2020**, *7* (23), 2000893. https://doi.org/10.1002/admi.202000893.

(12) Voiry, D.; Yamaguchi, H.; Li, J.; Silva, R.; Alves, D. C. B.; Fujita, T.; Chen, M.; Asefa, T.; Shenoy, V. B.; Eda, G.; Chhowalla, M. Enhanced Catalytic Activity in Strained Chemically Exfoliated WS_2 Nanosheets for Hydrogen Evolution. *Nat. Mater.* **2013**, *12* (9), 850–855. https://doi.org/10.1038/nmat3700.

(13) Li, Y.; Wu, X.; Zhang, H.; Zhang, J. Interface Designing over WS_2/W_2C for Enhanced Hydrogen Evolution Catalysis. *ACS Appl. Energy Mater.* **2018**, *1* (7), 3377–3384. https://doi.org/10.1021/acsaem.8b00550.

(14) Mohan, V. V.; Manuraj, M.; Anjana, P. M.; Rakhi, R. B. WS_2 Nanoflowers as Efficient Electrode Materials for Supercapacitors. *Energy Technol.* **2022**, *10* (3), 2100976. https://doi.org/10.1002/ente.202100976.

(15) Liang, A.; Zhang, Y.; Jiang, F.; Zhou, W.; Xu, J.; Hou, J.; Wu, Y.; Ding, Y.; Duan, X. Electrochemical Self-Assembly of a 3D Interpenetrating Porous Network PEDOT-PEG-WS_2 Nanocomposite for High-Efficient Energy Storage. *J. Phys. Chem. C* **2019**, *123* (41), 25428–25436. https://doi.org/10.1021/acs.jpcc.9b05227.

(16) Gong, F.; Luo, W.; Wang, J.; Wang, P.; Fang, H.; Zheng, D.; Guo, N.; Wang, J.; Luo, M.; Ho, J. C.; Chen, X.; Lu, W.; Liao, L.; Hu, W. High-Sensitivity Floating-Gate Phototransistors Based on WS_2 and MoS_2. *Adv. Funct. Mater.* **2016**, *26* (33), 6084–6090. https://doi.org/10.1002/adfm.201601346.

(17) Hwan Lee, S.; Lee, D.; Sik Hwang, W.; Hwang, E.; Jena, D.; Jong Yoo, W. High-Performance Photocurrent Generation from Two-Dimensional WS_2 Field-Effect Transistors. *Appl. Phys. Lett.* **2014**, *104* (19), 193113. https://doi.org/10.1063/1.4878335.

(18) Mia, A. K.; Meyyappan, M.; Giri, P. K. Two-Dimensional Transition Metal Dichalcogenide Based Biosensors: From Fundamentals to Healthcare Applications. *Biosensors* **2023**, *13* (2), 169. https://doi.org/10.3390/bios13020169.

(19) Sebastian, A.; Pendurthi, R.; Choudhury, T. H.; Redwing, J. M.; Das, S. Benchmarking Monolayer MoS_2 and WS_2 Field-Effect Transistors. *Nat. Commun.* **2021**, *12* (1), 693. https://doi.org/10.1038/s41467-020-20732-w.

(20) Chen, Y.; Sun, M. Two-Dimensional WS_2 /MoS_2 Heterostructures: Properties and Applications. *Nanoscale* **2021**, *13* (11), 5594–5619. https://doi.org/10.1039/D1NR00455G.

(21) Zhang, Z.; Huang, Z.; Li, J.; Wang, D.; Lin, Y.; Yang, X.; Liu, H.; Liu, S.; Wang, Y.; Li, B.; Duan, X.; Duan, X. Endoepitaxial Growth of Monolayer Mosaic Heterostructures. *Nat. Nanotechnol.* **2022**, *17* (5), 493–499. https://doi.org/10.1038/s41565-022-01106-3.

(22) Vu, V. T.; Phan, T. L.; Vu, T. T. H.; Park, M. H.; Do, V. D.; Bui, V. Q.; Kim, K.; Lee, Y. H.; Yu, W. J. Synthesis of a Selectively Nb-Doped WS_2–MoS_2 Lateral Heterostructure for a High-Detectivity PN Photodiode. *ACS Nano* **2022**, *16* (8), 12073–12082. https://doi.org/10.1021/acsnano.2c02242.

(23) Cong, C.; Shang, J.; Wang, Y.; Yu, T. Optical Properties of 2D Semiconductor WS_2. *Adv. Opt. Mater.* **2018**, *6* (1), 1700767. https://doi.org/10.1002/adom.201700767.

(24) Yuan, Y.; Pan, J.; Wang, X.; Fang, Y.; Song, C.; Wang, L.; He, K.; Ma, X.; Zhang, H.; Huang, F.; Li, W.; Xue, Q.-K. Evidence of Anisotropic Majorana Bound States in 2M-WS_2. *Nat. Phys.* **2019**, *15* (10), 1046–1051. https://doi.org/10.1038/s41567-019-0576-7.

(25) Voiry, D.; Mohite, A.; Chhowalla, M. Phase Engineering of Transition Metal Dichalcogenides. *Chem. Soc. Rev.* **2015**, *44* (9), 2702–2712. https://doi.org/10.1039/C5CS00151J.

(26) Zeng, H.; Liu, G.-B.; Dai, J.; Yan, Y.; Zhu, B.; He, R.; Xie, L.; Xu, S.; Chen, X.; Yao, W.; Cui, X. Optical Signature of Symmetry Variations and Spin-Valley Coupling in Atomically Thin Tungsten Dichalcogenides. *Sci. Rep.* **2013**, *3* (1), 1608. https://doi.org/10.1038/srep01608.
(27) Zhao, W.; Ghorannevis, Z.; Chu, L.; Toh, M.; Kloc, C.; Tan, P.-H.; Eda, G. Evolution of Electronic Structure in Atomically Thin Sheets of WS_2 and WSe_2. *ACS Nano* **2013**, *7* (1), 791–797. https://doi.org/10.1021/nn305275h.
(28) Ovchinnikov, D.; Allain, A.; Huang, Y.-S.; Dumcenco, D.; Kis, A. Electrical Transport Properties of Single-Layer WS_2. *ACS Nano* **2014**, *8* (8), 8174–8181. https://doi.org/10.1021/nn502362b.
(29) Mia, A. K.; Meyyappan, M.; Giri, P. K. Asymmetric Contact-Induced Selective Doping of CVD-Grown Bilayer WS_2 and Its Application in High-Performance Photodetection with an Ultralow Dark Current. *Nanoscale* **2024**, *16* (17), 8583–8596. https://doi.org/10.1039/D3NR06118C.
(30) Berkdemir, A.; Gutiérrez, H. R.; Botello-Méndez, A. R.; Perea-López, N.; Elías, A. L.; Chia, C.-I.; Wang, B.; Crespi, V. H.; López-Urías, F.; Charlier, J.-C.; Terrones, H.; Terrones, M. Identification of Individual and Few Layers of WS_2 Using Raman Spectroscopy. *Sci. Rep.* **2013**, *3* (1), 1755. https://doi.org/10.1038/srep01755.
(31) Bora, A.; Mawlong, L. P. L.; Mia, A. K.; Giri, P. K. Manipulating Trion and Biexciton Emissions in Monolayer WS_2 by Sandwiching with Ultrathin ZnO Layers for Excitonic Light Emission Applications. *ACS Appl. Nano Mater.* **2024**, *7* (8), 8612–8623. https://doi.org/10.1021/acsanm.3c06043.
(32) Iqbal, M. W.; Shahzad, K.; Hussain, G.; Arshad, M. K.; Akbar, R.; Azam, S.; Aftab, S.; Alharbi, T.; Majid, A. Gate Dependent Phonon Shift in Tungsten Disulfide (WS_2) Field Effect Transistor. *Mater. Res. Express* **2019**, *6* (11), 115909. https://doi.org/10.1088/2053-1591/ab485a.
(33) Zhu, B.; Chen, X.; Cui, X. Exciton Binding Energy of Monolayer WS_2. *Sci. Rep.* **2015**, *5* (1), 9218. https://doi.org/10.1038/srep09218.
(34) Gutiérrez, H. R.; Perea-López, N.; Elías, A. L.; Berkdemir, A.; Wang, B.; Lv, R.; López-Urías, F.; Crespi, V. H.; Terrones, H.; Terrones, M. Extraordinary Room-Temperature Photoluminescence in Triangular WS_2 Monolayers. *Nano Lett.* **2013**, *13* (8), 3447–3454. https://doi.org/10.1021/nl3026357.
(35) Li, H.; Wu, J.; Yin, Z.; Zhang, H. Preparation and Applications of Mechanically Exfoliated Single-Layer and Multilayer MoS_2 and WSe_2 Nanosheets. *Acc. Chem. Res.* **2014**, *47* (4), 1067–1075. https://doi.org/10.1021/ar4002312.
(36) Li, H.; Lu, G.; Wang, Y.; Yin, Z.; Cong, C.; He, Q.; Wang, L.; Ding, F.; Yu, T.; Zhang, H. Mechanical Exfoliation and Characterization of Single- and Few-Layer Nanosheets of WSe_2, TaS_2, and $TaSe_2$. *Small* **2013**, *9* (11), 1974–1981. https://doi.org/10.1002/smll.201202919.
(37) Wang, L.; Wang, Y.; Wong, J. I.; Palacios, T.; Kong, J.; Yang, H. Y. Functionalized MoS_2 Nanosheet-Based Field-Effect Biosensor for Label-Free Sensitive Detection of Cancer Marker Proteins in Solution. *Small* **2014**, *10* (6), 1101–1105. https://doi.org/10.1002/smll.201302081.
(38) Novoselov, K. S.; Geim, A. K.; Morozov, S. V.; Jiang, D.; Zhang, Y.; Dubonos, S. V.; Grigorieva, I. V.; Firsov, A. A. Electric Field Effect in Atomically Thin Carbon Films. *Science* **2004**, *306* (5696), 666–669. https://doi.org/10.1126/science.1102896.

(39) Iqbal, M. W.; Iqbal, M. Z.; Khan, M. F.; Shehzad, M. A.; Seo, Y.; Park, J. H.; Hwang, C.; Eom, J. High-Mobility and Air-Stable Single-Layer WS_2 Field-Effect Transistors Sandwiched between Chemical Vapor Deposition-Grown Hexagonal BN Films. *Sci. Rep.* **2015**, *5* (1), 10699. https://doi.org/10.1038/srep10699.

(40) You, Y. G.; Shin, D. H.; Ryu, J. H.; Campbell, E. E. B.; Chung, H.-J.; Jhang, S. H. Atomic Layer Deposited Al_2O_3 Passivation Layer for Few-Layer WS_2 Field Effect Transistors. *Nanotechnology* **2021**, *32* (50), 505702. https://doi.org/10.1088/1361-6528/ac2390.

(41) Cao, Y.; Wood, S.; Richheimer, F.; Blakesley, J.; Young, R. J.; Castro, F. A. Enhancing and Quantifying Spatial Homogeneity in Monolayer WS_2. *Sci. Rep.* **2021**, *11* (1), 14831. https://doi.org/10.1038/s41598-021-94263-9.

(42) Mishra, A. K.; Lakshmi, K. V.; Huang, L. Eco-Friendly Synthesis of Metal Dichalcogenides Nanosheets and Their Environmental Remediation Potential Driven by Visible Light. *Sci. Rep.* **2015**, *5* (1), 15718. https://doi.org/10.1038/srep15718.

(43) Pandey, K.; Jeong, H. K. Synthesis of Tungsten Disulfide for Electrocatalysts. **2023**, *73* (5), 403–412. https://doi.org/10.3938/NPSM.73.403.

(44) Xu, D.; Xu, P.; Zhu, Y.; Peng, W.; Li, Y.; Zhang, G.; Zhang, F.; Mallouk, T. E.; Fan, X. High Yield Exfoliation of WS_2 Crystals into 1–2 Layer Semiconducting Nanosheets and Efficient Photocatalytic Hydrogen Evolution from WS_2/CdS Nanorod Composites. *ACS Appl. Mater. Interfaces* **2018**, *10* (3), 2810–2818. https://doi.org/10.1021/acsami.7b15614.

(45) Peng, K.; Wang, H.; Li, X.; Wang, J.; Cai, Z.; Su, L.; Fan, X. Emerging WS_2/Montmorillonite Composite Nanosheets as an Efficient Hydrophilic Photocatalyst for Aqueous Phase Reactions. *Sci. Rep.* **2019**, *9* (1), 16325. https://doi.org/10.1038/s41598-019-52191-9.

(46) Dunklin, J. R.; Lafargue, P.; Higgins, T. M.; Forcherio, G. T.; Benamara, M.; McEvoy, N.; Roper, D. K.; Coleman, J. N.; Vaynzof, Y.; Backes, C. Production of Monolayer-Rich Gold-Decorated 2H–WS_2 Nanosheets by Defect Engineering. *Npj 2D Mater. Appl.* **2018**, *1* (1), 1–9. https://doi.org/10.1038/s41699-017-0045-z.

(47) Villamayor, M. M. S.; Husain, S.; Oropesa-Nuñez, R.; Johansson, F. O. L.; Lindblad, R.; Lourenço, P.; Bernard, R.; Witkowski, N.; Prévot, G.; Sorgenfrei, N. L. A. N.; Giangrisostomi, E.; Föhlisch, A.; Svedlindh, P.; Lindblad, A.; Nyberg, T. Wafer-Sized WS_2 Monolayer Deposition by Sputtering. *Nanoscale* **2022**, *14* (17), 6331–6338. https://doi.org/10.1039/D1NR08375A.

(48) Loh, T. A. J.; Chua, D. H. C.; Wee, A. T. S. One-Step Synthesis of Few-Layer WS_2 by Pulsed Laser Deposition. *Sci. Rep.* **2015**, *5* (1), 18116. https://doi.org/10.1038/srep18116.

(49) Singh, D. K.; Gupta, G. Van Der Waals Epitaxy of Transition Metal Dichalcogenides via Molecular Beam Epitaxy: Looking Back and Moving Forward. *Mater. Adv.* **2022**, *3* (15), 6142–6156. https://doi.org/10.1039/D2MA00352J.

(50) Villamayor, M. M. S.; Lindblad, A.; Johansson, F. O. L.; Tran, T.; Pham, N. H.; Primetzhofer, D.; Sorgenfrei, N. L. A. N.; Giangrisotomi, E.; Föhlisch, A.; Lourenço, P.; Bernard, R.; Witkowski, N.; Prévot, G.; Nyberg, T. Growth of Two-Dimensional WS_2 Thin Films by Reactive Sputtering. *Vacuum* **2021**, *188*, 110205. https://doi.org/10.1016/j.vacuum.2021.110205.

(51) Gu, Y.; Serna, M. I.; Mohan, S.; Londoño-Calderon, A.; Ahmed, T.; Huang, Y.; Lee, J.; Walia, S.; Pettes, M. T.; Liechti, K. M.; Akinwande, D. Sulfurization Engineering of One-Step Low-Temperature MoS_2 and WS_2 Thin Films for Memristor Device Applications. *Adv. Electron. Mater.* **2022**, *8* (2), 2100515. https://doi.org/10.1002/aelm.202100515.

(52) Cong, C.; Shang, J.; Wu, X.; Cao, B.; Peimyoo, N.; Qiu, C.; Sun, L.; Yu, T. Synthesis and Optical Properties of Large-Area Single-Crystalline 2D Semiconductor WS_2 Monolayer from Chemical Vapor Deposition. *Adv. Opt. Mater.* **2014**, *2* (2), 131–136. https://doi.org/10.1002/adom.201300428.
(53) Han, A.; Zhou, X.; Wang, X.; Liu, S.; Xiong, Q.; Zhang, Q.; Gu, L.; Zhuang, Z.; Zhang, W.; Li, F.; Wang, D.; Li, L.-J.; Li, Y. One-Step Synthesis of Single-Site Vanadium Substitution in 1T-WS_2 Monolayers for Enhanced Hydrogen Evolution Catalysis. *Nat. Commun.* **2021**, *12* (1), 709. https://doi.org/10.1038/s41467-021-20951-9.
(54) Qin, Z.; Loh, L.; Wang, J.; Xu, X.; Zhang, Q.; Haas, B.; Alvarez, C.; Okuno, H.; Yong, J. Z.; Schultz, T.; Koch, N.; Dan, J.; Pennycook, S. J.; Zeng, D.; Bosman, M.; Eda, G. Growth of Nb-Doped Monolayer WS_2 by Liquid-Phase Precursor Mixing. *ACS Nano* **2019**, *13* (9), 10768–10775. https://doi.org/10.1021/acsnano.9b05574.
(55) Li, W.; Qin, Q.; Li, X.; Huangfu, Y.; Shen, D.; Liu, J.; Li, J.; Li, B.; Wu, R.; Duan, X. Robust Growth of 2D Transition Metal Dichalcogenide Vertical Heterostructures via Ammonium-Assisted CVD Strategy. *Adv. Mater. n/a* (n/a), 2408367. https://doi.org/10.1002/adma.202408367.
(56) Wang, Z.; Xu, W.; Li, B.; Hao, Q.; Wu, D.; Qi, D.; Gan, H.; Xie, J.; Hong, G.; Zhang, W. Selective Chemical Vapor Deposition Growth of WS_2/MoS_2 Vertical and Lateral Heterostructures on Gold Foils. *Nanomaterials* **2022**, *12* (10), 1696. https://doi.org/10.3390/nano12101696.
(57) Lan, C.; Li, C.; Ho, J. C.; Liu, Y. 2D WS_2: From Vapor Phase Synthesis to Device Applications. *Adv. Electron. Mater.* **2021**, *7* (7), 2000688. https://doi.org/10.1002/aelm.202000688.
(58) Li, C.; Sang, D.; Ge, S.; Zou, L.; Wang, Q. Recent Excellent Optoelectronic Applications Based on Two-Dimensional WS_2 Nanomaterials: A Review. *Molecules* **2024**, *29* (14), 3341. https://doi.org/10.3390/molecules29143341.
(59) Wiersinga, W. J.; Rhodes, A.; Cheng, A. C.; Peacock, S. J.; Prescott, H. C. Pathophysiology, Transmission, Diagnosis, and Treatment of Coronavirus Disease 2019 (COVID-19): A Review. *JAMA* **2020**, *324* (8), 782–793. https://doi.org/10.1001/jama.2020.12839.
(60) Dey, S.; Dolci, M.; Zijlstra, P. Single-Molecule Optical Biosensing: Recent Advances and Future Challenges. *ACS Phys. Chem. Au* **2023**, *3* (2), 143–156. https://doi.org/10.1021/acsphyschemau.2c00061.
(61) Chiu, N.-F.; Yang, H.-T. High-Sensitivity Detection of the Lung Cancer Biomarker CYFRA21-1 in Serum Samples Using a Carboxyl-MoS_2 Functional Film for SPR-Based Immunosensors. *Front. Bioeng. Biotechnol.* **2020**, *8*.
(62) Kalantar-zadeh, K.; Ou, J. Z. Biosensors Based on Two-Dimensional MoS2. *ACS Sens.* **2016**, *1* (1), 5–16. https://doi.org/10.1021/acssensors.5b00142.
(63) Xi, Q.; Zhou, D.-M.; Kan, Y.-Y.; Ge, J.; Wu, Z.-K.; Yu, R.-Q.; Jiang, J.-H. Highly Sensitive and Selective Strategy for MicroRNA Detection Based on WS_2 Nanosheet Mediated Fluorescence Quenching and Duplex-Specific Nuclease Signal Amplification. *Anal. Chem.* **2014**, *86* (3), 1361–1365. https://doi.org/10.1021/ac403944c.
(64) Wang, S.; Zhang, Y.; Ning, Y.; Zhang, G.-J. A WS_2 Nanosheet-Based Platform for Fluorescent DNA Detection via PNA–DNA Hybridization. *Analyst* **2014**, *140* (2), 434–439. https://doi.org/10.1039/C4AN01738B.

(65) Wang, P.; Wang, A.; Hassan, M. M.; Ouyang, Q.; Li, H.; Chen, Q. A Highly Sensitive Upconversion Nanoparticles-WS_2 Nanosheet Sensing Platform for Escherichia Coli Detection. *Sens. Actuators B Chem.* **2020**, *320*, 128434. https://doi.org/10.1016/j.snb.2020.128434.

(66) Huiling Loo, A.; Bonanni, A.; Pumera, M. Strong Dependence of Fluorescence Quenching on the Transition Metal in Layered Transition Metal Dichalcogenide Nanoflakes for Nucleic Acid Detection. *Analyst* **2016**, *141* (15), 4654–4658. https://doi.org/10.1039/C6AN00454G.

(67) Dey, B.; Islam, Md. S.; Park, J. Numerical Design of High-Performance WS_2/Metal/WS_2/Graphene Heterostructure Based Surface Plasmon Resonance Refractive Index Sensor. *Results Phys.* **2021**, *23*, 104021. https://doi.org/10.1016/j.rinp.2021.104021.

(68) Wang, H.; Zhang, H.; Dong, J.; Hu, S.; Zhu, W.; Qiu, W.; Lu, H.; Yu, J.; Guan, H.; Gao, S.; Li, Z.; Liu, W.; He, M.; Zhang, J.; Chen, Z.; Luo, Y. Sensitivity-Enhanced Surface Plasmon Resonance Sensor Utilizing a Tungsten Disulfide (WS_2) Nanosheets Overlayer. *Photonics Res.* **2018**, *6* (6), 485–491. https://doi.org/10.1364/PRJ.6.000485.

(69) Shorie, M.; Kumar, V.; Kaur, H.; Singh, K.; Tomer, V. K.; Sabherwal, P. Plasmonic DNA Hotspots Made from Tungsten Disulfide Nanosheets and Gold Nanoparticles for Ultrasensitive Aptamer-Based SERS Detection of Myoglobin. *Microchim. Acta* **2018**, *185* (3), 158. https://doi.org/10.1007/s00604-018-2705-x.

(70) Yang, J.; Gao, L.; Peng, C.; Zhang, W. Construction of Self-Signal DNA Electrochemical Biosensor Employing WS_2 Nanosheets Combined with PIn6COOH. *RSC Adv.* **2019**, *9* (17), 9613–9619. https://doi.org/10.1039/C8RA10266J.

(71) Li, D.; Wei, H.; Hong, R.; Yue, X.; Dong, L.; Fan, K.; Yu, J.; Yao, D.; Xu, H.; Lu, J.; Wang, G. WS_2 Nanosheets-Based Electrochemical Biosensor for Highly Sensitive Detection of Tumor Marker miRNA-4484. *Talanta* **2024**, *274*, 125965. https://doi.org/10.1016/j.talanta.2024.125965.

(72) Bahri, M.; Shi, B.; Elaguech, M. A.; Djebbi, K.; Zhou, D.; Liang, L.; Tlili, C.; Wang, D. Tungsten Disulfide Nanosheet-Based Field-Effect Transistor Biosensor for DNA Hybridization Detection. *ACS Appl. Nano Mater.* **2022**, *5* (4), 5035–5044. https://doi.org/10.1021/acsanm.2c00067.

(73) Li, A.; Zhang, J.; Qiu, J.; Zhao, Z.; Wang, C.; Zhao, C.; Liu, H. A Novel Aptameric Biosensor Based on the Self-Assembled DNA–WS_2 Nanosheet Architecture. *Talanta* **2017**, *163*, 78–84. https://doi.org/10.1016/j.talanta.2016.10.088.

(74) Shuai, H.-L.; Huang, K.-J.; Chen, Y.-X. A Layered Tungsten Disulfide/Acetylene Black Composite Based DNA Biosensing Platform Coupled with Hybridization Chain Reaction for Signal Amplification. *J. Mater. Chem. B* **2016**, *4* (6), 1186–1196. https://doi.org/10.1039/C5TB02214B.

(75) Wei, X.; Liu, C.; Qin, H.; Ye, Z.; Liu, X.; Zong, B.; Li, Z.; Mao, S. Fast, Specific, and Ultrasensitive Antibiotic Residue Detection by Monolayer WS_2-Based Field-Effect Transistor Sensor. *J. Hazard. Mater.* **2023**, *443*, 130299. https://doi.org/10.1016/j.jhazmat.2022.130299.

(76) Park, H.; Baek, S.; Sen, A.; Jung, B.; Shim, J.; Park, Y. C.; Lee, L. P.; Kim, Y. J.; Kim, S. Ultrasensitive and Selective Field-Effect Transistor-Based Biosensor Created by Rings of MoS_2 Nanopores. *ACS Nano* **2022**, *16* (2), 1826–1835. https://doi.org/10.1021/acsnano.1c08255.

(77) Liu, X.; Hu, J.; Yue, C.; Della Fera, N.; Ling, Y.; Mao, Z.; Wei, J. High Performance Field-Effect Transistor Based on Multilayer Tungsten Disulfide. *ACS Nano* **2014**, *8* (10), 10396–10402. https://doi.org/10.1021/nn505253p.

(78) Pak, Y.; Park, W.; Alaal, N.; Kumaresan, Y.; Aravindh, S. A.; Mitra, S.; Xin, B.; Min, J.-W.; Kim, H.; Lim, N.; Cho, B.; Jung, G.-Y.; Hussain, M. M.; Roqan, I. S. Enhanced Photoresponse of WS_2 Photodetectors through Interfacial Defect Engineering Using a TiO2 Interlayer. *ACS Appl. Electron. Mater.* **2020**, *2* (3), 838–845. https://doi.org/10.1021/acsaelm.0c00011.

(79) Yao, J.; Yang, G. 2D Material Broadband Photodetectors. *Nanoscale* **2020**, *12* (2), 454–476. https://doi.org/10.1039/C9NR09070C.

(80) Liu, C.-H.; Chang, Y.-C.; Norris, T. B.; Zhong, Z. Graphene Photodetectors with Ultra-Broadband and High Responsivity at Room Temperature. *Nat. Nanotechnol.* **2014**, *9* (4), 273–278. https://doi.org/10.1038/nnano.2014.31.

(81) Wu, D.; Guo, C.; Wang, Z.; Ren, X.; Tian, Y.; Shi, Z.; Lin, P.; Tian, Y.; Chen, Y.; Li, X. A Defect-Induced Broadband Photodetector Based on WS_2/Pyramid Si 2D/3D Mixed-Dimensional Heterojunction with a Light Confinement Effect. *Nanoscale* **2021**, *13* (31), 13550–13557. https://doi.org/10.1039/D1NR03243G.

(82) Perea-López, N.; Elías, A. L.; Berkdemir, A.; Castro-Beltran, A.; Gutiérrez, H. R.; Feng, S.; Lv, R.; Hayashi, T.; López-Urías, F.; Ghosh, S.; Muchharla, B.; Talapatra, S.; Terrones, H.; Terrones, M. Photosensor Device Based on Few-Layered WS_2 Films. *Adv. Funct. Mater.* **2013**, *23* (44), 5511–5517. https://doi.org/10.1002/adfm.201300760.

(83) Huo, N.; Yang, S.; Wei, Z.; Li, S.-S.; Xia, J.-B.; Li, J. Photoresponsive and Gas Sensing Field-Effect Transistors Based on Multilayer WS_2 Nanoflakes. *Sci. Rep.* **2014**, *4* (1), 5209. https://doi.org/10.1038/srep05209.

(84) Zhao, S.; Zhang, Y.; Wang, S.; Zhao, D.; Kang, H.; Li, J.; Xiao, R.; Kong, Z.; Chen, Z.; Sui, Y.; Wang, J.; Chen, Y.; Yu, G. Controllable Growth of Bilayer WS_2 by Chemical Vapor Deposition and Application for Photodetectors. *Mater. Lett.* **2022**, *317*, 132103. https://doi.org/10.1016/j.matlet.2022.132103.

(85) D. Yao, J.; Q. Zheng, Z.; M. Shao, J.; W. Yang, G. Stable, Highly-Responsive and Broadband Photodetection Based on Large-Area Multilayered WS_2 Films Grown by Pulsed-Laser Deposition. *Nanoscale* **2015**, *7* (36), 14974–14981. https://doi.org/10.1039/C5NR03361F.

(86) Zeng, L.; Tao, L.; Tang, C.; Zhou, B.; Long, H.; Chai, Y.; Lau, S. P.; Tsang, Y. H. High-Responsivity UV-Vis Photodetector Based on Transferable WS_2 Film Deposited by Magnetron Sputtering. *Sci. Rep.* **2016**, *6* (1), 20343. https://doi.org/10.1038/srep20343.

(87) Yang, R.; Feng, S.; Xiang, J.; Jia, Z.; Mu, C.; Wen, F.; Liu, Z. Ultrahigh-Gain and Fast Photodetectors Built on Atomically Thin Bilayer Tungsten Disulfide Grown by Chemical Vapor Deposition. *ACS Appl. Mater. Interfaces* **2017**, *9* (48), 42001–42010. https://doi.org/10.1021/acsami.7b14853.

(88) Lan, C.; Zhou, Z.; Zhou, Z.; Li, C.; Shu, L.; Shen, L.; Li, D.; Dong, R.; Yip, S.; Ho, J. C. Wafer-Scale Synthesis of Monolayer WS_2 for High-Performance Flexible Photodetectors by Enhanced Chemical Vapor Deposition. *Nano Res.* **2018**, *11* (6), 3371–3384. https://doi.org/10.1007/s12274-017-1941-4.

(89) Liu, Y.; Huang, W.; Chen, W.; Wang, X.; Guo, J.; Tian, H.; Zhang, H.; Wang, Y.; Yu, B.; Ren, T.-L.; Xu, J. Plasmon Resonance Enhanced WS_2 Photodetector with Ultra-High

Sensitivity and Stability. *Appl. Surf. Sci.* **2019**, *481*, 1127–1132. https://doi.org/10.1016/j.apsusc.2019.03.179.

(90) Zhang, C.; Wang, S.; Yang, L.; Liu, Y.; Xu, T.; Ning, Z.; Zak, A.; Zhang, Z.; Tenne, R.; Chen, Q. High-Performance Photodetectors for Visible and near-Infrared Lights Based on Individual WS_2 Nanotubes. *Appl. Phys. Lett.* **2012**, *100* (24), 243101. https://doi.org/10.1063/1.4729144.

(91) Prasad, R. K.; Ghosh, K.; Giri, P. K.; Kim, D.-S.; Singh, D. K. High-Efficiency Photodetector Based on a CVD-Grown WS_2 Monolayer. *ACS Appl. Electron. Mater.* **2023**, *5* (7), 3634–3640. https://doi.org/10.1021/acsaelm.3c00366.

(92) Gao, W.; Zhang, S.; Zhang, F.; Wen, P.; Zhang, L.; Sun, Y.; Chen, H.; Zheng, Z.; Yang, M.; Luo, D.; Huo, N.; Li, J. 2D WS_2 Based Asymmetric Schottky Photodetector with High Performance. *Adv. Electron. Mater.* **2021**, *7* (7), 2000964. https://doi.org/10.1002/aelm.202000964.

(93) Zhou, C.; Zhang, S.; Lv, Z.; Ma, Z.; Yu, C.; Feng, Z.; Chan, M. Self-Driven WSe_2 Photodetectors Enabled with Asymmetrical van Der Waals Contact Interfaces. *Npj 2D Mater. Appl.* **2020**, *4* (1), 1–9. https://doi.org/10.1038/s41699-020-00179-9.

(94) Reale, F.; Palczynski, P.; Amit, I.; Jones, G. F.; Mehew, J. D.; Bacon, A.; Ni, N.; Sherrell, P. C.; Agnoli, S.; Craciun, M. F.; Russo, S.; Mattevi, C. High-Mobility and High-Optical Quality Atomically Thin WS_2. *Sci. Rep.* **2017**, *7* (1), 1–10. https://doi.org/10.1038/s41598-017-14928-2.

(95) Huang, M.; Ali, W.; Yang, L.; Huang, J.; Yao, C.; Xie, Y.; Sun, R.; Zhu, C.; Tan, Y.; Liu, X.; Li, S.; Li, Z.; Pan, A. Multifunctional Optoelectronic Synapses Based on Arrayed MoS_2 Monolayers Emulating Human Association Memory. *Adv. Sci.* **2023**, *10* (16), 2300120. https://doi.org/10.1002/advs.202300120.

(96) Zheng, Y.; Ghosh, S.; Das, S. A Butterfly-Inspired Multisensory Neuromorphic Platform for Integration of Visual and Chemical Cues. *Adv. Mater.* **2024**, *36* (13), 2307380. https://doi.org/10.1002/adma.202307380.

(97) Wali, A.; Das, S. Two-Dimensional Memtransistors for Non-Von Neumann Computing: Progress and Challenges. *Adv. Funct. Mater.* **2024**, *34* (15), 2308129. https://doi.org/10.1002/adfm.202308129.

(98) Park, B.; Hwang, Y.; Kwon, O.; Hwang, S.; Lee, J. A.; Choi, D.-H.; Lee, S.-K.; Kim, A. R.; Cho, B.; Kwon, J.-D.; Lee, J. I.; Kim, Y. Robust 2D MoS_2 Artificial Synapse Device Based on a Lithium Silicate Solid Electrolyte for High-Precision Analogue Neuromorphic Computing. *ACS Appl. Mater. Interfaces* **2022**, *14* (47), 53038–53047. https://doi.org/10.1021/acsami.2c14080.

(99) Sharmila, B.; Divyashree, P.; Dwivedi, P. MoS_2-Based Optical Device as Artificial Synapse for Neuromorphic Computing. *IEEE Trans. Electron Devices* **2023**, *70* (3), 1386–1392. https://doi.org/10.1109/TED.2023.3239435.

(100) Naqi, M.; Kang, M. S.; Liu, N.; Kim, T.; Baek, S.; Bala, A.; Moon, C.; Park, J.; Kim, S. Multilevel Artificial Electronic Synaptic Device of Direct Grown Robust MoS_2 Based Memristor Array for In-Memory Deep Neural Network. *Npj 2D Mater. Appl.* **2022**, *6* (1), 1–9. https://doi.org/10.1038/s41699-022-00325-5.

(101) Mallik, S. K.; Padhan, R.; Sahu, M. C.; Pradhan, G. K.; Sahoo, P. K.; Dash, S. P.; Sahoo, S. Ionotronic WS_2 Memtransistors for 6-Bit Storage and Neuromorphic Adaptation at High Temperature. *Npj 2D Mater. Appl.* **2023**, *7* (1), 1–12. https://doi.org/10.1038/s41699-023-00427-8.

(102) Qiu, D.; Lee, D. U.; Lee, K. S.; Pak, S. W.; Kim, E. K. Toward Negligible Charge Loss in Charge Injection Memories Based on Vertically Integrated 2D Heterostructures. *Nano Res.* **2016**, *9* (8), 2319–2326. https://doi.org/10.1007/s12274-016-1118-6.

(103) Wang, H.; Ren, D.; Lu, C.; Yan, X. Investigation of Multilayer WS_2 Flakes as Charge Trapping Stack Layers in Non-Volatile Memories. *Appl. Phys. Lett.* **2018**, *112* (23), 231903. https://doi.org/10.1063/1.5024799.

(104) Kumar, M.; Ban, D.-K.; Kim, S. M.; Kim, J.; Wong, C.-P. Vertically Aligned WS_2 Layers for High-Performing Memristors and Artificial Synapses. *Adv. Electron. Mater.* **2019**, *5* (10), 1900467. https://doi.org/10.1002/aelm.201900467.

(105) Xin, X.; Sun, L.; Chen, J.; Bao, Y.; Tao, Y.; Lin, Y.; Bian, J.; Wang, Z.; Zhao, X.; Xu, H.; Liu, Y. Real-Time Numerical System Convertor via Two-Dimensional WS_2-Based Memristive Device. *Front. Comput. Neurosci.* **2022**, *16*. https://doi.org/10.3389/fncom.2022.1015945.

(106) Yan, X.; Zhao, Q.; Chen, A. P.; Zhao, J.; Zhou, Z.; Wang, J.; Wang, H.; Zhang, L.; Li, X.; Xiao, Z.; Wang, K.; Qin, C.; Wang, G.; Pei, Y.; Li, H.; Ren, D.; Chen, J.; Liu, Q. Vacancy-Induced Synaptic Behavior in 2D WS_2 Nanosheet–Based Memristor for Low-Power Neuromorphic Computing. *Small* **2019**, *15* (24), 1901423. https://doi.org/10.1002/smll.201901423.

(107) Guan, K.; Li, Y.; Liu, L.; Sun, F.; Wang, Y.; Zheng, Z.; Zhou, W.; Zhang, C.; Cai, Z.; Wang, X.; Feng, S.; Zhang, T. Atomic Nb-Doping of WS_2 for High-Performance Synaptic Transistors in Neuromorphic Computing. *Microsyst. Nanoeng.* **2024**, *10* (1), 1–10. https://doi.org/10.1038/s41378-024-00779-1.

(108) Ferrarese Lupi, F.; Milano, G.; Angelini, A.; Rosero-Realpe, M.; Torre, B.; Kozma, E.; Martella, C.; Grazianetti, C. Synaptic Plasticity and Visual Memory in a Neuromorphic 2D Memitter Based on WS_2 Monolayers. *Adv. Funct. Mater.* **2024**, *34* (32), 2403158. https://doi.org/10.1002/adfm.202403158.

(109) Huang, F.; Ke, C.; Li, J.; Chen, L.; Yin, J.; Li, X.; Wu, Z.; Zhang, C.; Xu, F.; Wu, Y.; Kang, J. Controllable Resistive Switching in ReS_2/WS_2 Heterostructure for Nonvolatile Memory and Synaptic Simulation. *Adv. Sci.* **2023**, *10* (28), 2302813. https://doi.org/10.1002/advs.202302813.

(110) Zhang, W.; Gao, H.; Deng, C.; Lv, T.; Hu, S.; Wu, H.; Xue, S.; Tao, Y.; Deng, L.; Xiong, W. An Ultrathin Memristor Based on a Two-Dimensional WS_2 /MoS_2 Heterojunction. *Nanoscale* **2021**, *13* (26), 11497–11504. https://doi.org/10.1039/D1NR01683K.

(111) Varma, P.; Reddy, D. A. Effect of Phosphorus-Doped Phase-Modulated WS_2 Nanosheets on CdS Nanorods for Highly Efficient Photocatalytic Hydrogen Production. *ACS Appl. Energy Mater.* **2024**, *7* (10), 4581–4593. https://doi.org/10.1021/acsaem.4c00650.

(112) Zhou, Y.; Wang, S.; Xin, S.; Sayin, S.; Yi, Z.; Li, Z.; Zaghloul, M. Layer-Dependent Sensing Performance of WS_2-Based Gas Sensors. *Nanomaterials* **2024**, *14* (2), 235. https://doi.org/10.3390/nano14020235.

(113) Neog, A.; Biswas, R. WS_2 Nanosheets as a Potential Candidate towards Sensing Heavy Metal Ions: A New Dimension of 2D Materials. *Mater. Res. Bull.* **2021**, *144*, 111471. https://doi.org/10.1016/j.materresbull.2021.111471.

(114) Thiehmed, Z.; Shakoor, A.; Altahtamouni, T. Recent Advances in WS_2 and Its Based Heterostructures for Water-Splitting Applications. *Catalysts* **2021**, *11* (11), 1283. https://doi.org/10.3390/catal11111283.

(115) Shaheen, N.; Zulfiqar, S.; Alomar, T. S.; Farooq Warsi, M.; AlMasoud, N.; Cochran, E. W. One Dimensional WS_2 Nanoarchitectures Coupled with G-C_3N_4 Anchored rGO Sheets for High Performance Electrochemical Energy Storage Applications. *FlatChem* **2024**, *44*, 100628. https://doi.org/10.1016/j.flatc.2024.100628.

(116) Ali, M.; Afzal, A. M.; Iqbal, M. W.; Mumtaz, S.; Imran, M.; Ashraf, F.; Ur Rehman, A.; Muhammad, F. 2D-TMDs Based Electrode Material for Supercapacitor Applications. *Int. J. Energy Res.* **2022**, *46* (15), 22336–22364. https://doi.org/10.1002/er.8698.

भारतीय प्रौद्योगिकी संस्थान गुवाहाटी
Indian Institute of Technology Guwahati

Chapter 2

Controlled Growth of Monolayer and Bilayer WS_2 by Chemical Vapour Deposition Method

In this chapter, we discuss the optimization of large-area CVD growth for monolayer (1L) and bilayer (2L) WS_2 by precise control of various growth parameters. Tungsten oxide and sulfur powders were used as precursors for the complete vapor-phase CVD growth of 2D WS_2 on SiO_2/Si substrate. Our findings highlight the critical role of growth temperature, carrier gas flow, growth pressure, and precursor quantities in achieving uniform layer control over the large-area growth of WS_2. We observed multilayer, rod-like, defective WS_2 growth at a growth temperature of 850°C and pressure of 10 mbar. Increasing the temperature to 1000°C, a notable enhancement in lateral growth occurred. Through careful adjustment of growth pressure and duration, we successfully achieved uniform 1L and 2L WS_2 growth at 1000°C. Moreover, the addition of salt catalysts like NaCl significantly enhanced lateral growth, extending it to the millimeter scale. This work offers valuable insights into the controlled large-area growth of WS_2 and its lateral heterostructures with MoS_2, which is essential for exploring novel applications.

2.1 Introduction

The synthesis process of WS_2 plays a crucial role in its applications for optoelectronic devices, sensing technologies, drug delivery systems, and so on[1,2]. Controlling this growth process not only influences the materials properties but also enhances its performance in various applications[3]. One can improve the functionality and quality of WS_2 by precise tuning of synthesis parameters, making it a valuable material for advanced technology and healthcare applications[4,5]. As discussed in **Chapter 1,** the CVD technique offers the best quality WS_2 for optoelectronic applications and offers excellent control over layer number. Generally, the precursor materials (WO_3 and S for WS_2) are vaporized within a quartz tube under a carrier gas environment, facilitating the reaction between individual elements under certain conditions to form the desired material (WS_2 in this case)[6,7]. For the successful controlled growth of high-quality, large-area WS_2, factors such as the temperature of individual precursors, substrate placement, the distance between precursors, carrier gas flow, growth pressure, as well as growth duration play crucial roles[8]. Considering the complexity of the CVD process, it is essential to identify the key relationships between growth

parameters and the physical factors that govern crystal evolution[9]. Among these variables, growth temperature plays a critical role in achieving optimal material quality. Within specific temperature combinations in the WO_3 and sulfur zones, uniform growth can be attained[10]. However, deviations from these conditions often lead to undesirable outcomes such as thick nucleation centers or amorphous growth with small oxide structures and sometimes no growth[11]. Generally, WS_2 is grown at high temperatures, typically around 1000°C, but it is possible to lower the growth temperature by introducing a small fraction of reactive H_2 gas alongside inert Argon gas[12]. The addition of H_2 not only promotes low-temperature growth but also helps in controlling the layer number by inhibiting growth in the c-direction. This dual effect allows for greater precision in layer formation and improves the overall structural quality of the material[13]. The choice of the growth substrate is another critical factor in the CVD growth of 2D materials. Substantial efforts have been made in substrate engineering to optimize growth parameters, such as increasing domain sizes, accelerating growth rates, and achieving uniform, oriented growth of 2D compounds[14,15]. These advancements often depend on the careful selection of substrates that best complement the process[16]. The growth of WS_2 is significantly influenced by the synergistic interaction and precise delivery of tungsten and sulfur precursors to the growth substrate at a controlled flux. The carrier gas plays a pivotal role in maintaining the optimal concentration of these precursors throughout the growth process[10]. However, the large disparity in vapor pressures between the precursors can make it challenging to maintain a stable vapor flux[17]. To mitigate this, the carrier gas flow rate must be carefully adjusted to ensure a steady and controlled precursor supply[18]. Additionally, even small amounts of growth catalysts such as NaCl and KCl, can enhance lateral growth dimensions and enable growth at lower temperatures[19]. For instance, a mixture of NaCl, WO_3, and sulfur powder promotes reactions between the precursors, where NaCl reacts with WO_3 to increase its mass flux by forming highly volatile tungsten oxyhalides and intermediate sodium compounds at reduced temperatures[20–22].

In this chapter, we discuss the systematic optimization of the CVD process for the layered controlled growth of 2D WS_2 flakes. Our findings underscore the importance of growth temperatures and pressure for controlled growth of 2D WS_2 using CVD. In addition to growth temperature, the NaCl as a catalyst significantly promotes lateral growth, helping to achieve larger lateral dimensions and uniform thickness of 1L and 2L-WS_2 with lateral sizes in the range of

several hundred micrometers. This in-depth understanding of the growth mechanism will aid in synthesizing other 2D materials using the CVD technique.

2.2 Experimental Details

The WS_2 nanostructures, from rod-like shape to 2D flakes, were directly synthesized on SiO_2/Si substrates through a custom-built, two-zone, temperature-controlled CVD system. This setup enables precise control over the growth temperatures at each zone, resulting in the formation of diverse nanostructure morphologies. Commercially available WO_3 (99.9% purity) and S powders, procured from Sigma-Aldrich, were used as precursors for the CVD process. The schematic repres-

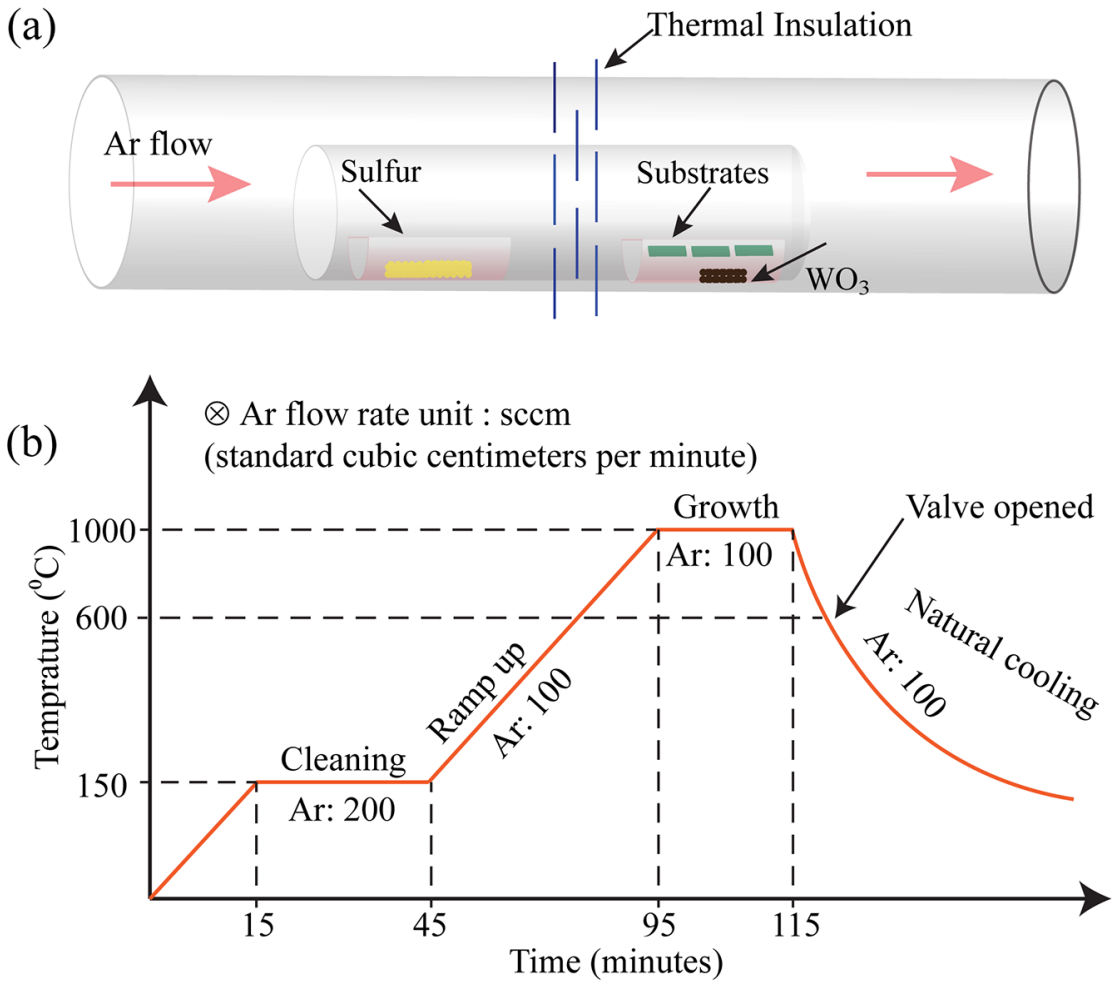

Figure 2.1: (a) Schematic representation of CVD set-up for the growth of 2D WS_2 flakes; (b) Temperature profile of the high temperature zone with gas flow rate for the optimized condition.

-entation of the experimental set-up is illustrated in **Fig. 2.1(a)**. The precursors, S and WO_3, were separately loaded into two mini quartz boats with an inner diameter of approximately 10 mm. Initially, 10 mg of WO_3 powder was placed at the center of the high-temperature heating zone of the furnace, with several cleaned bare SiO_2/Si substrate pieces positioned just above the WO_3 powder, with their polished surfaces facing downward. Simultaneously, 200 mg of the S precursor was placed in the middle of the low-temperature heating zone in the second mini quartz boat. Both precursors were housed inside a one-end-closed quartz tube with a diameter of 20 mm, which enhances the concentration of precursor vapors near the substrate during growth. High-purity Ar was used as the carrier gas. This configuration ensured stable evaporation of the S and WO_3 sources at appropriate temperatures and minimized the risk of cross-contamination during WS_2 growth.

To optimize the growth process, we tuned the growth temperature, pressure, and time to achieve large area, high-quality 2D WS_2 flakes. The final optimized temperature and carrier gas flow profile over time is shown in **Fig. 2.1(b)**. Initially, the quartz chamber was evacuated to a base pressure of 1.6×10^{-2} mbar before heating the system. The temperature of the high temperature zone was gradually raised to 150°C in 15 minutes. The high-purity Ar was then introduced with a flow rate of 200 sccm (standard cubic centimeters per minute) and maintained for 30 minutes, as shown in **Fig. 2.1 (b).** During this time, the Ar flow removed any residual moisture and contaminants. The temperature of the heating zone was then increased to 1000°C in 50 minutes with an Ar flow of 100 sccm. Simultaneously, the first zone was heated to 150°C. At this stage, the outlet valve was partially closed to achieve the required pressure. The system was allowed to stabilize at this temperature for 20 minutes with an Ar flow rate of 100 sccm (standard cubic centimeters per minute). After completion of the growth, the system was cooled naturally to room temperature. When the temperature dropped to 600°C, the outlet valve was opened, and the Ar flow was increased to 200 sccm. The system was finally shut down when the temperature reached 300°C. By controlling the growth pressure to 1.2 mbar and setting a duration of 15 minutes, we obtained a uniform 1L-WS_2. Increasing the growth pressure to 2.0 mbar and extending the growth time to 20 minutes resulted in maximum 2L-WS_2 coverage.

2.3 Characterization Techniques

The CVD-grown WS_2 nanostructures were first observed with optical microscope coupled to a micro-Raman Spectrometer. Raman spectra and spatial Raman mapping of the samples were recorded using a high-resolution micro-Raman spectrometer (LabRam HR800, Jobin–Yvon) with excitation wavelength of 532 nm with a 100X objective having a laser spot size of ~1 μm. The same spectrometer was utilized for photoluminescence (PL) spectra and spatial mapping measurements. Atomic force microscopy (AFM) (Cypher, Oxford Instruments) images were acquired in non-contact mode to confirm the layer thickness of CVD-grown WS_2. We have used three different transmission electron microscopy systems at different stages of our research work: (i) A Titan Themis 300 kV (FEI, now Thermo Fisher), (ii) JEOL-JEM 2010 ran at 200 kV, (iii) Jeol JEM-ARM200CF. The chemical composition and oxidation states of 2D WS_2 were analyzed using three different X-ray photoelectron spectroscopy (XPS) systems (ULVAC, PHI), (AXIS 165, AXIS ULTRA) and PREVAC. All electrical characterization in the present thesis was carried out using Keithley 4200 SCS source meter under an electromagnetic shielding environment.

2.4 Results and Discussion

2.4.1 CVD Growth of Rod-Like WS_2 Structure at 850˚C

Initially, we attempted to grow 1L-WS_2 at 850°C, following the method reported by Li et al.[13]. However, instead of using a mixture of Ar/H_2 gases, we employed highly purified Ar gas. Interestingly, instead of obtaining 1L and multilayered WS_2 flakes, we observed the formation of rod-like multilayer WS_2 structures, as shown in **Fig. 2.2(a)**. The low magnification image in **Fig. 2.2(a)** illustrates a multilayer unidirectional growth along one axis, accompanied by retraction along the perpendicular axis. This combined effect leads to the formation of a rod-shaped structure. A detailed magnified view of this rod-like structure is presented in **Fig. 2.2(d),** which reveals not only the non-uniform thickness of the rod but also suggests the possibility of lateral growth along its sides. To investigate the material characteristics, we conducted Raman spectroscopic analysis on the structure at two distinct locations, as indicated by two circles in **Fig. 2.2(d).** The Raman spectra corresponding to the red and blue circled spots are shown in **Fig. 2.2(b)** and **Fig. 2.2(c)**, respectively. The Raman spectra from the red circles indicate two low-intensity Raman modes as

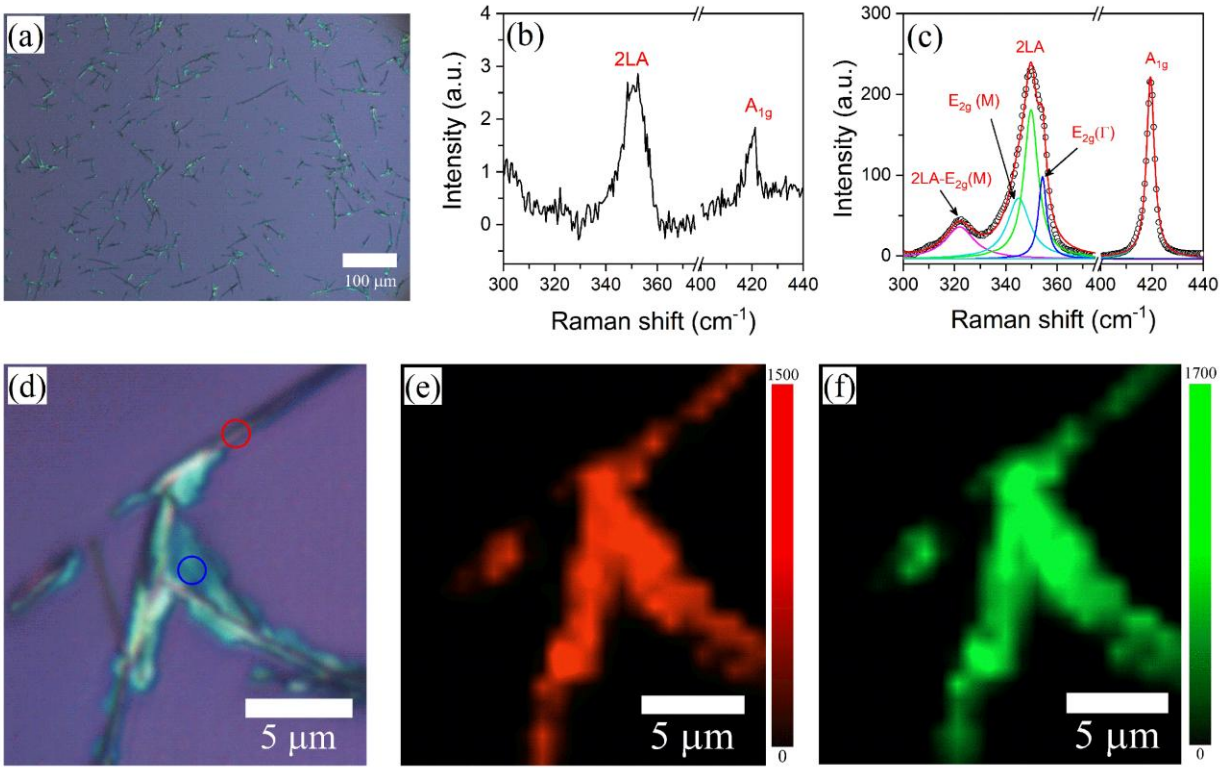

Figure 2.2: (a) Optical images of WS_2 nanostructure grown by CVD technique at 850˚C; (b), (c) The Raman spectra of the WS_2 nanostructure corresponding red and blue circle respectively of figure 2.2(d); (d) Magnified image of the CVD grown WS_2 nanostructure; (e) Spatial intensity distribution of A_{1g} Raman modes; (f) Spatial intensity distribution of 2LA summed with E_{2g} Raman modes.

displayed in **Fig. 2.2(b)**. These modes correspond to the out-of-plane mode (A_{1g}) and in-plane (E_{2g}) mode combined with the phonon mode (2LA) as labeled[23]. In the case of WS_2, when excited with 532 nm laser excitation, the Raman spectra consist of several other phonon modes along with the characteristic A_{1g} and E_{2g} modes, as labeled in **Fig. 2.2(c)**[24]**.** The presence of low-intensity Raman modes and diminishing E_{2g} mode from the red circle region indicates the partial reduction of WO_3 resulting in defective growth of WS_2[24]. There are several possible reasons for the partial reduction of WO_3, including inadequate sulfur vapor, a mismatch between the co-evaporation rates of the precursors, and insufficient transportation of sulfur vapor to the vicinity of WO_3. However, we repeated the process multiple times, ensuring the proper co-evaporation of precursors and supplying an excess of sulfur vapor to the reaction zone. This suggests that even in the presence of sufficient sulfur vapor, WO_3 does not undergo complete reduction at 850˚C. The Raman spectra

from the blue circle shows a high-intensity Raman spectrum as displayed in **Fig. 2.2(c)**[24]**.** The Raman spectrum was fitted using a Lorentz function to determine the contributions from each mode. From the fitted spectrum, we observe the A_{1g} mode at 419.4 cm^{-1} and the E_{2g} mode at 354.3 cm^{-1}, showing a separation of 65.1 cm^{-1} between these characteristic modes. The out-of-plane A_{1g} mode is highly sensitive to the number of layers and external doping[25]. The separation between these fundamental modes indirectly indicates the number of layers. For a monolayer, the separation is approximately 62 cm^{-1}, and it increases with the number of layers [24]. A separation of 65.1 cm^{-1} suggests multilayer WS_2, as expected from the optical image[23]. The Raman spectra obtained from two distinct locations show entirely different profiles, indicating the need for spatial mapping to analyze uniformity. Therefore, we performed Raman spatial mapping with a resolution of 1 µm. The spatial intensity mapping for the A_{1g} mode, which corresponds to the nanostructure shown in Fig. 2.2(d), is presented in **Fig. 2.2(e)**. The spatial intensity distribution mapping corresponding to the E_{2g} mode combined with the 2LA phonon mode is shown in **Fig. 2.2(f).** From the spatial intensity distribution, it is evident that areas of high intensity correspond to planar growth rather than rod-like structures. This suggests that the rod-shaped growths result from the partial reduction of oxides, indicating the need for improved growth conditions to achieve more controlled and uniform growth of 2D WS_2.

2.4.2 CVD Growth of 2D WS_2 at 900˚C

As previously observed, the partial reduction of WO_3 by sulfur at 850°C resulted in a rod-like non-uniform multilayered WS_2. To further investigate the impact of growth temperature on the morphology and crystallinity, we increased the growth temperature to 900°C while keeping all other parameters constant. The results of the CVD growth of WS_2 under these new conditions is presented in **Fig. 2.3(a)**, which illustrates an island-type growth of multilayered WS_2. The magnified image of WS_2 nanostructure grown at 900˚C is presented in **Fig. 2.3(d)**. In this image, rod-like WS_2 structures are observed alongside with enhanced 2D WS_2. This clearly indicates that as the temperature increases, the reduction of WO_3 by sulfur vapor becomes more pronounced. The elevated temperature significantly enhances the growth of 2D WS_2, promoting the formation of a film-like structure. The WS_2 nanostructures grown at this condition were qualitatively analyzed using Raman spectroscopy, which provided deeper insights into the characteristics of 2D materials like TMDs such as quality and uniformity. The Raman spectra recorded from two distinct positions are highlighted by red and blue circles in **Fig. 2.3(d)**. **Fig. 2.3(b)** and **2.3(c)** display the

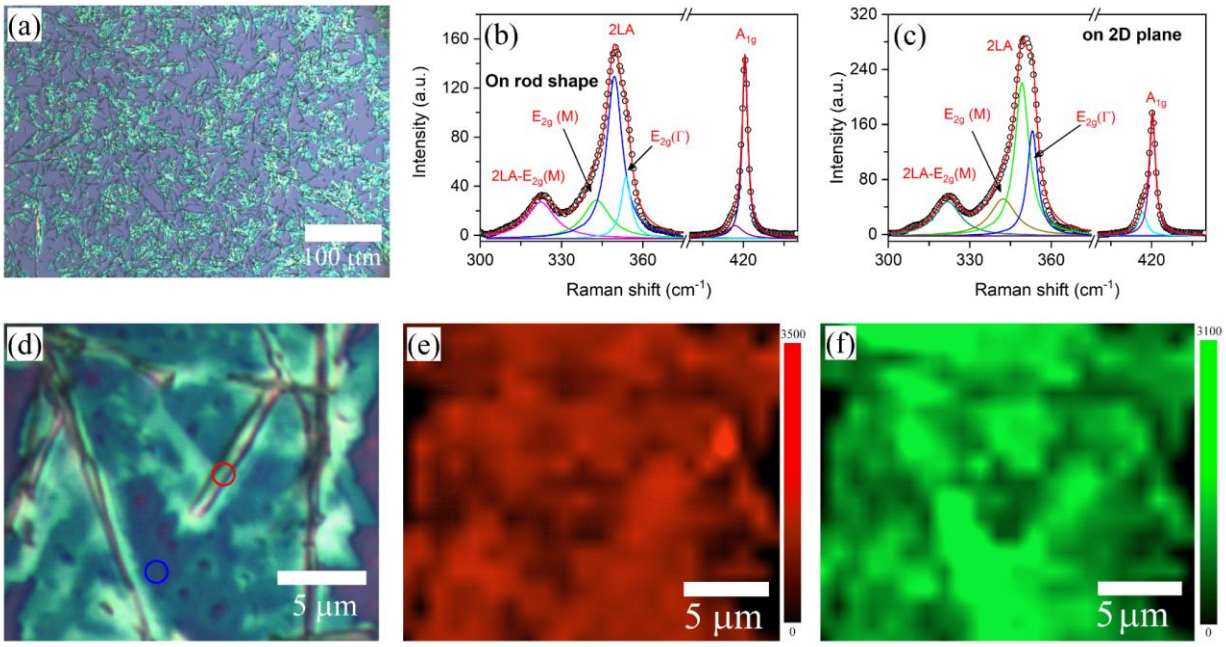

Figure 2.3: (a) Optical microscopic images of WS_2 nanostructure grown by CVD technique at 900˚C; (b), (c) The Raman spectra of the WS_2 nanostructure corresponding red and blue circle respectively of figure 2.2(d); (d) Magnified image of the CVD grown WS_2 nanostructure; (e) Spatial intensity distribution of A_{1g} Raman modes; (f) Spatial intensity distribution of 2LA summed with E_{2g} Raman modes.

Raman spectra for the rod-like WS_2 and 2D film-like WS_2 structures, respectively, corresponding to red and blue circles. In the Raman spectra, we observe a layer-number dependency in the intensity of the A_{1g} mode as we move from the rod-shaped structure to the film. This reduction in intensity can be attributed to the rods significantly greater thickness, which results in a higher number of layers, whereas the film, being much thinner, has fewer layers[23]. The reduced number of layers in the film leads to diminished electron-phonon coupling, which in turn lowers the intensity of the A_{1g} mode as this mode is sensitive to charge. Interestingly, apart from the change in intensity, we also detect a splitting of the A_{1g} mode[26]. Our analysis of the Raman spectra reveals that the separation between the characteristic modes increases to 66.5 cm^{-1} for the rod-shaped structure, while the separation is slightly lower at 65.7 cm^{-1} for the film. This higher value for the rod-shaped structure, which was grown at 850°C, can presumably be linked to the larger thickness of the WS_2 nanostructure and splitting of A_{1g} mode. The Raman spectra from two distinct points revels similar characteristics with different intensity. Thus, need to analyses the spatial distribution of Raman mode intensity. **Fig. 2.3(e)** presents the spatial intensity mapping of the A_{1g} mode, while

Fig.2.3(f) shows the combined E_{2g} and 2LA modes, both of which reveal significant non-uniformity across the sample. This non-uniformity is also evident in the magnified view provided in **Fig. 2.3(d).** These findings suggest that increasing the growth temperature from 850˚C to 900˚C promotes 2D WS_2 growth, as supported by both the optical images and Raman analysis. However, further adjustments to the growth parameters are necessary to achieve uniform, high-crystallinity growth, which is crucial for enhancing the performance of optoelectronic and biosensing applications.

2.4.3 CVD Growth of 2D WS_2 at 950˚C

Increasing the growth temperature promotes the lateral growth of 2D WS_2 with improved quality. We further increased the growth temperature to 950˚C while keeping other parameters constant to observe the temperature effect on 2D WS_2 growth. The 2D WS_2 synthesized at 950˚C using the CVD is shown in **Fig. 2.4(a)**, demonstrating significant improvement in growth quality via changing the growth temperature. The optical image reveals 2D triangular WS_2 flakes growth, accompanied by a few rod-like structures, highlighting the critical role of growth temperature.

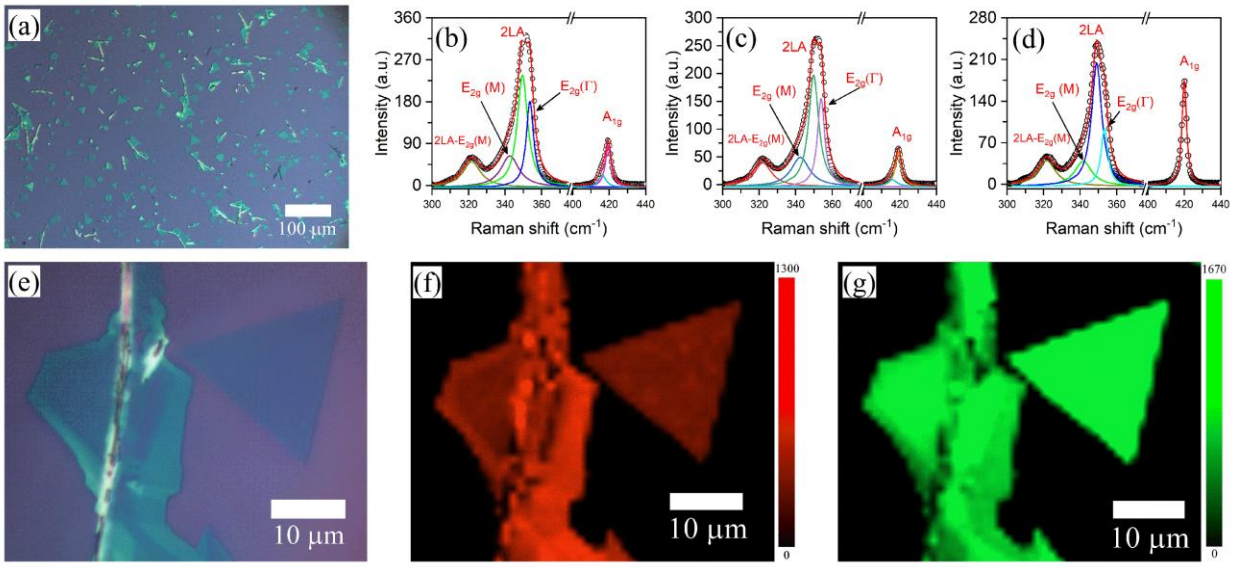

Figure 2.4: (a) Optical image of WS_2 nanostructure grown by CVD technique at 950˚C; (b), (c) and (d) The Raman spectra of the WS_2 nanostructure corresponding thick region of WS_2 flake, from the distinct triangular WS_2 flake and from WS_2 rod, respectively of figure 2.4(e); (d) Magnified image WS_2 nanostructure grown at 950°C; (f) Spatial intensity distribution of A_{1g} Raman modes; (g) Spatial intensity distribution of 2LA summed with E_{2g} Raman modes.

Table 2.1 Fitted peak parameters for the WS_2 nanostructure grown at 950°C by CVD technique.

Sample position	A_{1g} mode		E_{2g} mode		Mode separation (cm^{-1})	Mode intensity ratio (A_{1g}/E_{2g})
	Position (cm^{-1})	Intensity (a.u.)	Position (cm^{-1})	Intensity (a.u.)		
Distinct WS_2 flake	419.2	38930	353.9	116102	65.3	0.34
Thick WS_2	419.5	52855	353.6	138466	65.9	0.38
WS_2 rod	420	83178	353.3	67524	66.7	1.23

Notably, there are substantial advancements in achieving high crystalline growth of 2D WS_2 as compared to previous conditions. In the magnified image in **Fig. 2.4(e)**, a well-defined triangular flake are observed, along with a WS_2 rod surrounded by a 2D film. Raman spectroscopy and spatial Raman mapping were employed to assess the quality and spatial uniformity of the CVD-grown 2D WS_2. Raman spectra were collected from three distinct positions: at the WS_2 flake connected to the rod, the distinct WS_2 flake, the rod shaped WS_2, and are shown in **Fig. 2.4 (b), (c), and (d),** respectively. The intensity of the A_{1g} mode peak is lowest for the distinct flakes, increases for the thicker region, and reaches its maximum at the rod shape WS_2. This trend of reduction in the intensity of A_{1g} mode is expected as the electron-phonon coupling diminishes with decreasing electron density because of the lower WS_2 layer numbers[27]. Furthermore, the separation between characteristic out-of-plane A_{1g} and in-plane E_{2g} modes follows a similar pattern across these three points, as this separation is also related to WS_2 layer numbers. The Raman spectra from these three points were fitted with the Lorentz function for further understanding, and the peak properties are summarized in **Table 2.1**. The fitted spectra reveal systematic enhancements in the spectral intensity ratio between A_{1g} to E_{2g} mode underscoring the effect of thickness on A_{1g} mode intensity. Finally, the spatial uniformity of the 2D WS_2 nanostructures grown at 950°C was analyzed using spatial intensity distribution of characteristics Raman modes as they strongly depend upon layer numbers. The spatial uniformity was analyzed corresponding to the region shown in **Fig. 2.4(e).** The spatial intensity distribution corresponding to the layer-sensitive out-of-plane A_{1g} mode is presented in **Fig. 2.4(f)**, while in-plane E_{2g} mode summed with 2LA phonon modes intensity is

presented in **Fig. 2.4(g).** Both the characteristics modes spatial intensity distribution mapping demonstrates uniform intensity for the region corresponding to the distinct triangular flake. While the intensity distribution for other regions associated with the rod-like WS_2 is non-uniform, employing partial reductions causes the rod-like structure along with non-uniform growth. In **Fig. 2.4(f)**, which corresponds to the mapping of the A_{1g} mode, the intensity is higher in regions with greater thickness and lower in thinner regions. The film experiences significant strain near the rod, leading to an increased intensity of the strain-dependent E_{2g} mode, as illustrated in **Fig. 2.4(g).** Thus, the A_{1g} mode exhibits a strong dependence on thickness and charge, and the E_{2g} mode shows a strain dependence. Therefore, the triangular-shaped WS_2 structure exhibits the highest spatial uniformity and crystallinity, requiring minimal further adjustments in temperature and other parameters for the growth of uniform triangular WS_2 flakes.

2.4.4 CVD Growth of 2D WS_2 at 1000˚C

Finally, we observed uniform triangular WS_2 flakes without any rod-like structures by increasing the growth temperature to 1000°C. Low magnification image, shown in **Fig. 2.5(a)**, clearly display triangular flakes uniformly distributed across the substrate. To further assess the uniformity within

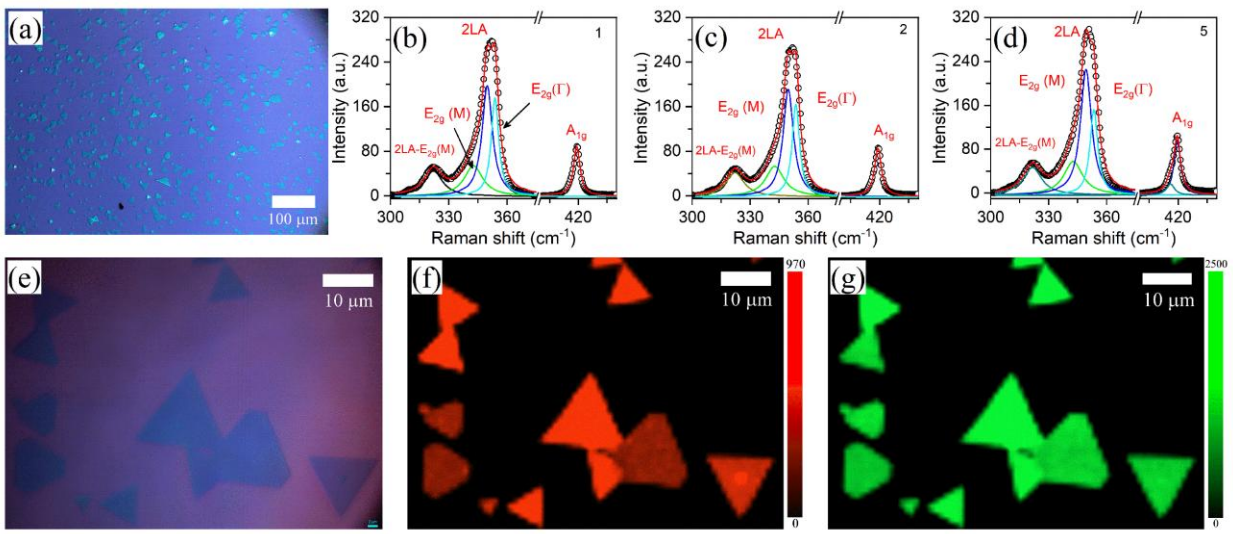

Figure 2.5: (a) Low magnification optical images of WS_2 flakes grown by CVD technique at 1000˚C; (b), (c) and (d) The Raman spectra recorded from 3 different WS_2 flakes; (e) Magnified image of the CVD grown WS_2 flakes; (f) Spatial intensity distribution of A_{1g} Raman modes; (g) Spatial intensity distribution of 2LA summed with E_{2g} Raman modes.

different regions of flakes as well as among different flakes, we have used the highly sensitive Raman spectroscopy technique. Raman spectra from three distinct flakes are presented in **Fig. 2.5(b)–2.5(d)**. The Raman spectra clearly exhibit a low-intensity A_{1g} mode for all the flakes, which is a clear signature of reduced thickness, unlike for rods like WS_2, which gives a very high intense A_{1g} mode. Additionally, we have fitted Raman spectra obtained from five different flakes. The mode parameters obtained from those fitted spectra are summarized in **Table 2.2**. The variations in peak parameters in **Table 2.2** indicate that even though there are significant improvements in the growth quality and reduction in layer numbers, there is still poor control of the layer numbers of 2D WS_2. Especially the variations in the peak positions and intensity ratio of the characteristic modes among the flakes underscores the non-uniformity. A highly magnified image of the CVD-rown WS_2 flakes is shown in **Fig. 2.5(e),** highlighting their lateral dimensions, which are on the order of tens of micrometers. For a better understanding of uniformity, we have carried out the spatial Raman mapping over the magnified image in **Fig. 2.5(e).** The non-uniformity among the flakes is evident from the intensity variations in the Raman spatial mapping. Specifically, the A_{1g} mode intensity varies significantly between the flakes, as shown in **Fig. 2.5 (f)**, as it is highly sensitive to the number of layers. However, the in-plane mode summed with 2LA mode intensity indicates almost uniform intensity, as seen from F**ig. 2.5 (g)** with minute variation. This is because the in-plane mode is sensitive to induced strain but non-sensitive to layer number[25]. Interestingly, the intensity distribution is highly uniform within the distinct flakes. Thus, even though we successfully synthesized triangular WS_2 flakes, further optimization of growth parameters such as pressure and time are required to achieve precise layer control and large area growth of WS_2.

Table 2.2: Fitted peak parameters for five different WS_2 flakes grown at 1000°C by CVD technique.

Flake number	A_{1g} mode		E_{2g} mode		Mode separation (cm^{-1})	Mode intensity ratio (A_{1g}/E_{2g})
	Position (cm^{-1})	Intensity (a.u.)	Position (cm^{-1})	Intensity (a.u.)		
1	419.1	55102	353.7	127283	65.4	0.43
2	419.0	55917	353.6	119050	65.4	0.47
3	419.4	69529	353.1	91411	66.3	0.76
4	419.3	61892	353.4	117690	65.9	0.52
5	419.5	62798	353.4	116828	66.1	0.53

2.4.5 Layer-Controlled CVD Growth of Large Area WS_2.

Since we achieved the best quality growth of WS_2 at 1000˚C, we maintained this temperature while varying the growth pressure and time to achieve large-area controlled growth. Although the chemical reactions involved in the CVD growth process are highly complex, we assume that higher growth pressure and extended time will increase the precursor density near the substrate, thereby enhancing the probability of reactions. We have observed that higher pressure leads to vertical growth rather than lateral growth, resulting in smaller, multilayer WS_2 flakes. To explore the dependence of growth pressure on morphologies, we conducted experiments under varying pressures of five, two, and one mbar with a growth time of 20 minutes. The optical images of the CVD-grown WS_2 corresponding to each growth pressure are displayed in **Fig. 2.6**. From the optical images in **Fig. 2.6(a)**, we observe that when the pressure was reduced from ten mbar to five mbar, the lateral size of the WS_2 flakes increased significantly as compared to **Fig. 2.5(a)**, even though the thickness remained non-uniform. Further reducing the growth pressure to two mbar increases uniformity throughout the substrate, as displayed in **Fig. 2.6 (b),** underscoring the

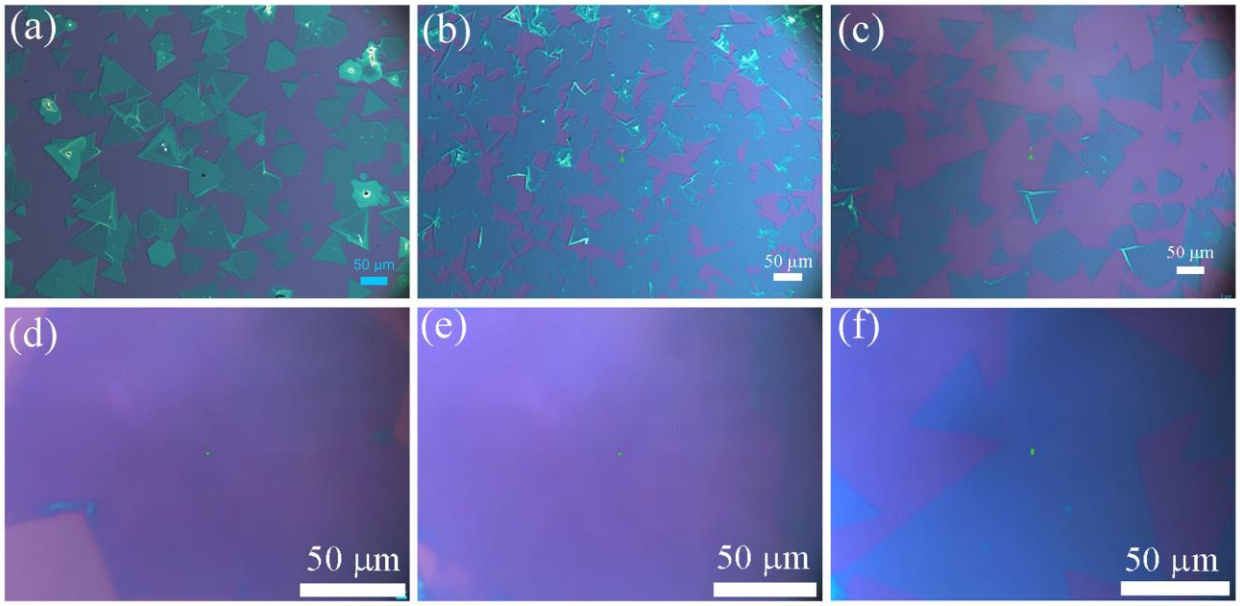

Figure 2.6: Optical microscope images of the CVD-grown WS_2 at 1000°C under growth pressure of (a) 5 mbar, (b) 2 mbar, and (c) 1 mbar. The high-magnified optical image of the WS_2 flakes grown at (d) 5 mbar, (e) 2 mbar, and (f) 1 mbar growth pressure.

importance of growth pressure. In addition to the uniform growth of 2D WS_2 across the substrate area, the WS_2 flake density has increased substantially under this condition. After further decreasing the growth pressure to 1 mbar, the thickness of WS_2 flakes remain highly uniform, but the flake density decreases, as seen in **Fig. 2.6(c)**. This is because the lower pressure leads to reduced precursor density near the substrate surface. The high-magnification images of different growth pressures are shown just below the corresponding low-magnification images. Thus, via systematic understanding of the importance of growth conditions we have synthesized large area WS_2 in the order of few hundred micrometers with excellent uniformity by CVD but have still not

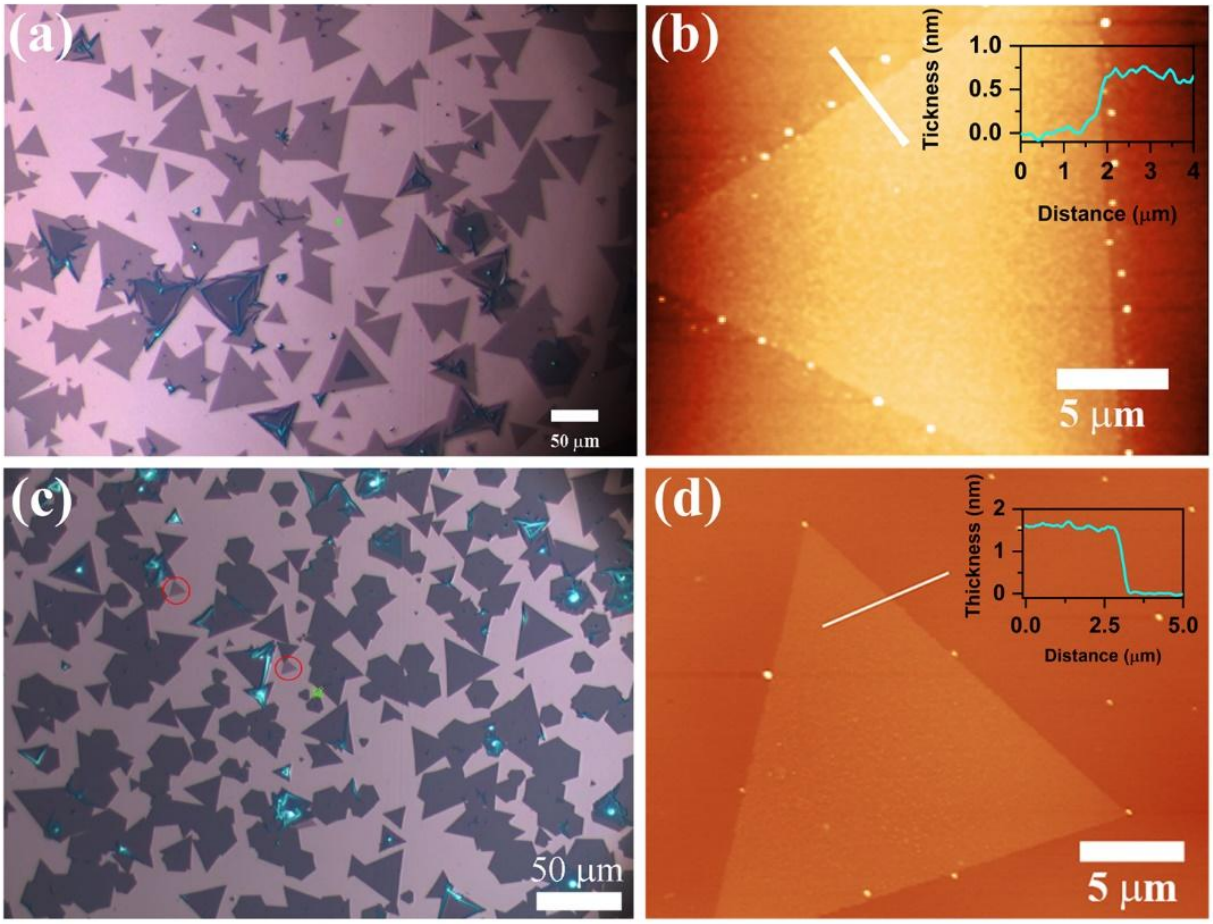

Figure 2.7: (a) Optical image of the monolayer WS_2 flakes on SiO_2/Si wafer showing uniform large area coverage. (b) AFM image a monolayer WS_2 flake with the thickness profile showing 1L-WS_2 thickness of 0.75 nm. (c) Optical image of bilayer WS_2 flakes on SiO2/Si wafer showing uniform large area coverage. (d) AFM image a bilayer WS_2 flake with the thickness profile showing 2L-WS_2 thickness of 1.65 nm.

obtained 1L-WS_2 and 2L-WS_2 growth. Hence further tuning of growth conditions is needed. In this regard catalysts like NaCl can be useful as they have been used in the CVD technique to promote lateral growth while suppressing vertical growth, leading to controlled layer synthesis[28]. To investigate the impact of NaCl catalyst on our growth process, we mixed 1 mg of NaCl with 10 mg of WO_3 during CVD growth. The results demonstrate excellent control in synthesizing 1L-WS_2 and 2L-WS_2, as illustrated in **Fig. 2.7.** The optical image in **Fig. 2.7(a)** shows the growth of uniform 1L-WS_2 over large area at 1000°C, with a growth pressure of 1.2 mbar over 15 minutes. In the optical images in addition to the 1L-WS_2 there are some flakes with higher thickness and bulk in nature, but that fraction is very low. The 1L-WS_2 growth was confirmed via measuring the thickness of WS_2 via atomic force microscopy. The AFM image of a 1L-WS_2 with thickness profile in the inset is shown in **Fig. 2.7(b)**. The thickness profile in the inset of **Fig.2.7(b)** indicates a thickness of 0.75 nm for 1L-WS_2 consistent with previously reported values[29]. Furthermore, by increasing the growth pressure to 2 mbar and extending the time to 20 minutes, we achieved uniform synthesis of 2L-WS_2, as shown in **Fig. 2.7(c)**. The substrate was predominantly covered by 2L-WS_2, with only a few regions of 1L-WS_2, as marked by red circles. The 2L-WS_2 has a thickness of 1.65 nm as measured by AFM and is shown in **Fig. 2.7(d)**. Through fine tuning of growth parameters, here we successfully optimized the controlled CVD growth of 1L-WS_2 and 2L-WS_2. This systematic optimization and deeper understanding of the growth parameters will assist in the controlled synthesis of other 2D materials.

2.4.6 Structural Characterization

Finally, the chemical composition and stoichiometry of the WS_2 flakes were analyzed through XPS spectra. The survey spectra shown in **Fig. 2.8(a)** reveal two characteristic peaks corresponding to tungsten 4f and sulfur 2p, confirming the successful synthesis of WS_2 using WO_3 and sulfur precursors. All peak positions were calibrated against the carbon peak at 284.8 eV. The high resolution XPS spectra for C_{1s} shows an additional signature C=O at 286.0 eV, as shown in **Fig. 2.8(b).** The high-resolution binding energy spectrum of S 2p, presented in **Fig. 2.8(c)**, exhibits a doublet at 162.6 eV and 163.8 eV, which correspond to S $2p_{3/2}$ and S $2p_{1/2}$, respectively[30]. These

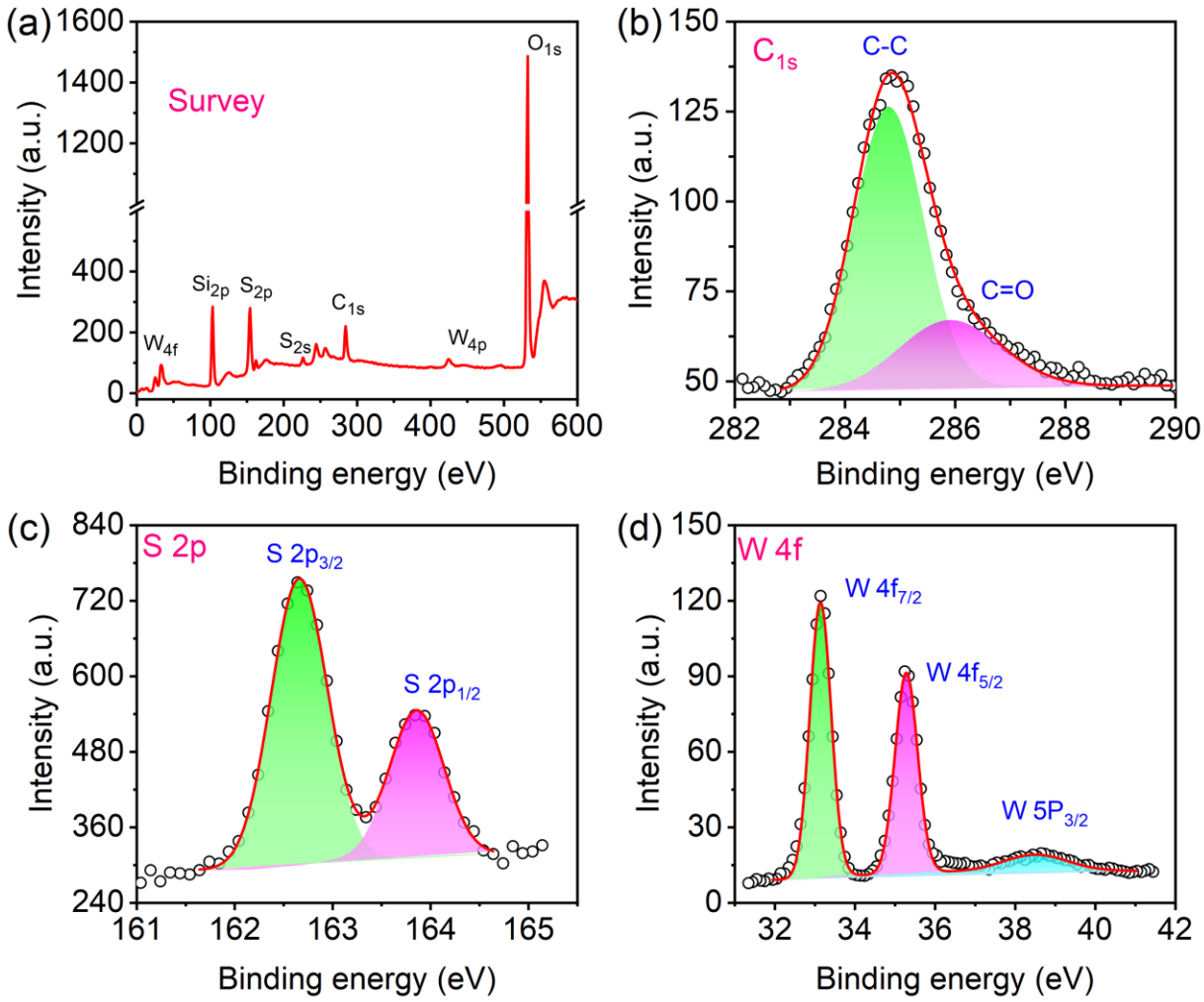

Figure 2.8: (a) XPS survey spectra for CVD grown 2D WS_2; (b) High resolution fitted spectra for C_{1s}; (c) High resolution fitted of W4f; (d) High resolution fitted of W4f.

peaks indicate the S^{2-} reduction state of sulfur, further validating the formation of WS_2. This observation highlights the excellent growth quality of WS_2 achieved via CVD. The high-resolution XPS spectra of W 4f, as illustrated in **Fig. 2.8(d)**, display two dominant peaks at 33.1 eV and 35.2 eV, corresponding to W $4f_{7/2}$ and W $4f_{5/2}$, respectively, which are associated with the W^{4+} oxidation state. These findings confirm the presence of tungsten in the W^{4+} state, supporting the successful synthesis of the semiconducting 2H phase WS_2[30]. Additionally, one low-intensity peak at 38.5 eV associated with W $5p_{3/2}$ also observed. This peak is characteristic of tungsten-containing materials. Hence WO_3 is fully reduced under the experimental conditions as suggested by Raman spectra. The S-to-W ratio was determined through curve fitting of the XPS spectrum using the

formula: , $\frac{S}{W} = \frac{\frac{A_{S3/2}}{S_{v(S_{3/2})}} + \frac{A_{S1/2}}{S_{v(S_{1/2})}}}{\frac{A_{W7/2}}{S_{v(W_{7/2})}} + \frac{A_{w5/2}}{S_{v(w_{5/2})}}}$, where A_x is the area under the fitted curve for x-orbital and S_{vx} is the corresponding sensitivity factor[34]. This calculation yielded a ratio of 2.14, which aligns closely with the expected value of 2, providing further evidence for the accurate stoichiometry of the synthesized WS_2.

2.5 Conclusion

This chapter concludes the controlled growth of 2D WS_2 flakes using the CVD technique, emphasizing the systematic optimization of growth conditions. It highlights the critical roles of growth temperature, pressure, and precursor co-evaporation in achieving desired material properties and uniformity. At a lower temperature of 850°C and a high pressure of 10 mbar, WO_3 undergoes partial reduction in the presence of excess sulfur, leading to the formation of rod-like structures due to unidirectional growth. As the temperature increases and the pressure decreases, this growth extends perpendicular to the initial axis, facilitating the structural evolution into 2D WS_2 flakes. At 1000°C, fully formed 2D WS_2 flakes are achieved, albeit with limited control over thickness. To enhance thickness control, growth pressure and time were systematically varied, and a small fraction of the growth promoter NaCl was introduced. This approach enabled the uniform synthesis of 1L-WS_2 and 2L WS_2 flakes with excellent precision.

References

(1) Wang, P.; Wang, A.; Hassan, M. M.; Ouyang, Q.; Li, H.; Chen, Q. A Highly Sensitive Upconversion Nanoparticles-WS_2 Nanosheet Sensing Platform for Escherichia Coli Detection. *Sens. Actuators B Chem.* 2020, *320*, 128434. https://doi.org/10.1016/j.snb.2020.128434.

(2) Uthappa, U. T.; Nehra, M.; Kumar, R.; Dilbaghi, N.; Marrazza, G.; Kaushik, A.; Kumar, S. Trends and Prospects of 2-D Tungsten Disulphide (WS_2) Hybrid Nanosystems for Environmental and Biomedical Applications. *Adv. Colloid Interface Sci.* 2023, *322*, 103024. https://doi.org/10.1016/j.cis.2023.103024.

(3) Gutiérrez, H. R.; Perea-López, N.; Elías, A. L.; Berkdemir, A.; Wang, B.; Lv, R.; López-Urías, F.; Crespi, V. H.; Terrones, H.; Terrones, M. Extraordinary Room-Temperature Photoluminescence in Triangular WS_2 Monolayers. *Nano Lett.* 2013, *13* (8), 3447–3454. https://doi.org/10.1021/nl3026357.

(4) Jayachandran, D.; Pendurthi, R.; Sadaf, M. U. K.; Sakib, N. U.; Pannone, A.; Chen, C.; Han, Y.; Trainor, N.; Kumari, S.; Mc Knight, T. V.; Redwing, J. M.; Yang, Y.; Das, S. Three-Dimensional Integration of Two-Dimensional Field-Effect Transistors. *Nature* 2024, *625* (7994), 276–281. https://doi.org/10.1038/s41586-023-06860-5.

(5) Sebastian, A.; Pendurthi, R.; Choudhury, T. H.; Redwing, J. M.; Das, S. Benchmarking Monolayer MoS_2 and WS_2 Field-Effect Transistors. *Nat. Commun.* 2021, *12* (1), 693. https://doi.org/10.1038/s41467-020-20732-w.

(6) Zhao, S.; Zhang, Y.; Wang, S.; Zhao, D.; Kang, H.; Li, J.; Xiao, R.; Kong, Z.; Chen, Z.; Sui, Y.; Wang, J.; Chen, Y.; Yu, G. Controllable Growth of Bilayer WS_2 by Chemical Vapor Deposition and Application for Photodetectors. *Mater. Lett.* 2022, *317*, 132103. https://doi.org/10.1016/j.matlet.2022.132103.

(7) Rong, Y.; Fan, Y.; Koh, A. L.; Robertson, A. W.; He, K.; Wang, S.; Tan, H.; Sinclair, R.; Warner, J. H. Controlling Sulphur Precursor Addition for Large Single Crystal Domains of WS_2. *Nanoscale* 2014, *6* (20), 12096–12103. https://doi.org/10.1039/C4NR04091K.

(8) Tang, L.; Tan, J.; Nong, H.; Liu, B.; Cheng, H.-M. Chemical Vapor Deposition Growth of Two-Dimensional Compound Materials: Controllability, Material Quality, and Growth Mechanism. *Acc. Mater. Res.* 2021, *2* (1), 36–47. https://doi.org/10.1021/accountsmr.0c00063.

(9) Zhang, J.; Wang, F.; Shenoy, V. B.; Tang, M.; Lou, J. Towards Controlled Synthesis of 2D Crystals by Chemical Vapor Deposition (CVD). *Mater. Today* 2020, *40*, 132–139. https://doi.org/10.1016/j.mattod.2020.06.012.

(10) Yang, W.; Mu, Y.; Chen, X.; Jin, N.; Song, J.; Chen, J.; Dong, L.; Liu, C.; Xuan, W.; Zhou, C.; Cong, C.; Shang, J.; He, S.; Wang, G.; Li, J. CVD Growth of Large-Area Monolayer WS_2 Film on Sapphire through Tuning Substrate Environment and Its Application for High-Sensitive Strain Sensor. *Discov. Nano* 2023, *18* (1), 13. https://doi.org/10.1186/s11671-023-03782-z.

(11) Aggarwal, P.; Kaushik, S.; Bisht, P.; Sharma, M.; Singh, A.; Mehta, B. R.; Singh, R. Centimeter-Scale Synthesis of Monolayer WS_2 Using Single-Zone Atmospheric-Pressure Chemical Vapor Deposition: A Detailed Study of Parametric Dependence, Growth Mechanism, and Photodetector Properties. *Cryst. Growth Des.* 2022, *22* (5), 3206–3217. https://doi.org/10.1021/acs.cgd.2c00049.

(12) Han, J.; Fang, R.; Zhu, L.; Geng, Z.; He, X. CVD Growth of Monolayer WS_2 through Controlled Growth Temperature and Time. *Ferroelectrics* 2020, *562* (1), 51–57. https://doi.org/10.1080/00150193.2020.1760592.

(13) Li, X.; Zhang, J.; Zhou, N.; Xu, H.; Yang, R. Insight into the Role of H2 in WS_2 Growth by Chemical Vapor Deposition. *ACS Appl. Electron. Mater.* 2021, *3* (11), 5138–5146. https://doi.org/10.1021/acsaelm.1c00891.

(14) Yin, H.; Zhang, X.; Lu, J.; Geng, X.; Wan, Y.; Wu, M.; Yang, P. Substrate Effects on the CVD Growth of MoS_2 and WS_2. *J. Mater. Sci.* 2020, *55* (3), 990–996. https://doi.org/10.1007/s10853-019-03993-9.

(15) Wang, Z.; Xu, W.; Li, B.; Hao, Q.; Wu, D.; Qi, D.; Gan, H.; Xie, J.; Hong, G.; Zhang, W. Selective Chemical Vapor Deposition Growth of WS_2/MoS_2 Vertical and Lateral Heterostructures on Gold Foils. *Nanomaterials* 2022, *12* (10), 1696. https://doi.org/10.3390/nano12101696.

(16) Hossain, M. T.; Jena, T.; Nath, U.; Sarma, M.; Giri, P. K. Room Temperature Exciton Formation and Robust Optical Properties of CVD-Grown Ultrathin Bi2O2Se Crystals on Arbitrary Substrates. *Nanoscale* 2023, *15* (26), 11222–11236. https://doi.org/10.1039/D3NR01201H.

(17) Kang, K. N.; Godin, K.; Yang, E.-H. The Growth Scale and Kinetics of WS_2 Monolayers under Varying H2 Concentration. *Sci. Rep.* 2015, *5* (1), 13205. https://doi.org/10.1038/srep13205.

(18) Campbell, W. R.; Reale, F.; Sundaram, R.; Bending, S. J. Optimisation of Processing Conditions during CVD Growth of 2D WS_2 Films from a Chloride Precursor. *J. Mater. Sci.* 2022, *57* (2), 1215–1229. https://doi.org/10.1007/s10853-021-06708-1.

(19) Lei, J.; Xie, Y.; Kutana, A.; Bets, K. V.; Yakobson, B. I. Salt-Assisted MoS_2 Growth: Molecular Mechanisms from the First Principles. *J. Am. Chem. Soc.* 2022, *144* (16), 7497–7503. https://doi.org/10.1021/jacs.2c02497.

(20) Pokhrel, H.; Duncan, J. A., Jr.; Krause, B.; Hoang, T. B.; Pollard, S. D. Transformation from Dendritic to Triangular Growth of WS_2 via NaCl Assisted Low-Pressure Chemical Vapor Deposition. *J. Vac. Sci. Technol. A* 2024, *42* (4), 042203. https://doi.org/10.1116/6.0003543.

(21) An, G. H.; Jin Kim, S.; Kim, S.; Shin, S. J.; Choi, M.; Kim, D.; Rahman, I. N.; Bang, J.; Kim, K.; Kim, D.-H.; Lee, H. S. Growth Mode Control of CVD-Grown WS_2 Monolayer Flakes *via* O2 Pre-Annealing for Organic Surfactant Oxidation. *Appl. Surf. Sci.* 2022, *585*, 152564. https://doi.org/10.1016/j.apsusc.2022.152564.

(22) Singh, A.; Sharma, M.; Singh, R. NaCl-Assisted CVD Growth of Large-Area High-Quality Trilayer MoS_2 and the Role of the Concentration Boundary Layer. *Cryst. Growth Des.* 2021, *21* (9), 4940–4946. https://doi.org/10.1021/acs.cgd.1c00390.

(23) Berkdemir, A.; Gutiérrez, H. R.; Botello-Méndez, A. R.; Perea-López, N.; Elías, A. L.; Chia, C.-I.; Wang, B.; Crespi, V. H.; López-Urías, F.; Charlier, J.-C.; Terrones, H.; Terrones, M. Identification of Individual and Few Layers of WS_2 Using Raman Spectroscopy. *Sci. Rep.* 2013, *3* (1), 1755. https://doi.org/10.1038/srep01755.

(24) Wan, Y.; Li, E.; Yu, Z.; Huang, J.-K.; Li, M.-Y.; Chou, A.-S.; Lee, Y.-T.; Lee, C.-J.; Hsu, H.-C.; Zhan, Q.; Aljarb, A.; Fu, J.-H.; Chiu, S.-P.; Wang, X.; Lin, J.-J.; Chiu, Y.-P.; Chang, W.-H.; Wang, H.; Shi, Y.; Lin, N.; Cheng, Y.; Tung, V.; Li, L.-J. Low-Defect-Density WS_2 by Hydroxide Vapor Phase Deposition. *Nat. Commun.* 2022, *13* (1), 4149. https://doi.org/10.1038/s41467-022-31886-0.

(25) Iqbal, M. W.; Shahzad, K.; Hussain, G.; Arshad, M. K.; Akbar, R.; Azam, S.; Aftab, S.; Alharbi, T.; Majid, A. Gate Dependent Phonon Shift in Tungsten Disulfide (WS_2) Field Effect Transistor. *Mater. Res. Express* 2019, *6* (11), 115909. https://doi.org/10.1088/2053-1591/ab485a.

(26) Staiger, M.; Gillen, R.; Scheuschner, N.; Ochedowski, O.; Kampmann, F.; Schleberger, M.; Thomsen, C.; Maultzsch, J. Splitting of Monolayer Out-of-Plane A_1' Raman Mode in Few-layer WS_2. *Phys. Rev. B* 2015, *91* (19), 195419. https://doi.org/10.1103/PhysRevB.91.195419.

(27) Liu, Y.; Hu, X.; Wang, T.; Liu, D. Reduced Binding Energy and Layer-Dependent Exciton Dynamics in Monolayer and Multilayer WS_2. *ACS Nano* 2019, *13* (12), 14416–14425. https://doi.org/10.1021/acsnano.9b08004.

(28) Xie, Y.; Ma, X.; Wang, Z.; Nan, T.; Wu, R.; Zhang, P.; Wang, H.; Wang, Y.; Zhan, Y.; Hao, Y. NaCl-Assisted CVD Synthesis, Transfer and Persistent Photoconductivity Properties of Two-Dimensional Transition Metal Dichalcogenides. *MRS Adv.* 2018, *3* (6), 365–371. https://doi.org/10.1557/adv.2018.156.

(29) Prasad, R. K.; Ghosh, K.; Giri, P. K.; Kim, D.-S.; Singh, D. K. High-Efficiency Photodetector Based on a CVD-Grown WS_2 Monolayer. *ACS Appl. Electron. Mater.* 2023, *5* (7), 3634–3640. https://doi.org/10.1021/acsaelm.3c00366.

(30) McCreary, K. M.; Hanbicki, A. T.; Jernigan, G. G.; Culbertson, J. C.; Jonker, B. T. Synthesis of Large-Area WS_2 Monolayers with Exceptional Photoluminescence. *Sci. Rep.* 2016, *6* (1), 19159. https://doi.org/10.1038/srep19159.

(31) Bora, A.; Paul, S.; Hossain, M. T.; Giri, P. K. Quantitative Understanding of the Photoluminescence Modulation and Doping of Monolayer WS_2 by Heterostructuring with Non-van Der Waals 2D Bi_2O_2Se Quantum Dots. *J. Phys. Chem. C* 2022, *126* (30), 12623–12634. https://doi.org/10.1021/acs.jpcc.2c03245.

(32) Mia, A. K.; Bora, A.; Hossain, M. T.; Sinha, S.; Giri, P. K. Fast Detection of Staphylococcus Aureus Using Thiol-Functionalized WS_2 Quantum Dots and Bi2O2Se Nanosheets Hybrid through a Fluorescence Recovery Mechanism. *J. Mater. Chem. B* 2023, *11* (42), 10206–10217. https://doi.org/10.1039/D3TB01465G.

(33) Mullapudi, K.; Addou, R.; Dezelah, Charles. L.; Moser, D. F.; Kanjolia, R. K.; Woodruff, J. H.; Conley, John. F. Synthesis of Micron-Sized WS_2 Crystallites Using Atomic Layer Deposition and Sulfur Annealing. *Chem. Mater.* 2023, *35* (12), 4649–4659. https://doi.org/10.1021/acs.chemmater.3c00013.

(34) Lavini, F.; Calò, A.; Gao, Y.; Albisetti, E.; Li, T.-D.; Cao, T.; Li, G.; Cao, L.; Aruta, C.; Riedo, E. Friction and Work Function Oscillatory Behavior for an Even and Odd Number of Layers in Polycrystalline MoS_2. *Nanoscale* 2018, *10* (17), 8304–8312. https://doi.org/10.1039/C8NR00238J.

Chapter 3

Asymmetric Contact-Induced Selective Doping of CVD-grown Bilayer WS_2 and Its Application in High-Performance Photodetection

In this chapter, we have explored metal contact-induced asymmetric doping in CVD-grown bilayer WS_2 (2L-WS_2) via contact engineering and its application toward high-performance photodetection. The 2D WS_2 grown by the CVD technique is an excellent candidate for high-performance optoelectronics due to its high carrier mobility, air stability, and strong optical absorption. However, photodetectors made with monolayer WS_2 (1L-WS_2) often exhibit high dark current with instability for a longer duration, and thus, there is scope for further improvement. Herein, we have developed a 2D 2L-WS_2-based photodetector with asymmetric contacts that exhibits an exceptionally low dark current and high specific detectivity. Compared to conventional symmetric contact electrodes, utilizing metal electrodes with higher and lower work functions relative to 2L-WS_2 aids in achieving asymmetric lateral doping in the WS_2 flakes. This doping asymmetry was confirmed through photoluminescence spectral profile and Raman mapping analysis. With the asymmetric contacts on 2L-WS_2, we find evidence of selective doping of electrons and holes near the Ti and Au contacts, respectively, while the WS_2 region away from the contacts remains intrinsic. When compared to the symmetric contacts case, the WS_2 photodetector with asymmetric (Au, Ti) contacts decreased the dark current by an order of magnitude under reverse bias and increased the photocurrent, resulting in an excellent on/off ratio of ~10^5 and overall improved device performance under identical illumination conditions. We explain this improved performance based on the energy band alignment showing unidirectional charge flow under light illumination. Our results indicate that the planar device structure and compatibility with current nanofabrication technologies can facilitate its integration into advanced chips for futuristic low-power optoelectronic and nanophotonic applications.

3.1 Introduction

There is an ever-growing demand for advancements in the development of energy-efficient optoelectronic devices with low power consumption for diverse applications ranging from

optoelectronics to point-of-care usage[1–3]. 2D layered materials such as graphene, transition metal dichalcogenides (TMDs), and MXenes have attracted attention due to their capability to scale down electronic devices to the atomic level.[4–6] Among all 2D materials, semiconducting TMDs, characterized by their tunable bandgap, planar structure, and high carrier mobility, have been explored for a diverse range of applications from photodetectors (PDs) and biosensors to energy storage devices.[7–9] The formation of P-N junctions through heterostructures involving TMDs such as MoS_2/WSe_2[10], WS_2/WSe_2[11], WS_2/MoS_2[12], and $MoSe_2/WS_2$[13] has been explored for enhanced photovoltaics and electronic switching applications. There is a lack of direct and precisely adjustable doping methods in 2D TMD semiconductors when compared to silicon technology. As a result, alternative attempts have been made to create precise asymmetric control of doping in 2D TMDs. These methods encompass local electrostatic gating[14], chemical doping[15], carrier adjustment through plasma treatment[16] and carrier injection using uneven metal contacts.[17,18]

WS_2 is a member of the TMD family and has been identified as an excellent candidate for optoelectronic applications due to its high stability, high carrier mobility, and potential for mass production.[19,20] There have been reports on WS_2-based photodetectors in the visible spectrum using monolayer, few layers, and multilayer WS_2.[21–27] However, the performance of these devices is not up to the standard of typical commercial photodetectors. For instance, Perea-López et al. observed a low responsivity on the order of μA/W in multilayer WS_2 photodetector within the visible range.[21] By passivating the sulfur vacancy sites, the responsivity of few-layered WS_2 was enhanced to few mA/W to 5.7 A/W; however, the on/off ratio dropped by a few orders. This decrease was caused by the increase in dark current due to the electron doping effect.[22,28] Thus, one can enhance the WS_2 photodetector performance by tuning the doping. The formation of Schottky junction with WS_2 improves the performance in contrast to the Ohmic junctions[29] by reducing the dark current and facilitating charge separation due to the built-in potential.[17] Interestingly, the carrier mobility in 2D WS_2 is layer-dependent. Specifically, 2L-WS_2 displays mobility that is twice that of the monolayer WS_2, and it possesses enhanced photo-absorption due to higher thickness, underscoring the significance of using 2L-WS_2 in photodetection applications.[30] Chemical doping on the WS_2 surface yields improved photodetection performance. However, indigenous asymmetric doping through an asymmetric contact-based photodetector using 2D WS_2 has not been explored yet.

Herein, we report an asymmetric contact-based 2L-WS_2 photodetector in planar configuration showing significant performance. We have synthesized uniform large-area high-quality monolayer and 2L-WS_2 on SiO_2/Si substrate by CVD. The WS_2 flakes were transferred from the growth substrate to a dry SiO_2/Si substrate using a polymethyl methacrylate (PMMA)-assisted wet transfer method, ensuring that the optoelectronic properties remained intact. We conducted comparative analyses between symmetric and asymmetric contacts to differentiate the impact of asymmetric contacts on photodetection performance. The asymmetric contacts lead to the creation of two lateral junctions in 2L-WS_2, resulting in a p-n-n^+ type junction. This configuration significantly reduces the dark current under reverse bias and enhances the on/off ratio by an order of magnitude with a peak responsivity of 1.2 A/W.

3.2. Experimental Details

3.2.1. Synthesis of Monolayer and Bilayer WS_2 Flakes by CVD

The WS_2 flakes were synthesized through thermal CVD using a two-zone muffle furnace. A detailed schematic representation of the experimental setup, along with specific growth conditions, was provided in **Chapter 2**, specifically in **sections 2.2 and 2.4.5**.

3.2.2 Transfer of WS_2 Flakes and Device Fabrication

The WS_2 flakes grown via CVD were transferred from the growth substrate to a dry SiO_2/Si substrate using a modified PMMA-assisted wet transfer process using two different methods[31]. The first method involved heating at 120°C for 5 minutes, while the second method omitted heating and allowed the sample to rest for 24 hours after PMMA coating, with all other steps remaining the same. The transfer method is schematically represented in **Fig. 3.1**. First, PMMA was coated on the substrate using a spin coater, as schematically shown in **Fig. 3.1(b)**. Following this, the PMMA-coated wafer was immersed in a 1.0 M NaOH solution for 3 hours, resulting in the detachment of the PMMA film with the WS_2 flakes from the substrate, as illustrated in **Fig. 3.1(c) and Fig. 3.1(d)**. Then the film was washed multiple times in DI water to remove additional impurities and ions. The film was subsequently transferred onto a dry SiO_2/Si wafer, as illustrated in **Fig. 3.1(e)**. Finally, the top PMMA layer was eliminated by immersing it in acetone overnight, as shown in **Fig.3.1(f)**. After transferring the flakes, we observed them under an optical microscope. The magnified optical image of transferred WS_2 flakes involving heat treatment, is

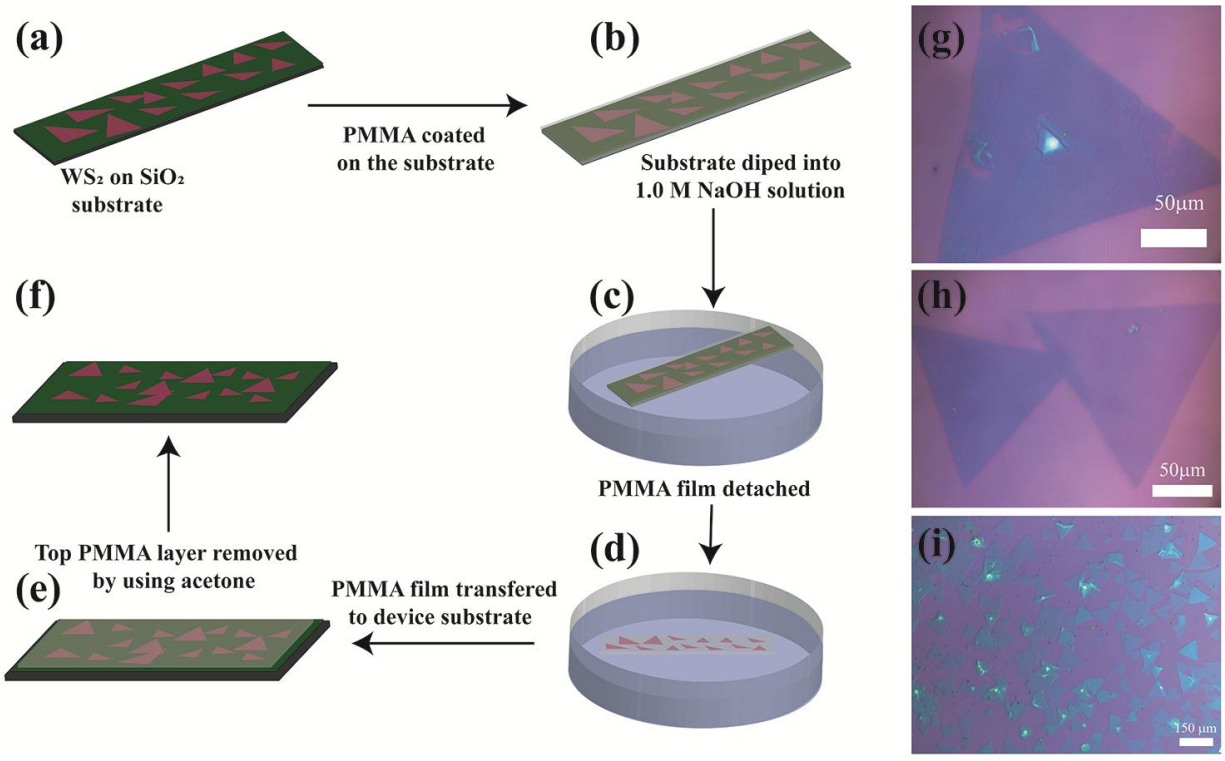

Figure 3.1: Schematic representation for the transfer process of WS_2 flakes (a) CVD grown 2D WS_2 flakes on SiO_2/Si substrate; (b) Spin coating of PMMA of the substrate; (c) The PMMA coated substrate is dipped in 1 M NaOH solution; (d) Detachment of the PMMA film with the WS_2 flakes and washing it with DI water multiple times; (e) Transferring the PMMA film to the device substrate; (f) WS_2 flakes on the device substrate after removing the top PMMA layer using acetone; (g) Optical image of the heat-assisted transfer process; (h) Optical image of the WS_2 flakes transferred without involving any heat treatments; (i) Low magnification optical image of the transferred WS_2 flakes

displayed in Fig. 3.1 (g), and of the flakes involving heat treatment is displayed in Fig. 3.1 (h). There is mechanical damage on the substrate involving heating as shown in **Fig. 3.1(g)** but **Fig. 3.1(h)** displays no mechanical damage to the flake transferred without any heating, suggesting that the flakes undergo mechanical deformation due to thermal heating in the presence of PMMA. The low-magnification image of the transferred flakes on the SiO_2/Si substrate is shown in **Fig. 3.1(i)**, which reveals that almost all the flakes remain intact during this transfer process. Thus, the process without any heat treatment was employed to transfer WS_2 flakes on TEM grids for FETEM characterization and device fabrication.

3.3 Results and Discussion

3.3.1 Optical, Chemical, and Structural Analysis

The optical image corresponding to the large area uniform synthesis of 1L-Ws_2 and 2L-WS_2, along with the AFM height profile, is displayed in **Fig. 2.7 of Chapter 2**. When excited with a 532 nm laser, the Raman spectrum of WS_2 flake shows several phonon modes in addition to two characteristic modes as displayed in **Fig. 3.2(a).** The two characteristics Raman modes, A_{1g} and E_{2g}, corresponding to out-of-plane and in-plane vibrations of W and S atoms, are observed at 418.8

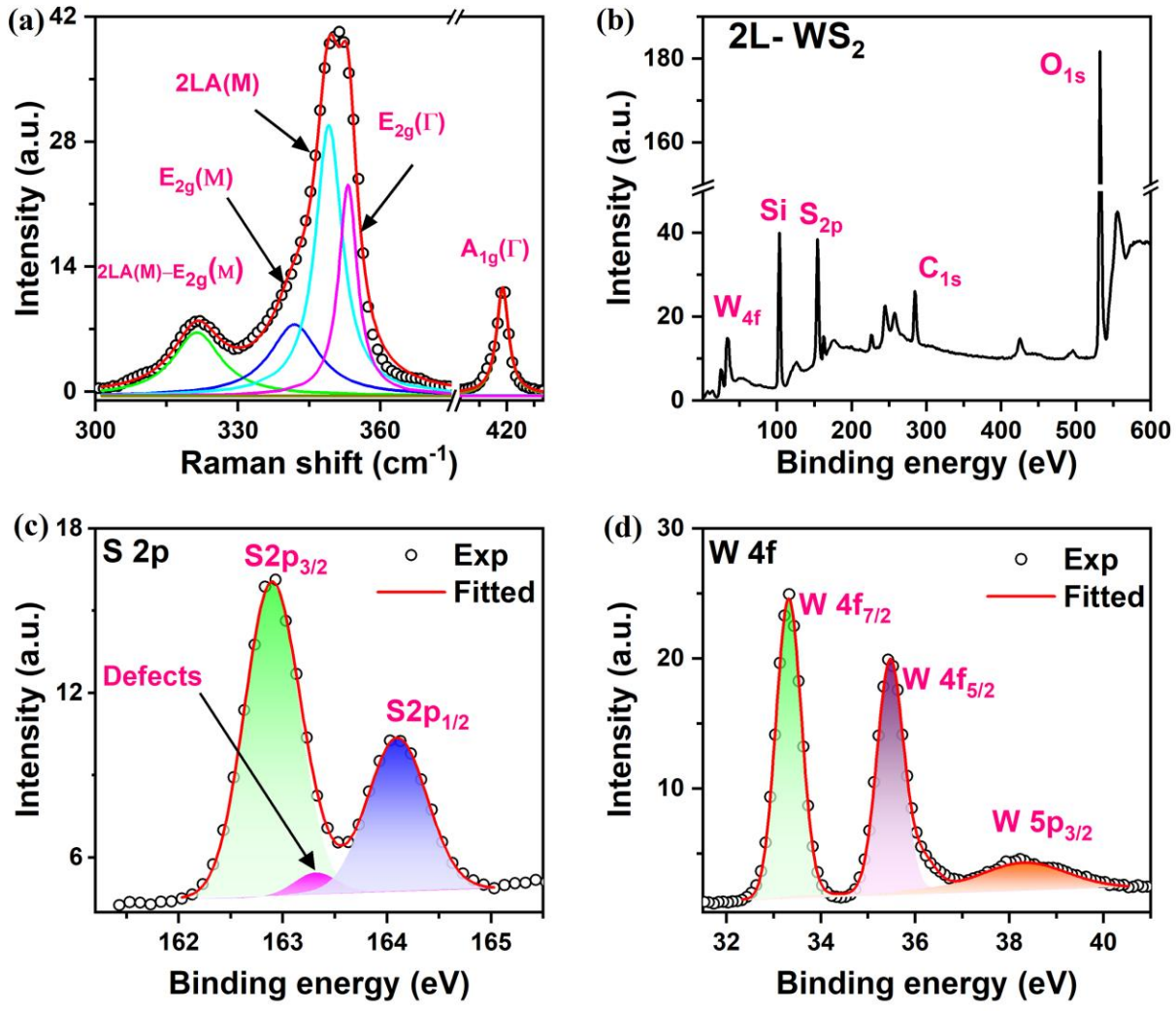

Figure 3.2: (a) Deconvoluted Raman spectra of 2L-WS_2 under 532 nm laser excitation. (b) XPS survey spectra of CVD-grown WS_2. (c) The high-resolution core binding energy for S2p. (d) The high-resolution core binding energy of W4f.

cm^{-1} and 355.1 cm^{-1}, respectively for 2L-WS_2. Other observed optical phonon modes are labeled in the deconvoluted spectra in **Fig. 3.2(a).**[33] Charge doping and layer numbers immensely influence the out-of-plane A_{1g} mode, and the in-plane mode E_{2g} is sensitive to the induced strain.[34] The separation between these two modes is characteristic of layer thickness, providing an indirect way to know layer numbers.[35] The chemical composition and stoichiometry of the as-grown 2L-WS_2 flakes were analyzed using XPS. The presence of two characteristic peaks of tungsten and sulfur in the survey spectra of **Fig. 3.2(b)** confirms the synthesis of WS_2 using transition metal oxide and chalcogen precursors. All the peak positions were measured with respect to the carbon peak at 284.8 eV. The high-resolution binding energy spectrum of S 2p in **Fig. 3.2(c)** shows a doublet at 162.9 eV and 164.1 eV, corresponding to S $2p_{3/2}$ and S $2p_{1/2}$, respectively.[39] These two peaks correspond to the S^{2-} reduction state of sulfur, confirming WS_2 synthesis. Furthermore, we noticed a minor peak at 163.3 eV (with a spectral weight of 3.0%), corresponding to sulfur vacancy defect.[40,41] This observation underscores the excellent growth quality of WS_2 achieved through the CVD method. In the high-resolution XPS spectra of W 4f, we observed two prominent peaks centered at 33.3 eV and 35.4 eV in **Fig. 3.2(d)**, corresponding to the W $4f_{7/2}$ and W $4f_{5/2}$, respectively, associated with W^{4+} oxidation states. These findings confirm the presence of tungsten in the W^{4+} oxidation state, providing evidence for the successful synthesis of the semiconducting 2H WS_2 phase.[39] The additional low-intensity peak is associated with W $5p_{3/2}$. The curve fitting of the XPS spectrum was employed to determine the S to W ratio. The S to W ratio was calculated using the formula, $\frac{S}{W} = \frac{\frac{A_{S3/2}}{S_{v(S_{3/2})}} + \frac{A_{S1/2}}{S_{v(S_{1/2})}}}{\frac{A_{W7/2}}{S_{v(W_{7/2})}} + \frac{A_{w5/2}}{S_{v(w_{5/2})}}}$, where A_x is the area under the fitted curve for x-orbital and S_{vx} is the corresponding sensitivity factor[43], yielding a value of 2.04, which closely corresponds to the anticipated value of 2.

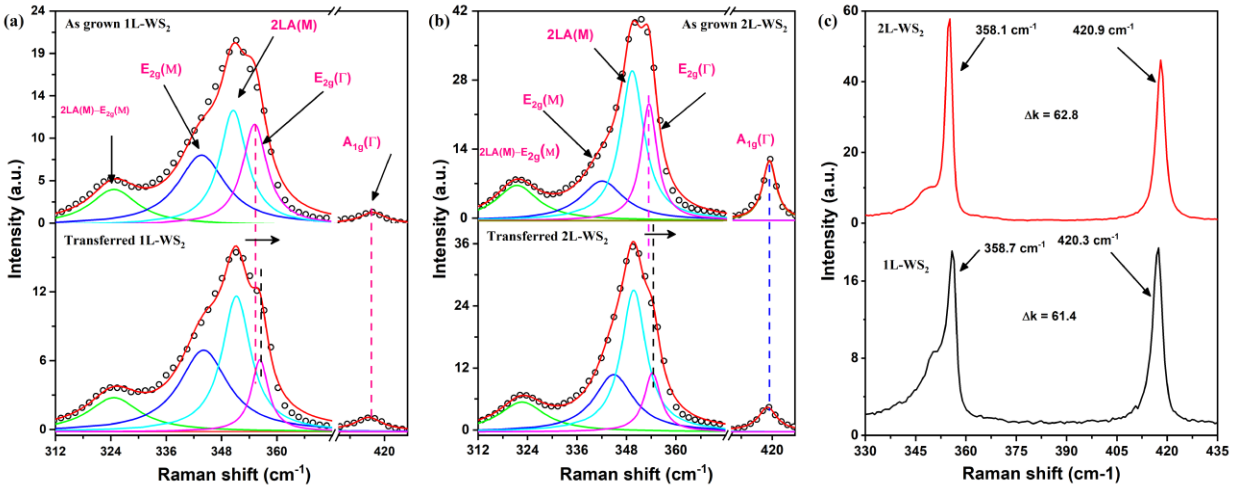

Figure 3.3: (a) Raman spectra of 1L-WS_2 before and after transfer; (b) The Raman spectra of 2L-WS_2 before and after transfer; (c) Raman spectra of 1L and 2L-WS_2 using 488 nm laser excitation.

Since the transferred WS_2 was to be used for photodetector fabrication, the quality of transferred WS_2 flakes was analyzed with the help of Raman spectroscopy. The fitted Raman spectra of 1L-WS_2 and 2L-WS_2 before and after transfer are shown in **Fig. 3.3**. The distinct Raman modes after transfer indicate seamless transfer to the device substrate without compromising its quality[36]. The E_{2g} mode experiences a blue shift of 1.1 cm^{-1} after the transfer of WS_2, which is consistent with the anticipated reduction in strain following the transfer process.[36,37] The lattice mismatch and difference in thermal expansion coefficients between SiO_2 and WS_2 cause significant strain in the high-temperature CVD-grown WS_2 flakes, which are subsequently reduced due to the transfer process.[38] The 532 nm laser excites various phonon modes, and the peak fitting can notoriously be error-prone. Hence, the Raman spectra obtained by the 532 nm laser are not ideal for finding the characteristic mode separation. When excited with a 488 nm laser, only intense in-plane and out-of-plane characteristics Raman modes are observed along with low-intensity 2LA mode, as shown in **Fig. 3.3(c)**. Hence, the separation of the A_{1g} and E_{2g} modes was measured using 488 nm laser excitation. The 1L-WS_2 exhibits a separation of ~61.4 cm-1, which increases to ~62.8 cm^{-1} for 2L-WS_2[35].

The FETEM images of the CVD-grown WS_2 flakes are displayed in **Fig. 3.4**. **Fig. 3.4(a)** shows a single free-standing monolayer WS_2. The flake underwent folding during the transfer from the growth substrate to the TEM grid. **Fig. 3.4(b)** illustrates the presence of hexagonal bright spots in

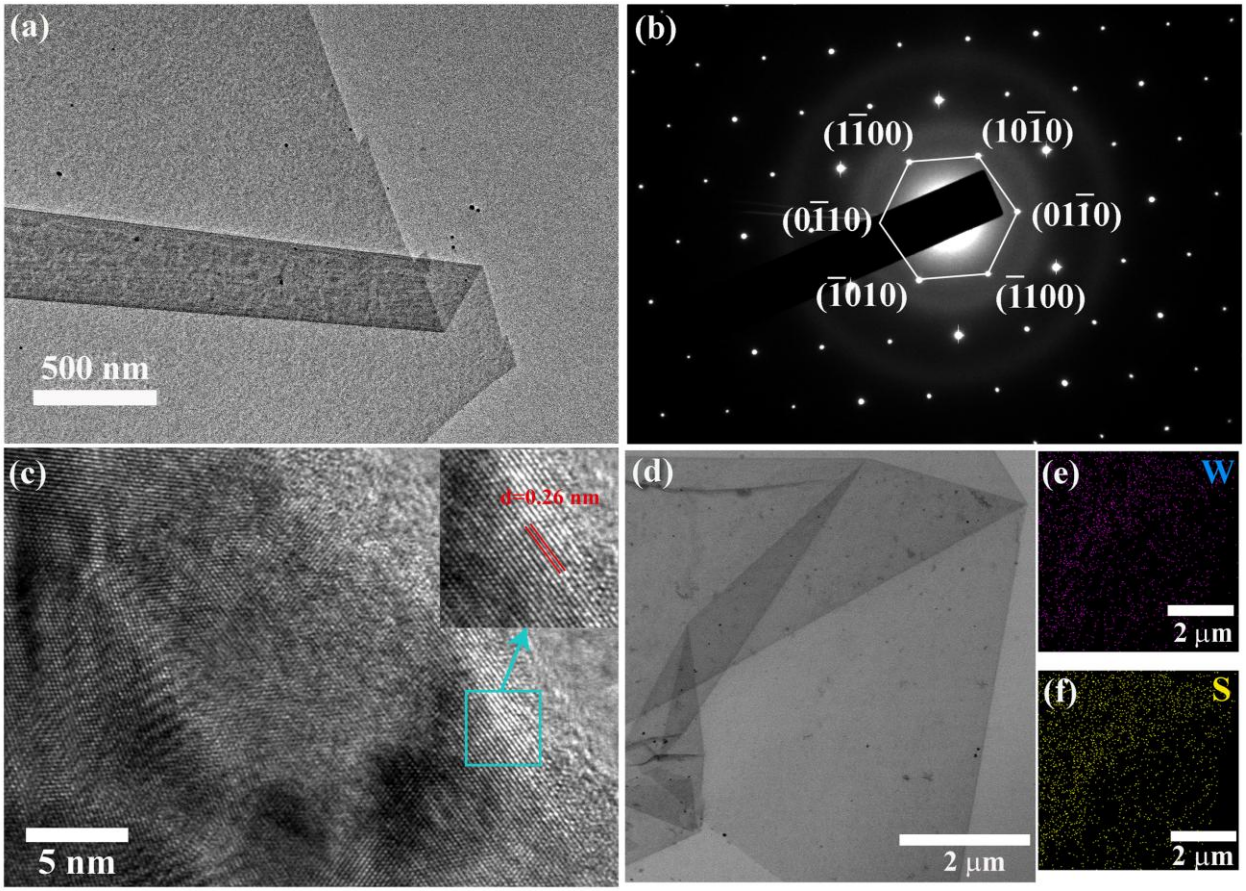

Figure 3.4: TEM images of transferred WS_2 flakes. (a) Freestanding 1L-WS_2 flake, folded during the transfer process; (b) Hexagonal diffraction pattern (SAED) on 1L-WS_2; (c) HRTEM image with lattice planes; the inset shows an interplanar spacing of 0.26 nm. (d) WS_2 flake for EDS elemental mapping. (e), (f) Elemental mapping of tungsten and sulfur, respectively.

the reciprocal space when performing Selected Area Electron Diffraction (SAED) on a monolayer of WS_2. The diffraction spots were labeled, and the lattice parameter was observed to be around 0.295 nm from the SAED pattern, which aligns with previous reports.[44,45] **Fig. 3.4(c)** displays the high-resolution TEM (HRTEM) image of a monolayer of WS_2, revealing an interplanar spacing of 0.26 nm associated with the <100> crystallographic plane of hexagonal WS_2.[46] The composition was additionally determined through EDS elemental mapping using TEM. The EDS analysis reveals the existence of 40.0% tungsten and 60.0% sulfur, resulting in a sulfur-to-tungsten ratio of 1.5, suggesting the presence of sulfur vacancies. The XPS analysis determined a sulfur-to-tungsten

ratio of 2.04, suggesting the creation of additional vacancy sites due to the high-energy electron beam during the prolonged EDS examination in FETEM.[47]

The UV-Vis absorption spectrum in **Fig. 3.5(a)** shows two strong excitonic absorption peaks.[48] The A and B excitonic absorption peaks that arise from direct bandgap transition at K points are found to be at 622 nm and 514 nm, respectively 1L-WS_2.[49] The spin-orbit coupling-induced splitting in the valence band at K point gives rise to an energy gap of approximately 0.42 eV

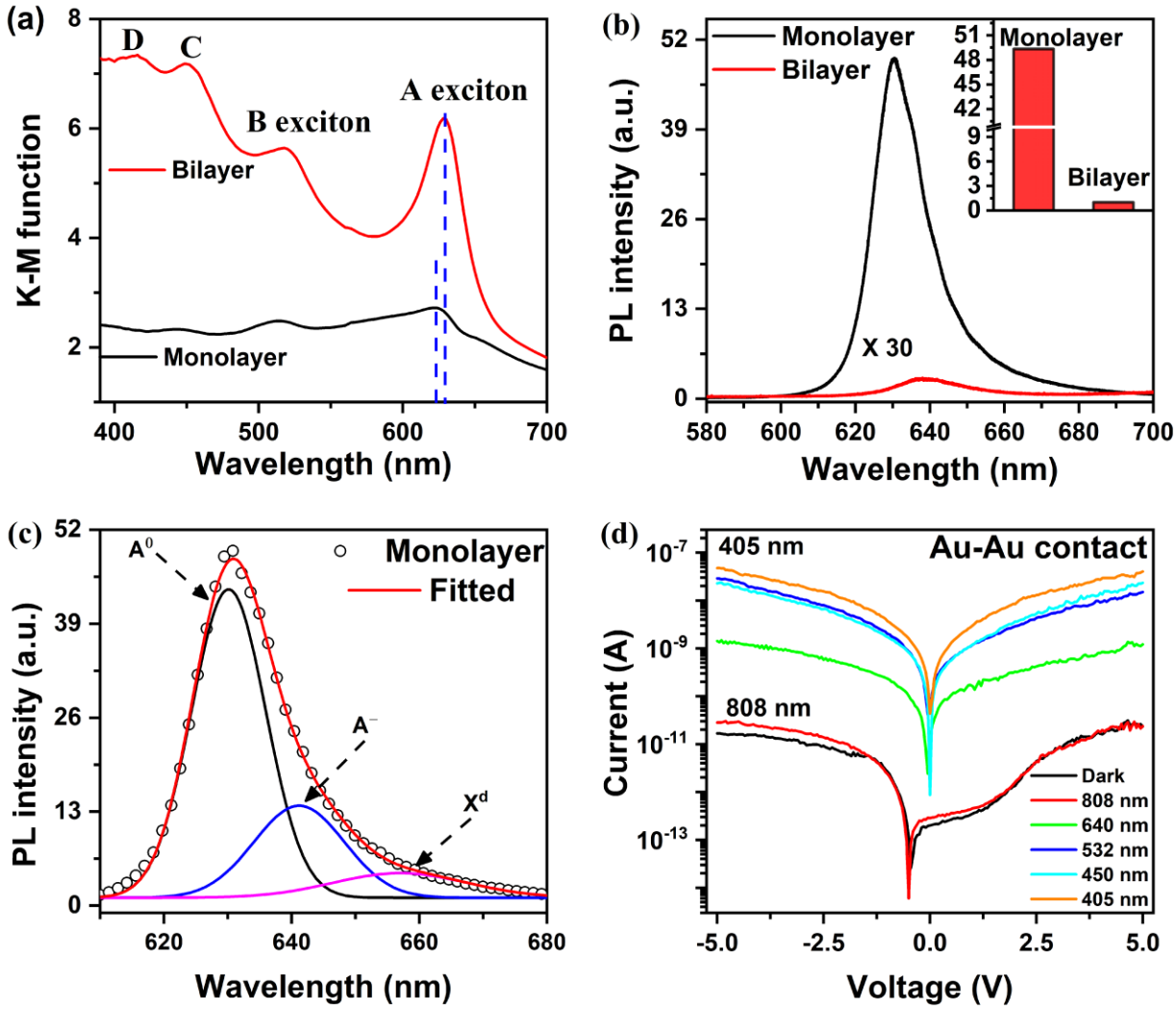

Figure 3.5: (a) UV-Vis absorption spectrum of 1L and 2L-WS_2 flakes; (b) PL emission spectra of 1L and 2L-WS_2 under 532 nm laser excitation. The inset shows the bar diagram of relative PL intensity for 1L and 2L-WS_2; (c) Deconvoluted PL emission spectrum for 1L-WS_2; (d) Excitation wavelength-dependent photo I-V characteristics of WS_2 PD for symmetric Au contacts.

between those peaks. There is a redshift in the absorption peaks for the 2L-WS_2, which are found at 628 nm and 518 nm, corresponding to A and B excitonic absorption, respectively. Besides the redshift, there is a substantial rise in absorption intensity that can be attributed to the increased thickness in 2L-WS_2, implying higher absorption. Moreover, two faint absorption peaks exist at 453 nm and 415 nm, denoted as C and D in the absorption spectrum. These peaks result from optical transitions between the peaks of the density of states in the valence and conduction bands.[49,50] **Figure 3.5(b)** compares the PL emission spectra for 1L and 2L-WS_2. When the thickness of 2D WS_2 is reduced to 1L, there is a transition from an indirect to a direct bandgap, resulting in a significantly enhanced PL emission.[51] The low-dimensional 1L-WS_2 exhibits high exciton binding energy at room temperature, aiding the strong PL emission.[52] This heightened PL at room temperature is a distinguishing characteristic that sets 1L-WS_2 apart from other morphologies.[53] When excited by a 532 nm laser, the 2L-WS_2 PL exhibits an almost 99% reduction in intensity compared to monolayer WS_2, accompanied by a shift towards longer wavelengths from 630 nm to 638 nm. The bar diagram in the inset of **Fig. 3.5(b)** compares the intensity of PL emission of 1L and 2L-WS_2. The laser excitation also generates trions and defect-bound excitons, which can be attributed to excess carrier generation and defects induced by local heating.[54,55] PL spectrum of monolayer WS_2 was deconvoluted to find contributions from neutral exciton (A^o), trion (A^-), and defect-bound excitons (X^d), as shown in **Fig. 3.5(c)**. 1L-WS_2 has high trion binding energy in the range of 30-40 meV at room temperature, leading to strong trion emission at room temperature.[56] We observed a neutral exciton (A^o) peak at 630.0 nm along with a trion (A^-) peak at 641.0 nm and a defect-bound exciton (X^d) peak at 656.0 nm. The low spectral weight of defect-bound excitons indicates high-quality growth of WS_2 by CVD, as revealed by Raman, XPS and FETEM analyses.

A suitable energy photon can modulate the carrier concentration in the semiconducting 2H phase WS_2, hence the conductivity by photoinduced carrier generation. **Fig. 3.5(d)** displays the I-V characteristics under dark and light (various wavelength laser excitations) conditions. There is a minimal change in current with respect to dark conditions when exposed to 808 nm laser illumination, while the current increases by several orders of magnitude under 640 nm, 533 nm, 450 nm and 405 nm laser illuminations. The bandgap of monolayer and 2L-WS_2 is approximately 2.0 eV. However, the energy of the 808 nm laser excitation is only 1.5 eV, significantly lower than the bandgap of 2L-WS_2. Consequently, the 808 nm laser excitation cannot generate excess

electron-hole pairs in 2L-WS_2, resulting in no change in current upon excitation by 808 nm laser. The excitation energy for lasers with wavelengths other than 808 nm approaches or exceeds the bandgap of 2L-WS_2, which leads to the generation of excess electron-hole pairs, thus increasing the current. This aligns with the UV-Vis absorption data, which shows no absorption beyond 700 nm but significant absorption below 650 nm. These observations confirm that the current enhancement results from carrier generation in the 2L-WS_2 after suitable wavelength laser illumination, enabling it to function as a Photodetector.

3.3.2. Device Fabrication and Electrical Performance

UV lithography was used for device fabrication, and the metal contacts were deposited via an e-beam evaporations system. First, the photoresist (PR) S1813 (MICROPOSIT™) was coated by a spin coater. For the symmetric contact-based device, both metal pads were patterned simultaneously by a direct UV laser writing process on a single flake, followed by metal deposition and lift-off. The detailed fabrication process for asymmetric contact-based PDs is presented in **Fig. 3.6(a)**. First, one contact was patterned on one side of a flake by selective opening via UV lithography followed by 45 nm of Ti deposition and lift-off. The second electrode was patterned after fine adjustments of the previously deposited Ti contact followed by Au deposition and lift-off. Finally, the devices were heated at 90ºC for 10 minutes to remove the residual solvents. Metal-induced lateral electronic charge doping in WS_2 was examined using line Raman mapping and PL spectrum of the monolayer WS_2. As mentioned previously, the monolayer WS_2 exhibits remarkable PL emission at room temperature when exposed to 532 nm laser excitation. External charge doping significantly affects its PL emission, leading to significant changes in neutral and trion contribution[58]. Following the formation of asymmetric contacts, the PL emission spectra after contact deposition on transferred WS_2 at various locations are depicted in **Fig. 3.6(b)**. The inset shows the relative change in the ratio of the intensities of the trion peak to the neutral exciton peak for three different locations. The PL spectra show a low trion contribution near the Au contact, dropping from 32.1% to 19.5%. This decrease in the trion formation can be attributed to the electron transfer from the WS_2 monolayer to Au due to band alignments, which is analogous to p-doping in WS_2. The electron transfer from WS_2 to Au decreases the electron concentration in WS_2, resulting in reduced trion formation compared to the transferred monolayer WS_2. We observed an increase in the trion contribution in the vicinity of the Ti contact from 32.1% to 38.8%. This indicates an increase in electron density due to electron transfer from Ti to WS_2 which is analogous

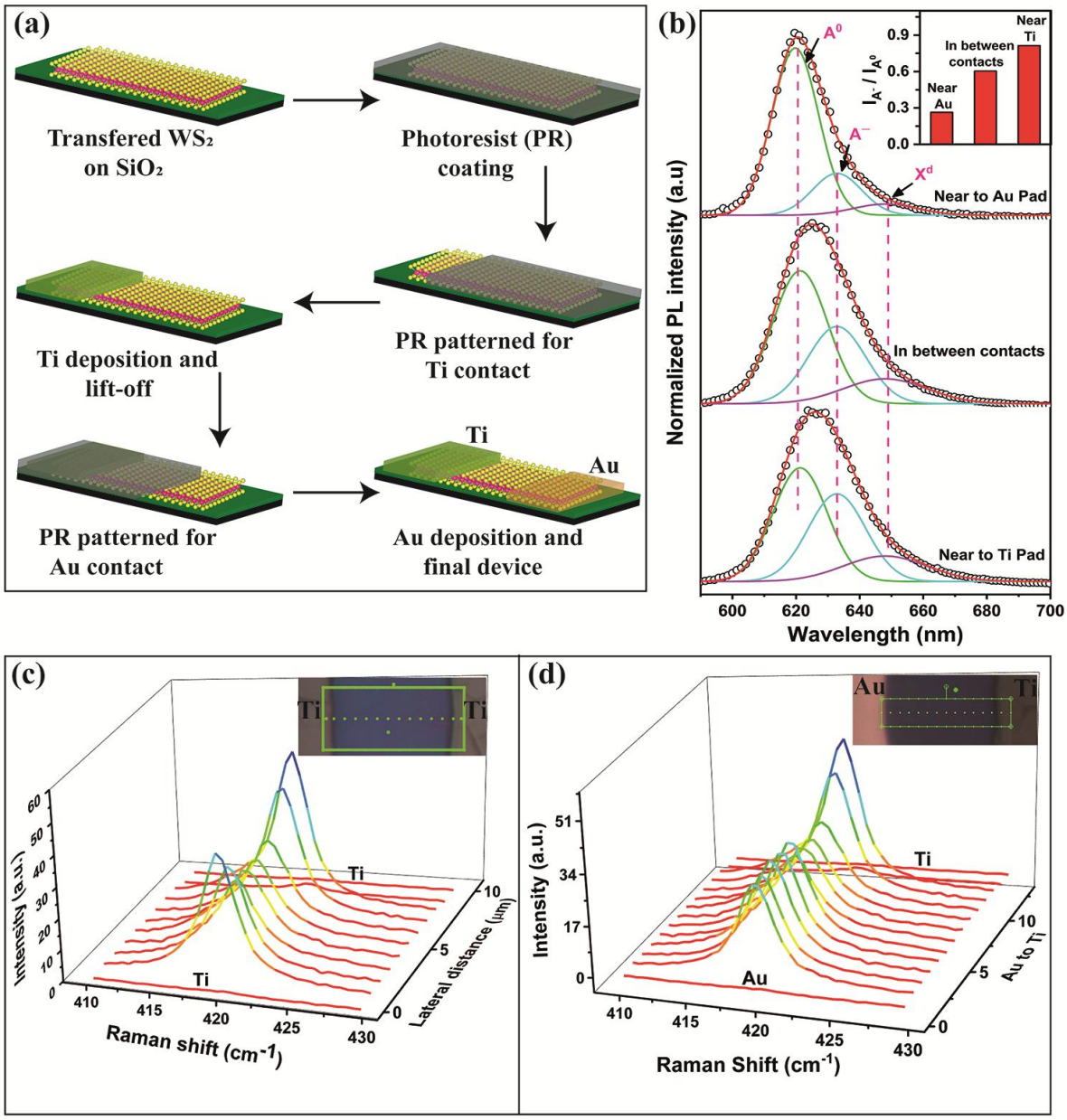

Figure 3.6: (a) Schematic representation of fabrication process for asymmetric contacts based WS_2 PD. (b) PL spectra of monolayer WS_2 at different locations after the fabrication of asymmetric contacts based WS_2 PD on transferred monolayer WS_2. The inset shows bar chat of the variation of trion to neutral exciton rations in the corresponding points. (c) Raman mapping of A_{1g} mode of WS_2 at different locations after fabricating symmetric Ti contact-based PD; The inset shows the optical image of the symmetric Ti contact PD with mapping points (dots). (d) Raman mapping of A_{1g} mode of WS_2 at different locations after fabricating asymmetric contacts-based PD; The inset shows the optical image of the asymmetric contacts PD with mapping points (dots).

to n-type doping in WS_2 by Ti electrode. Thus, we can selectively introduce electron and hole doping near the Au and Ti contacts, respectively, while the central region of the WS_2 flake remains intrinsic. Hence, a p-n-n^+ type junction is formed with WS_2 due to the asymmetric metal contacts. For further validation, we conducted Raman line mapping of WS_2 flakes after forming Ti-Ti and Ti-Au asymmetric contacts, as shown in **Fig. 3.6(c) and (d),** respectively. As the A_{1g} Raman mode is responsive to charge density, the doping effect is expected to be reflected in the A_{1g} mode spatial profile. **Fig. 3.6(c)** illustrates the Raman mapping of the A_{1g} mode following symmetric Ti-Ti contacts. The inset displays an optical image of the device, highlighting the measurement points. Examining the spectra reveals a more pronounced A_{1g} mode near the contacts, contrasted with a weaker signal at the central region. The electron doping near the Ti contact gives rise to stronger electron-phonon coupling and hence stronger A_{1g} mode, whereas the effect of doping from the Ti electrode at the center is minimum and hence weak vibration, thus confirming the n-type doping by the Ti electrode. The A_{1g} Raman mode mapping after the formation of asymmetric contacts is displayed in **Fig. 3.6(d)**. The inset displays an optical image of the device, highlighting the measurement points. The mapping shows that the A_{1g} mode intensity increases toward the Ti contacts, verifying the enhanced electron-phonon coupling. No Raman signal is detected at the point above the metal contacts, indicating that the metal pads fully absorb the laser light. The A_{1g} mode intensity is supposed to decrease near the Au metal pads as the electron density decreases, but the plasmonic effect of gold, when excited by a 532 nm laser, increases the Raman intensity[59], and hence a significant reduction in intensity is not observed. Thus, mapping the A_{1g} mode also confirms the asymmetric doping in WS_2, forming a p-n-n^+ type junction.

The current-voltage (I-V) characteristics under dark and light with different intensities (405 nm laser) are shown in **Fig. 3.7**. The Ti pad was grounded, and the Au contact pad was biased with voltage sweep from -5V to +5V during the I-V measurements of asymmetric contact WS_2 PD. The illumination intensity-dependent I-V characteristics with symmetric Ti-Ti and Au-Au contacts are shown in **Fig. 3.7(a) and 3.7(b)**, respectively. The monolayer and 2L-WS_2 have a work function of 4.9 eV and are generally an n-type semiconducting material.[40] Since Ti has a work function of 4.3 eV, there is no potential barrier between the Ti-WS_2 junction, resulting in a symmetric I-V characteristic, as shown in **Fig. 3.7(a)**. In contrast, the Au has a higher work function of 5.1 eV

than the n-type WS_2, forming a Schottky junction giving asymmetric I-V characteristics.[60] Fig. **3.7(c)** displays the I-V characteristics of the WS_2 PD with asymmetric Ti-Au contacts, revealing a significant reduction in dark current by an order of magnitude. The formation of a p-n-n+ junction along the WS_2 flakes creates two depletion regions, allowing the unidirectional flow of carriers (electrons), resulting in lower dark current under reverse bias conditions. Excess electron-hole pairs are generated under 405 nm laser illumination, and hence, there is an increase in current. The

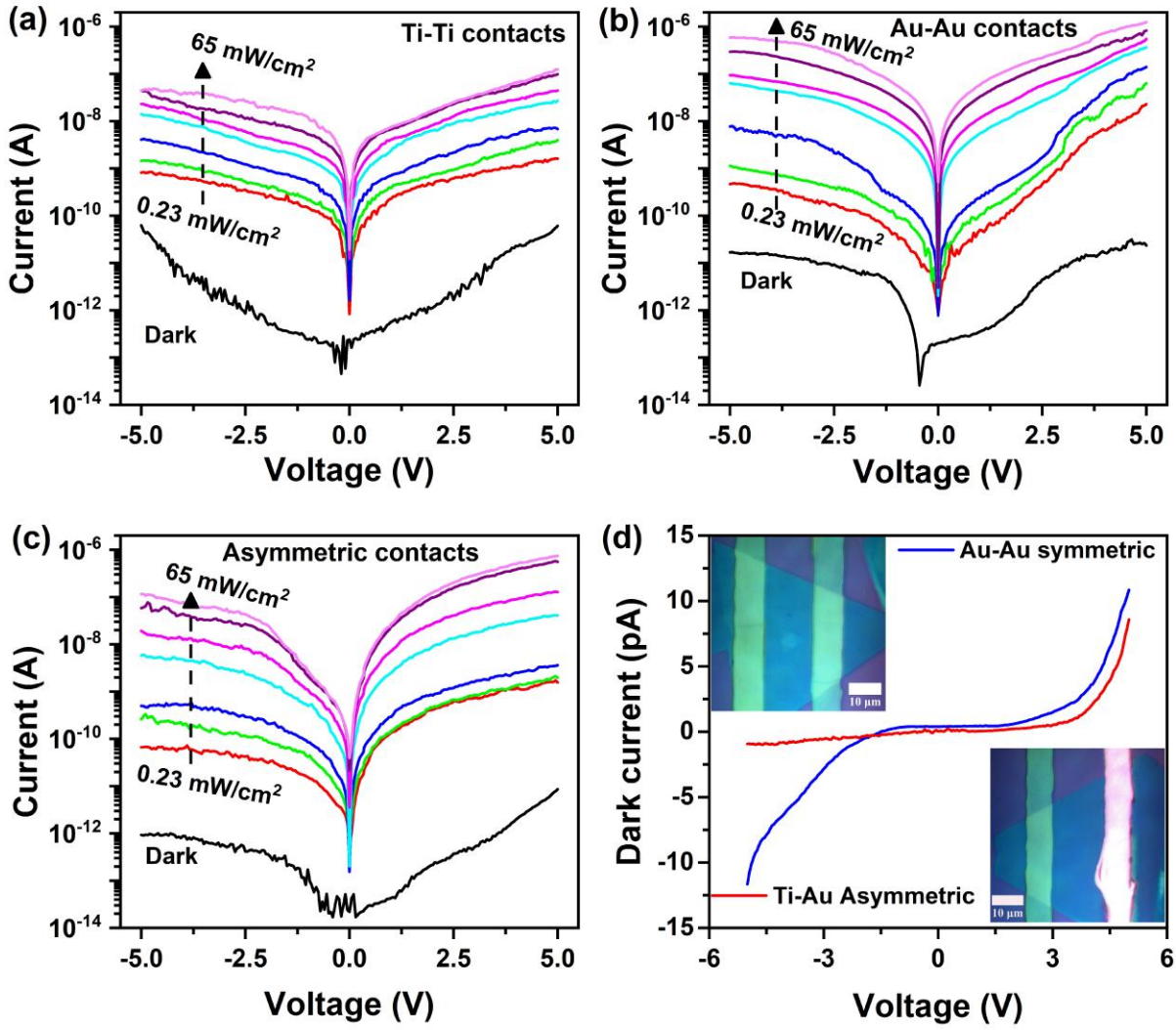

Figure 3.7: Dark and photo I-V characteristics of WS_2 photodetector with different intensity levels of 405 nm laser illumination corresponding to (a) symmetric Ti; (b) symmetric Au; (c) asymmetric (Au, Ti) contact; (d) A comparison of the dark current for symmetric Au-Au contacts and asymmetric Ti-Au contacts; the inset shows optical images of PDs with symmetric (left) and asymmetric (right) contacts.

on/off ratios of the devices at a low laser intensity of 0.23 mW/cm² under 5 V reverse bias were ~35, ~42, and ~180 for Ti-Ti, Au-Au, and Ti-Au (asymmetric) contacts, respectively. Thus, asymmetric contacts help to obtain a higher current on/off ratio. The formation of two distinct inhomogeneous junctions contributes to reduced dark current and improved separation of photocarriers under illumination. Note that the WS_2 PD with symmetric Ti contacts exhibits an on/off ratio of 4.5×10^3 under 405 nm laser illumination at 65 $mW.cm^{-2}$. This ratio is enhanced to 1.83×10^4 when using symmetric Au contacts, a result attributed to the built-in potential created through charge transfer. The on/off ratio increases further to 1.38×10^5 with the Ti-Au asymmetric configuration due to an order reduction of dark current under reverse bias. We have compared the dark current of symmetric Au-Au contacts and asymmetric Ti-Au contacts based WS_2 PD in **Fig. 3.7(d)**. It is evident that the dark current for the asymmetric contact under reverse bias is very low when compared to the Au-Au contacts. The selective doping assisted by asymmetric metal contacts acts as a Schottky /p-n junction type diode, enabling the directional flow of carriers as understood by the band alignments and I-V characteristics. The I-V characteristics of asymmetric Ti-Au contacts under dark conditions, displayed in **Fig. 3.7(d)**, clearly reveal the rectifying behavior of the asymmetric junction and, thus, a directional flow of carriers. The inset of **Fig. 3.7(d)** shows the optical microscopy images with symmetric Ti-Ti and asymmetric Ti-Au contacts on the actual device fabricated on a WS_2 flake through lithography.

Next, we investigated the power-dependent photoresponse of the WS_2 PD using a 405 nm pulse laser. The photoresponse was measured over the 0.23 to 65 mW/cm^2 intensity range under 5 V reverse bias. The photo response for the device utilizing symmetric Ti contacts is depicted in **Fig. 3.8(a)**. A minimal dark current of 31 pA was observed without laser illumination, progressively increasing to 230 nA with laser illumination at an intensity of 65 mW/cm² for symmetric Ti contacts. The inset of **Fig. 3.8(a)** displays the photo response under low illumination intensity. The calibration curve was constructed to correlate the laser intensity with power using $I_{ph}=AP^{\theta}$, where I_{ph} signifies the photocurrent under a laser intensity of P, A is a proportionality constant, and θ denotes the exponential constant, which has an ideal value of 1, signifying linear response of the photodetector. The slope of the logarithmic plot determines the θ value, which is measured to be 0.73 for the photodetector with Ti contacts, as shown in **Fig. 3.9(b)**. The deviation from the ideal θ value of 1 signifies a reduced photocurrent than anticipated, which can be ascribed to Auger re-

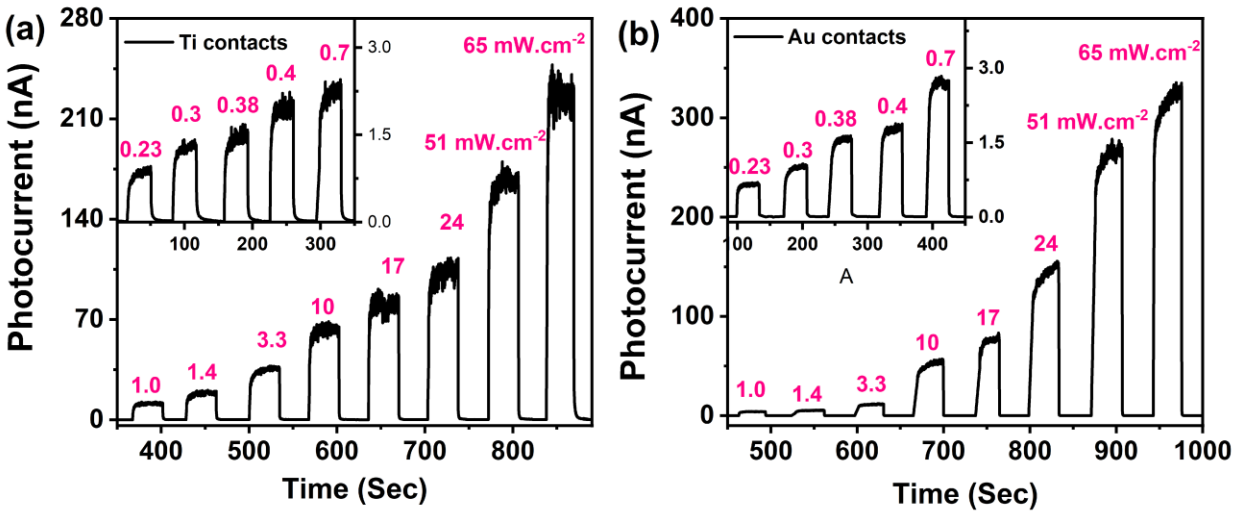

Figure 3.8: Pulse light response of 2L-WS_2 photodetector with symmetric (a) Ti-Ti contacts; (b) symmetric Au-Au contacts.

combination and trapping of photoelectrons by defects and trap sites at the interface.[61–63] The photoresponse under identical illumination conditions for the WS_2 photodetector with Au contact is depicted in **Fig. 3.8(b)**. The built-in potential established by the Schottky junction at the Au-WS_2 interface reduces the dark current threefold to 11 pA and elevates the photocurrent to 316 nA, thereby contributing to the enhancement of the on/off ratio. The calibration curve in **Fig. 3.9(b)** demonstrates a θ value of 1.04, suggesting that the built-in potential aids in charge separation, contributing to an elevated photocurrent by minimizing the carrier recombination.[64] Turning our attention to the asymmetric configuration, the photoresponse of the asymmetric contact-based 2L-WS_2 PD is shown in **Fig. 3.9(a)**. Two junctions along WS_2 behave like a p-n-n^+ configuration due to asymmetric doping. This configuration confines the carrier flow along one direction and diminishes the dark current by order of magnitude, reducing it from 31 pm to 3 pA under 5 V reverse bias. Simultaneously, the photocurrent is increased to 415 nA under an illumination of 65 $mW.cm^{-2}$, leading to a significant on/off ratio of 1.38×10^5. The θ value remains nearly at unity while the photocurrent exhibits an enhancement. This reduction in dark current, coupled with the amplification in photocurrent, is ascribed to the built-in potential at the p-n-n^+ junction, facilitating more efficient charge separation.[18] The performance improvement achieved with asymmetric contacts can be understood by carefully examining the band alignment..

The band diagram of WS_2 with three different contact configurations under illumination conditions at zero bias is shown in **Fig. 3.9(c-e)**. WS_2 is an n-type semiconducting material with a bandgap of ~2.0 eV, and its Fermi level is at 4.9 eV with reference to the vacuum[9]. The energy band positions of different layers and the band diagram of each metal/WS_2 junction under zero bias at dark condition are shown in **Fig. 3.10**. The work functions of Au and Ti are 5.1 eV and 4.3 eV, respectively. In contrast, the generation of excess carriers by 405 nm laser excitation moves the Fermi level of WS_2 upward via photoinduced carrier doping.[65] This leads to a change in its work function. The band alignment for the symmetric Au-Au contacts with WS_2 is shown in **Fig. 3.9(c)**.

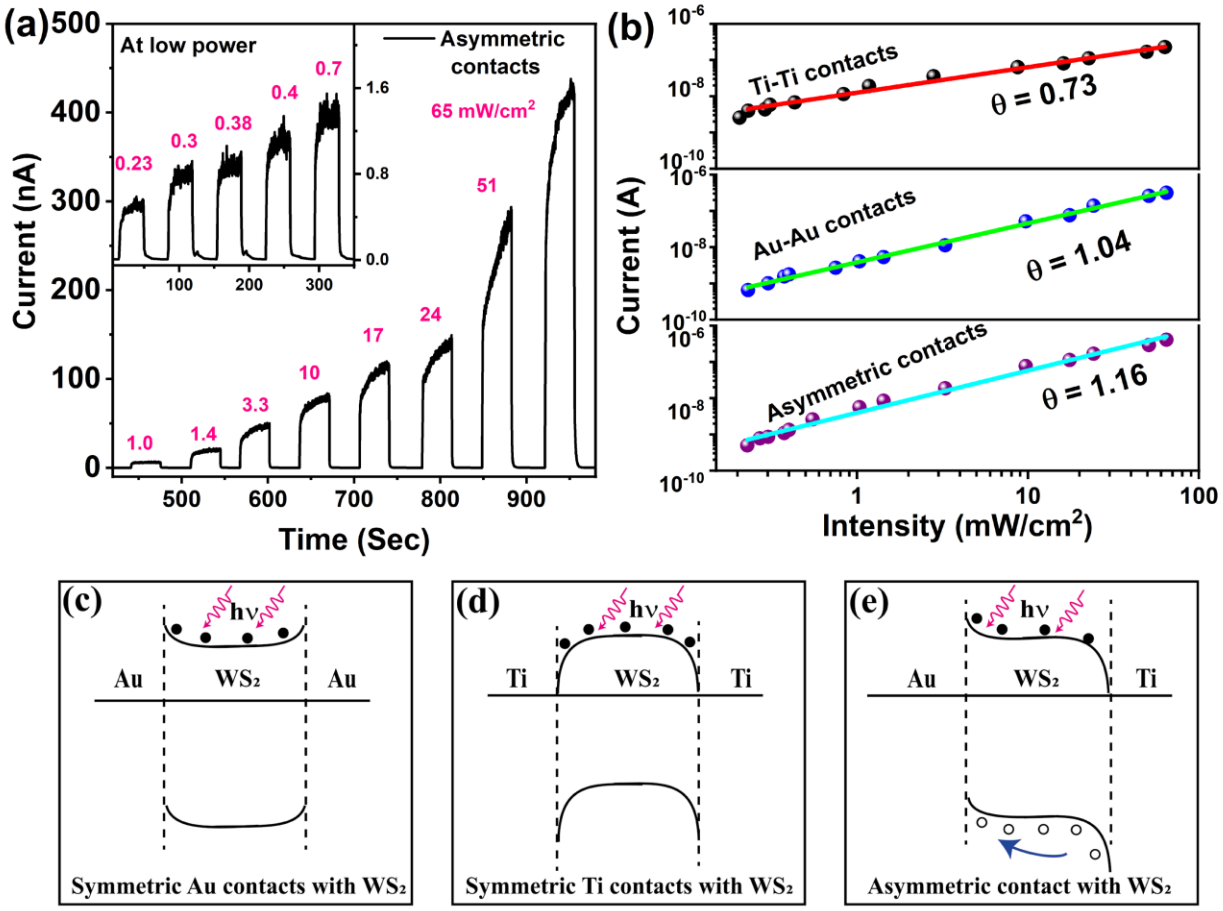

Figure 3.9: (a) Pulsed photocurrent response to 405 nm laser illumination at different intensities by WS_2 based photodetector with asymmetric contacts; (b) The photoresponse calibration curve as a function of illumination intensity for three different configurations of the photodetectors; Band diagrams of the WS_2 based photodetectors under illumination condition at zero bias for; (c) symmetric Au-Au contacts, (d) symmetric Ti-Ti contacts, and (e) Asymmetric Au-Ti contacts with WS_2.

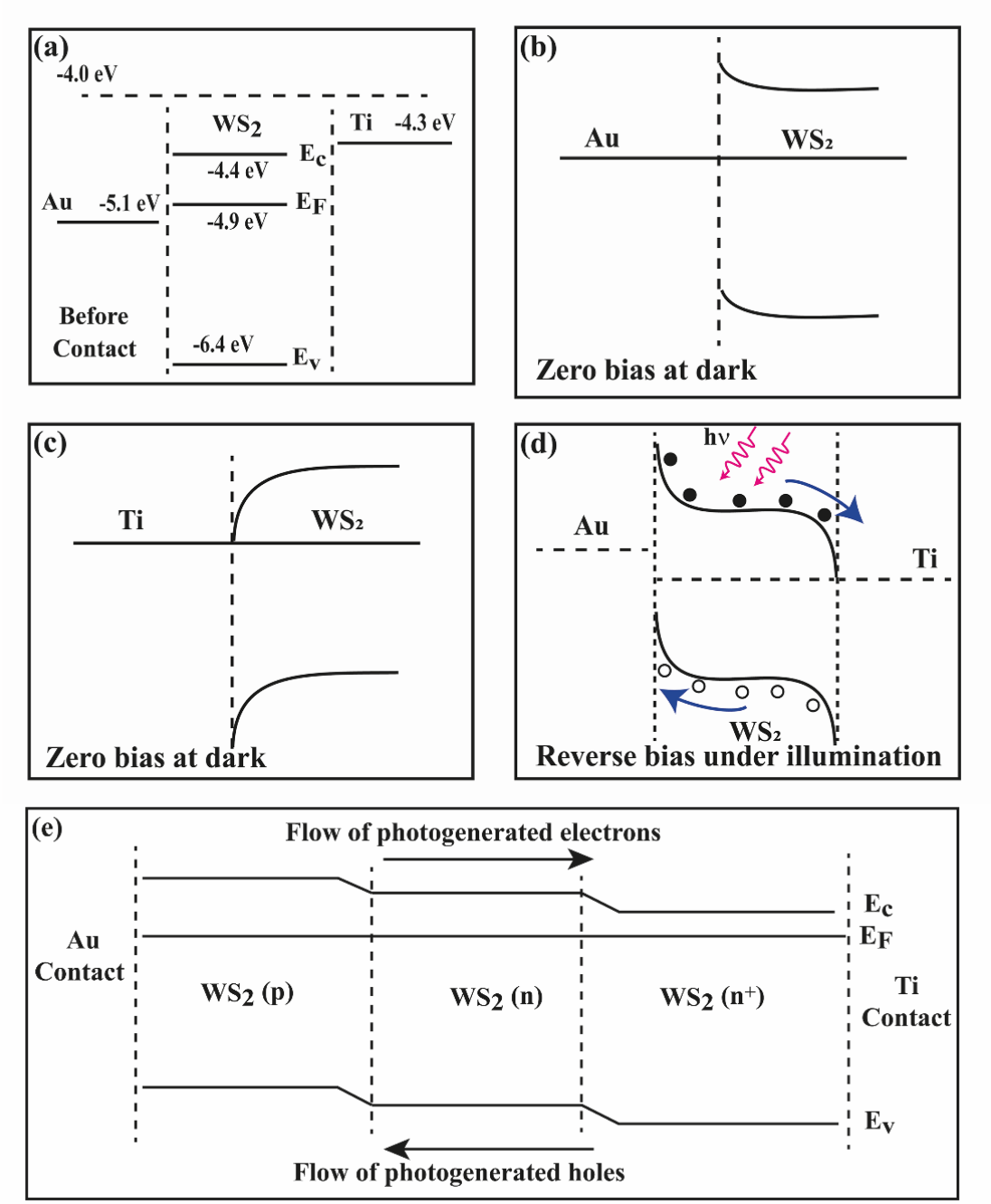

Figure 3.10: Energy band diagram of WS_2 with Au and Ti metal contacts: (a) energy band position of WS_2 and metals before contact. (b) Energy band diagram at Au/WS_2 interface after contact formation under zero bias at dark conditions. (c) Energy band diagram at Ti/WS_2 interface after contact formation under zero bias at dark conditions. (d) Energy band diagram under illumination at reverse bias after the formation of asymmetric Au/WS_2/Ti junctions. (e) Energy band diagram for the asymmetric contact-induced doping in WS_2.

The junction between Au and WS_2 under dark conditions creates a potential barrier of 0.2 eV ($V_{bi} = \Phi_m - E_F$) due to electron transfer from WS_2 to Au, thereby limiting electron movement through this junction. One of the two WS_2-Au junctions is always forward-biased during the voltage sweep from -5 V to +5 V, thus allowing the carriers to flow. The junction at the WS_2-Ti interface allows electron movement without any potential barrier because Ti work function is lower than that of n-type WS_2, as shown in **Fig. 3.9(d)**. Now, referring to the asymmetric contacts with WS_2, a potential barrier is present only at the Au/WS_2 junction but no barrier at the Ti/WS_2 configuration, hence blocking the carrier flow under reverse bias only. Beyond this metal-semiconductor junction, there are two other semiconductor-semiconductor (homo) junctions along the WS_2 due to asymmetric contact-induced inhomogeneous doping. The proximity of Au results in an effect equivalent to p-type doping in WS_2 near the Au contact, while the WS_2 away from the Au contact remains intrinsic. This leads to creating a p-n junction in the WS_2 region near the Au contact. Similarly, electrons are transferred from Ti to WS_2 near the Ti contact due to band alignments, increasing the electron concentration close to the Ti contact and forming an n-n^+ junction. These two junctions further restrict the movement of carriers, leading to an order of magnitude decrease in dark current from 31 pA to 3.0 pA under 5 V reverse bias. There are opposite doping types only near the metal contacts, while WS_2 remains intrinsic in the region away from the junction. Therefore, these two junctions are equivalent to a p-n-n^+ configuration. The energy band diagram of WS_2 after the formation of p-n-n^+ after asymmetric contact is shown in **Fig. 3.10**. In dark conditions, there are electron carriers in WS_2 as it is an n-type semiconductor nature. Asymmetric contact based WS_2 photodetector facilitates directional carrier flow, evident from band alignments, akin to a single p-n junction diode. During reverse bias in dark conditions, the barrier height at the Au/WS_2 junction increases, reducing electron flow and consequently lowering dark current. Conversely, the barrier height decreases under forward bias, promoting smoother electron flow and resulting in higher current. The applied reverse bias not only reduces the carrier flow in dark condition but also facilitates faster separation of photo-generated carriers in the depletion regions due to the high electric field across the junction. Electrons are collected at the Ti contacts, while holes are collected at the Au contacts. This enhances the photocurrent and consequently, the improved on/off ratio.

The photodetector performance parameters are characterized by the following quantities: responsivity (R), specific detectivity (D*), and external quantum efficiency (EQE). Responsivity pertains to the generation of photocurrent under unit power illumination, while specific detectivity

indicates the minimum light intensity that a photodetector can discern. The formulae below were used to compute these metrics:[66] $R = \frac{I_{ph}}{P \times A^*}$; $D^* = \frac{R}{\sqrt{(2ej_d)}}$ and $EQE = R \times \frac{1240}{\lambda} \times 100\ \%$ .Here, I_{ph} represents the photocurrent, P is the intensity of the incident laser and A* denotes the effective device area, specifically the area of the WS_2 flake situated between the contact pads. e is the electronic charge, j_d dark current density, and λ is the wavelength of light used for the photoresponse measurements. The variation of the responsivity with incident laser intensity is shown in **Fig. 3.11(a)**. A maximum responsivity of 0.3 A/W is seen at low light intensity for the

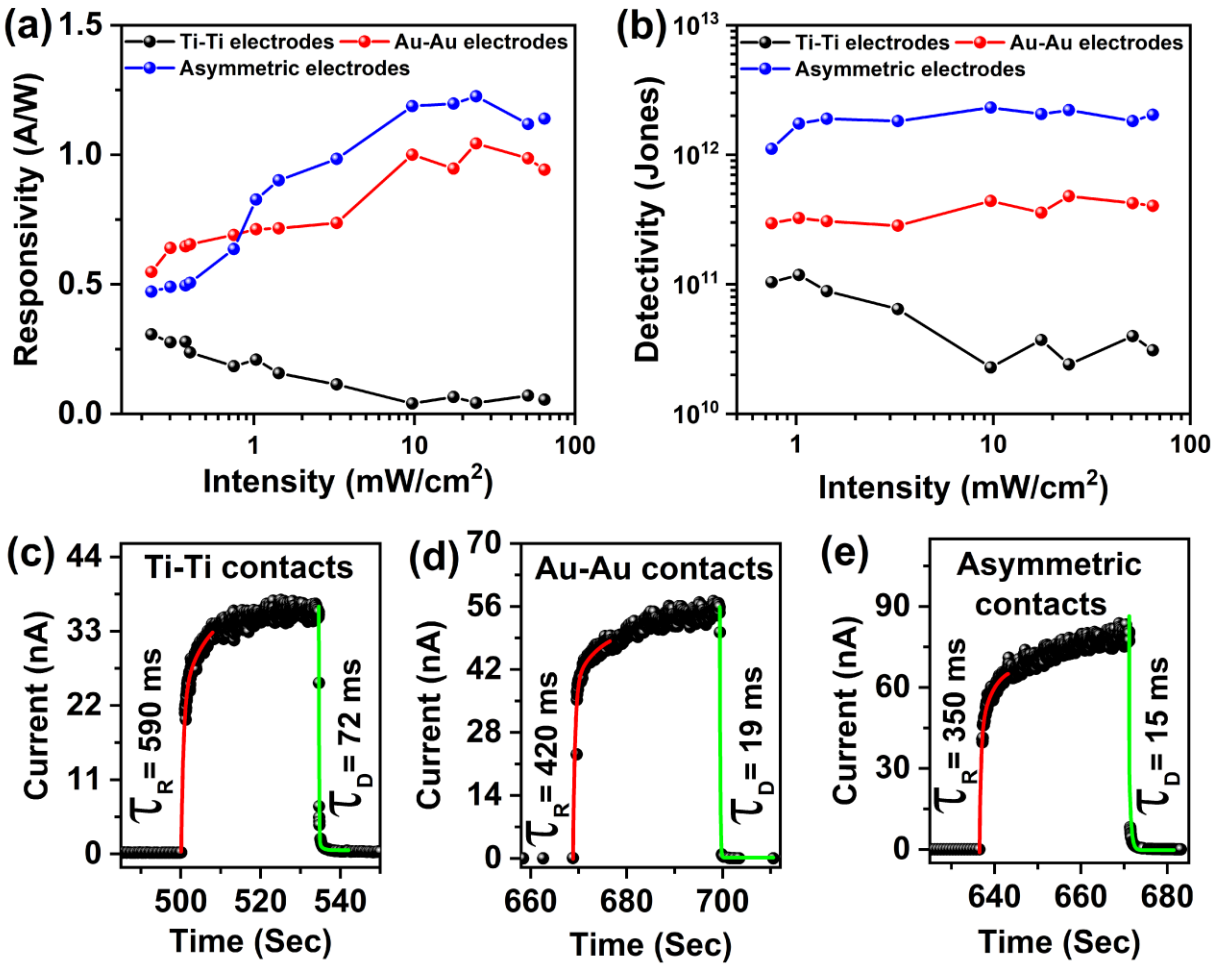

Figure 3.11: (a) A comparison of the responsivity for WS_2 photodetector based on different metal electrodes. (b) A comparison of the detectivity for 2L-WS_2 photodetector based on different metal electrodes. (c), (d) and (e) Temporal response and time are constant for symmetric Ti-Ti, Au-Au, and asymmetric Ti-Au contact-based WS_2 photodetector.

symmetric Ti contact. However, recombination causes a reduction in photocurrent at more intense levels, which subsequently decreases the responsivity, reaching 0.05 A/W at 65 $mW.cm^{-2}$, as shown in **Fig. 3.11(a)**. The responsivity spans from 0.5 to 1.2 A/W across the spectrum for the remaining two configurations. The symmetric Au contact exhibits superior responsivity at intensities below 1 mW/cm^2. The asymmetric contact-based PD, however, displays an increased responsivity with a peak value of 1.2 A/W for intensities exceeding this 1.0 mW/cm^2. This is due to the fact that the photocurrent for the PDs with asymmetric contacts increases at higher power compared to the two devices with symmetric contacts. The detectivity is influenced by both the responsivity and the dark current density. **Fig. 3.11(b)** illustrates the changes in detectivity with variation of incident intensity. The detectivity in the case of asymmetric contact sees an enhancement factor of 5 compared to the other two devices with symmetric contacts due to dark current reduced by an order. The photodetector with asymmetric contacts boasts the highest detectivity, registering at 2.3×10^{12} Jones. In contrast, the other two have detectivities of 1.2×10^{11} and 4.6×10^{11} Jones, respectively. The EQE at 65 mW/cm^2 intensity of 405 nm laser illumination was 162%, 287 %, and 345 %, corresponding to Ti-Ti, Au-Au, and Ti-Au asymmetric contacts. The response time of the WS_2 PDs with three different configurations is displayed in **Fig. 3.11(c-e)**. The time response was measured by the Keithley 4200 SCS source meter which has a slow response in the low current (10^{-12}A) range. The dark current here is very low (few pA) with the photocurrent in the order of nA. Using the exponential fitting function, we have fitted one response peak by 10 $mW.cm^{-2}$ intensity of 405 nm laser. The response and decay times of the devices, which are limited by the measuring instrument response time, are tabulated in **Table 4.1**. The response time decreases when moving from symmetric Ti contacts to asymmetric contact-based WS_2 PDs. which is attributed to the faster charge separation aided by the built-in potential at the p-n-n^+

Table 4.1. Device parameters such as on/off ratio, response time, and external quantum efficiency (EQE) under 405 nm laser pulse excitation.

Device configuration	On/off ratio	Response time (ms)	Decay time (ms)	EQE (%)
Symmetric Ti contacts	4.5×10^3	590	72	162
Symmetric Au contacts	1.83×10^4	420	19	287
Asymmetric contacts	1.38×10^5	350	15	345

junction. These values are faster with respect to earlier reports on PDs with monolayer WS_2[67] as shown in **Table 1.2 in section 1.3.2 of chapter 1** and the observed on/off ratio of 1.38×10^5 is the highest for two-terminal WS_2 photodetectors though higher values are possible with FET configurations.[23]

3.4 Conclusion

We have successfully synthesized large-area monolayer and 2L-WS_2 flakes via CVD. We were able to achieve selective lateral electron/hole doping by employing metal-semiconductor-metal junctions using two different metal electrodes with different work functions, leading to the establishment of a p-n-n^+ type configuration on the 2L-WS_2 flakes. The formation of a p-n-n^+ junction for the asymmetric contact-based devices enables the directional flow of carriers. The low work function metal, Ti, facilitates the seamless movement of carriers without any potential barrier, resulting in mirror-symmetric I-V characteristics and an on/off ratio of 10^3 under 405 nm laser illumination. In contrast, the high work function metal, Au, establishes a potential barrier at the WS_2-Au junction, hindering the free movement of carriers and resulting in rectifying I-V characteristics. The built-in potential aids in the enhanced separation of photo-generated carriers, thereby increasing the on/off ratio to 10^4 under the same illumination conditions. On the other hand, utilizing asymmetric metal contacts on WS_2 flakes results in a significant increase in the rectification ratio and an on/off ratio of 1.38×10^5 under identical conditions. The detectivity in the case of asymmetric contacts also improves by an order of magnitude by reducing the dark current, rising from 10^{11} to 10^{12} Jones. These results are significant for the future development of high-performance planar photodetectors using ultrathin 2D materials.

References

(1) Aftab, S.; Hegazy, H. H.; Iqbal, M. Z. Recent Advances in 2D TMD Circular Photo-Galvanic Effects. *Nanoscale* 2023, *15* (8), 3651–3665. https://doi.org/10.1039/D2NR05337C.

(2) Lee, S.; Kim, J.; Kwon, H.; Son, D.; Kim, I. S.; Kang, J. Photoactive Materials and Devices for Energy-Efficient Soft Wearable Optoelectronic Systems. *Nano Energy* 2023, *110*, 108379. https://doi.org/10.1016/j.nanoen.2023.108379.

(3) Kawabata, S.; Bai, S.; Obata, K.; Miyaji, G.; Sugioka, K. Two-Dimensional Laser-Induced Periodic Surface Structures Formed on Crystalline Silicon by GHz Burst Mode Femtosecond Laser Pulses. *Int. J. Extreme Manuf.* 2023, *5* (1), 015004. https://doi.org/10.1088/2631-7990/acb133.

(4) Zheng, J.; Wang, L.; Quhe, R.; Liu, Q.; Li, H.; Yu, D.; Mei, W.-N.; Shi, J.; Gao, Z.; Lu, J. Sub-10 Nm Gate Length Graphene Transistors: Operating at Terahertz Frequencies with Current Saturation. *Sci. Rep.* 2013, *3* (1), 1314. https://doi.org/10.1038/srep01314.

(5) Wu, F.; Tian, H.; Shen, Y.; Hou, Z.; Ren, J.; Gou, G.; Sun, Y.; Yang, Y.; Ren, T.-L. Vertical MoS2 Transistors with Sub-1-Nm Gate Lengths. *Nature* 2022, *603* (7900), 259–264. https://doi.org/10.1038/s41586-021-04323-3.

(6) Desai, S. B.; Madhvapathy, S. R.; Sachid, A. B.; Llinas, J. P.; Wang, Q.; Ahn, G. H.; Pitner, G.; Kim, M. J.; Bokor, J.; Hu, C.; Wong, H.-S. P.; Javey, A. MoS2 Transistors with 1-Nanometer Gate Lengths. *Science* 2016, *354* (6308), 99–102. https://doi.org/10.1126/science.aah4698.

(7) Susarla, S.; Kutana, A.; Hachtel, J. A.; Kochat, V.; Apte, A.; Vajtai, R.; Idrobo, J. C.; Yakobson, B. I.; Tiwary, C. S.; Ajayan, P. M. Quaternary 2D Transition Metal Dichalcogenides (TMDs) with Tunable Bandgap. *Adv. Mater.* 2017, *29* (35), 1702457. https://doi.org/10.1002/adma.201702457.

(8) Mia, A. K.; Meyyappan, M.; Giri, P. K. Two-Dimensional Transition Metal Dichalcogenide Based Biosensors: From Fundamentals to Healthcare Applications. *Biosensors* 2023, *13* (2), 169. https://doi.org/10.3390/bios13020169.

(9) Soares, D. M.; Mukherjee, S.; Singh, G. TMDs beyond MoS2 for Electrochemical Energy Storage. *Chem. – Eur. J.* 2020, *26* (29), 6320–6341. https://doi.org/10.1002/chem.202000147.

(10) Nourbakhsh, A.; Zubair, A.; Dresselhaus, M. S.; Palacios, T. Transport Properties of a MoS2/WSe2 Heterojunction Transistor and Its Potential for Application. *Nano Lett.* 2016, *16* (2), 1359–1366. https://doi.org/10.1021/acs.nanolett.5b04791.

(11) Kim, H.; Kim, J.; Uddin, I.; Phan, N. A. N.; Whang, D.; Kim, G.-H. Dual-Channel WS_2/WSe_2 Heterostructure with Tunable Graphene Electrodes. *ACS Appl. Electron. Mater.* 2023, *5* (2), 913–919. https://doi.org/10.1021/acsaelm.2c01465.

(12) Gong, Y.; Lin, J.; Wang, X.; Shi, G.; Lei, S.; Lin, Z.; Zou, X.; Ye, G.; Vajtai, R.; Yakobson, B. I.; Terrones, H.; Terrones, M.; Tay, B. K.; Lou, J.; Pantelides, S. T.; Liu, Z.; Zhou, W.; Ajayan, P. M. Vertical and In-Plane Heterostructures from WS_2/MoS_2 Monolayers. *Nat. Mater.* 2014, *13* (12), 1135–1142. https://doi.org/10.1038/nmat4091.

(13) Meng, Y.; Wang, T.; Jin, C.; Li, Z.; Miao, S.; Lian, Z.; Taniguchi, T.; Watanabe, K.; Song, F.; Shi, S.-F. Electrical Switching between Exciton Dissociation to Exciton Funneling in $MoSe_2/WS_2$

Heterostructure. *Nat. Commun.* 2020, *11* (1), 2640. https://doi.org/10.1038/s41467-020-16419-x.

(14) Wu, Y.; Li, D.; Wu, C.-L.; Hwang, H. Y.; Cui, Y. Electrostatic Gating and Intercalation in 2D Materials. *Nat. Rev. Mater.* 2023, *8* (1), 41–53. https://doi.org/10.1038/s41578-022-00473-6.

(15) Wang, Y.; Slassi, A.; Stoeckel, M.-A.; Bertolazzi, S.; Cornil, J.; Beljonne, D.; Samorì, P. Doping of Monolayer Transition-Metal Dichalcogenides via Physisorption of Aromatic Solvent Molecules. *J. Phys. Chem. Lett.* 2019, *10* (3), 540–547. https://doi.org/10.1021/acs.jpclett.8b03697.

(16) Azcatl, A.; Qin, X.; Prakash, A.; Zhang, C.; Cheng, L.; Wang, Q.; Lu, N.; Kim, M. J.; Kim, J.; Cho, K.; Addou, R.; Hinkle, C. L.; Appenzeller, J.; Wallace, R. M. Covalent Nitrogen Doping and Compressive Strain in MoS2 by Remote N2 Plasma Exposure. *Nano Lett.* 2016, *16* (9), 5437–5443. https://doi.org/10.1021/acs.nanolett.6b01853.

(17) Zhou, C.; Zhang, S.; Lv, Z.; Ma, Z.; Yu, C.; Feng, Z.; Chan, M. Self-Driven WSe2 Photodetectors Enabled with Asymmetrical van Der Waals Contact Interfaces. *Npj 2D Mater. Appl.* 2020, *4* (1), 1–9. https://doi.org/10.1038/s41699-020-00179-9.

(18) Li, Y.; Xiao, J.; Cao, X.; Gu, Z.; Zhang, W. Lateral WSe2 Homojunction through Metal Contact Doping: Excellent Self-Powered Photovoltaic Photodetector. *Adv. Funct. Mater.* 2023, *33* (17), 2213385. https://doi.org/10.1002/adfm.202213385.

(19) Lan, C.; Li, C.; Ho, J. C.; Liu, Y. 2D WS_2: From Vapor Phase Synthesis to Device Applications. *Adv. Electron. Mater.* 2021, *7* (7), 2000688. https://doi.org/10.1002/aelm.202000688.

(20) Dodda, A.; Jayachandran, D.; Pannone, A.; Trainor, N.; Stepanoff, S. P.; Steves, M. A.; Radhakrishnan, S. S.; Bachu, S.; Ordonez, C. W.; Shallenberger, J. R.; Redwing, J. M.; Knappenberger, K. L.; Wolfe, D. E.; Das, S. Active Pixel Sensor Matrix Based on Monolayer MoS2 Phototransistor Array. *Nat. Mater.* 2022, *21* (12), 1379–1387. https://doi.org/10.1038/s41563-022-01398-9.

(21) Perea-López, N.; Elías, A. L.; Berkdemir, A.; Castro-Beltran, A.; Gutiérrez, H. R.; Feng, S.; Lv, R.; Hayashi, T.; López-Urías, F.; Ghosh, S.; Muchharla, B.; Talapatra, S.; Terrones, H.; Terrones, M. Photosensor Device Based on Few-Layered WS_2 Films. *Adv. Funct. Mater.* 2013, *23* (44), 5511–5517. https://doi.org/10.1002/adfm.201300760.

(22) Huo, N.; Yang, S.; Wei, Z.; Li, S.-S.; Xia, J.-B.; Li, J. Photoresponsive and Gas Sensing Field-Effect Transistors Based on Multilayer WS_2 Nanoflakes. *Sci. Rep.* 2014, *4* (1), 5209. https://doi.org/10.1038/srep05209.

(23) Sun, J.; Lin, Z.; Jia, X.; Li, H.; Song, C.; Pan, F.; Fang, L.; Zhang, J.; Wang, Y. High-Performance 2D WS_2 Photodetector Enhanced by Charge-Transfer Doping through NH3 Annealing. *Mater. Today Phys.* 2023, *35*, 101133. https://doi.org/10.1016/j.mtphys.2023.101133.

(24) Zhao, S.; Zhang, Y.; Wang, S.; Zhao, D.; Kang, H.; Li, J.; Xiao, R.; Kong, Z.; Chen, Z.; Sui, Y.; Wang, J.; Chen, Y.; Yu, G. Controllable Growth of Bilayer WS_2 by Chemical Vapor Deposition and Application for Photodetectors. *Mater. Lett.* 2022, *317*, 132103. https://doi.org/10.1016/j.matlet.2022.132103.

(25) D. Yao, J.; Q. Zheng, Z.; M. Shao, J.; W. Yang, G. Stable, Highly-Responsive and Broadband Photodetection Based on Large-Area Multilayered WS 2 Films Grown by Pulsed-Laser Deposition. *Nanoscale* 2015, *7* (36), 14974–14981. https://doi.org/10.1039/C5NR03361F.

(26) Zeng, L.; Tao, L.; Tang, C.; Zhou, B.; Long, H.; Chai, Y.; Lau, S. P.; Tsang, Y. H. High-Responsivity UV-Vis Photodetector Based on Transferable WS_2 Film Deposited by Magnetron Sputtering. *Sci. Rep.* 2016, *6* (1), 20343. https://doi.org/10.1038/srep20343.

(27) Yang, R.; Feng, S.; Xiang, J.; Jia, Z.; Mu, C.; Wen, F.; Liu, Z. Ultrahigh-Gain and Fast Photodetectors Built on Atomically Thin Bilayer Tungsten Disulfide Grown by Chemical Vapor Deposition. *ACS Appl. Mater. Interfaces* 2017, *9* (48), 42001–42010. https://doi.org/10.1021/acsami.7b14853.

(28) Lan, C.; Zhou, Z.; Zhou, Z.; Li, C.; Shu, L.; Shen, L.; Li, D.; Dong, R.; Yip, S.; Ho, J. C. Wafer-Scale Synthesis of Monolayer WS_2 for High-Performance Flexible Photodetectors by Enhanced Chemical Vapor Deposition. *Nano Res.* 2018, *11* (6), 3371–3384. https://doi.org/10.1007/s12274-017-1941-4.

(29) Gao, W.; Zhang, S.; Zhang, F.; Wen, P.; Zhang, L.; Sun, Y.; Chen, H.; Zheng, Z.; Yang, M.; Luo, D.; Huo, N.; Li, J. 2D WS_2 Based Asymmetric Schottky Photodetector with High Performance. *Adv. Electron. Mater.* 2021, *7* (7), 2000964. https://doi.org/10.1002/aelm.202000964.

(30) Ovchinnikov, D.; Allain, A.; Huang, Y.-S.; Dumcenco, D.; Kis, A. Electrical Transport Properties of Single-Layer WS_2. *ACS Nano* 2014, *8* (8), 8174–8181. https://doi.org/10.1021/nn502362b.

(31) Sebastian, A.; Pendurthi, R.; Choudhury, T. H.; Redwing, J. M.; Das, S. Benchmarking Monolayer MoS2 and WS_2 Field-Effect Transistors. *Nat. Commun.* 2021, *12* (1), 693. https://doi.org/10.1038/s41467-020-20732-w.

(32) Chakraborty, B.; Bera, A.; Muthu, D. V. S.; Bhowmick, S.; Waghmare, U. V.; Sood, A. K. Symmetry-Dependent Phonon Renormalization in Monolayer MoS_2 Transistor. *Phys. Rev. B* 2012, *85* (16), 161403. https://doi.org/10.1103/PhysRevB.85.161403.

(33) Molas, M. R.; Nogajewski, K.; Potemski, M.; Babiński, A. Raman Scattering Excitation Spectroscopy of Monolayer WS_2. *Sci. Rep.* 2017, *7* (1), 5036. https://doi.org/10.1038/s41598-017-05367-0.

(34) Iqbal, M. W.; Shahzad, K.; Hussain, G.; Arshad, M. K.; Akbar, R.; Azam, S.; Aftab, S.; Alharbi, T.; Majid, A. Gate Dependent Phonon Shift in Tungsten Disulfide (WS_2) Field Effect Transistor. *Mater. Res. Express* 2019, *6* (11), 115909. https://doi.org/10.1088/2053-1591/ab485a.

(35) Berkdemir, A.; Gutiérrez, H. R.; Botello-Méndez, A. R.; Perea-López, N.; Elías, A. L.; Chia, C.-I.; Wang, B.; Crespi, V. H.; López-Urías, F.; Charlier, J.-C.; Terrones, H.; Terrones, M. Identification of Individual and Few Layers of WS_2 Using Raman Spectroscopy. *Sci. Rep.* 2013, *3* (1), 1755. https://doi.org/10.1038/srep01755.

(36) Mlack, J. T.; Masih Das, P.; Danda, G.; Chou, Y.-C.; Naylor, C. H.; Lin, Z.; López, N. P.; Zhang, T.; Terrones, M.; Johnson, A. T. C.; Drndić, M. Transfer of Monolayer TMD WS_2 and Raman Study of Substrate Effects. *Sci. Rep.* 2017, *7* (1), 43037. https://doi.org/10.1038/srep43037.

(37) Wang, Y.; Cong, C.; Yang, W.; Shang, J.; Peimyoo, N.; Chen, Y.; Kang, J.; Wang, J.; Huang, W.; Yu, T. Strain-Induced Direct–Indirect Bandgap Transition and Phonon Modulation in Monolayer WS_2. *Nano Res.* 2015, *8* (8), 2562–2572. https://doi.org/10.1007/s12274-015-0762-6.

(38) McCreary, K. M.; Hanbicki, A. T.; Singh, S.; Kawakami, R. K.; Jernigan, G. G.; Ishigami, M.; Ng, A.; Brintlinger, T. H.; Stroud, R. M.; Jonker, B. T. The Effect of Preparation Conditions on Raman and Photoluminescence of Monolayer WS_2. *Sci. Rep.* 2016, *6* (1), 35154. https://doi.org/10.1038/srep35154.

(39) McCreary, K. M.; Hanbicki, A. T.; Jernigan, G. G.; Culbertson, J. C.; Jonker, B. T. Synthesis of Large-Area WS_2 Monolayers with Exceptional Photoluminescence. *Sci. Rep.* 2016, *6* (1), 19159. https://doi.org/10.1038/srep19159.

(40) Bora, A.; Paul, S.; Hossain, M. T.; Giri, P. K. Quantitative Understanding of the Photoluminescence Modulation and Doping of Monolayer WS_2 by Heterostructuring with Non-van Der Waals 2D Bi2O2Se Quantum Dots. *J. Phys. Chem. C* 2022, *126* (30), 12623–12634. https://doi.org/10.1021/acs.jpcc.2c03245.

(41) Mia, A. K.; Bora, A.; Hossain, M. T.; Sinha, S.; Giri, P. K. Fast Detection of Staphylococcus Aureus Using Thiol-Functionalized WS_2 Quantum Dots and Bi2O2Se Nanosheets Hybrid through a Fluorescence Recovery Mechanism. *J. Mater. Chem. B* 2023, *11* (42), 10206–10217. https://doi.org/10.1039/D3TB01465G.

(42) Mullapudi, K.; Addou, R.; Dezelah, Charles. L.; Moser, D. F.; Kanjolia, R. K.; Woodruff, J. H.; Conley, John. F. Synthesis of Micron-Sized WS_2 Crystallites Using Atomic Layer Deposition and Sulfur Annealing. *Chem. Mater.* 2023, *35* (12), 4649–4659. https://doi.org/10.1021/acs.chemmater.3c00013.

(43) Lavini, F.; Calò, A.; Gao, Y.; Albisetti, E.; Li, T.-D.; Cao, T.; Li, G.; Cao, L.; Aruta, C.; Riedo, E. Friction and Work Function Oscillatory Behavior for an Even and Odd Number of Layers in Polycrystalline MoS2. *Nanoscale* 2018, *10* (17), 8304–8312. https://doi.org/10.1039/C8NR00238J.

(44) Guan, Y.; Yao, H.; Zhan, H.; Wang, H.; Zhou, Y.; Kang, J. Optoelectronic Properties and Strain Regulation of the 2D WS_2/ZnO van Der Waals Heterostructure. *RSC Adv.* 2021, *11* (23), 14085–14092. https://doi.org/10.1039/D1RA01877A.

(45) Zhang, G.; Wang, C.; Yan, B.; Ning, B.; Zhao, Y.; Zhou, D.; Shi, X.; Chen, S.; Shen, J.; Xiao, Z.; Zhao, H. Synthesis of Centimeter-Scale WS_2 Membrane by Chemical Vapor Deposition. *J. Mater. Sci. Mater. Electron.* 2022, *33* (28), 22560–22572. https://doi.org/10.1007/s10854-022-09034-7.

(46) Rout, C. S.; Joshi, P. D.; Kashid, R. V.; Joag, D. S.; More, M. A.; Simbeck, A. J.; Washington, M.; Nayak, S. K.; Late, D. J. Superior Field Emission Properties of Layered WS_2-RGO Nanocomposites. *Sci. Rep.* 2013, *3* (1), 3282. https://doi.org/10.1038/srep03282.

(47) Shi, H.; Zou, B.; Li, Z.; Luo, M.; Wang, W. Direct Observation of Oxygen-Vacancy Formation and Structural Changes in Bi2WO6 Nanoflakes Induced by Electron Irradiation. *Beilstein J. Nanotechnol.* 2019, *10* (1), 1434–1442. https://doi.org/10.3762/bjnano.10.141.

(48) Mishra, A. K.; Lakshmi, K. V.; Huang, L. Eco-Friendly Synthesis of Metal Dichalcogenides Nanosheets and Their Environmental Remediation Potential Driven by Visible Light. *Sci. Rep.* 2015, *5* (1), 15718. https://doi.org/10.1038/srep15718.

(49) Zhao, W.; Ghorannevis, Z.; Chu, L.; Toh, M.; Kloc, C.; Tan, P.-H.; Eda, G. Evolution of Electronic Structure in Atomically Thin Sheets of WS_2 and WSe_2. *ACS Nano* 2013, *7* (1), 791–797. https://doi.org/10.1021/nn305275h.

(50) Sharma, S.; Bhagat, S.; Singh, J.; Singh, R. C.; Sharma, S. Excitation-Dependent Photoluminescence from WS_2 Nanostructures Synthesized via Top-down Approach. *J. Mater. Sci.* 2017, *52* (19), 11326–11336. https://doi.org/10.1007/s10853-017-1303-3.

(51) Ernandes, C.; Khalil, L.; Almabrouk, H.; Pierucci, D.; Zheng, B.; Avila, J.; Dudin, P.; Chaste, J.; Oehler, F.; Pala, M.; Bisti, F.; Brulé, T.; Lhuillier, E.; Pan, A.; Ouerghi, A. Indirect to Direct

Band Gap Crossover in Two-Dimensional $WS_{2(1-x)}Se_{2x}$ Alloys. *Npj 2D Mater. Appl.* 2021, *5* (1), 1–7. https://doi.org/10.1038/s41699-020-00187-9.

(52) Zhu, B.; Chen, X.; Cui, X. Exciton Binding Energy of Monolayer WS_2. *Sci. Rep.* 2015, *5* (1), 9218. https://doi.org/10.1038/srep09218.

(53) Gutiérrez, H. R.; Perea-López, N.; Elías, A. L.; Berkdemir, A.; Wang, B.; Lv, R.; López-Urías, F.; Crespi, V. H.; Terrones, H.; Terrones, M. Extraordinary Room-Temperature Photoluminescence in Triangular WS_2 Monolayers. *Nano Lett.* 2013, *13* (8), 3447–3454. https://doi.org/10.1021/nl3026357.

(54) Tongay, S.; Suh, J.; Ataca, C.; Fan, W.; Luce, A.; Kang, J. S.; Liu, J.; Ko, C.; Raghunathanan, R.; Zhou, J.; Ogletree, F.; Li, J.; Grossman, J. C.; Wu, J. Defects Activated Photoluminescence in Two-Dimensional Semiconductors: Interplay between Bound, Charged and Free Excitons. *Sci. Rep.* 2013, *3* (1), 2657. https://doi.org/10.1038/srep02657.

(55) Kesarwani, R.; Simbulan, K. B.; Huang, T.-D.; Chiang, Y.-F.; Yeh, N.-C.; Lan, Y.-W.; Lu, T.-H. Control of Trion-to-Exciton Conversion in Monolayer WS_2 by Orbital Angular Momentum of Light. *Sci. Adv.* 2022, *8* (13), eabm0100. https://doi.org/10.1126/sciadv.abm0100.

(56) Chernikov, A.; Berkelbach, T. C.; Hill, H. M.; Rigosi, A.; Li, Y.; Aslan, B.; Reichman, D. R.; Hybertsen, M. S.; Heinz, T. F. Exciton Binding Energy and Nonhydrogenic Rydberg Series in Monolayer ${\mathrm{WS}}_{2}$. *Phys. Rev. Lett.* 2014, *113* (7), 076802. https://doi.org/10.1103/PhysRevLett.113.076802.

(57) Chowdhury, T.; Paul, D.; Nechiyil, D.; A, G. M.; Watanabe, K.; Taniguchi, T.; Kumar, G. V. P.; Rahman, A. Modulation of Trion and Exciton Formation in Monolayer WS_2 by Dielectric and Substrate Engineering. *2D Mater.* 2021, *8* (4), 045032. https://doi.org/10.1088/2053-1583/ac234f.

(58) Peimyoo, N.; Yang, W.; Shang, J.; Shen, X.; Wang, Y.; Yu, T. Chemically Driven Tunable Light Emission of Charged and Neutral Excitons in Monolayer WS_2. *ACS Nano* 2014, *8* (11), 11320–11329. https://doi.org/10.1021/nn504196n.

(59) Liu, Y.; Huang, W.; Chen, W.; Wang, X.; Guo, J.; Tian, H.; Zhang, H.; Wang, Y.; Yu, B.; Ren, T.-L.; Xu, J. Plasmon Resonance Enhanced WS_2 Photodetector with Ultra-High Sensitivity and Stability. *Appl. Surf. Sci.* 2019, *481*, 1127–1132. https://doi.org/10.1016/j.apsusc.2019.03.179.

(60) Huang, H.; Sheng, Y.; Zhou, Y.; Zhang, Q.; Hou, L.; Chen, T.; Chang, R.-J.; Warner, J. H. 2D-Layer-Dependent Behavior in Lateral Au/WS_2/Graphene Photodiode Devices with Optical Modulation of Schottky Barriers. *ACS Appl. Nano Mater.* 2018, *1* (12), 6874–6881. https://doi.org/10.1021/acsanm.8b01695.

(61) Zhou, C.; Raju, S.; Li, B.; Chan, M.; Chai, Y.; Yang, C. Y. Self-Driven Metal–Semiconductor–Metal WSe2 Photodetector with Asymmetric Contact Geometries. *Adv. Funct. Mater.* 2018, *28* (45). https://doi.org/10.1002/adfm.201802954.

(62) Ghosh, J.; Mawlong, L. P. L.; B, M. G.; Pattison, A. J.; Theis, W.; Chakraborty, S.; Giri, P. K. Solid-State Synthesis of Stable and Color Tunable Cesium Lead Halide Perovskite Nanocrystals and the Mechanism of High-Performance Photodetection in a Monolayer MoS2/CsPbBr3 Vertical Heterojunction. *J. Mater. Chem. C* 2020, *8* (26), 8917–8934. https://doi.org/10.1039/D0TC01306D.

(63) Zeng, L.-H.; Chen, Q.-M.; Zhang, Z.-X.; Wu, D.; Yuan, H.; Li, Y.-Y.; Qarony, W.; Lau, S. P.; Luo, L.-B.; Tsang, Y. H. Multilayered PdSe2/Perovskite Schottky Junction for Fast, Self-Powered,

Polarization-Sensitive, Broadband Photodetectors, and Image Sensor Application. *Adv. Sci.* 2019, *6* (19), 1901134. https://doi.org/10.1002/advs.201901134.

(64) Ezhilmaran, B.; Patra, A.; Benny, S.; R, S. M.; V, A. V.; Bhat, S. V.; Rout, C. S. Recent Developments in the Photodetector Applications of Schottky Diodes Based on 2D Materials. *J. Mater. Chem. C* 2021, *9* (19), 6122–6150. https://doi.org/10.1039/D1TC00949D.

(65) Wang, X. H.; Ning, J. Q.; Su, Z. C.; Zheng, C. C.; Zhu, B. R.; Xie, L.; Wu, H. S.; Xu, S. J. Photoinduced Doping and Photoluminescence Signature in an Exfoliated WS_2 Monolayer Semiconductor. *RSC Adv.* 2016, *6* (33), 27677–27681. https://doi.org/10.1039/C6RA01836J.

(66) Bora, A.; Mawlong, L. P.; Giri, P. K. Highly Suppressed Dark Current and Fast Photoresponse from Au Nanoparticle-Embedded, Si/Au/WS_2 Quantum-Dot-Based, Self-Biased Schottky Photodetectors. *ACS Appl. Electron. Mater.* 2021, *3* (11), 4891–4904.

(67) Prasad, R. K.; Ghosh, K.; Giri, P. K.; Kim, D.-S.; Singh, D. K. High-Efficiency Photodetector Based on a CVD-Grown WS_2 Monolayer. *ACS Appl. Electron. Mater.* 2023, *5* (7), 3634–3640. https://doi.org/10.1021/acsaelm.3c00366.

Chapter 4

Non-Metal Contact Engineering on Monolayer MoS_2 for High-Performance Field Effect Transistor and Flexible Photodetector

In this chapter, we investigated the potential application of Bi_2Se_3 as a contact material for monolayer (1L-MoS_2) in the development of high-performance field-effect transistors and flexible photodetectors. The metal-semiconductor interface is crucial in determining the performance of optoelectronic devices. Deposition of conventional metal contacts on ultrathin layer often introduce defects in the semiconductor due to the high mass and kinetic energy of the metals, adversely affecting device performance. Using topologically insulating Bi_2Se_3 as a contact material for 1L-MoS_2 results in a better Bi_2Se_3-MoS_2 interface, which improves electron mobility and field control. Enhanced field control leads to a reduction in off-state current and an increase in on-state current, resulting in an improved on-off current ratio of approximately 10^7. The application of Bi_2Se_3 contacts also significantly reduces subthreshold swing compared to conventional Cr/Au contacts, indicating fewer interface defects. Furthermore, the Bi_2Se_3-contacted 1L-MoS_2 was explored as a flexible photodetector, achieving an impressive current on-off ratio of ~10^3, which is double that of devices with traditional Cr/Au metal contacts. The key performance metrics for the Bi_2Se_3-contacted 1L-MoS_2 flexible photodetector show significant improvement. This combination of 2D TMDs along with the highly stable and cost-effective Bi_2Se_3 contact material, demonstrates its great potential for future flexible electronics.

4.1 Introduction

Since the invention of transistors in 1947, silicon-based semiconductor technology has revolutionized the information age, driving continuous device miniaturization[1]. However, as transistors approach channel scales below 10 nm, short-channel effects present significant challenges to achieving high integration levels and low power consumption[2–4]. Novel materials and device structures are urgently needed to extend Moore's Law and improve device performance[5]. Two-dimensional (2D) materials, with their atomically thin layers, offer promising solutions for next-generation nanoelectronics, as they mitigate the short-channel effects prevalent in silicon-based complementary metal-oxide-semiconductor (CMOS) devices[6–8]. These 2D

materials, such as graphene[9], transition metal dichalcogenides (TMDs) like MoS_2[10] and WS_2[11], and hexagonal boron nitride (h-BN)[12], exhibit extraordinary electronic and optical properties, making them ideal candidates for applications in FETs, photodetectors, spintronics, and more[13,14]. In parallel, three-dimensional integration presents another promising avenue for enhancing transistor density and computational power[15]. This three-dimensional integration has shown great promise for 3D heterogeneous integration, which combines the benefits of both 'More Moore' and 'More than Moore' approaches[16]. These advancements are pushing the limits of semiconductor technology, as industries explore hybrid solutions that blend 2D semiconductors and traditional silicon for future very large-scale integration (VLSI) circuits and processors[17,18]. Despite the extensive investigation into 2D material-based devices, several challenges remain, particularly in forming efficient contacts between semiconductors and metal electrodes[19]. The Schottky barrier (SB) and contact resistance at the 2D/metal interface significantly impact device performance[20,21]. Unlike silicon, 2D materials are free from surface dangling bonds, allowing for better ohmic contact formation[22,23]. However, the delicate nature of 2D materials makes them susceptible to damage during standard fabrication processes involving electron beam lithography and metal deposition, which introduce defects and interfacial states at the 2D/metal contacts[24]. The applications of nonmetal graphene contacts reduce the interface defects and improve the device performance significantly[25,26]. However, aligning graphene with 2D materials like MoS_2 presents significant challenges and remains an obstacle to large-scale device fabrication.

Herein, we present a simple contact engineering approach for reducing defects at the 1L-MoS_2 and contact interface. We have utilized the highly conductive semi-metal multilayer Bi_2Se_3 as contact material for 1L-MoS_2. The Bi_2Se_3 was deposited using the well-established thermal evaporation technique following patterning, which effectively eliminates alignment issues typically encountered with graphene contacts. This study investigates the vacuum annealing of the Bi_2Se_3 films deposited using the thermal evaporation technique, revealing improved conductivity and stability. A comparison of the performance of twenty 1L-MoS_2 devices, using Bi_2Se_3 contacts instead of conventional Cr/Au, demonstrated enhanced device performance. Furthermore, the high flexibility of Bi_2Se_3 films opens potential applications for flexible devices.

4.2. CVD growth of uniform Monolayer MoS_2

Herein we employed the same CVD technique as described in **Chapter 2** to achieve uniform, large-area growth of 1L-MoS_2, with modifications to the growth temperature and pressure. Considering the lower evaporation temperature and higher chemical reactivity of MoO_3[27] compared to WO_3, the growth temperature was significantly reduced to 800°C, with a controlled ramping rate of 15°C per minute, and the pressure was adjusted to 1 mbar.

4.3. Result and discussions

4.3.1 Optical, Structural, and Chemical Analysis

The optical images of millimeter-scale large-area 1L-MoS_2 grown via thermal CVD are shown in **Fig. 4.1(a)**. An intentional scratch was made on the substrate in order to distinguish between 1L-MoS_2 and SiO_2/Si substrate, which indicated uniform contrast throughout the film. The magnified optical microscopy image of the 1L-MoS_2 from the labeled area is displayed in the inset of **Fig. 4.1(a)**. The crystallinity and layer number were analyzed via Raman spectroscopy, a powerful tool for analyzing 2D materials and are commonly used for determining layer number[28,29]. The Raman spectra of as grown 1L-MoS_2 as well as after transferring to Al_2O_3 and the plastic substrate is shown in **Fig. 4.1(b)**. The Raman spectra from CVD grown MoS_2 shows two high intensity peaks at 386.5 cm^{-1} and 405.1 cm^{-1} corresponding to in-plane mode (E_{2g}) and out of the plane (A_{1g}) at 386.5 cm^{-1} and 405.1 cm^{-1} corresponding to in-plane mode (E_{2g}) and out-of-plane mode (A_{1g}) respectively[30]. The separation between these two characteristic modes is a function of layer number[31]. For our case the separation of these two modes is 18.6 cm^{-1} which is equivalent to 1L-MoS_2 and it reduces to 17.9 cm^{-1} after transferring to Al_2O_3 substrate resulting from anticipated strain reduction. The strain reduction resulted in blueshift of the E_{2g} modes to 387.4 cm^{-1} as this mode is highly influenced by strain[32]. Raman intensity for 1L-MoS_2 reduces significantly for the plastic substrate as the Raman intensity depends on substrate[33]. Hence, we need to use higher intensity of laser to observe Raman signal for plastic substrate. For the plastic substrate, the Raman mode separation increases to 18.7 cm^{-1} caused by redshift of E_{2g} made. This shift was attributed to the high-power laser induced local heating and strain. We have also measured the PL emission spectra from 1L-MoS_2 under those three different conditions as shown in **Fig.4.1(c)**. 1L-MoS_2 has a strong PL emission in the visible region with a peak maxima at 676 nm arising from the band to

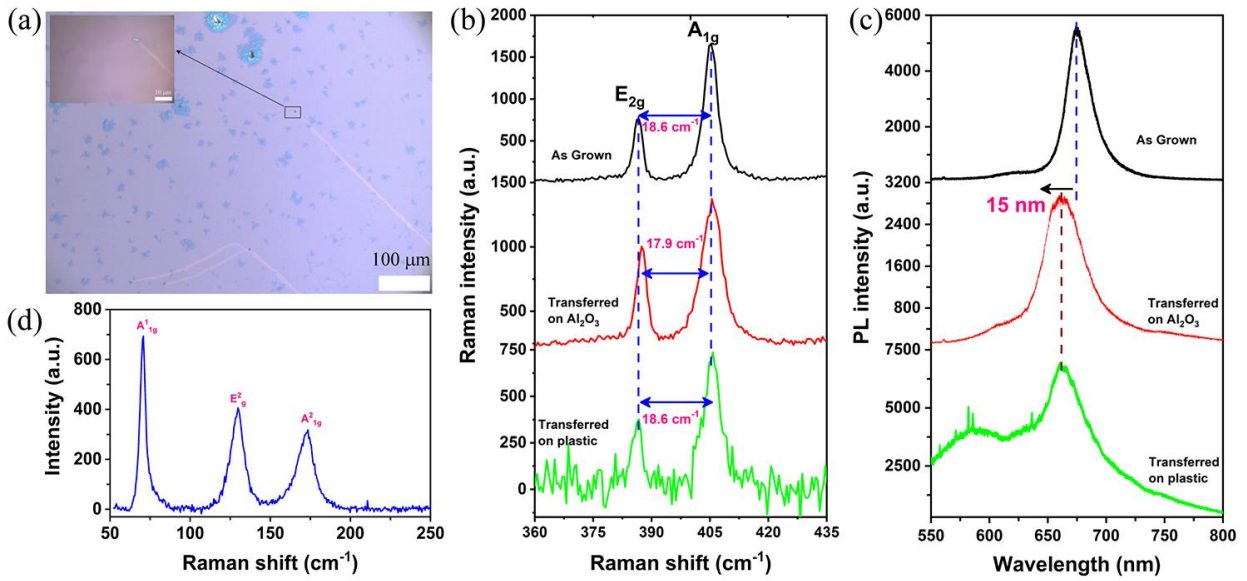

Figure 4.1: (a) Optical image of large area CVD growth of 1L-MoS_2, Inset shows the magnified optical image corresponds to the marked area; (b) Raman spectra of 1L-MoS_2 at three different conditions, CVD-grown, after transferred to Al_2O_3 and plastic substrate; (c) PL spectra of 1L-MoS_2, CVD grown, after transferred to Al_2O_3 and plastic substrate; (d) Raman spectra of thermally deposited Bi_2Se_3 after Ar annealing.

band transition[34] which subsequently shifted to 661 nm after transferring to the Al_2O_3 substrate. This shift is caused by strain reduction after the transfer process, as evident from the Raman analysis. The PL spectra of 1L-MoS_2 from the plastic substrate have shown intense PL emission after transferring, indicating there is no degradation after PMMA-assisted transfer of MoS_2. We have used Bi_2Se_3 as a contact material on 1L-MoS_2 and the Raman spectra of Bi_2Se_3 deposited by thermal evaporation is displayed in **Fig.4.1(d)**. The Raman spectra shows three prominent peaks at 70.5, 129.5 and 172.1 cm^{-1} and these are associated with A^1_{1g}, E^2_g and A^2_{1g} modes, respectively, as reported previously[35,36]. To evaluate the spatial uniformity across the flakes, we performed Raman and PL mapping on the as-grown 1L-MoS_2, after transfer, and following device fabrication with Bi_2Se_3 contacts. The results are shown in **Fig. 4.2**. The Raman mapping for the as-grown 1L-MoS_2 corresponds to the intensity distribution of the out-of-plane A_{1g} mode and the in-plane E_{2g} mode, depicted in **Fig. 4.2(b)** and **Fig. 4.2(c)**, respectively, while **Fig. 4.2(a)** represents the optical image over which the mapping was performed. For the mapping, an area was chosen where a small region of the substrate was not covered by 1L-MoS_2, allowing a clear distinction between the

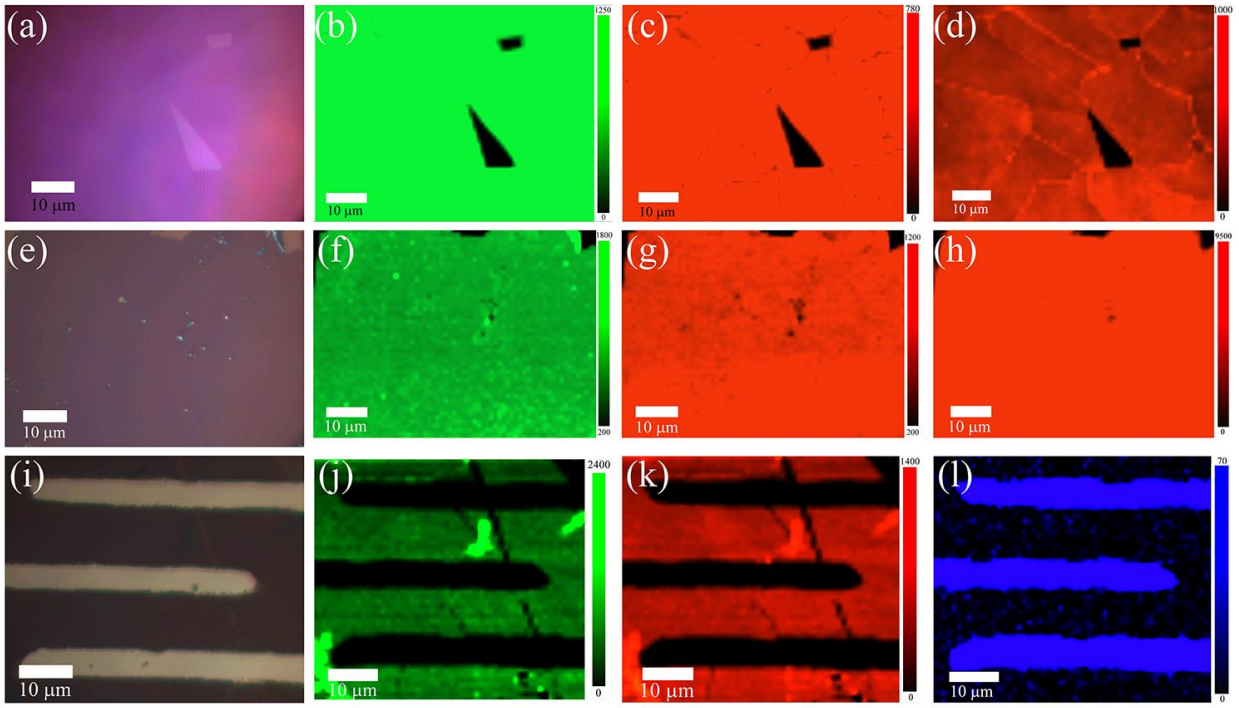

Figure 4.2: (a) Optical image for large area growth of 1L-MoS_2 on SiO_2 substrate corresponding to Raman and PL mapping before transfer. (b) The Spatial Raman mapping corresponding doping and layer number sensitive A_{1g} mode of MoS_2 with the spatial resolution of 1 μm. (c) The Spatial Raman mapping corresponding strain sensitive E_{2g} mode of MoS_2 with the spatial resolution of 1 μm. (d) PL emission spatial mapping of 1L-MoS_2 under 532 nm laser excitation. (e) Optical image of transferred 1L-MoS_2 on Al_2O_3 substrate corresponding to Raman and PL mapping. (f) The Spatial Raman mapping corresponding to A_{1g} mode after transfer with the spatial resolution of 1 μm. (g) The Spatial Raman mapping corresponding to E_{2g} mode after transfer with the spatial resolution of 1 μm. (h) PL emission spectrum of 1L-MoS_2 after transfer. (i) Optical image of 1L-MoS_2 device with Bi_2Se_3 contacts corresponding to spatial Raman mapping. (j) Spatial Raman mapping of A_{1g} mode of 1L-MoS_2 after complete devices fabrication with Bi_2Se_3 contacts. (k) Spatial Raman mapping of E_{2g} mode of 1L-MoS_2 after complete devices fabrication with Bi_2Se_3 contacts. (l) Spatial Raman mapping corresponding to A_{1g} mode of Bi_2Se_3 contacts.

substrate and 1L-MoS_2. The uniform color contrast in the Raman mapping indicates excellent uniformity over the entire 70×50 μm^2 area. Additionally, PL spatial mapping was conducted over the same region, as shown in **Fig. 4.2(d)**. This mapping reveals some non-uniformity, with boundary lines of higher intensity. These lines represent the boundaries where individual 1L flakes have merged to form a continuous MoS_2 film. The PL emissions of MoS_2 is highly sensitive to

external doping and defect sites, the enhanced intensity likely originating from interfacial defects or sulfur vacancy sites. The spatial uniformity after the transfer of 1L-MoS_2 was also examined using Raman and PL mapping, as shown in **Fig. 4.2(e-h)**. The results confirm that uniformity is preserved after transferring the 1L to the Al_2O_3 substrate. The spatial resolution corresponding to the intensity of the out-of-plane A_{1g} mode increases in areas where the film folds at top right corner, as this mode is highly sensitive to the number of layers, as shown in **Fig. 4.2(f)**. However, no significant changes are observed in the strain-sensitive E_{2g} mode intensity, as seen in **Fig. 4.2(g)**. Notably, the PL emission after transfer exhibits excellent spatial uniformity, indicating that the crystalline quality of the 1L-MoS_2 remains intact following the chemical-assisted transfer, as illustrated in **Fig. 4.2(h)**. **Fig.4.2(i)** displays the optical images of 1L-MoS_2 with Bi_2Se_3 contacts over which the Raman mapping was performed. **Fig. 4.2(l)** represents Raman mapping for Bi_2Se_3 corresponding to A^1_{1g} mode confirming the 1L-MoS_2 contact with Bi_2Se_3.

4.3.2 Structural and Chemical Analysis

The structural information was acquired from the atomic resolution high-angle annular dark-field scanning transmission electron microscopy (HAADF-STEM). From the HAADF-STEM image shown in **Fig. 4.3(a),** we have observed hexagonal arrangements of sulfur and tungsten atoms without any defect sites confirming CVD growth of highly crystalline 1L-MoS_2. **Fig. 4.3(b)** shows the SAED pattern for the 1L-MoS_2, which also reveals the hexagonal 2H phase. The interplanar spacing calculated from the SAED pattern is approximately 0.275 nm, which matches well with previous reports[37]. The larger area HAADF-STEM image also did not reveal any defect sites as shown in **Fig. 4.3(c).** The oxidation state and stoichiometry was analyzed from the XPS spectra. The XPS survey spectrum shows the S_{2p} and Mo_{3d} peaks, as illustrated in **Fig. 4.3(d)**. The high-resolution binding energy spectrum for S 2p displays a prominent doublet, with peaks at 162.2 eV and 163.4 eV, corresponding to S $2p_{3/2}$ and S $2p_{1/2}$, respectively. These peaks are indicative of the sulfur in the S^{-2} reduction state[38]. In addition, we have observed a very low intensity peak at 161.3 eV with spectral weight of 3.7% and it corresponds to sulfur vacancies[39]. For molybdenum, the two high-intensity peaks at 229.4 eV and 232.5 are corresponding to Mo $3d_{5/2}$ and Mo $3d_{3/2}$, respectively, and these are associated with Mo^{4+} oxidation state[40]. This further confirms the synthesis of the semiconducting 2H-phase of MoS_2. Besides these two peaks, there are two low-intensity peaks, a

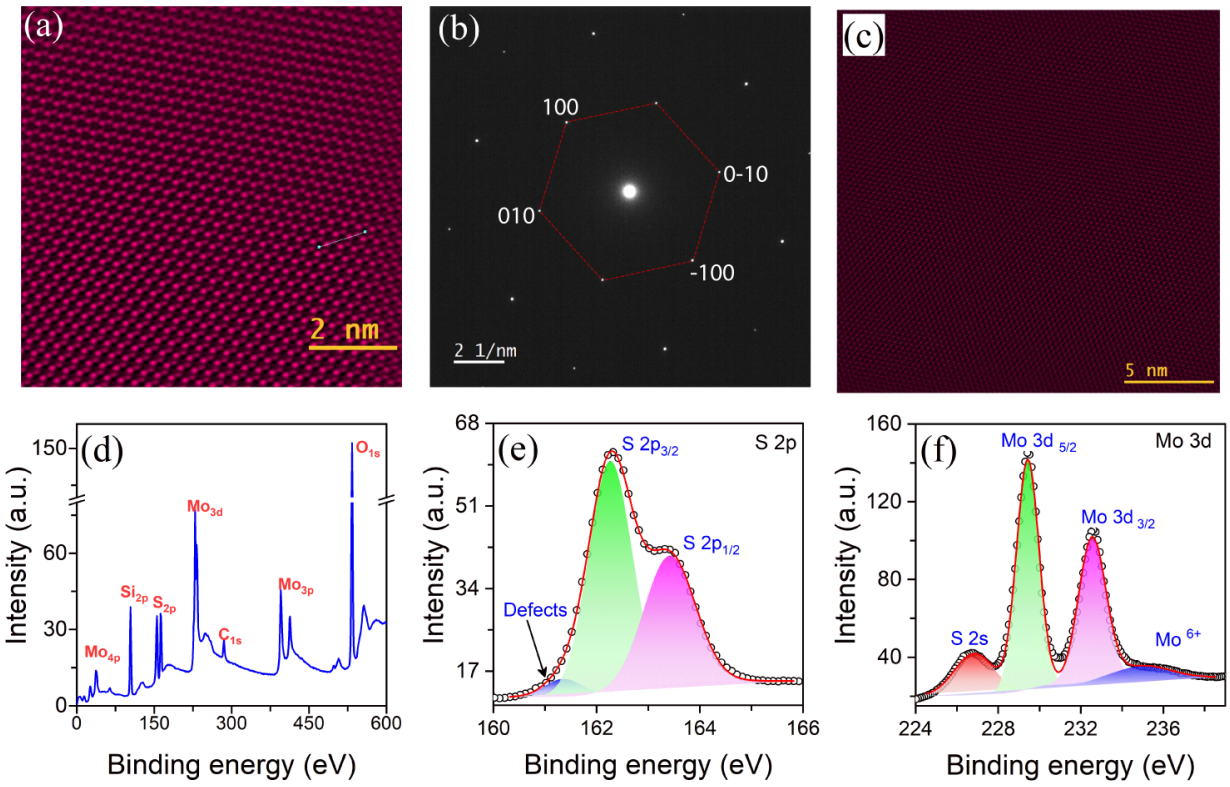

Figure 4.3: (a) The atomic resolution HAADF-STEM image of 1L-MoS_2; (b) The hexagonal bright spots correspond to the SAED pattern of 1L-MoS_2; (c) Log magnification HAADF-STEM image of 1L-MoS_2; (d) XPS survey spectrum for 1L-MoS_2; (e) High resolution core binding energy for sulfur 2p. (f) High-resolution core binding energy corresponding to molybdenum 3d.

low energy peak at 226.8 eV corresponding to S 2s and a high energy peak at 235.1 eV associated with the Mo^{6+} oxidation state[41]. Interestingly, there was no indication of MoO_3 in the Raman spectra as well as Raman mapping. Therefore, the presence of the Mo^{6+} oxidation state probably originates from a small fraction of unreacted MoO_3 that remained adsorbed on the substrate, as the substrate was positioned just above the MoO_3 powder.

4.3.3 Device Fabrication and Electrical Performance

To investigate the electrical performance of CVD-grown 1L-MoS_2 and its impact on the junction interface, we fabricated back-gated 1L-MoS_2 FETs on an Al_2O_3/TiN/P^{++}-Si substrate. The gate dielectric, a 50 nm layer of Al_2O_3, was deposited on top of a 20 nm TiN layer using an ALD system. Since the Bi_2Se_3 was utilized as a contact electrode to measure electrical performance

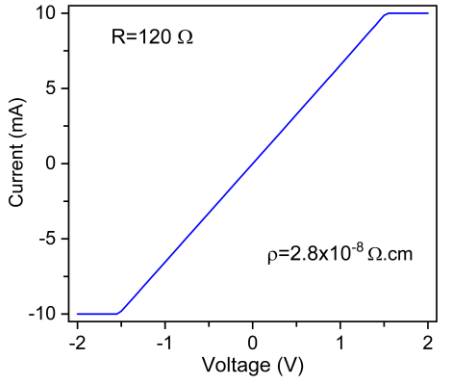

Figure 4.4: Electrical characterization via voltage sweeping of 50 nm Bi_2Se_3 film.

of 1L-MoS_2 devices, we first examined the electrical properties of 50 nm Bi_2Se_3 films. The I–V characteristics for a voltage sweep over ±2.0 V are presented in **Fig. 4.5.** The current reaches the compliance limit within 1.5 V, indicating the highly conductive nature of the Bi_2Se_3 film. To quantify its electrical properties, we measured the resistivity using a four-probe system, obtaining a value of 2.8×10^{-8} Ω·cm, which is comparable to that of gold (Au). The device configuration, along with an optical image of the 1L-MoS_2 FET with Bi_2Se_3 contact, is shown in **Fig. 4.5(a)** and **Fig. 4.5(b)**, respectively. The transfer characteristics of the 1L-MoS_2 FETs with Cr/Au and Bi_2Se_3

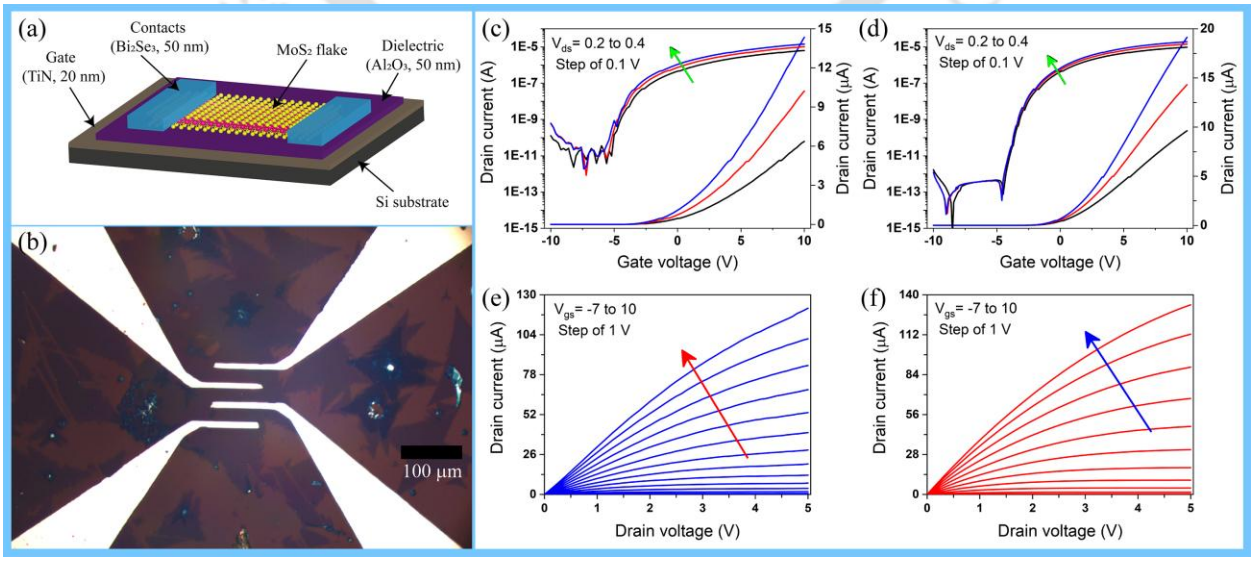

contacts are presented in **Fig. 4.5(c)** and **Fig. 4.5(d)**, demonstrating the n-type semiconducting nature of MoS_2, as the channel turns on at positive gate biases due to electron accumulation. The transfer characteristics indicate that the average off-state current is of the order of 10^{-11} A for 1L-MoS_2 with Cr/Au contacts, which has decreased significantly by two orders of magnitude to 10^{-13} A for the Bi_2Se_3 contact configuration. whereas the on-state current remains almost the same (~10^{-5} A), thus resulting in two orders of magnitude enhancement in the on-off ratio by changing the contact configurations. The output characteristics of 1L-MoS_2 with Cr/Au and Bi_2Se_3 contact configurations are displayed in **Fig. 4.5(e) and Fig. 4.5(f),** respectively, which show the enhancements of drain current with increasing gate voltage as anticipated. For further comparison, we have calculated the on-off ratio, threshold voltage (V_{th}), electron mobility, and sub-threshold

Figure 4.5: (a) Schematic representation of 1L-MoS_2 FETs on Al_2O_3 substrate using Bi_2Se_3 contacts; (b) Optical image of 1L-MoS_2 FET with Bi_2Se_3 contacts; The transfer characteristics of back gated 1L-MoS_2 FETs with (c) Cr/Au contacts and (d) Bi_2Se_3 contacts; The output characteristics for (e) Cr/Au and (f) Bi_2Se_3 contacts.

swings (SS) for both contact configurations for 20 devices, as illustrated in **Fig. 4.6**. Careful analysis of these device parameters indicates a significant improvement in device performance for 1L-MoS_2 with Bi_2Se_3 contacts in comparison to Cr/Au contacts.

4.3.4 Statistical distribution of performance parameters

On-off ratio:

The transfer characteristics for 20 numbers of 1L-MoS_2 FETs with Cr/Au contacts, measured at drain voltages of 0.2 V, 0.3 V, and 0.4 V, are presented in **Fig. 4.6(a)**, **Fig. 4.6(b)**, and **Fig. 4.6(c)**, respectively. Similarly, the transfer characteristics for Bi_2Se_3 contact configurations at the same drain voltages are depicted in **Fig. 4.6(d)**, **Fig. 4.6(e)**, and **Fig. 4.6(f)**. The on-off ratio was calculated using the average off-state current over 20 data points and the maximum on-state current at a gate bias of 10 V. The statistical distribution of the on-off ratio for 1L-MoS_2 FETs with Cr/Au and Bi_2Se_3 contacts is displayed in **Fig. 4.6(g), and Fig. 4.6(k),** respectively. From the distribution, it is evident that the on-off ratio for the devices with Cr/Au contact varies from 4.2×10^5 to 8.7×10^6 with an average value of $2.8\times10^{6,}$ but for devices with Bi_2Se_3 contact varies from 9×10^6 to 1×10^8 with an average value of 3.38×10^7. Thus, on an average, the on-off ratio is enhanced by an order

of magnitude by replacing Cr/Au contact with non-metal Bi_2Se_3. This confirms that the performance enhancements via contact engineering is a clear sign of reduced defect densities at the contact interface for Bi_2Se_3 and favorable band alignments for smoother carrier flow.

Threshold voltage:

The threshold voltage of the devices was determined using two different methods: linear extrapolation ($V_{t,\ lin}$) and the tangent at the peak of transconductance ($V_{t,\ gm}$). For $V_{t,\ lin}$, the threshold voltage was obtained by calculating the intercept on the x-axis, corresponding to the linear extrapolation of the transfer characteristics. In contrast, $V_{t,\ gm}$ was derived from the tangent to the transfer characteristics at the point where the transconductance reached its maximum value[42]. The statistical variation of threshold voltage with Cr/Au and Bi_2Se_3 contact-based 1L-MoS_2 FET is displayed in **Fig. 4.6(h) and Fig.4.6(l)**, respectively. From the distribution, we observe a wide distribution of V_t from -1.1 to 2.2 V, having a median value of 0.86 ± 1.76 V for 1L-MoS_2 FET with Cr/Au contacts, but with Bi_2Se_3 contact, the same has increased to 2.95 ± 1.02 V with distribution range between 0.35 V to 5.72 V. The threshold voltage strongly depends upon the work function of the contact material and the intrinsic doping of the 1L-MoS_2 channel.[42] Since semiconducting channel 1L-MoS_2 is identical for both contact configurations, this shift in V_t is because of the contact material work function only. MoS_2 is an intrinsically n-type semiconductor,

and the shifting of V_t toward higher positive voltage is equivalent to lower intrinsic n-doping in

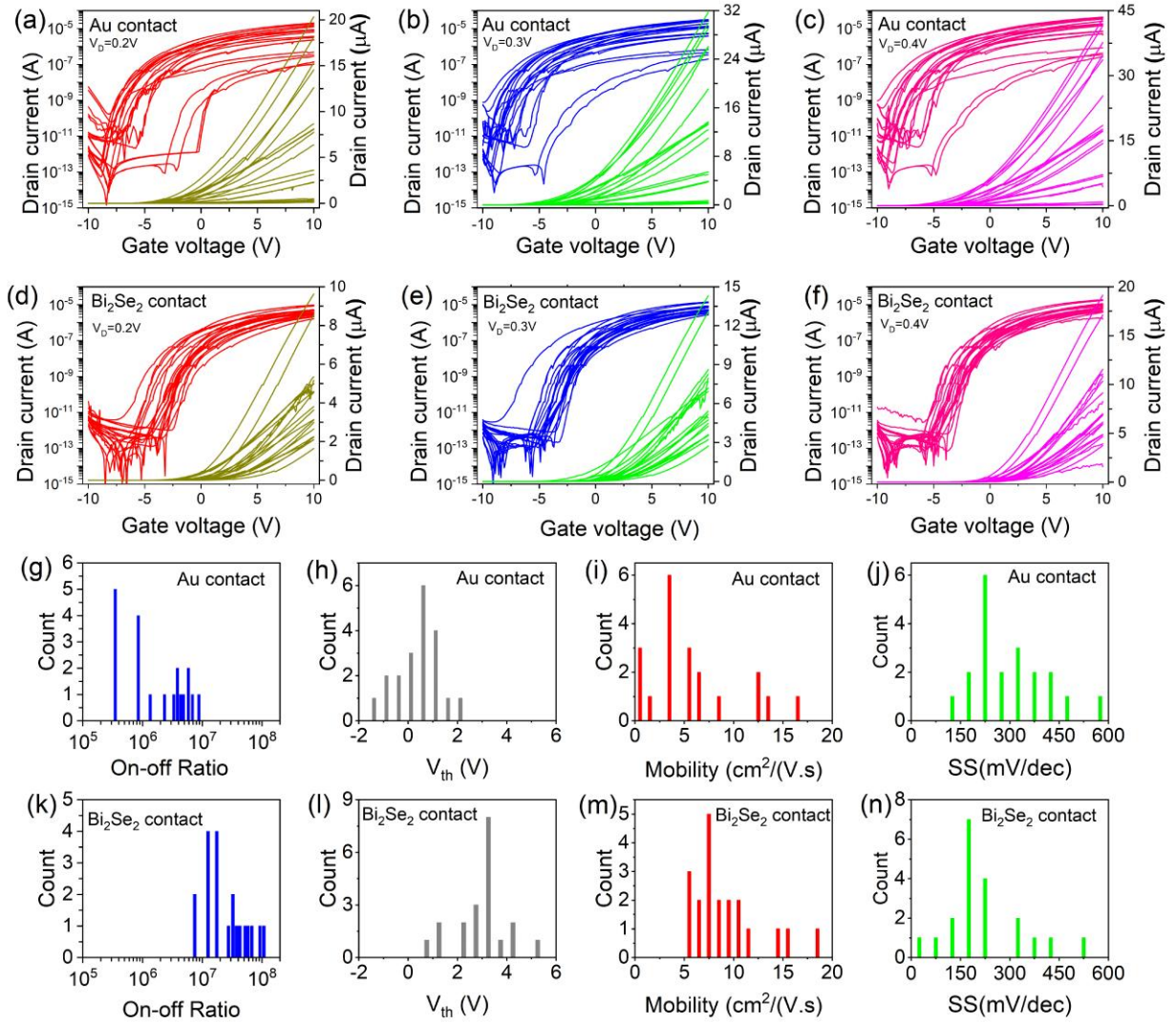

Figure 4.6: Statistical variation of the figure of merits over 20 1L-MoS_2 FETs with Cr/Au and Bi_2Se_3 contacts each. (a), (b), (c) The transfer characteristics of 1L-MoS_2 FETs with Cr/Au contacts with drain voltage of 0.2, 0.3 and 0.4V, respectively; (d), (e), (f) The transfer characteristics of 1L-MoS_2 FETs with Bi_2Se_3 contacts with drain voltage of 0.2, 0.3 and 0.4V respectively: Statistical variation of the device parameters corresponds to Cr/Au electrode at drain voltage of 0.3 V; (g) on-off; (h) threshold voltage; (i) electron mobility; (j) subthreshold swing: Statistical variation of the device parameters corresponds to Bi_2Se_3 electrode at drain voltage of 0.3 V; (k) on-off; (l) threshold voltage; (m) electron mobility; (m) subthreshold swing.

1L-MoS_2, which arises from the effect of the contact material Bi_2Se_3 only. Instead of V_t, the variation in V_t (σV_t) is a more appropriate benchmark for evaluating emerging devices made with

new materials. It is essential to understand that the median V_t is influenced by the work function of the gate metal and any unintentional or intrinsic doping of the 2D material, but V_t and σV_t are affected by the thickness of the gate oxide. Thus, to better understand the effect of Bi_2Se_3 contact

we have compared the projected threshold voltage variation ($S\sigma_{V_t}$) at scale effective oxide thickness (SEOT) using the equation below[43].

$$S\sigma_{V_t} = \sigma_{V_t}\frac{SEOT}{EOT}$$

Using this above equation, the obtained $S_{\sigma Vt}$ for 1L-MoS_2 FETs with Cr/Au contacts is 72 meV and it significantly decreased to 42 meV for Bi_2Se_3 contacts, assuming SEOT = 0.9 nm. This lower value $S\sigma_{Vt}$ for Bi_2Se_3 contact-based 1L-MoS_2 FETs can be attributed to the reduced defect densities at the contact interface. Hence, 1L-MoS_2 with Bi_2Se_3 contacts exhibits better electrical performance as compared with Cr/Au contacts.

Field effect mobility:

The field effect mobility is one of the most crucial parameters for FET-based devices and it measures how easily the carriers can move through the material in the presence of an external electric field. Mobility is an intrinsic material property and is highly influenced by gate dielectric, contact resistance, and contact materials. We have calculated the mobility by using the peak transconductance value using the formula[44]. $\mu = \frac{dI_{ds}}{dV_{gs}} \times \frac{L}{W \times C_i \times V_{ds}}$, where L is the channel length, W is the channel width, and C_i is the gate capacitance per unit area. The variations of electron mobility for 1L-MoS_2 FET with Cr/Au and Bi_2Se_3 contacts are shown in **Fig. 4.6(i)** and **Fig . 4.6(m),** respectively. For 1L-MoS_2 FETs with Cr/Au contacts, field mobility varies from 0.5 to 16.2 $cm^2/(V.s)$ with a mean value of 5.8 ± 4.8 $cm^2/(V.s)$, indicating a large variation in mobility. In contrast, for the Bi_2Se_3 contact field, mobility enhanced almost two-fold to 10.2 ± 3.46 $cm^2/(V.s)$. However, there are still large variations in the mobility from 5.6 to 18.7 $cm^2/(V.s)$. These two-fold enhancements in the mobility further confirm the reductions of interface defect densities in the 1L-MoS_2-Bi_2Se_3 contact interface.

Subthreshold swing:

Subthreshold swing (SS) is the measure of gate voltage over which the drain current changes by an order of magnitude and is mathematically defined by the formula[42].

$$ss = \ln(10) \times \frac{dV_g}{d(\ln(I_d))}$$

$$= \ln(10) \times \frac{mk_BT}{q}\ ; m = \left(1 + \frac{C_s}{C_{ox}} + \frac{C_T}{C_{ox}}\right); C_T = qD_T$$

Here, k_B is the Boltzmann constant, T is the temperature, q is the electronic charge, m is the body factor, C_S is the semiconductor capacitance, C_{IT} is the interface trap capacitance, C_{OX} is the oxide capacitance, and D_{IT} is the interface trap density. The variation of SS for 1L-MoS_2 FETs with Cr/Au and Bi_2Se_3 contacts are displayed in **Fig. 4.6(j)** and **Fig. 4.4(n)**, respectively. The 1L-MoS_2 FETs with Cr/Au contact configuration have a median SS value of 263 ± 102 mV/dec, which significantly decreased to 173 ± 97 mV/dec. Now, for fully ultrathin body FETs such as 1L-MoS_2 FETs, CS = 0 with a clean oxide-semiconductor and contact-semiconductor interface, $C_T \ll C_{ox}$, ensuring that m ~ 1 and hence SS = 60 mV/dec. Clearly, in our 1L-MoS_2 FETs, the SS values are many folds higher than the ideal value of 60 mV/dec indicating the presence of interface traps at the 1L-MoS_2-dielectric and 1L-MoS_2-contact interface. We have calculated the defect density (D_T) using the above formula, assuming C_S = 0, thus

$$D_T = \frac{C_{ox}}{q} \times \left(\frac{SS \times q}{k_BT \times \ln(10)} - 1\right)$$

Using the above formula, we have calculated the interface trap/defect densities for 1L-MoS_2 and its variations with contact materials. The mean values for the trap/defect densities were found be 3.88×10^{12} /(eV.cm^2) for the devices with Cr/Au contacts and 1.88×10^{12} /(eV.cm^2) for the devices with Bi_2Se_3 contacts. Now for each contact configuration, the dielectric surface and channel material are the same and hence the observed change in the trap/defect densities is contributed by the 1L-MoS_2-contact interface. Thus, we can conclude that the non-metal contact of Bi_2Se_3 on 1L-MoS_2 provides smoother interface resulting overall device performance enhancement. The variation of output characteristics for 20 1L-MoS_2 FETs devices with Cr/Au and Bi_2Se_3 contacts are displayed in **Fig. 4.7 and Fig. 4.8,** respectively.

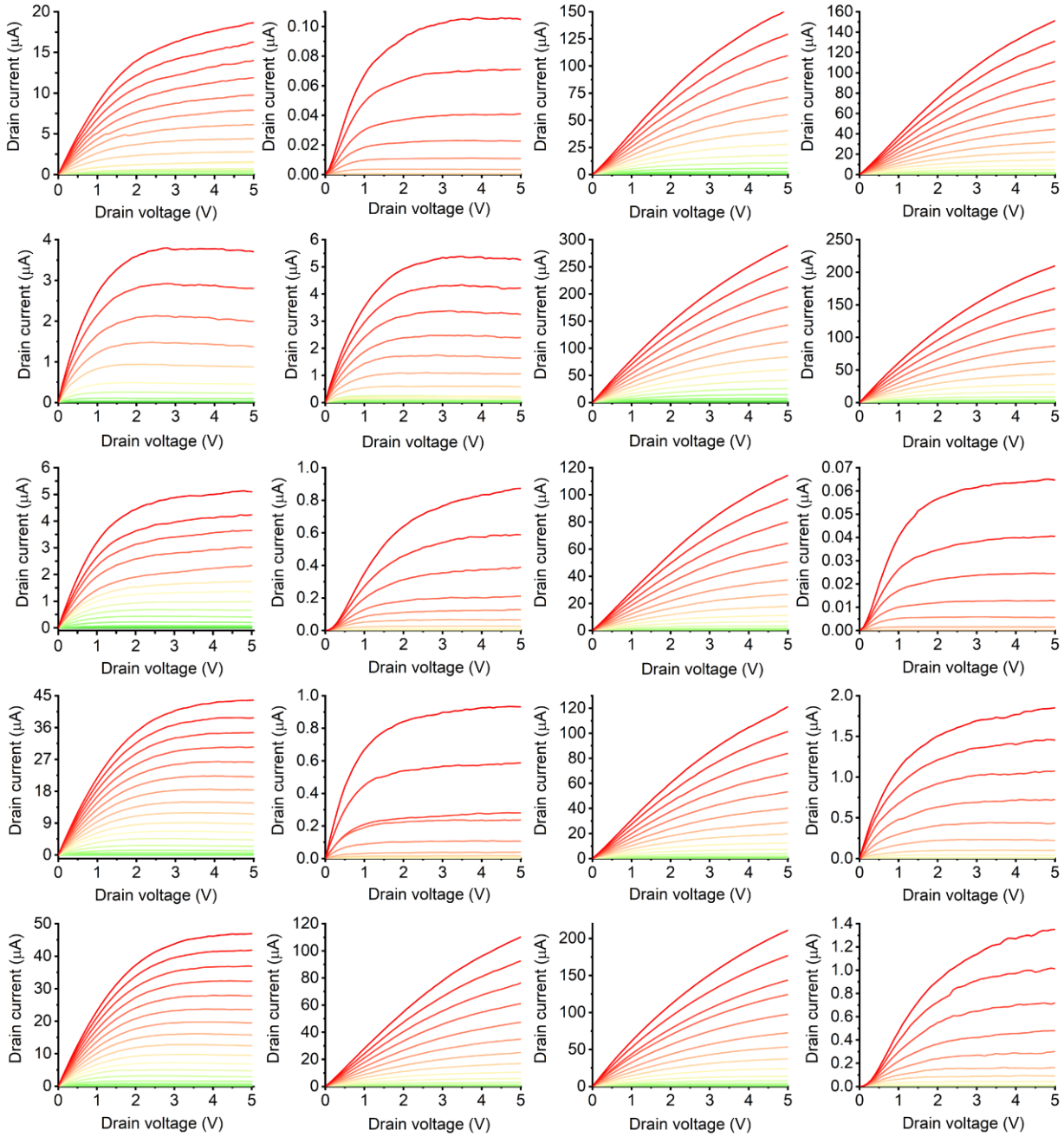

Figure 4.7: Output characteristics of 20 1L-MoS_2 FETs with Bi_2Se_3 contacts.

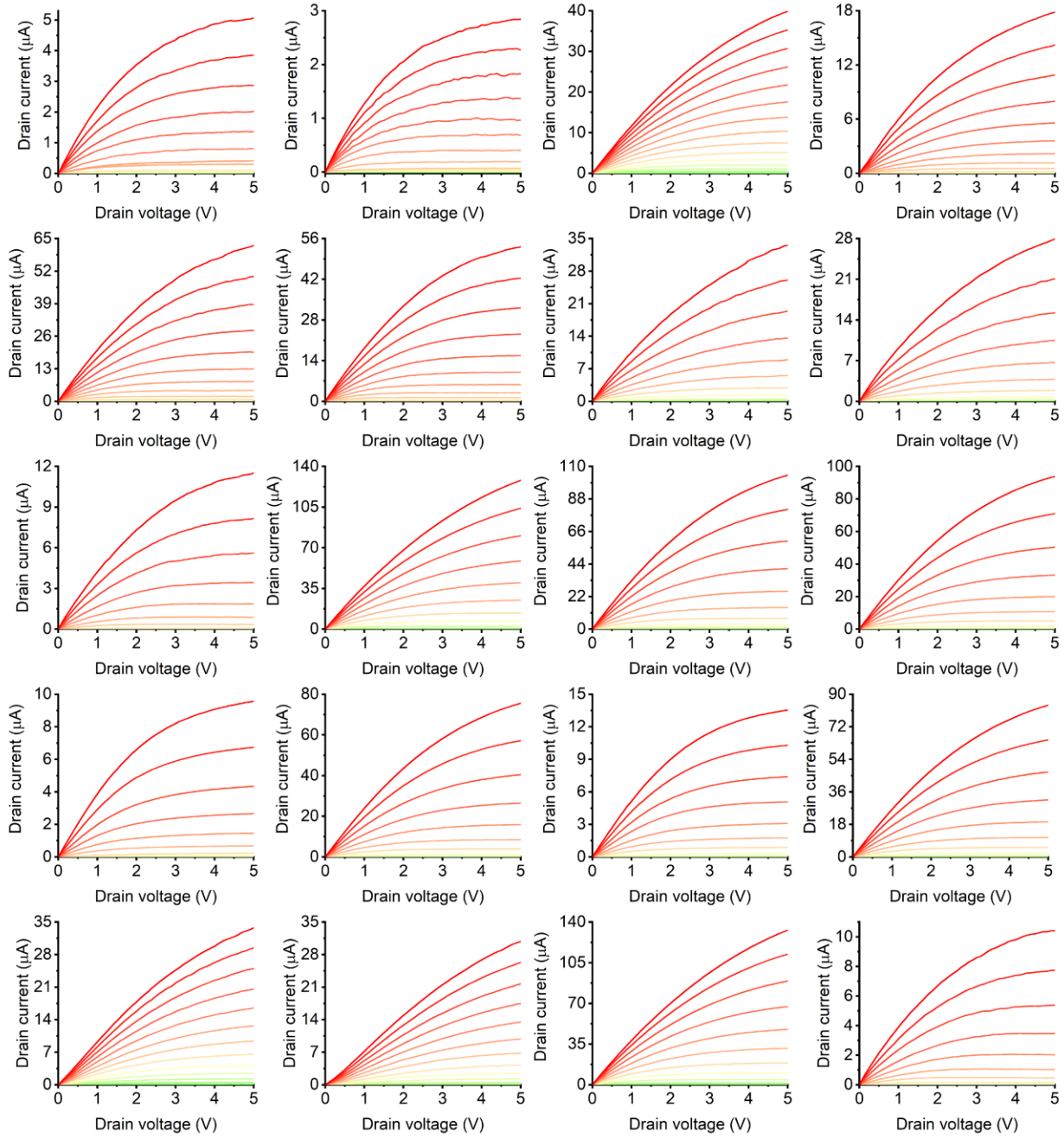

Figure 4.8: Output characteristics of 20 1L-MoS_2 FETs with Cr/Au contacts.

4.4 Application of monolayer MoS_2 with Bi_2Se_3 contact as flexible PD

As reveled from the electrical characterization, 1L-MoS_2 has higher mobility and lower interface defects with Bi_2Se_3 contacts leading to improved device performance parameters. As a proof of concept, we have fabricated a flexible PD based on 1L-MoS_2 with Cr/Au and Bi_2Se_3 contacts for

comparative analysis. The optical image of the flexible PD under 532 nm laser illumination, along with the schematic diagram, is displayed in **Fig. 4.9(a)**. The 1L-MoS_2 is a finite bandgap semiconducting material and has high absorption in the visible range. We studied photo I-V with excitation wavelength ranging from 405 to 808 nm, as shown in **Fig. 4.9(b)**. From the wavelength-dependent I-V measurements, there is negligible change in the photocurrent under 808 nm laser illuminations. This is because the incident photon energy (1.53 eV) is lower than that of the bandgap of 1L-MoS_2 (1.8 eV), unable to generate excess electron-hole pairs. For the other wavelengths, 640 nm, 532 nm, and 405 nm illumination, the current increases a few orders of magnitude. This is because the higher energies of those wavelengths create excess electron-hole pairs and change the effective carrier density, resulting in high photocurrent. Hence, 1L-MoS_2 can be used as a photodetector as its photocurrent can be modulated by incident photons. The highest change in photocurrent is observed using 532 nm wavelength illumination, and hence this wavelength was used for further measurements. Here, our main aim is to study the 1L-MoS_2 based photodetectors performance via contact modulations. The I-V sweeping of 1L-MoS_2 in the presence of different intensity 532 nm laser illuminations are shown in **Fig. 4.9(c)** and **Fig. 4.9(d),** corresponding to Bi_2Se_3 and Cr/Au contacts, respectively. It shows progressively increased currents with increasing light intensity and has a much higher current in the case of Bi_2Se_3 contacts. For Cr/Au contact on 1L-MoS_2, dark current under 5 V reverse bias is 62.7 pA, which increases to 5.5 nA with a low intensity of 1.0 mW/cm^2, thus giving an on-off ratio of 87, while for Bi_2Se_3 contact, the current increases from 67.5 pA to 6.9 nA, hence an on-off ratio of 100 under the same illumination conditions. As the intensity increases to 65 mW/cm^2, the photoinduced current increases to 33.5 nA and 86.3 nA for Cr/Au and Bi_2Se_3 contacts, respectively. Thus, under identical experimental conditions, by only changing the contact from metal Cr/Au to non-metal Bi_2Se_3, the photocurrent increased by more than two times. This is attributed to the efficient separation of carriers resulting from low interface defects and higher carrier mobility, as confirmed by previously measured FETs characteristics. Hence, enhanced performance is observed by contact engineering.

Further, we have investigated the intensity-dependent pulse photoresponse of 1L-MoS_2 photodetector with a 532 nm laser pulse. The pulse photoresponse for 1L-MoS_2 with Bi_2Se_3 contact under 5 V reverse is displayed in **Fig. 4.9(e)**. Before the laser illumination, there was a dark current of 67.5 pA, which progressively increased with the pulse intensity to a maximum value of 86.9 nA

for the intensity of 65 mW/cm^2. The calibration curve correlating the photocurrent with intensity was plotted using the formula $I_{ph}=AP^{\theta}$, where I_{ph} represents the photocurrent corresponding to the illumination intensity of P, and θ is the exponent (constant) with an ideal value of 1, signifying the linear dependency of photocurrent with intensity. The θ values were calculated by logarithmic plot

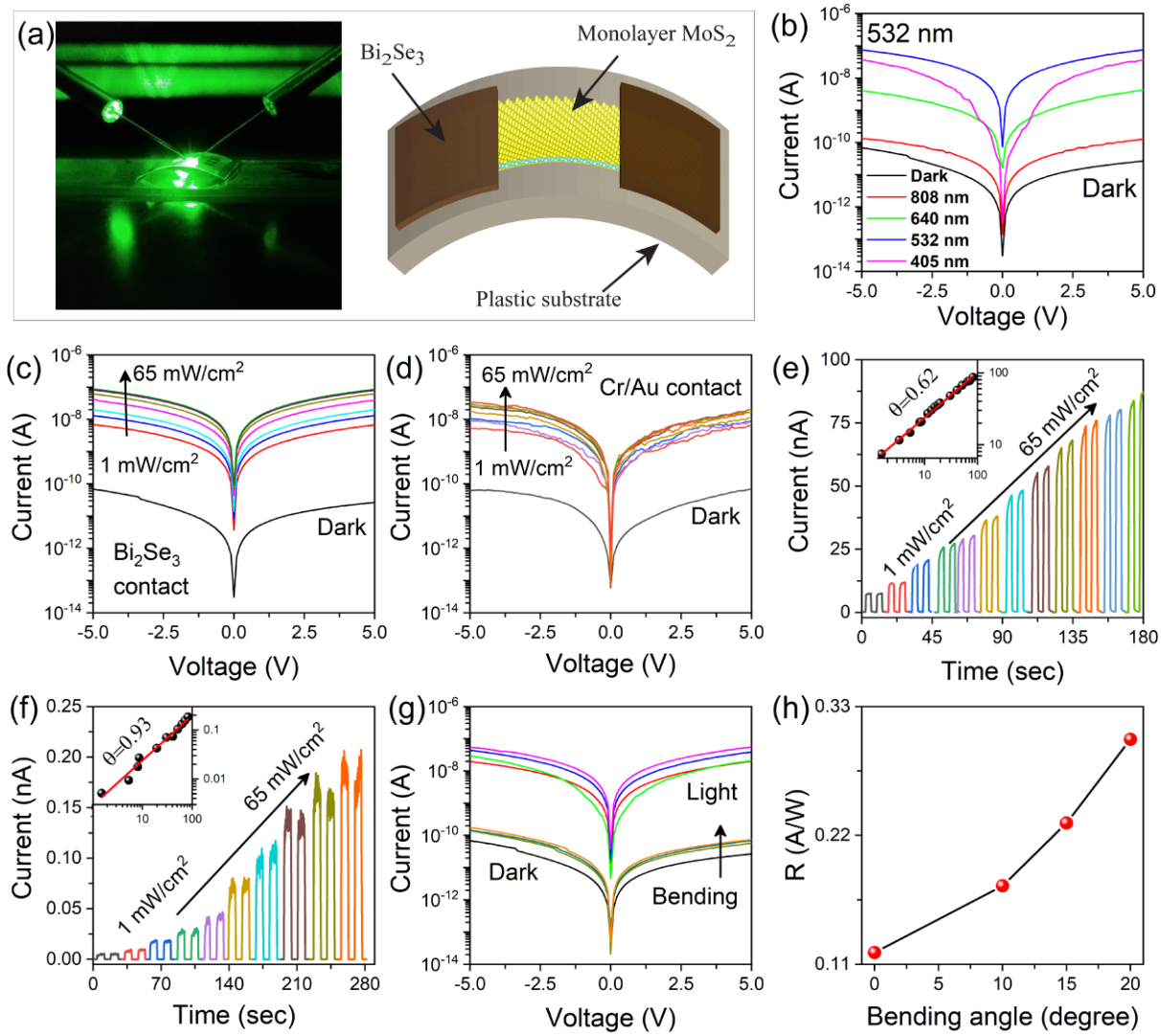

Figure 4.9: (a) Optical image and schematic representation of 1L-MoS_2 photodetector on plastic substrate using Bi_2Se_3 contacts; (b) Wavelength-dependent photoresponse of 1L-MoS_2 photodetector with Bi_2Se_3 contacts; (c), (d) Power dependent variation of photoresponse for 1L-MoS_2 with Bi_2Se_3 and Cr/Au contacts, respectively; (e) Power dependent pulse response for 1L-MoS_2 under 5V reverse bias with Bi_2Se_3 contacts, inset shows the corresponding calibration curve; (f) Power dependent pulse response for 1L-MoS_2 at self-bias with Bi_2Se_3 contacts, inset shows the corresponding calibration curve; (g) Strain dependent I-V

characteristics of 1L-MoS_2 with Bi_2Se_3 contacts; (h) Strain dependent responsivity of 1L-MoS_2 with Bi_2Se_3 contacts.

between photocurrent and illumination intensity. For Bi_2Se_3 contact configuration, θ value is observed to 0.62 (as shown in the inset of **Fig. 4.9(e)**), which is lower than the ideal value of 1. This low value of θ is attributed to the defect sites at the MoS_2-Bi_2Se_3 contact interface and the trap state between the dielectric surface and MoS_2[45,46]. The pulse response of 1L-MoS_2 based flexible photodetector with Cr/Au contacts is displayed in **Fig. 4.8(a)**, with inset presenting the calibration curve. From the fitting of the calibration curve, we obtained θ = 0.57 for the Cr/Au contact configuration, and the deviation of θ value from the ideal value of 1 indicates recombination to photo-excited carriers at intra band traps at the defect sites. Since the contact interface defect densities is higher for the Cr/Au contacts, the exponent contact reduces further to 0.57, as shown in **Fig. 4.10(a).** Interestingly, the θ value increases for self-bias mode, each reaching toward unity for Bi_2Se_3 contact, but the photocurrent is significantly low, as shown in **Fig 4.9(f)**. Furthermore, we have also analyzed the effect of mechanical stress on the performance of the PD under dark and illumination conditions at different bending angles, as displayed in **Fig. 4.9(g).** Interestingly, photocurrent increases significantly with bending angles in comparison to dark conditions, which is attributed to enhanced electron mobility in MoS_2 under stressed conditions[44,47] and generation of excess carries under illuminations. The increased photocurrent will enhance the photodetector performance in terms of responsivity with strain, as shown in **Fig. 4.9(h)**.

Finally, we have compared the figures of merit for the 1L-MoS_2 photodetector, such as responsivity (R), specific detectivity (D*), and external quantum efficiency (EQE) with two different contact materials, and the results are displayed in **Fig. 4.10**. The formulae below were used to compute these metrics[48]: $R = \frac{I_{ph}}{P \times A^*}$; $D^* = \frac{R}{\sqrt{(2ej_d)}}$ and $EQE = R \times \frac{1240}{\lambda} \times 100\ \%$. Here, I_{ph} represents the photocurrent, P is the intensity of the incident laser and A* denotes the effective device area, specifically the area of the MoS_2 flake situated between the contact pads. e is the electronic charge, j_d dark current density and λ is the wavelength of light used for the photoresponse measurements. The responsivity is the measure of photocurrent generation per unit power illumination. The responsivity at different wavelengths for the 1L-MoS_2 with Bi2Se3 contacts is displayed in **Fig. 4.9(c)**, showing the highest responsivity corresponding to 532 nm laser excitation. This is because 1L-MoS_2 has higher absorbance at that wavelength. The power

dependent responsivity for the 1L-MoS_2 with both contact configurations is shown in **Fig. 4.10(d)**. For the Cr/Au contacts-based 1L-MoS_2 photodetector, the resistivity has the highest value of 0.08

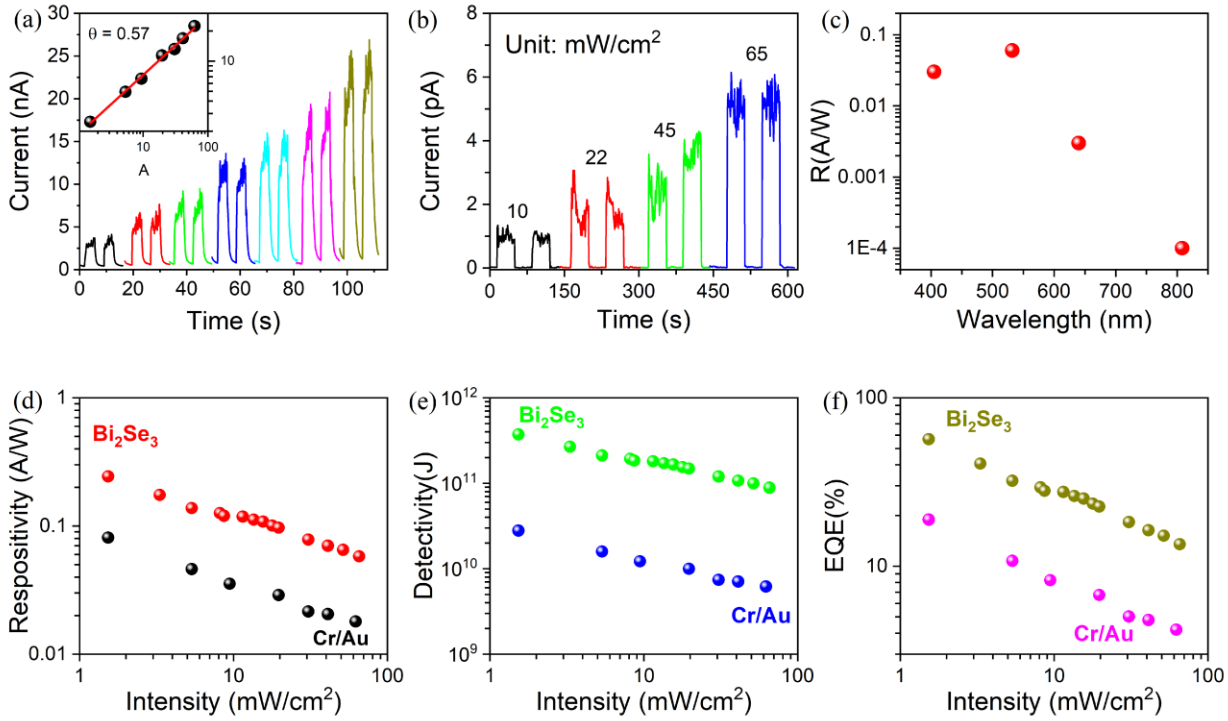

Figure 4.10: (a) Power dependent pulse response for 1L-MoS_2 under 5V reverse bias with Cr/Au contacts, inset shows the corresponding calibration curve; (b) Power dependent pulse response for 1L-MoS_2 at self-bias with Cr/Au contacts, inset shows the corresponding calibration curve; (c) Wavelength dependent responsivity for 1L-MoS_2 photodetector with Bi_2Se_3 contacts; Comparison of power dependent variation of (d) responsivity, (e) detectivity and (f) external quantum efficiency for both contact configurations.

A/W for low power and decreases with increasing power to 0.02 A/W at 65 mW/cm^2. Interestingly, the responsivity is increased significantly by about three times to 0.25 A/W at low power and 0.05 A/W at 65 mW/cm^2 for 1L-MoS_2 with Bi_2Se_3 contacts, as shown in **Fig. 4.10(d)**. This three-fold enhancement in the responsivity with Bi_2Se_3 is because of higher photocurrent and is attributed to the lower interface defects. In addition to responsivity, there is an order of magnitude increase in specific detectivity and a four-fold increase in EQE, as shown in **Fig. 4.10(e)** and **Fig. 4.10(f),** respectively. Hence the photodetector performance can be improved for 1L-MoS_2 via contact engineering.

4.5 Conclusions

In this work, we have introduced a novel approach by using non-metallic topological insulator Bi_2Se_3 as a contact material on 1L-MoS_2, which significantly enhances its optoelectronic performance. Incorporating Bi_2Se_3 contacts with 1L-MoS_2 effectively reduces the off-state current under negative gate voltage, while maintaining a nearly unchanged on-state current, thereby improving the on/off current ratio. Beyond the improved on/off ratio, there has also been a notable reduction in subthreshold swing through contact engineering alone. The lower subthreshold swing values indicate fewer interface defects, which in turn results in higher electron mobility. Furthermore, the optoelectronic performance of the 1L-MoS_2 photodetector shows marked improvement due to similar contact engineering. The use of low-cost plastic substrates and the straightforward thermal evaporation process for Bi_2Se_3 simplifies the device fabrication, reducing both complexity and cost. Thus, we demonstrate a novel, cost-effective method for enhancing device performance by employing non-metal contacts.

References

(1) Chen, Y.; Shu, Z.; Zhang, S.; Zeng, P.; Liang, H.; Zheng, M.; Duan, H. Sub-10 Nm Fabrication: Methods and Applications. *Int. J. Extreme Manuf.* 2021, *3* (3), 032002. https://doi.org/10.1088/2631-7990/ac087c.

(2) Chien, N. D.; Shih, C.-H. Short-Channel Effect and Device Design of Extremely Scaled Tunnel Field-Effect Transistors. *Microelectron. Reliab.* 2015, *55* (1), 31–37. https://doi.org/10.1016/j.microrel.2014.09.028.

(3) Wei, Z.; Jacquemod, G.; Leduc, Y.; Foucauld, E. de; Prouvee, J.; Blampey, B. Reducing the Short Channel Effect of Transistors and Reducing the Size of Analog Circuits. *Act. Passive Electron. Compon.* 2019, *2019* (1), 4578501. https://doi.org/10.1155/2019/4578501.

(4) Larrieu, G.; Guerfi, Y.; Han, X. L.; Clément, N. Sub-15 Nm Gate-All-around Field Effect Transistors on Vertical Silicon Nanowires. *Solid-State Electron.* 2017, *130*, 9–14. https://doi.org/10.1016/j.sse.2016.12.008.

(5) Zhu, J.; Liu, J.; Xu, T.; Yuan, S.; Zhang, Z.; Jiang, H.; Gu, H.; Zhou, R.; Liu, S. Optical Wafer Defect Inspection at the 10 Nm Technology Node and Beyond. *Int. J. Extreme Manuf.* 2022, *4* (3), 032001. https://doi.org/10.1088/2631-7990/ac64d7.

(6) Nourbakhsh, A.; Zubair, A.; Sajjad, R. N.; Tavakkoli K. G., A.; Chen, W.; Fang, S.; Ling, X.; Kong, J.; Dresselhaus, M. S.; Kaxiras, E.; Berggren, K. K.; Antoniadis, D.; Palacios, T. MoS_2 Field-Effect Transistor with Sub-10 Nm Channel Length. *Nano Lett.* 2016, *16* (12), 7798–7806. https://doi.org/10.1021/acs.nanolett.6b03999.

(7) Yang, X.; He, R.; Lu, Z.; Chen, Y.; Liu, L.; Lu, D.; Ma, L.; Tao, Q.; Kong, L.; Xiao, Z.; Liu, S.; Li, Z.; Ding, S.; Liu, X.; Li, Y.; Wang, Y.; Liao, L.; Liu, Y. Large-Scale Sub-5-Nm Vertical Transistors by van Der Waals Integration. *Nat. Commun.* 2024, *15* (1), 7676. https://doi.org/10.1038/s41467-024-52150-7.

(8) Wu, F.; Tian, H.; Shen, Y.; Hou, Z.; Ren, J.; Gou, G.; Sun, Y.; Yang, Y.; Ren, T.-L. Vertical MoS_2 Transistors with Sub-1-Nm Gate Lengths. *Nature* 2022, *603* (7900), 259–264. https://doi.org/10.1038/s41586-021-04323-3.

(9) Deng, T.; Zhang, Z.; Liu, Y.; Wang, Y.; Su, F.; Li, S.; Zhang, Y.; Li, H.; Chen, H.; Zhao, Z.; Li, Y.; Liu, Z. Three-Dimensional Graphene Field-Effect Transistors as High-Performance Photodetectors. *Nano Lett.* 2019, *19* (3), 1494–1503. https://doi.org/10.1021/acs.nanolett.8b04099.

(10) Tian, J.; Wang, Q.; Huang, X.; Tang, J.; Chu, Y.; Wang, S.; Shen, C.; Zhao, Y.; Li, N.; Liu, J.; Ji, Y.; Huang, B.; Peng, Y.; Yang, R.; Yang, W.; Watanabe, K.; Taniguchi, T.; Bai, X.; Shi, D.; Du, L.; Zhang, G. Scaling of MoS_2 Transistors and Inverters to Sub-10 Nm Channel Length with High Performance. *Nano Lett.* 2023, *23* (7), 2764–2770. https://doi.org/10.1021/acs.nanolett.3c00031.

(11) Shi, X.; Li, X.; Guo, Q.; Zeng, M.; Wang, X.; Wu, Y. Ultrashort Channel Chemical Vapor Deposited Bilayer WS_2 Field-Effect Transistors. *Appl. Phys. Rev.* 2023, *10* (1), 011405. https://doi.org/10.1063/5.0119375.

(12) Zhang, K.; Feng, Y.; Wang, F.; Yang, Z.; Wang, J. Two Dimensional Hexagonal Boron Nitride (2D-hBN): Synthesis, Properties and Applications. *J. Mater. Chem. C* 2017, *5* (46), 11992–12022. https://doi.org/10.1039/C7TC04300G.

(13) Lemme, M. C.; Akinwande, D.; Huyghebaert, C.; Stampfer, C. 2D Materials for Future Heterogeneous Electronics. *Nat. Commun.* 2022, *13* (1), 1392. https://doi.org/10.1038/s41467-022-29001-4.

(14) Liu, C.; Chen, H.; Wang, S.; Liu, Q.; Jiang, Y.-G.; Zhang, D. W.; Liu, M.; Zhou, P. Two-Dimensional Materials for next-Generation Computing Technologies. *Nat. Nanotechnol.* 2020, *15* (7), 545–557. https://doi.org/10.1038/s41565-020-0724-3.

(15) Jayachandran, D.; Pendurthi, R.; Sadaf, M. U. K.; Sakib, N. U.; Pannone, A.; Chen, C.; Han, Y.; Trainor, N.; Kumari, S.; Mc Knight, T. V.; Redwing, J. M.; Yang, Y.; Das, S. Three-Dimensional Integration of Two-Dimensional Field-Effect Transistors. *Nature* 2024, *625* (7994), 276–281. https://doi.org/10.1038/s41586-023-06860-5.

(16) Kim, K. S.; Kwon, J.; Ryu, H.; Kim, C.; Kim, H.; Lee, E.-K.; Lee, D.; Seo, S.; Han, N. M.; Suh, J. M.; Kim, J.; Song, M.-K.; Lee, S.; Seol, M.; Kim, J. The Future of Two-Dimensional Semiconductors beyond Moore's Law. *Nat. Nanotechnol.* 2024, *19* (7), 895–906. https://doi.org/10.1038/s41565-024-01695-1.

(17) Ghosh, S.; Zheng, Y.; Zhang, Z.; Sun, Y.; Schranghamer, T. F.; Sakib, N. U.; Oberoi, A.; Chen, C.; Redwing, J. M.; Yang, Y.; Das, S. Monolithic and Heterogeneous Three-Dimensional Integration of Two-Dimensional Materials with High-Density Vias. *Nat. Electron.* 2024, 1–12. https://doi.org/10.1038/s41928-024-01251-8.

(18) Jayachandran, D.; Sakib, N. U.; Das, S. 3D Integration of 2D Electronics. *Nat. Rev. Electr. Eng.* 2024, *1* (5), 300–316. https://doi.org/10.1038/s44287-024-00038-5.

(19) Contacts in 2D. *Nat. Electron.* 2022, *5* (5), 255–255. https://doi.org/10.1038/s41928-022-00783-1.

(20) Shen, P.-C.; Su, C.; Lin, Y.; Chou, A.-S.; Cheng, C.-C.; Park, J.-H.; Chiu, M.-H.; Lu, A.-Y.; Tang, H.-L.; Tavakoli, M. M.; Pitner, G.; Ji, X.; Cai, Z.; Mao, N.; Wang, J.; Tung, V.; Li, J.;

Bokor, J.; Zettl, A.; Wu, C.-I.; Palacios, T.; Li, L.-J.; Kong, J. Ultralow Contact Resistance between Semimetal and Monolayer Semiconductors. *Nature* 2021, *593* (7858), 211–217. https://doi.org/10.1038/s41586-021-03472-9.

(21) Kwon, G.; Choi, Y.-H.; Lee, H.; Kim, H.-S.; Jeong, J.; Jeong, K.; Baik, M.; Kwon, H.; Ahn, J.; Lee, E.; Cho, M.-H. Interaction- and Defect-Free van Der Waals Contacts between Metals and Two-Dimensional Semiconductors. *Nat. Electron.* 2022, *5* (4), 241–247. https://doi.org/10.1038/s41928-022-00746-6.

(22) Zheng, Y.; Gao, J.; Han, C.; Chen, W. Ohmic Contact Engineering for Two-Dimensional Materials. *Cell Rep. Phys. Sci.* 2021, *2* (1), 100298. https://doi.org/10.1016/j.xcrp.2020.100298.

(23) Hou, X.; Jin, T.; Zheng, Y.; Chen, W. Atomic-Scale Interface Engineering for Two-Dimensional Materials Based Field-Effect Transistors. *SmartMat* 2024, *5* (4), e1236. https://doi.org/10.1002/smm2.1236.

(24) Ghani, M. A.; Sarkar, S.; Lee, J.-I.; Zhu, Y.; Yan, H.; Wang, Y.; Chhowalla, M. Metal Films on Two-Dimensional Materials: Van Der Waals Contacts and Raman Enhancement. *ACS Appl. Mater. Interfaces* 2024, *16* (6), 7399–7405. https://doi.org/10.1021/acsami.3c15598.

(25) Schneider, D. S.; Lucchesi, L.; Reato, E.; Wang, Z.; Piacentini, A.; Bolten, J.; Marian, D.; Marin, E. G.; Radenovic, A.; Wang, Z.; Fiori, G.; Kis, A.; Iannaccone, G.; Neumaier, D.; Lemme, M. C. CVD Graphene Contacts for Lateral Heterostructure MoS_2 Field Effect Transistors. *Npj 2D Mater. Appl.* 2024, *8* (1), 1–6. https://doi.org/10.1038/s41699-024-00471-y.

(26) Hoque, M. A.; George, A.; Ramachandra, V.; Najafidehaghani, E.; Gan, Z.; Mitra, R.; Zhao, B.; Sahoo, S.; Abrahamsson, M.; Liang, Q.; Wiktor, J.; Turchanin, A.; Kubatkin, S.; Lara-Avila, S.; Dash, S. P. All-2D CVD-Grown Semiconductor Field-Effect Transistors with van Der Waals Graphene Contacts. *Npj 2D Mater. Appl.* 2024, *8* (1), 1–7. https://doi.org/10.1038/s41699-024-00489-2.

(27) Wang, Z.; Xu, W.; Li, B.; Hao, Q.; Wu, D.; Qi, D.; Gan, H.; Xie, J.; Hong, G.; Zhang, W. Selective Chemical Vapor Deposition Growth of WS_2/MoS_2 Vertical and Lateral Heterostructures on Gold Foils. *Nanomaterials* 2022, *12* (10), 1696. https://doi.org/10.3390/nano12101696.

(28) Cong, X.; Liu, X.-L.; Lin, M.-L.; Tan, P.-H. Application of Raman Spectroscopy to Probe Fundamental Properties of Two-Dimensional Materials. *Npj 2D Mater. Appl.* 2020, *4* (1), 1–12. https://doi.org/10.1038/s41699-020-0140-4.

(29) Berkdemir, A.; Gutiérrez, H. R.; Botello-Méndez, A. R.; Perea-López, N.; Elías, A. L.; Chia, C.-I.; Wang, B.; Crespi, V. H.; López-Urías, F.; Charlier, J.-C.; Terrones, H.; Terrones, M. Identification of Individual and Few Layers of WS_2 Using Raman Spectroscopy. *Sci. Rep.* 2013, *3* (1), 1755. https://doi.org/10.1038/srep01755.

(30) Jin, K.; Xie, L.; Tian, Y.; Liu, D. Au-Modified Monolayer MoS_2 Sensor for DNA Detection. *J. Phys. Chem. C* 2016, *120* (20), 11204–11209. https://doi.org/10.1021/acs.jpcc.6b01193.

(31) Chakraborty, B.; Matte, H. S. S. R.; Sood, A. K.; Rao, C. N. R. Layer-Dependent Resonant Raman Scattering of a Few Layer MoS_2. *J. Raman Spectrosc.* 2013, *44* (1), 92–96. https://doi.org/10.1002/jrs.4147.

(32) Chakraborty, B.; Bera, A.; Muthu, D. V. S.; Bhowmick, S.; Waghmare, U. V.; Sood, A. K. Symmetry-Dependent Phonon Renormalization in Monolayer MoS_2 Transistor. *Phys. Rev. B* 2012, *85* (16), 161403. https://doi.org/10.1103/PhysRevB.85.161403.

(33) Buscema, M.; Steele, G. A.; van der Zant, H. S. J.; Castellanos-Gomez, A. The Effect of the Substrate on the Raman and Photoluminescence Emission of Single-Layer MoS_2. *Nano Res.* 2014, *7* (4), 561–571. https://doi.org/10.1007/s12274-014-0424-0.

(34) De Fazio, D.; Goykhman, I.; Yoon, D.; Bruna, M.; Eiden, A.; Milana, S.; Sassi, U.; Barbone, M.; Dumcenco, D.; Marinov, K.; Kis, A.; Ferrari, A. C. High Responsivity, Large-Area Graphene/MoS_2 Flexible Photodetectors. *ACS Nano* 2016, *10* (9), 8252–8262. https://doi.org/10.1021/acsnano.6b05109.

(35) Zhang, J.; Peng, Z.; Soni, A.; Zhao, Y.; Xiong, Y.; Peng, B.; Wang, J.; Dresselhaus, M. S.; Xiong, Q. Raman Spectroscopy of Few-Quintuple Layer Topological Insulator Bi2Se3 Nanoplatelets. *Nano Lett.* 2011, *11* (6), 2407–2414. https://doi.org/10.1021/nl200773n.

(36) Nandi, S.; Ghosh, K.; Meyyappan, M.; Giri, P. K. 2D MXene Electrode-Enabled High-Performance Broadband Photodetector Based on a CVD-Grown 2D Bi2Se3 Ultrathin Film on Silicon. *ACS Appl. Electron. Mater.* 2023, *5* (12), 6985–6995. https://doi.org/10.1021/acsaelm.3c01363.

(37) Rajput, M.; Mallik, S. K.; Chatterjee, S.; Shukla, A.; Hwang, S.; Sahoo, S.; Kumar, G. V. P.; Rahman, A. Defect-Engineered Monolayer MoS_2 with Enhanced Memristive and Synaptic Functionality for Neuromorphic Computing. *Commun. Mater.* 2024, *5* (1), 1–14. https://doi.org/10.1038/s43246-024-00632-y.

(38) Mia, A. K.; Meyyappan, M.; Giri, P. K. Asymmetric Contact-Induced Selective Doping of CVD-Grown Bilayer WS_2 and Its Application in High-Performance Photodetection with an Ultralow Dark Current. *Nanoscale* 2024, *16* (17), 8583–8596. https://doi.org/10.1039/D3NR06118C.

(39) Backes, C.; Smith, R. J.; McEvoy, N.; Berner, N. C.; McCloskey, D.; Nerl, H. C.; O'Neill, A.; King, P. J.; Higgins, T.; Hanlon, D.; Scheuschner, N.; Maultzsch, J.; Houben, L.; Duesberg, G. S.; Donegan, J. F.; Nicolosi, V.; Coleman, J. N. Edge and Confinement Effects Allow in Situ Measurement of Size and Thickness of Liquid-Exfoliated Nanosheets. *Nat. Commun.* 2014, *5* (1), 4576. https://doi.org/10.1038/ncomms5576.

(40) Dodda, A.; Jayachandran, D.; Pannone, A.; Trainor, N.; Stepanoff, S. P.; Steves, M. A.; Radhakrishnan, S. S.; Bachu, S.; Ordonez, C. W.; Shallenberger, J. R.; Redwing, J. M.; Knappenberger, K. L.; Wolfe, D. E.; Das, S. Active Pixel Sensor Matrix Based on Monolayer MoS_2 Phototransistor Array. *Nat. Mater.* 2022, *21* (12), 1379–1387. https://doi.org/10.1038/s41563-022-01398-9.

(41) Duraisamy, S.; Ganguly, A.; Sharma, P. K.; Benson, J.; Davis, J.; Papakonstantinou, P. One-Step Hydrothermal Synthesis of Phase-Engineered MoS_2/MoO_3 Electrocatalysts for Hydrogen Evolution Reaction. *ACS Appl. Nano Mater.* 2021, *4* (3), 2642–2656. https://doi.org/10.1021/acsanm.0c03274.

(42) Sebastian, A.; Pendurthi, R.; Choudhury, T. H.; Redwing, J. M.; Das, S. Benchmarking Monolayer MoS_2 and WS_2 Field-Effect Transistors. *Nat. Commun.* 2021, *12* (1), 693. https://doi.org/10.1038/s41467-020-20732-w.

(43) Smithe, K. K. H.; Suryavanshi, S. V.; Muñoz Rojo, M.; Tedjarati, A. D.; Pop, E. Low Variability in Synthetic Monolayer MoS_2 Devices. *ACS Nano* 2017, *11* (8), 8456–8463. https://doi.org/10.1021/acsnano.7b04100.

(44) Zhang, Y.; Zhao, H. L.; Huang, S.; Hossain, M. A.; van der Zande, A. M. Enhancing Carrier Mobility in Monolayer MoS_2 Transistors with Process-Induced Strain. *ACS Nano* 2024, *18* (19), 12377–12385. https://doi.org/10.1021/acsnano.4c01457.

(45) Zhou, C.; Raju, S.; Li, B.; Chan, M.; Chai, Y.; Yang, C. Y. Self-Driven Metal–Semiconductor–Metal WSe_2 Photodetector with Asymmetric Contact Geometries. *Adv. Funct. Mater.* 2018, *28* (45). https://doi.org/10.1002/adfm.201802954.

(46) Zeng, L.-H.; Chen, Q.-M.; Zhang, Z.-X.; Wu, D.; Yuan, H.; Li, Y.-Y.; Qarony, W.; Lau, S. P.; Luo, L.-B.; Tsang, Y. H. Multilayered $PdSe_2$/Perovskite Schottky Junction for Fast, Self-Powered, Polarization-Sensitive, Broadband Photodetectors, and Image Sensor Application. *Adv. Sci.* 2019, *6* (19), 1901134. https://doi.org/10.1002/advs.201901134.

(47) Datye, I. M.; Daus, A.; Grady, R. W.; Brenner, K.; Vaziri, S.; Pop, E. Strain-Enhanced Mobility of Monolayer MoS_2. *Nano Lett.* 2022, *22* (20), 8052–8059. https://doi.org/10.1021/acs.nanolett.2c01707.

(48) Bora, A.; Mawlong, L. P.; Giri, P. K. Highly Suppressed Dark Current and Fast Photoresponse from Au Nanoparticle-Embedded, Si/Au/WS_2 Quantu m-Dot-Based, Self-Biased Schottky Photodetectors. *ACS Appl. Electron. Mater.* 2021, *3* (11), 4891–4904.

Chapter 5

Single-Step Controlled CVD Growth of WS_2-MoS_2 Lateral Heterostructure and Its Application in Field Effect Transistor

In this chapter, we report a single-step in-situ chemical vapor deposition growth of bilayer WS_2-MoS_2 lateral HS, which ensures a clean diffused interface between WS_2 and MoS_2, enabling an efficient charge transport. The spatial Raman, photoluminescent (PL), and Auger mapping of in-situ WS_2-MoS_2 lateral HS shows a clear transition from pure WS_2 to pure MoS_2 region through a graded $WS_{(1-x)}Mo_xS_2$ alloy interface. The composition and the width of the alloy interface could be tuned by careful choice of the proportion of precursor materials. Spatially resolved PL spectra and PL mapping reveal a strongly enhanced (more than one order of magnitude) PL intensity in the HS interface attributed to the strain-induced bandstructure modification in the alloyed interface. Interestingly, the alloyed interface in the lateral HS also dramatically improves the electronic properties, resulting in an on-off ratio of 10^8 in the fabricated field effect transistor, which is two orders of magnitude higher than their individual counterpart. These results on lateral HS are significant, and they pave the way to synthesize other different HSs for future electronic devices and integrated circuits.

5.1 Introduction

The 2D semiconducting TMDs, such as MoS_2, WS_2, $MoSe_2$, and WSe_2, have garnered considerable attention from the scientific community due to their exceptional electrical and optical properties[1–5]. However, progress in their growth of HSs for optoelectronic applications has been limited, especially the in situ lateral HS[6–8]. By integrating different TMDs, the HSs offer new functionalities that are crucial for high-speed optoelectronics applications[9–11]. The 2D TMD HSs, with their versatile properties and advanced fabrication methods, are opening new avenues for research in optoelectronics, photonics, and semiconductor technology[12–14]. The development of vertical and lateral HSs in atomically thin TMD-based devices enables the exploration of novel electronic and photonic behaviors, paving the way for advanced applications in future electronic and optoelectronic devices[15–17]. Although methods like CVD have achieved notable success in synthesizing highly crystalline 2D TMDs[18,19], they still face challenges in in-situ growth of

controlled HS. Traditionally, transferring one 2D material to another one or epitaxial two step growth methods are used for creating HS[20,21]. However, those methods are cumbersome and often result in lower performance because of lattice mismatch between different 2D materials and interfacial contamination. The in-situ growth of the HS can overcome those limitations, especially may offer an ultraclean interface[22]. In this regard, the two-step CVD method has advantages in synthesizing high-quality lateral HSs[23]. In this approach, one material is synthesized in the first step on a substrate, and the same substrate is then used to synthesize the second material, forming the HS[8,24]. This method reduces alloy formation and improves interface clarity, offering superior control over electronic properties. Nevertheless, this two-step process is time consuming and makes it a complex process. Recently, solution process assisted single-step CVD showed the synthesis of in situ WS_2-MoS_2 lateral HS[25]. This advanced synthesis process has enabled lateral HSs with atomically sharp interfaces, making them promising candidates for next-generation nanoelectronics[13]. This sharp interface between the HS enables the fabrication of PN junction diodes with a high rectification ratio[26,27]. Interestingly, a new approach of periodic change of carrier gases enables a large periodic synthesis of 2D material HS[28]. But in that case, the precursor materials were the 2D materials themselves instead of conventionally the oxides and chalcogens. In addition to the above-mentioned achievements recently, there has been reports in modulation of electronic properties via selective doping in single step lateral HS leading to advance properties[29,30]. This in-situ doping ability in the lateral HS via CVD method further enhanced the performance of these materials. There are still many challenges in controlling the shape, scale, and quality of HSs, and further improvements in growth strategies are required for more robust and well-controlled methods. As fabrication techniques advance, these materials are expected to revolutionize future electronic devices and integrated circuits.

In this work, we present a novel approach for the single-step controlled CVD growth in-situ WS_2-MoS_2 lateral HSs. By fine-tuning the relative precursors amounts and positions, we successfully achieved the controlled in-situ growth of WS_2-MoS_2 lateral HSs via single-step CVD technique. Controlling the weight percentages of WO_3 and MoO_3 enabled the synthesis of intrinsic WS_2, intrinsic MoS_2, and WS_2-MoS_2 lateral HSs with varying relative area, as confirmed by Raman, PL and Auger mapping. The in-situ formation of the lateral HS leads to a remarkable enhancement in PL near the interface, primarily due to local strain or 1L-WS_2. When applied as FET channel, the WS_2-MoS_2 lateral HS demonstrated electron inversions in the off-state current, resulting in an

ultralow off-current and a significant improvement in the on-off ratio. Additionally, other device parameters also enhance significantly, indicating that the performance of our synthesized in-situ HS surpasses that of previously reported methods.

5.2. In-situ CVD-growth of WS_2-MoS_2 Lateral Heterostructure

As discussed in **Section 2.4.6** of **Chapter 2**, we optimized the CVD growth parameters to achieve layer-controlled growth of WS_2. Building on this, we further modified the CVD process to enable the controlled growth of in-situ WS_2-MoS_2 lateral HSs. The co-evaporation of the oxide precursors

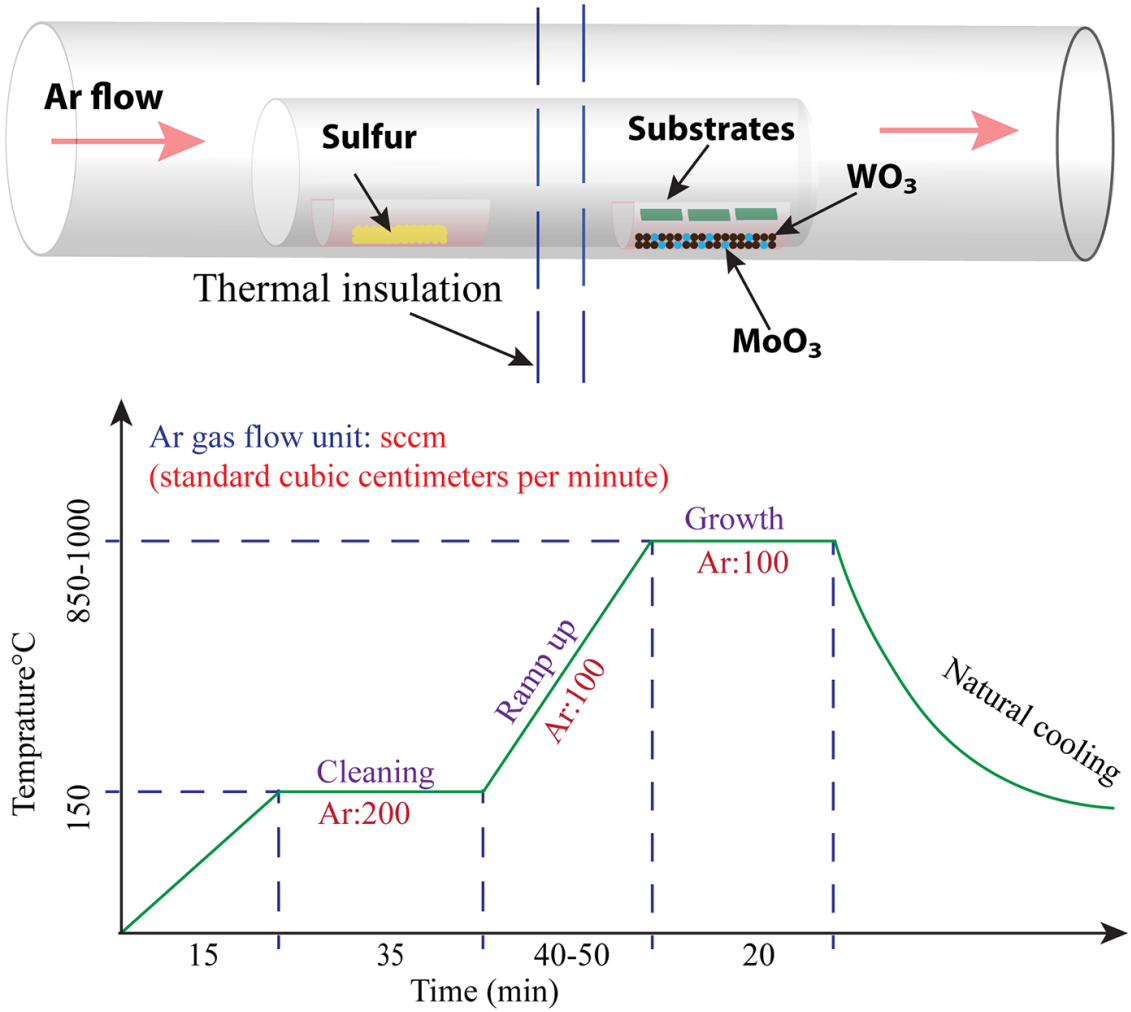

Figure 5.1: Schematic representation for the in-situ CVD growth of WS_2-MoS_2 lateral HS with the temperature profile of the heating zone with argon carrier gas flow.

(WO_3 and MoO_3) posed a challenge due to their different evaporation temperatures. To address this, MoO_3 powder was ball-milled at 450 rpm for 5 hours to produce finer particles, facilitating co-evaporations and better mixing with WO_3 at lower weight fractions. For intrinsic WS_2 and MoS_2 growth, we used 12 mg of oxide precursors and 200 mg of sulfur, maintaining growth temperatures of 1000°C and 850°C, respectively. In the case of in-situ WS_2-MoS_2 lateral HSs, we varied the weight fractions of WO_3 and MoO_3, ensuring the total oxide weight remained constant at 12 mg. For the in-situ lateral HS, we have used 4 different weight fractions (WO_3:MoO_3), 11:1, 10:2, 9:3, and 8:4. As the MoO_3 fraction increased, the high-temperature zone was adjusted from 1000°C to 850°C, while the sulfur zone temperature was consistently set to reach 250°C during the growth process. **Fig. 5.1** provides a schematic representation of the single-step in-situ growth of WS_2-MoS_2 lateral HSs, illustrating the carrier gas flow and the temperature profile in the high-temperature zone. While the detailed CVD process is outlined in **Section 2.4.6 of Chapter 2**, here we focused on varying the weight fractions and temperature profiles to precisely control HS growth. Under optimal growth conditions, we achieved controlled variation in the relative areas of WS_2 and MoS_2 within a single flake by adjusting the oxide precursor ratios and growth temperatures. This novel single-step technique eliminates the need for the conventional two-step growth and transfer processes typically used to create HSs. By avoiding polymer-assisted transfer, this method ensures a cleaner WS_2-MoS_2 interface, free from contamination, thereby enhancing device performance.

5.3. Results and discussions

5.3.1 Optical and Structural Analysis

The CVD-grown 2D flakes grown at different conditions were first observed under an optical microscope which confirmed the large area uniform growth. The synthesized intrinsic WS_2, MoS_2, and in-situ WS_2-MoS_2 lateral HS were analyzed with Raman spectroscopy as it is one of the most efficient tools for analyzing 2D materials[31]. The Raman spectra for intrinsic WS_2, MoS_2, and in-situ WS_2-MoS_2 lateral HS under 532 nm laser excitation are shown in **Fig. 5.2**. The fitted Raman spectra in **Fig. 5.2(a)** display the Raman spectra for intrinsic WS_2 as reported by our group[18]. From

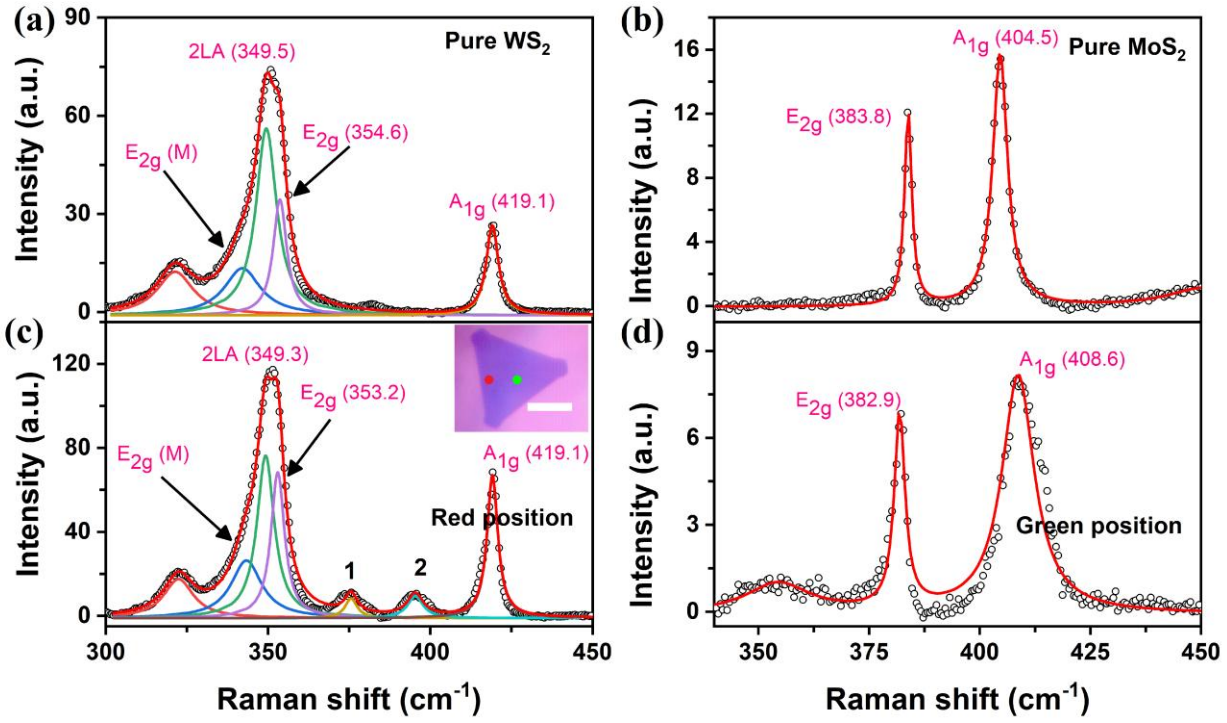

Figure 5.2: (a) Raman spectra from intrinsic 2L-WS_2; (b) Raman spectra from intrinsic 2L-MoS_2; (c) Raman spectra from the outer region of the HS flake as marked by the red circle in the inset optical image; (d) Raman spectra from the central region of the HS flake as marked by the green circle in the inset optical image of Fig. 5.2(c).

the Raman spectra, we have observed the charge and layer number sensitive out-of-plane A_{1g} mode at 419.1 cm^{-1}, whereas the strain-sensitive in-plane E_{2g} mode was observed at 353.6 cm^{-1}. The A_{1g} mode of WS_2 is highly sensitive to layer number, and the position of 419.1 cm^{-1} indicates the WS_2 flake is bilayer[18]. In addition to those characteristics, other phonon modes are also observed when excited with 532 nm laser excitations as labeled in the deconvoluted spectrum[31] shown in **Fig. 5.2(a).** The Raman of CVD-grown MoS_2 is displayed in **Fig. 5.2(b)**, which has a signature of two strong Raman modes at 383.8 cm^{-1} and 404.6 cm^{-1} corresponding to in-plane E_{2g} mode and out-of-plane A_{1g} mode respectively. The separation of these two modes also strongly depends upon the layer number, and the 20.4 cm^{-1} separation of these two fundamental modes indicates bilayer MoS_2[19]. For the in-situ CVD-grown WS_2-MoS_2 HSs, Raman spectra were analyzed from two specific points: the edge and the center of the flakes, indicated by red and green circles, respectively, as shown in the inset of **Fig. 5.2(c)**. The Raman spectra from those two positions indicate that the edge contains WS_2 layer, whereas the middle part contains MoS_2 layers as shown

in **Fig. 5.2(c)** and **Fig. 5.2(d),** respectively. From the Raman spectra at the edge, we observed two additional Raman modes, which are labeled by 1 and 2. Those modes are observed only in the heterostructure and are not reported earlier. It may be due to some interaction between the two materials and requires more investigation. From the middle part, we observed Raman spectra corresponding to MoS_2 without any additional modes, unlike the edge part. Thus, the middle part is intrinsically MoS_2. From the Raman spectra, it is quite clear that there may be a boundary between WS_2 and MoS_2, which can be identified via spatial Raman mapping. The optical images for the controlled HS growth via CVD and spatial Raman mapping are displayed in **Fig. 5.3.** From the images, we can observe a continuous flake without any distinct boundary, indicating a smooth interface between WS_2 and MoS_2. The spatial Raman mapping of the triangular flakes corresponding to out-of-plane A_{1g} mode and in-plane E_{2g} modes is displayed in red and green colors, respectively. As expected, from the spatial Raman mapping corresponding to intrinsic WS_2, we can see uniform intensity distribution across the flake for A_{1g} and E_{2g} modes. When we introduce MoO_3 precursors during CVD growth, the HS formation started, and the same has been

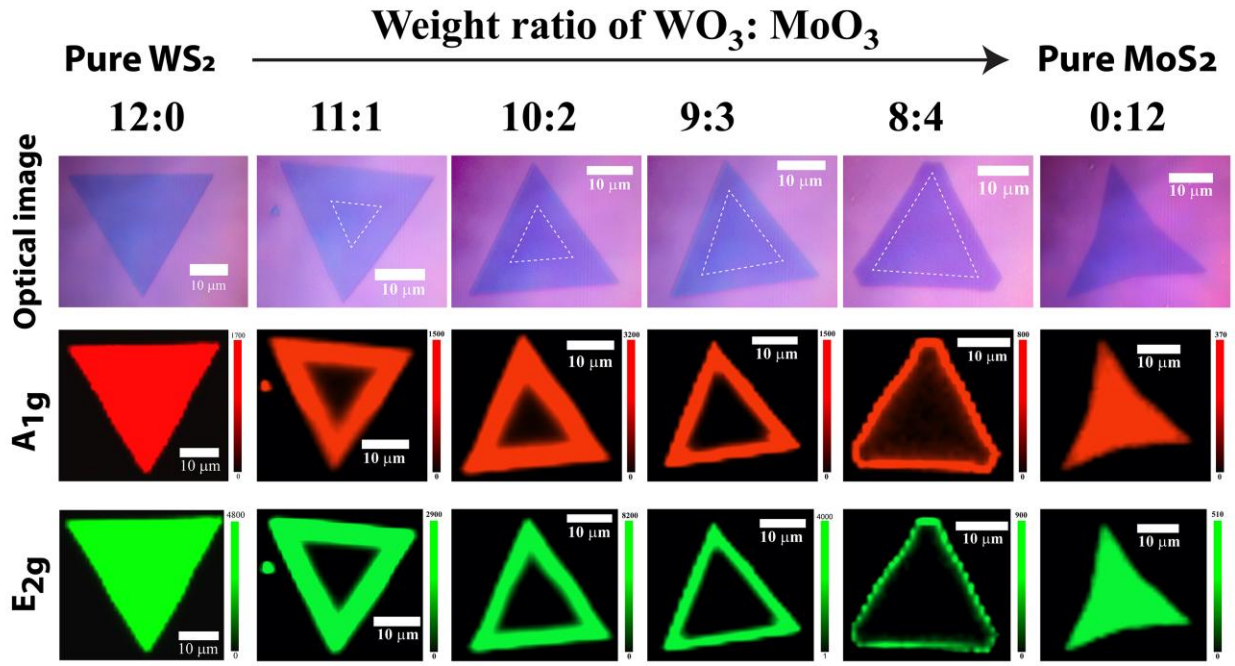

Figure 5.3: Spatial Raman mapping of the CVD-grown WS_2, MoS_2 and WS_2-MoS_2 lateral HS; The top row represents the optical image of intrinsic WS_2 (leftmost), lateral HS (middle region), intrinsic MoS_2 (rightmost); The middle row represents the spatial Raman mapping corresponding to out of plane A_{1g} Raman modes; the bottom row is corresponding to in-plane E_{2g} Raman mode.

reflected in the spatial Raman mapping as the red and green areas corresponding to A_{1g} and E_{2g} modes of WS_2, which started disappearing from the center region of the flakes. Thus, the middle part for the CVD-grown flake is not WS_2 but is MoS_2, as seen from the Raman spectra from the green circle in **Fig.5.2**. In order to have control over the HS growth, we have varied the relative oxide precursors fraction as discussed in the experimental section. From the growth of different fractions of oxide precursors, we have observed excellent control over the relative area between WS_2 and MoS_2 within a single flake. For the HS, the better chemically reactive MoO_3 than the WO_3 resulted in the growth of MoS_2 in the central region and surrounded by WS_2[25]. Finally, we have synthesized intrinsic MoS_2 by using only MoO_3 and sulfur precursors, and it has an uniform Raman intensity distribution throughout the flake. Hence, we have achieved the optimum growth

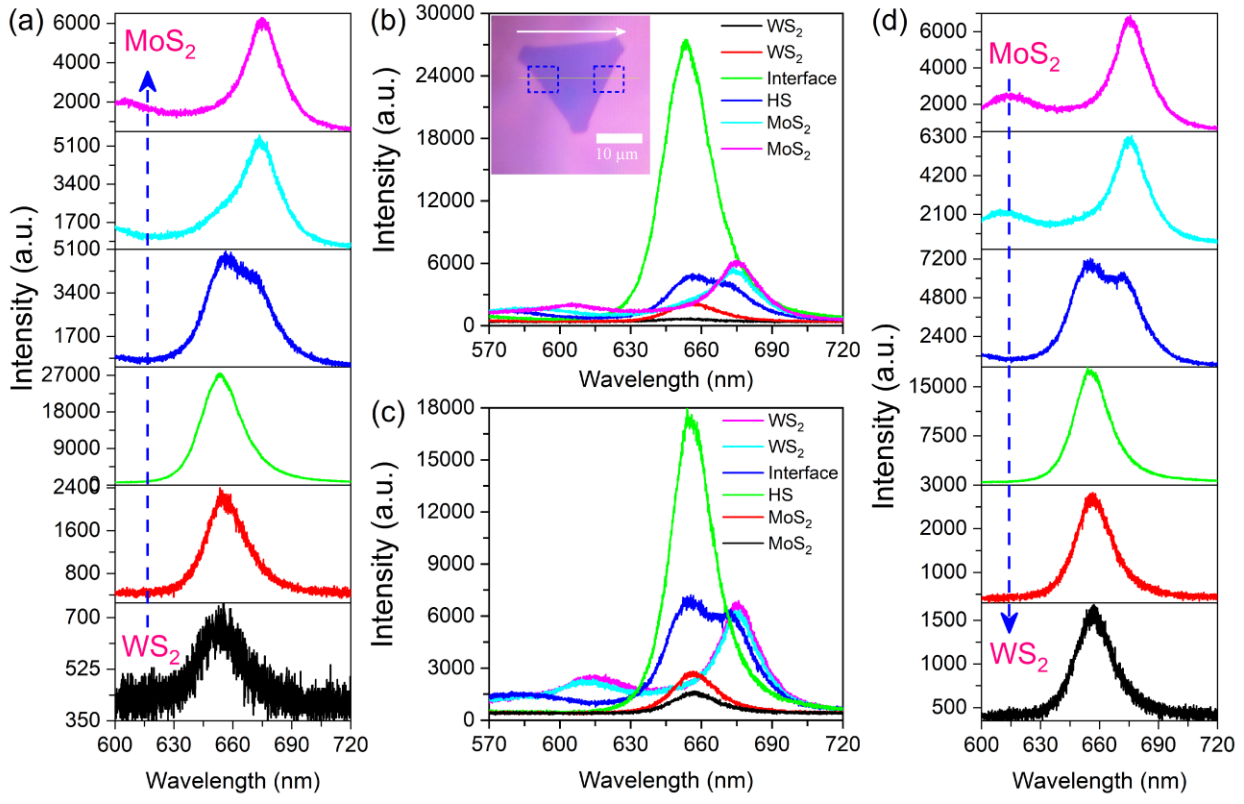

Figure. 5.4: The PL line mapping spectra of WS_2-MoS_2 lateral HS with a spatial gap of 1 μm; (a) PL line mapping of the lateral HS from edge toward center (from bottom to top) corresponding to the flake shown in the inset Fig. 5.3(b); (b) The PL emission from the lateral HS corresponding to the points of left square mark as shown in the inset; (c) The PL emission from the lateral HS corresponding to the points of right square mark as shown in the inset of Fig. 5.3(b); (d) PL line mapping of the lateral HS from center toward edge (from top to bottom) corresponding to the flake shown in the inset Fig. 5.3(b).

conditions for control growth of in-situ WS_2-MoS_2 lateral HS using the single- step CVD technique. Additionally, the lateral HS formation was confirmed via PL emission analysis. 2D WS_2 and MoS_2 are both luminescent under 532 nm laser excitations. 1L-WS_2 exhibits strong luminescence with a peak maximum of around 630 nm, corresponding to a direct transition from the conduction band to the valence band[32]. In contrast, the PL emission diminishes in bilayer WS_2, with the peak maximum shifting to 650 nm as its band structure changes from direct to indirect[18]. Whereas the bilayer MoS_2 has a strong PL emission with the peak maxima at 675 nm[33]. Thus, for the HS, we expect a PL emission peak around 675 nm from the central region and around 650 nm from the edges corresponding to MoS_2 and WS_2, respectively. The PL emission spectrum from the HS is displayed in **Fig. 5.4**. The PL emissions were measured along a line from left to right with a step size (special separation) of 1 μm through a HS flake, as shown in the inset of **Fig. 5.4(b)**. The PL emission corresponding to the points in the left and right rectangle is displayed in **Fig. 5.4(a)** and **Fig. 5.4(d),** respectively. There is weak PL emission from the edge with the maxima at 653 nm corresponding to 2L-WS_2, and as we move towards the central region PL emission peak remains at 653 nm up to 3 μm, but at the next position, a broader PL emission is observed containing the WS_2 signature at 653 nm as well as MoS_2 signature at 675 nm, as indicated by the blue curve in **Fig. 5.4(a)**. Further moving towards the central region, we observed the PL emissions corresponding to MoS_2. Similar characteristics were observed from another opposite edge, as marked in the inset of **Fig. 5.4(b)** and are displayed in **Fig. 5.4(d)**. This linear mapping of PL also confirms the formation of lateral HS via the single-step CVD technique. Interestingly, a thorough investigation of the PL emission intensity for the HS indicates an anomalous PL enhancement in the interface, as displayed in **Fig. 5.4(b)** and **Fig. 5.4(c)**. This strong enhancement in the PL intensity in the bilayer region is an indication of transformation to the direct band structure from the indirect band structure in 2L-WS_2. There are two possible explanations for this anomalous PL enhancement near the interface: the growth of WS_2 from the edges of MoS_2 induces strain near the interface resulting in the PL enhancement as induced strain enhances the PL emissions[34]. The lattice mismatch and diffuse interface let the formation in strain in the interface region. The enhanced PL emission peak ~ at 650 nm indicates 2L-WS_2 , Since 1L-WS_2 has a PL emission peak at ~ 630 nm[32]. Thus, the lattice strain at the interface, may be responsible for the anomalous enhancement in PL intensity, which will further aid in efficient carrier flow and eventually lead to enhanced device performance. In addition to the linear PL mapping, we further

analyzed the spatial PL mapping of the intrinsic WS_2, MoS_2, and their in-situ lateral HS, as shown in **Fig. 5.5**. In the linear mapping of the intrinsic WS_2 and MoS_2, both the intensity and central maxima remain consistent across the entire flake as seen at the middle row of **Fig. 5.5**. For the HS, the PL emission peak initially remains constant at 650 nm, corresponding to WS_2. At the interface, the PL emission exhibits two peaks, associated with both WS_2 and MoS_2. Beyond the interface, the emission peak shifts to 675 nm, attributed to MoS_2, and persists until the second interface, where it finally returns to 650 nm, associated again with WS_2, as shown in **Fig. 5.5**. This periodic shift of the PL emission peak associated with WS_2 and MoS_2 certainly confirms the in-situ CVD

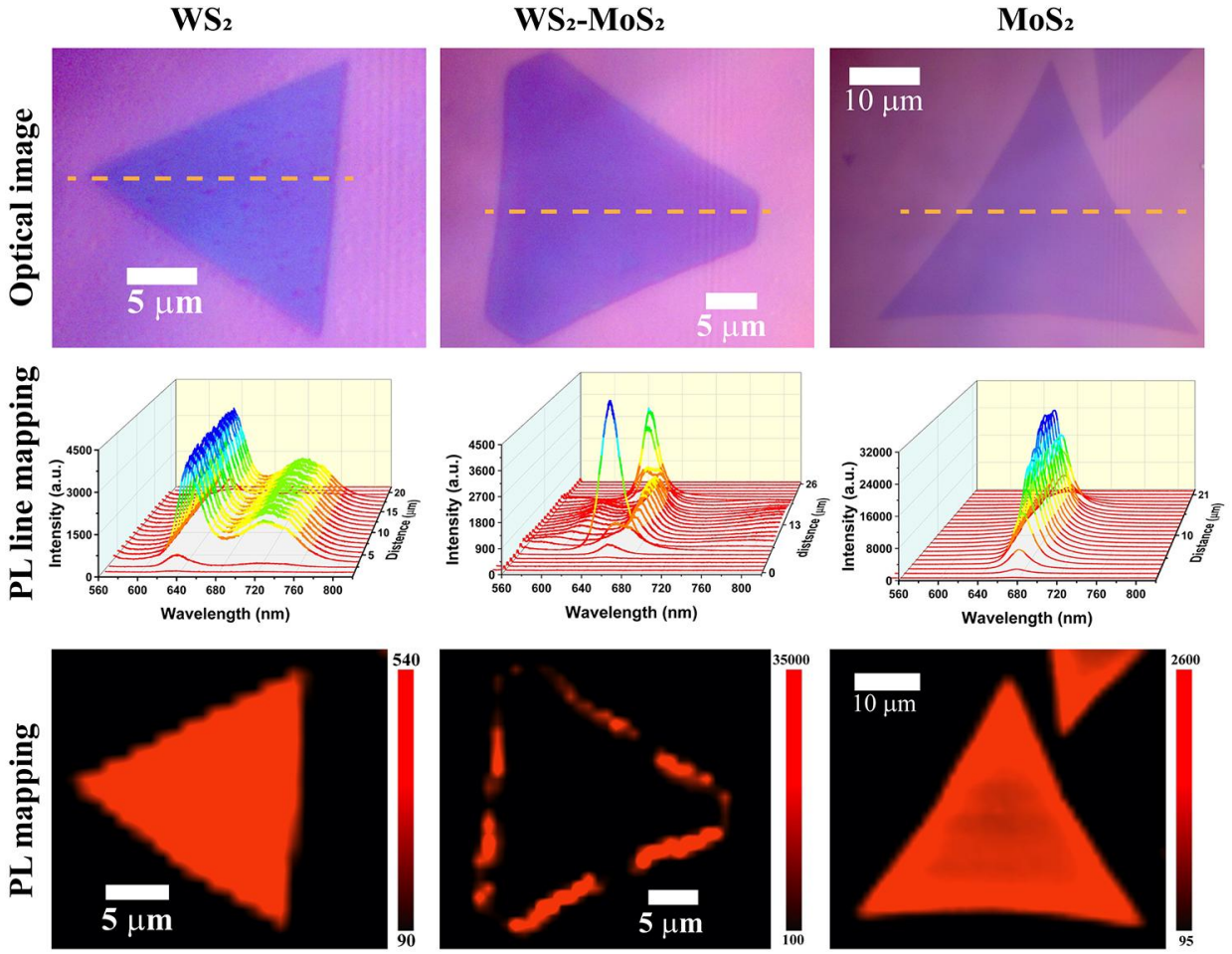

Figure 5.5: Spatial and linear PL mapping for intrinsic WS_2, intrinsic MoS_2, and spectra of WS_2-MoS_2 lateral HS with a spatial gap of 1 μm; The top row represents the optical images corresponding to intrinsic WS_2, WS_2-MoS_2 lateral HS and intrinsic MoS_2 (from left to right). The middle row represents the linear PL mapping corresponding to the line shown in the first row. The bottom row corresponds to the spatial PL mapping of intrinsic WS_2, in-situ WS_2-MoS_2 lateral HS, and intrinsic MoS_2 (from left to right).

growth WS_2-MoS_2 lateral HS. In addition to the shift in the PL emission peak the intensity also changes across the interface being highest near the interfaces. Finally, the spatial PL mappings are displayed in the bottom row of **Fig. 5.5**. which also shows uniform intensity distribution throughout the flakes for intrinsic WS_2 and MoS_2 and the HS, the intensity being highest at the interfaces. This observation clearly confirms the formation of a lateral HS between MoS_2 and WS_2 during the single-step CVD growth. Additionally, Auger Electron Spectroscopy (AES), a highly effective, surface-sensitive technique, is utilized for quantitative elemental analysis and the in-situ

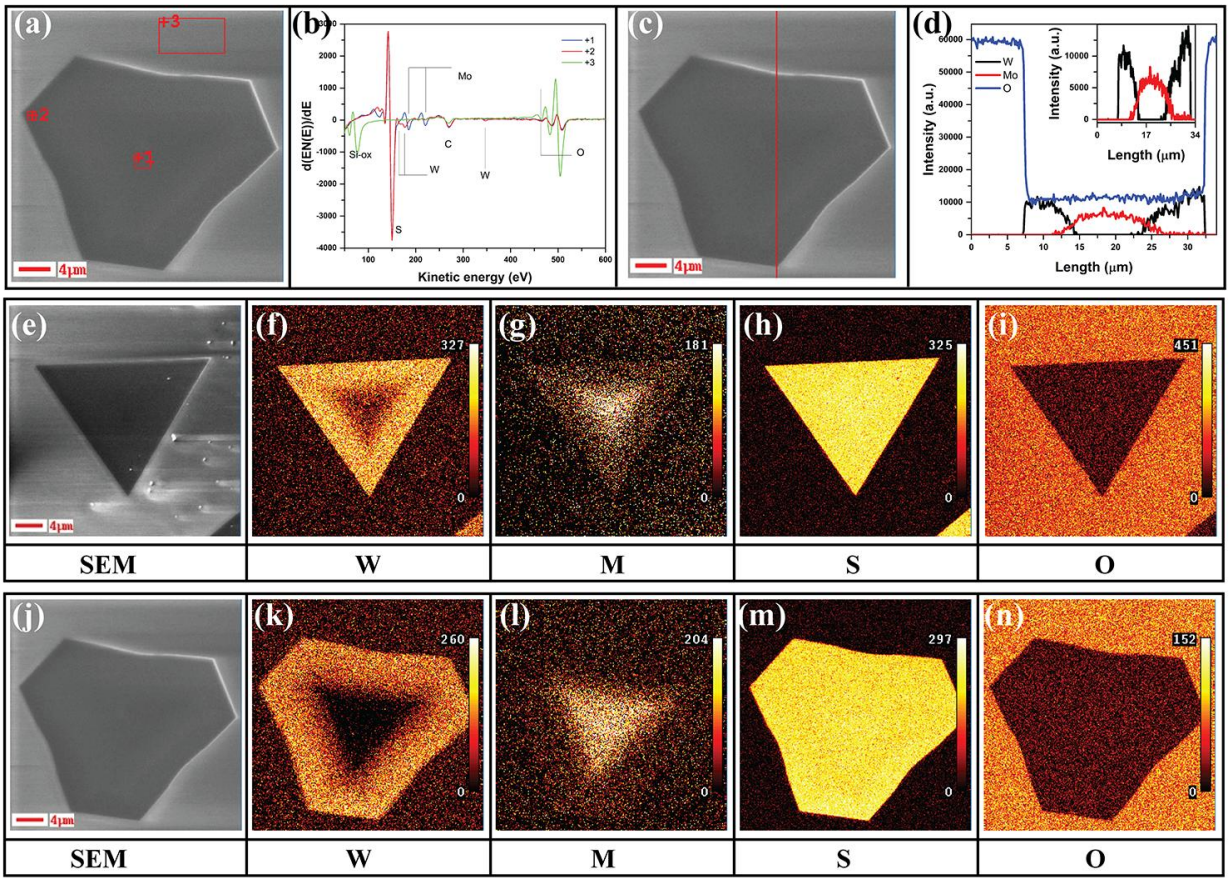

Figure 5.6: Auger Electron Spectroscopy analysis of the in-situ lateral HS (a) SEM image of a lateral HS flake; (b) First derivative of the Auger spectra from three different spots; (c) SEM image for linear Auger mapping; (d) Linear Auger spectral mapping across the lateral HS flake; (e) SEM image of HS flakes grown with 11:1 oxide ratio; (f) Spatial Auger mapping of tungsten; (g) Spatial Auger mapping of molybdenum; (h) Spatial Auger mapping of sulfur; (i) Spatial Auger mapping of oxygen; (j) SEM image of HS flakes grown with 9:3 oxide ratio; (k) Spatial Auger mapping of tungsten; (l) Spatial Auger mapping of molybdenum; (m) Spatial Auger mapping of sulfur; (n) Spatial Auger mapping of oxygen.

growth of lateral HSs[35]. AES leverages the Auger effect, where radiation-free transitions occur after ionizing an atoms inner electron levels, leading to the emission of Auger electrons[36]. By analyzing these emitted electrons, AES enables high-resolution mapping of elemental distributions within the top few atomic layers, offering exceptional chemical and spatial sensitivity at the surface[37]. The Auger spectra were analyzed in three ways: from distinct points, along a linear line across a heterostructure flake, and spatial surface mapping. **Fig. 5.6(a)** is the SEM image of a lateral heterostructure flake over which the Auger spectra were analyzed at three distinct points, as illustrated in the SEM image. The first derivative of the Auger spectra for these points is shown in **Fig. 5.6(b)**, clearly revealing the presence of molybdenum at the center of the flake (**point 1**) and tungsten at its edge (**point 2**) and oxygen outside the flake region (**point3**). The point analysis confirms the presence of tungsten at the edges, molybdenum at the center, and sulfur across the two points. This indicates that the edge region contains WS_2, and the middle part contain MoS_2, and there will be an interface among them, thus confirming the synthesis of WS_2-MoS_2 lateral heterostructure. Fig**. 5.5(d)** illustrates the linear Auger spectral intensity distribution along the line across the flakes indicated by the SEM image in Fig. 5.6(c). This highlights that tungsten intensity is highest at two edges, tapering to zero within a few μm, as expected. Conversely, the molybdenum signal peaks near the central region, as shown in the inset of **Fig. 5.6(d)** hence confirming two interfaces along a line through the HS consistent with the linear PL intensity distribution in **Fig. 5.5**. It is clear from the Aguer line scan that the interface is not sharp in nature but alloy diffusive interface. The spatial Auger mapping for two HSs flakes with varying WO_3:MoO_3 ratio (11:1 in **Fig. 5.6(e)** and 9:3 in **Fig. 5.6 (j)**) are displayed in **Fig. 5.6 (e-n)**. The mapping shows tungsten concentrated at the outer boundary, molybdenum in the central region, and sulfur distributed uniformly across the entire flake. For the low concentration of MoO_3 (*1 mg out of 12 mg of total oxides*), a higher proportion of flakes contain tungsten, as shown in **Fig. 5.6(f)**. Consequently, a lower concentration of molybdenum is observed at the center, as illustrated in **Fig. 5.6(g)**, with sulfur distributed uniformly throughout the flake, as expected and displayed in **Fig. 5.6(h)**. However, with the increasing fraction of the MoO_3 (*3 mg out of 12 mg of total oxides*), we can see a clear, distinct boundary between WS_2 and MoS_2 with increased MoS_2 fraction. **Fig. 5.6(k)** presents the spatial Auger mapping for tungsten, revealing its presence only in the outer regions of the flakes, corresponding to the FESEM image in **Fig. 5.6(j)**. Molybdenum, on the other hand, is detected solely in the central area, as shown in **Fig 5.6(l)**. Finally, sulfur was present

uniformly across the flake, and oxygen was absent only from the flake region, as displayed in **Fig. 5.6(m)** and **Fig. 5.6(n)**, respectively. This clearly confirms the successful synthesis of the WS_2-MoS_2 lateral HS through a single-step CVD process via adjusting the growth parameters. The same AES was used to estimate the thickness of the layer with the help of the O-KLL Auger peak. Since O is coming from the SiO_2/Si substrate beneath the grains, its signal is attenuated by the deposited layer. For the calculation, we use exponential approximation, and the thickness *t* can be represented mathematically via the equation $t = \lambda \cos(\varphi) \ln\left(\frac{I}{I_0}\right)$, where λ is the effective attenuation length for O-KLL electrons, φ is the emission angle (the angle between sample normal and analyzer axis), *I* is the intensity

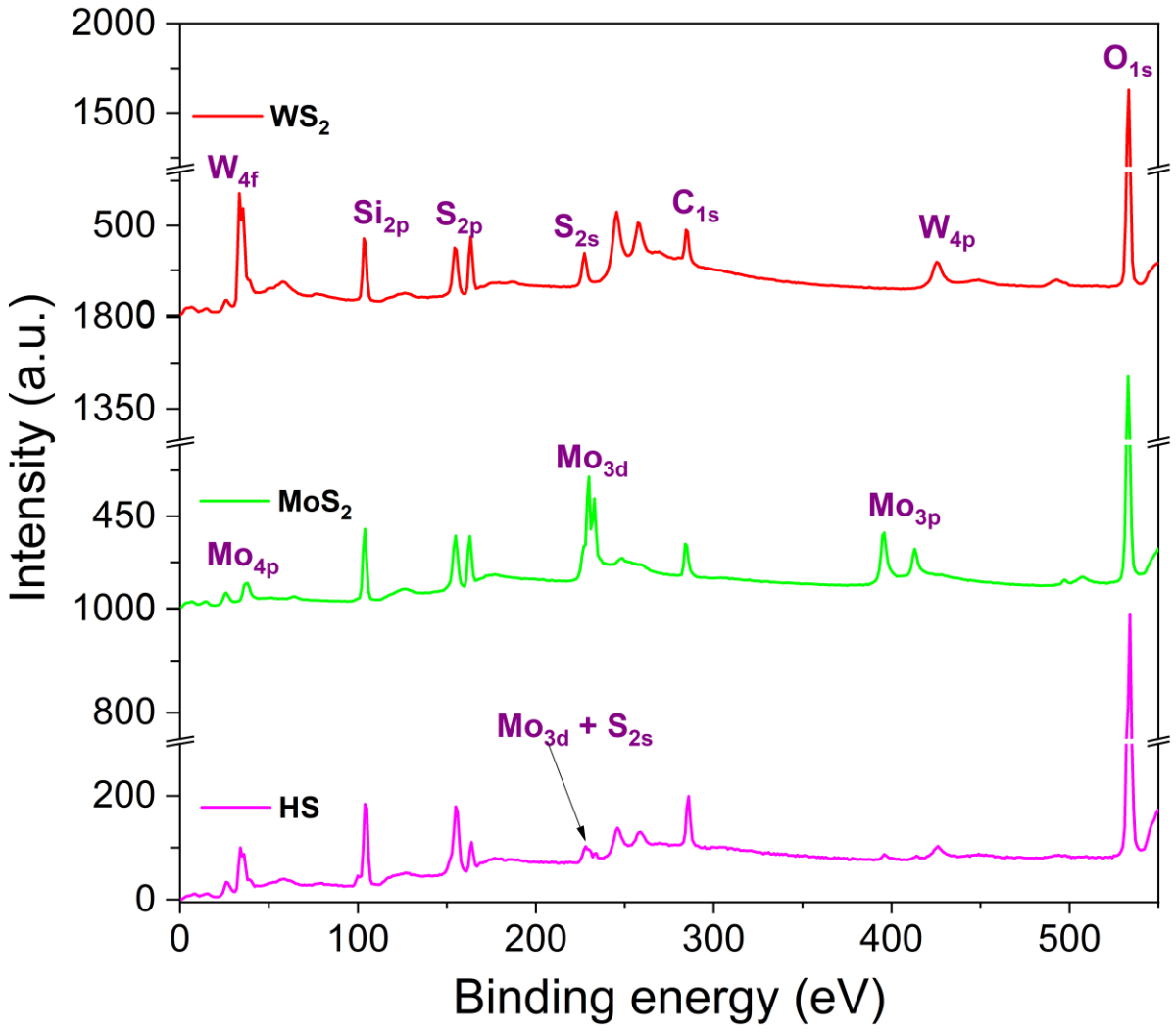

Figure 5.7: XPS survey spectrum for the intrinsic WS_2, MoS_2, and in-situ WS_2-MoS_2 lateral HS grown by CVD technique.

of attenuated O-KLL peak measured on the layer, and I_0 is the intensity of O-KLL peak on the uncovered substrate. We assume that O contribution from the adsorbed species on the surface of the grains is negligible and that they are rather covered with hydrocarbons showing up C-KLL peak. The calculated thickness using O-KLL suggests a bilayer of WS_2-MoS_2 HS with a thickness of 1.65 nm, matching well with the Raman analysis[18].

We further performed the XPS analysis to investigate the chemical composition and oxidation states of CVD-grown flakes. The survey spectra for the three samples are shown in **Fig. 5.7**. The WS_2 survey spectrum reveals the presence of W 4f and S 2p peaks, indicating the W^{4+} oxidation state of tungsten and the S^{2-} reduction state of sulfur, confirming the synthesis of WS_2 from WO_3 and sulfur precursors[18]. Similarly, the survey spectrum for intrinsic MoS_2 shows Mo 3d and S 2p peaks, which are characteristic of MoS_2 synthesis[19]. In the HS, both W4f and Mo3d peaks appear alongside the S 2p peak, signifying the formation of a WS_2-MoS_2 HS from the combined oxide precursors in the presence of sulfur. For further analysis, we examined the high-resolution XPS spectra of the main elements in each configuration, shown in **Fig. 5.8**, with all high-resolution peaks referenced to the C_{1s} peak at 284.8 eV. The S 2p spectra for each material, shown in **Fig. 5.8(a)**, display a prominent doublet with peaks at 164.1 eV and 162.9 eV, separated by 1.2 eV,

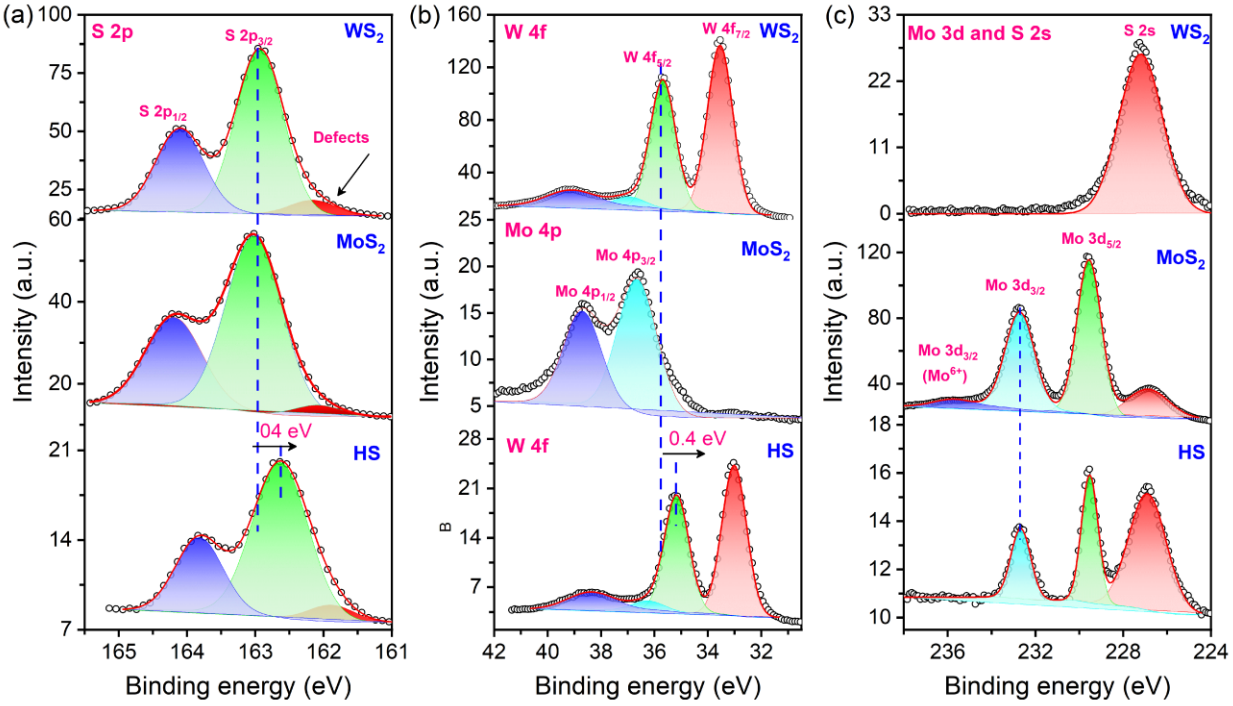

Figure 5.8: High-resolution XPS spectra for (a) S 2p; (b) W 4f; (c) Mo 3d.

corresponding to S $2p_{3/2}$ and S $2p_{1/2}$, respectively[18]. Additionally, there is a low-intensity peak at 162.1 eV, which is associated with defects and sulfur vacancies. The XPS spectra for S 2p match well with 2L-WS_2, as discussed in **section 3.3.1 of chapter 3.** Notably, in the HS, the S2p spectra exhibit a redshift of 0.4 eV, attributed to a shift of the Fermi energy by 0.4 eV toward the valence band. The high-resolution spectra for W 4f show two strong peaks at 33.5 and 35.6 eV separated by 2.1 eV, as displayed in **Fig. 5.8(b)** associated with W^{4+} oxidation state of tungsten corresponding to W 4f7/2 and 4f5/2 respectively[38] as discussed previously in **section 3.3.1 of chapter 3**. For molybdenum, the two characteristic high-intensity peaks at 229.5 eV and 232.6 correspond to Mo $3d_{5/2}$ and Mo $3d_{3/2}$, respectively, and are associated with the Mo^{4+} oxidation state[39]. This further confirms the synthesis of the semiconducting 2H-phase of MoS_2. Other than these two peaks, there are two low-intensity peaks. The low energy peak at 226.8 eV corresponds to S 2s, and the high energy peak at 235.7 eV is associated with Mo^{6+} oxidation state[40] as discussed in **section 4.3.2 of chapter 4**. For the HS, we have observed all the characteristics XPS peaks associated with the W^{4+} and Mo^{4+} oxidation states along with the S^{2-} reduction state. Hence, the XPS analysis confirmed the synthesis of the semiconducting 2H phase of WS_2-MoS_2 lateral HS. Furthermore, high-angle annular dark-field scanning transmission electron microscopy (HAADF-STEM) images for the CVD grown 2L-WS_2 and 1-2L MoS_2 are displayed in **Fig. 5.9.** The HAADF-STEM image for 2L-WS_2 shown in **Fig. 5.9(a)** shows an array of atomic columns in a hexagonal pattern of equal intensity (AA' stacking) within this scale thus confirming the excellent crystalline quality of the samples without any vacancy or defects sites. Similarly, for MoS_2, we have a very good crystalline quality, as can be seen from the HAADF-STEM image shown in **Fig. 5.9(b**). Nonetheless, according to the corresponding line profile (Fig. 6(d)), the second layer is not fully developed within the inspected area, and the samples might be characterized as 1-2L MoS_2 with AA order stacking. However, we were not able to observe any distinct boundary between WS_2 and MoS_2 in the HAADF-STEM image of the HS region, as displayed in **Fig. 5.9(c)**. This is due to the diffused interface between 2L-WS_2 and 2L-MoS_2 over a region larger than the much smaller region imaged in STEM. This is consistent with the AES line scan which showed a gradual change in the intensity distribution for W and Mo at the interface region, as displayed in **Fig. 5.6(d).** Thus, we have a diffused interface at the junction of WS_2-MoS_2 grown lateral HS. To detect the W-Mo alloyed HS structure, we plotted the atomic intensity distribution profile along the metallic columns, see the dashed cyan rectangle in **Fig. 5.9(c)** and the corresponding HS line

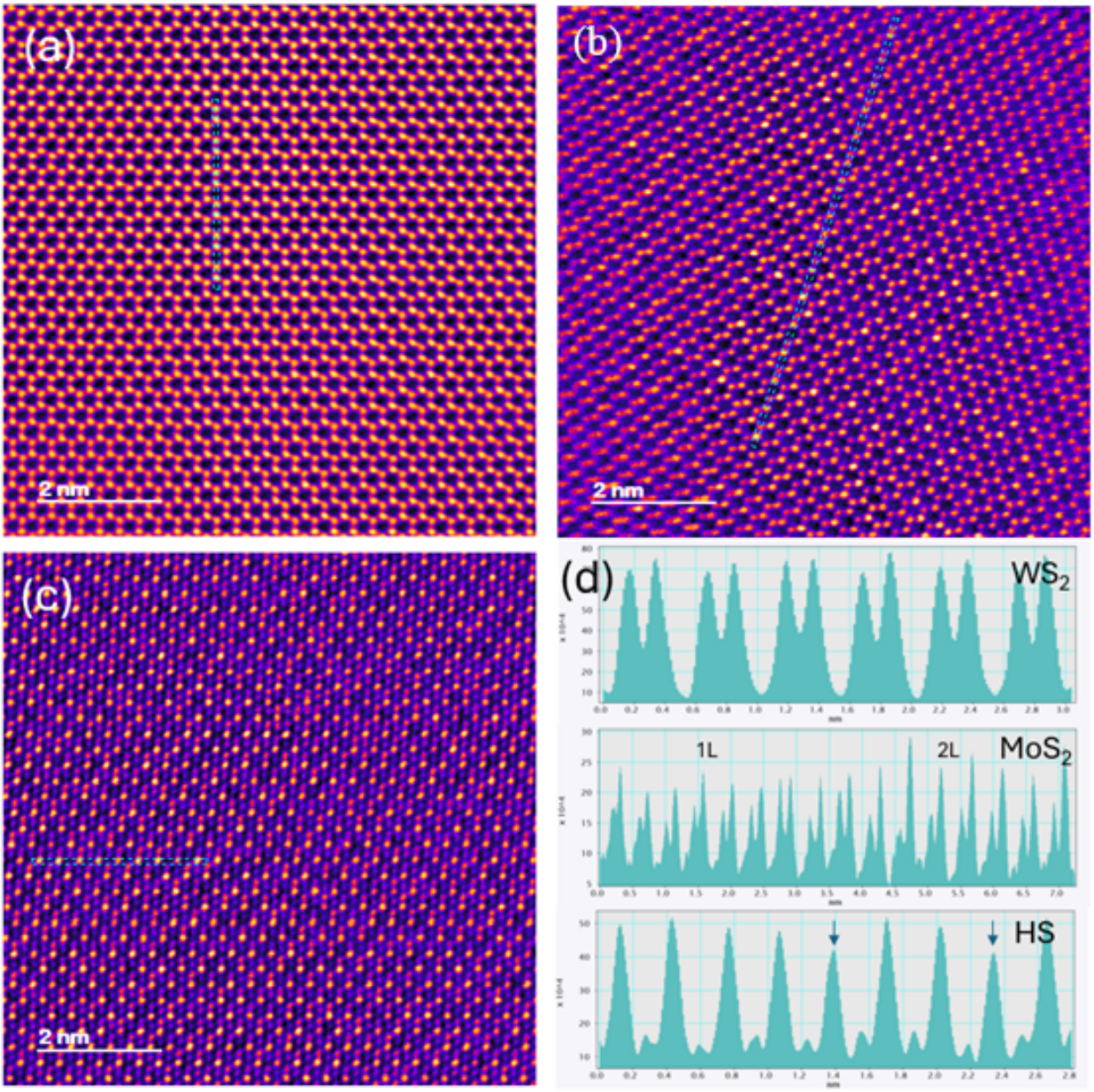

Figure 5.9: Atomic resolution HAADF-STEM images of (a) pure WS_2, (b) pure MoS_2, (c) WS_2-MoS_2 lateral HS. All images are ABSF filtered. (d) Corresponding atomic intensity profiles.

profle in **Fig. 5.9(d).** Here the intensity drop clearly suggests Mo alloying within 2L-WS_2 (marked as black arrows). Therefore, the interface region contains $W_{(1-x)}Mo_xS_2$ alloy. In addition, the pattern of the atomic columns confirms a two-layer 3R phase structure of the alloy in the HS.

5.3.2 Device Fabrication and Electrical Performance Comparison

We fabricated backgated FETs using CVD-grown intrinsic WS_2, MoS_2, and their lateral HS to analyze the electrical performance. For the FETs we have used the ALD deposited Al_2O_3 as gate dielectric as described in **section 4.2.1 of chapter 4.** The selection of a thin, high-k gate dielectric with an effective oxide thickness (EOT) of 22 nm, in contrast to the conventionally used 300 nm SiO_2, was made to enhance gate electrostatics. Additionally, the Pt/TiN/p^{++}-Si stack serves as the gate electrode for the devices. A schematic diagram and optical image of WS_2-MoS_2 HS-based

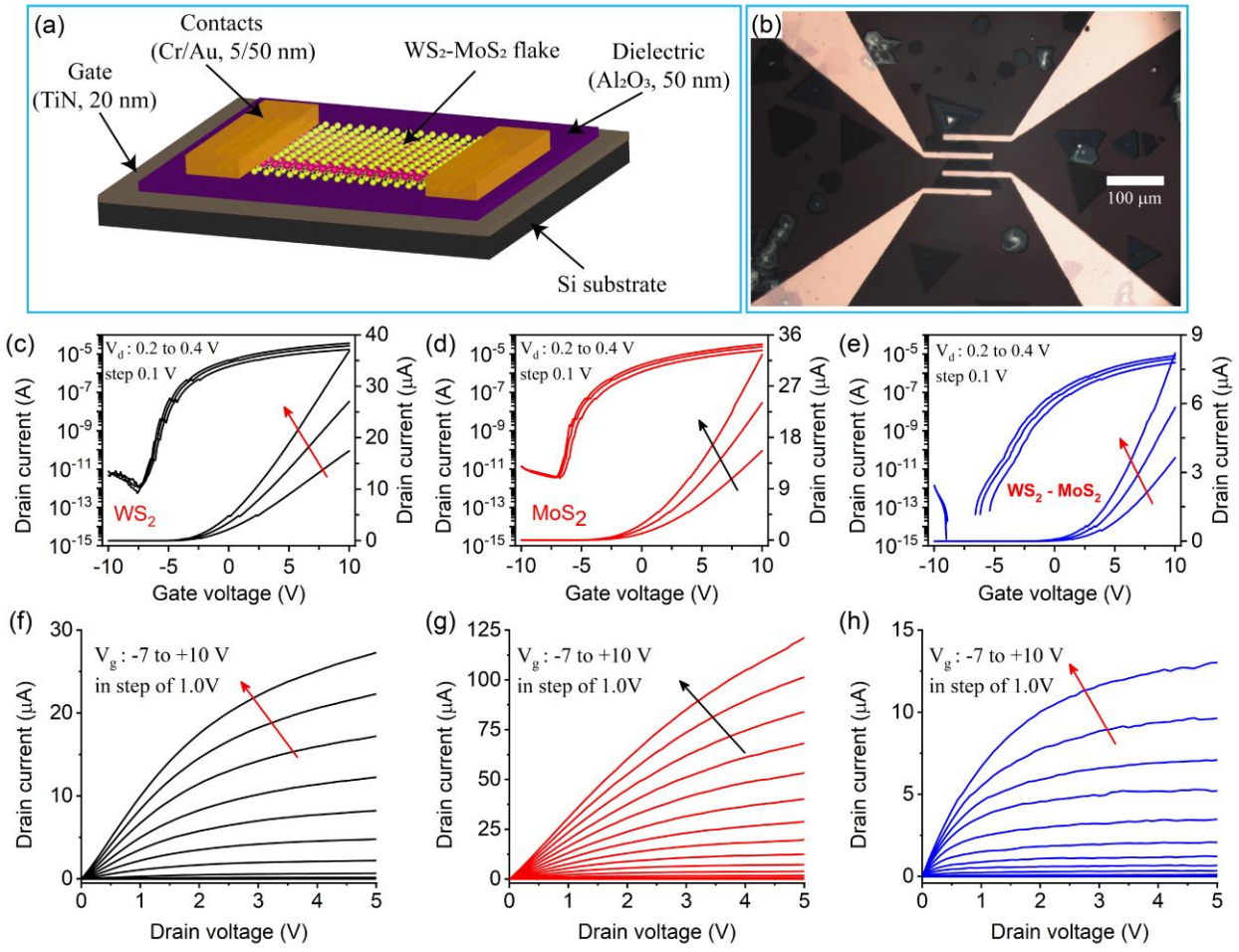

Figure 5.10: (a) Schematic representation of device configuration; (b) Optical image of the lateral HS device: transfer characteristics of the FETs devices with (c) intrinsic WS_2; (d) intrinsic MoS_2; (e) in-situ WS_2-MoS_2 laterals HS: output characteristics of the FET devices with (f) intrinsic WS_2; (g) intrinsic MoS_2; (h) in-situ WS_2-MoS_2 laterals HS.

FET are shown in **Fig. 5.10(a)** and **Fig. 5.10(b),** respectively. The transfer and output characteristics of intrinsic WS_2, MoS_2, and their lateral HSs are displayed in **Fig. 5.10.** From the transfer characteristics in **Fig. 5.10(c-e)** it is quite clear that all the channel materials have n-type nature as the channel remains off under negative gate bias voltage and turns on at positive gate bias voltages due to the electron accumulation in the semiconducting channel under positive gate voltage and electron depletion at negative gate voltage. These indicate that the average off-state current for WS_2 and MoS_2 are in the order of around 10^{-11} A, whereas the HS channel is completely

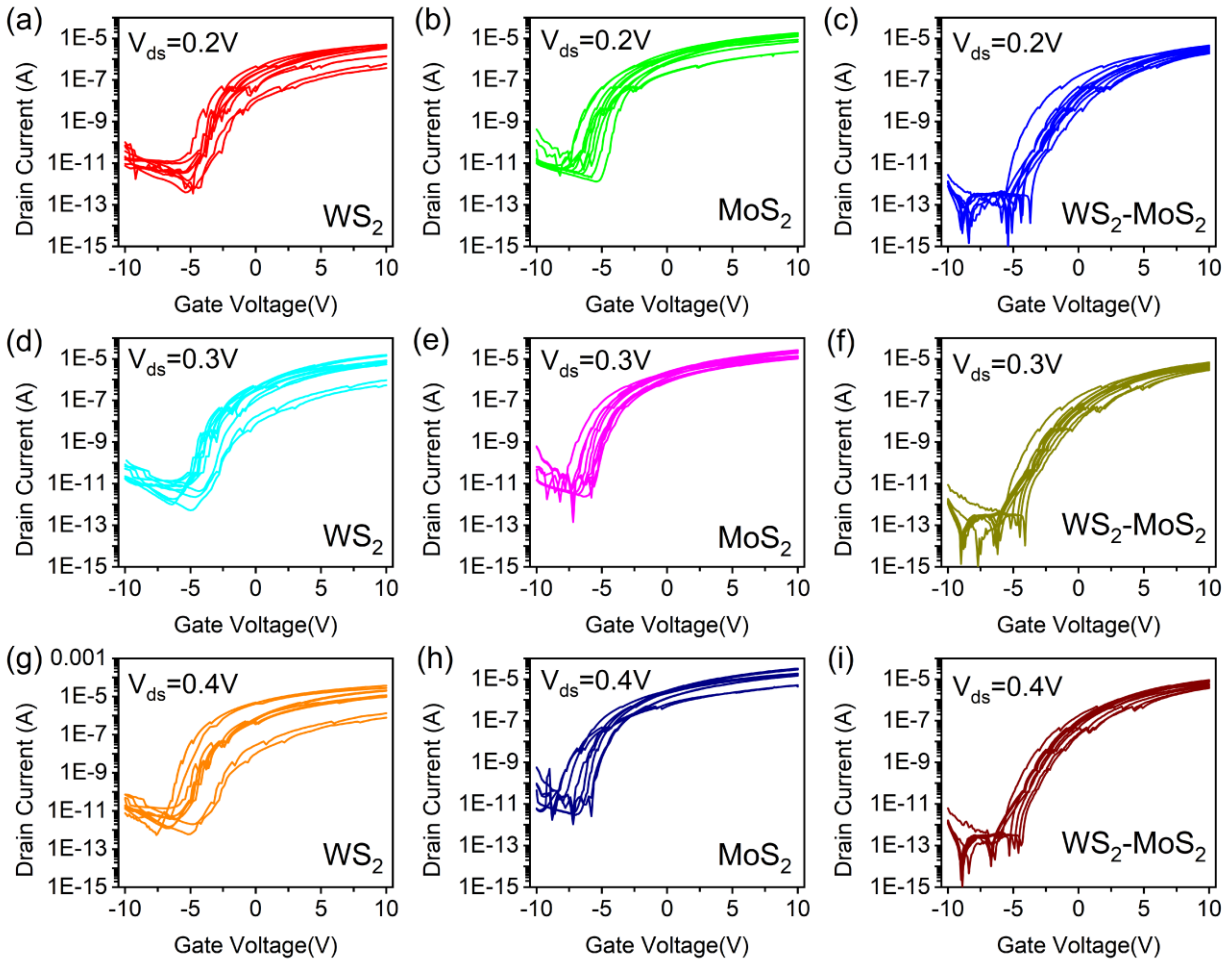

Figure 5.11: Transfer characteristics for ten different FETs under various drain bias conditions: under 0.2V drain bias: (a) intrinsic WS_2; (b) intrinsic MoS_2; (c) WS_2-MoS_2 laterals HS: under 0.3V drain bias: (d) intrinsic WS_2; (e) intrinsic MoS_2; (f) in-situ WS_2-MoS_2 laterals HS: under 0.4V drain bias: (g) intrinsic WS_2; (h) intrinsic MoS_2; (i) WS_2-MoS_2 laterals HS.

blocked and current flows in opposite directions, leading to missing points in the log plot, in the absolute scale it is reduced by two orders of magnitude to around 10^{-13} A. whereas the on-state currents remain almost in the same order for all three configurations of around 10^{-5} A. Thus, for the heterostructure device it results in orders of magnitude increment in the on-off ratio as compared to the individuals. The output characteristics of these devices are displayed in **Fig. 5.10(f-h)**, which shows the devices are in depletion modes under negative gate bias and active modes in positive gate bias. The drain current with increasing gate voltage toward a saturation value as anticipated. Interestingly, the drain saturation voltage for the HS reduces significantly, thus signify its applications for low-power devices. Further, we have calculated the on-off ratio, threshold voltage (V_{th}), electron mobility, and sub-threshold swings (SS) for intrinsic WS_2, MoS_2, and WS_2-MoS_2 lateral HS configurations over ten devices as illustrated in **Fig. 5.11**. Careful analysis of these device parameters indicates a significant improvement in the device performance for lateral HSs in comparison to intrinsic WS_2 and MoS_2-based FETs.

On-off ratio:

The on-off ratio in FETs is an important parameter that indicates the range of current levels between the on-state and the off-state. A high on-off current ratio is effective for fast switching and low power consumption in electrical devices. This is mathematically defined as $\frac{I_{on}}{I_{off}}$; Where I_{on} is the on-stage current and I_{off} is the current corresponding to off-stage. The transfer characteristics for intrinsic WS_2, MoS_2, and WS_2-MoS_2 lateral HS-based FETs (10 devices each) with Cr/Au contacts, with varying drain voltage, are presented in **Fig. 5.11**. The on-off ratio was determined using the average off-state current over 20 data points and the maximum on-state

Table 5.1: The average value of the on-off ratio with drain bias voltage and channel materials.

2D materials	On-off Ratio		
	V_{ds} = 0.2 V	V_{ds} = 0.3 V	V_{ds} = 0.4 V
WS_2	$(1.3\pm0.4) \times 10^6$	$(1.4\pm0.4) \times 10^6$	$(1.5\pm0.6) \times 10^6$
MoS_2	$(5.5\pm1) \times 10^5$	$(7.6\pm1.5) \times 10^5$	$(1.2\pm0.5) \times 10^6$
WS_2-MoS_2	$(1.5\pm0.5) \times 10^7$	$(5.6\pm0.5) \times 10^7$	$(6.5\pm0.6) \times 10^7$

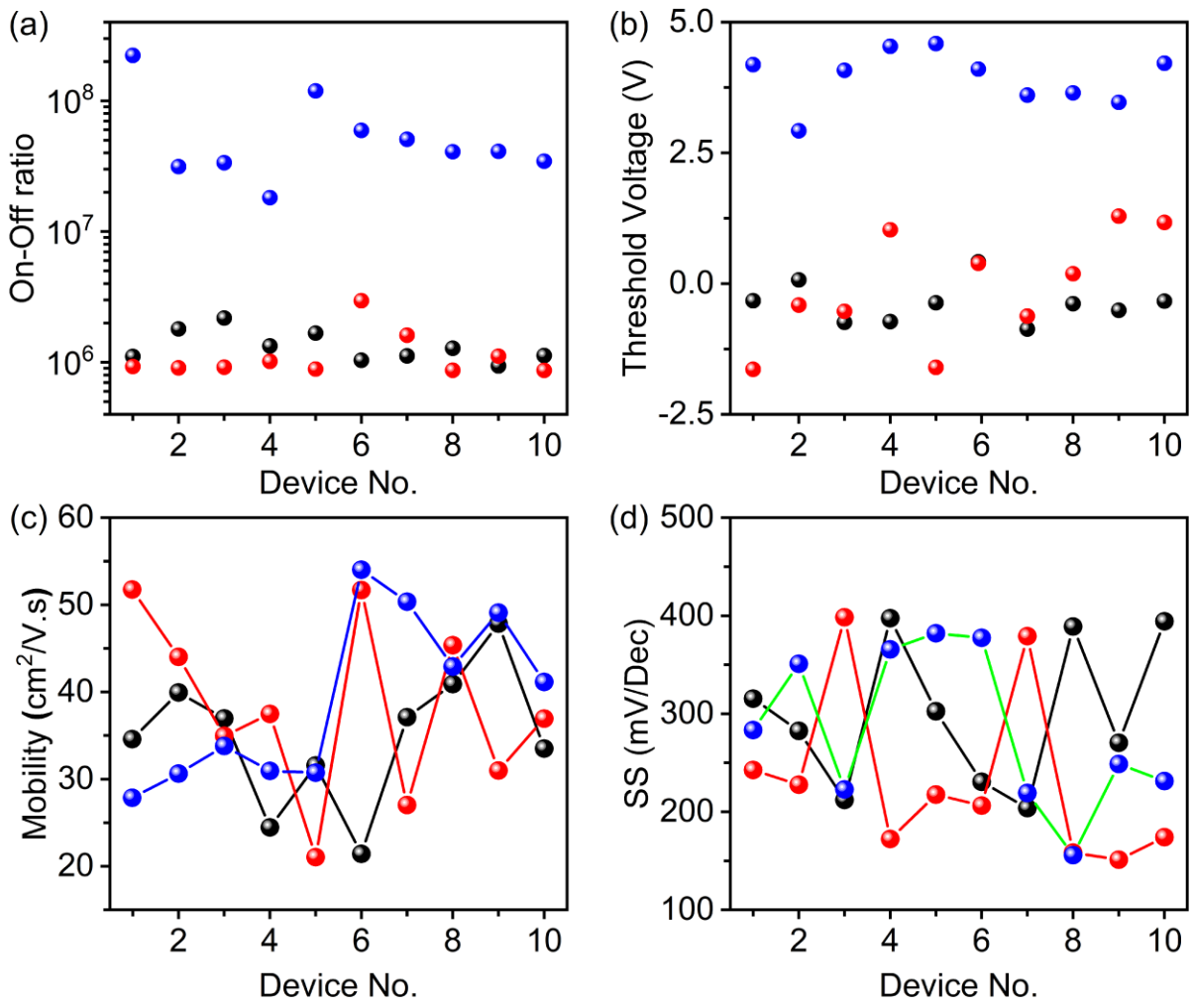

Figure 5.12: Statistical variation of device parameters for intrinsic WS_2 (black), intrinsic MoS_2(green), in-situ WS_2-MoS_2 lateral HS (blue): (a) Device on-off ratio; (b) Threshold voltage; (c) electron mobility; (d) sub-threshold swing

current at a gate bias of 10V. The detailed calculation shows the on-off ratio remains in the order .of 10^6 for the intrinsic WS_2 and MoS_2 devices with slight variations in the drain bias voltage. In contrast for the HS, the on-off ratio increases by an order of magnitude. This enhanced on-off ratio originated from the lower off-state current in the HS case with minimal reduction in the on-state current. The variation of the on-off ratio over ten devices for the three device configurations is displayed in **Fig. 5.12(a),** which clearly shows the higher on-off ratio for the HS.

Threshold voltage:

The threshold voltage is the minimum voltage required to turn on the semiconducting channel of a FET. Generally, there are mainly two different methods to measure threshold voltages: one is linear extrapolation ($V_{t, lin}$), and the other one is tangent at the peak of transconductance ($V_{t, gm}$). For $V_{t, lin}$, the threshold voltage is obtained by calculating the intercept on the x-axis, corresponding to the linear extrapolation of the transfer characteristics. In contrast, $V_{t, gm}$ is derived from the tangent to the transfer characteristics when the transconductance reaches its maximum value. The drain bias voltage strongly modulates the threshold voltage. The variation of threshold voltages for intrinsic WS_2, MoS_2, and WS_2-MoS_2 lateral HS-based FETs are displayed in **Fig. 5.12(b)**. The average values for the threshold voltage under the three different drain bias voltages are tabulated in **Table 5.2.**

The threshold voltage strongly depends upon the work function of the contact material, properties of the gate dielectric and the intrinsic doping of the semiconducting channel material[4]. Since the gate dielectric material is identical for all three devices, the variation of threshold voltage will be

intrinsic material property. The threshold voltage of WS_2 FETs was observed to be more positive compared to MoS_2 FETs, likely due to the higher intrinsic n-type doping in MoS_2, which may result from the specific impurities or nature of MoS_2. For the HS, the threshold voltage is much materials.more positive compared to individual counterparts, meaning it has n-type properties. As discussed in **section 4.3.3 of chapter 4**, the variation in threshold voltage (σV_t) serves as a more reliable benchmark for assessing emerging devices fabricated using new materials. While the mean threshold voltage is primarily determined by factors such as the gate metals work function and any unintentional or intrinsic doping in the 2D material, both V_t and σV_t are also influenced by the thickness of the gate oxide. The variation of threshold voltage was calculated using $S\sigma V_t =$

Table 5.2: The average value of the threshold voltage with drain bias voltage and channel

2D materials	V_{ds} = 0.2 V		V_{ds} = 0.3 V		V_{ds} = 0.4 V	
	V_t (V)	σV_t (V)	V_t (V)	$S\sigma_{V_t}$(mV)	V_t (V)	$S\sigma_{V_t}$(mV)
WS_2	-0.3±0.2	6.4	-0.4±0.3	9.6	-0.5±0.4	12.8
MoS_2	0.5±0.6	19	0.5±0.8	26	-0.05±1.0	31
WS_2-MoS_2	3.9±0.5	16	4.0±0.5	16	4.0±0.7	22

$\sigma V_t \times \frac{SEOT}{EOT}$; where SEOT is the scale effective oxide thickness and EOT is the effective oxide thickness[41]. For our case the high-k Al_2O_3 gate dielectric with an effective oxide thickness (EOT) of 22 nm, in contrast to the conventionally used 300 nm SiO_2, was made to enhance gate electrostatics. The variation of $S\sigma_{V_t}$ for all three configurations is tabulated in **Table 5.2**. We have obtained the $S\sigma V_t$ for WS_2 in the range of 6.4 mV to 12.8 mV and for MoS_2, which increases to 19-38 mV, and finally, for the HS, it ranges in between the individual material of 16-22 mV, assuming SEOT = 0.9 nm.

Electric field effect mobility:

One of the most important parameters for FET-based devices is mobility, which measures how easily the carriers can move through the material in the presence of an external electric field. Mobility is an intrinsic property of a material that is highly influenced by the gate dielectric, contact resistance, contact materials, channel thickness, confinement, HS formation, and material interfaces. We have calculated the mobility by using the peak transconductance value using the formula[4].

$$\mu = \frac{dI_{ds}}{dV_{gs}} \times \frac{L}{W \times C_i \times V_{ds}} \qquad (1)$$

where L is the channel length, W is the channel width, and C_i is the gate capacitance per unit area. The variations of electron mobility for intrinsic WS_2, MoS_2, and the lateral HS-based FETs are shown in **Fig. 5.12(c)**. There is not much variation in the electron mobility with the channel materials. We have calculated the electron mobility corresponding to 0.3V drain bias voltage, which reveals similar values for these three channel materials. The electron mobility for intrinsic WS_2 and MoS_2 was found to be 34.8 ± 7.6 $cm^2/(V.s)$ and 38.1 ± 9.8 $cm^2/(V.s)$ respectively. For the in-situ lateral HS, the electron mobility slightly improves to 39.1 ± 9.4 cm2/(V.s) but remains in the same order.

Subthreshold Swings:

The subthreshold swing (SS) is one of the essential parameters in FETs that measure how the transistor switches from the off-state to the on-state. It indicates how much gate voltage is required to increase the drain current by one order of magnitude when the transistor operates in the

subthreshold region. A smaller SS implies better-switching characteristics, which plays a crucial role for low-power and high-speed devices and is mathematically defined by the formula[4]

$$ss = \ln(10) \times \frac{dV_g}{d(\ln(I_d))}$$

$$= \ln(10) \times \frac{mk_BT}{q}\ ; m = \left(1 + \frac{C_s}{C_{ox}} + \frac{C_T}{C_{ox}}\right); C_T = qD_T \qquad (2)$$

Here, k_B is the Boltzmann constant, T is the temperature, q is the electronic charge, m is the body factor, C_S is the semiconductor capacitance, C_{IT} is the interface trap capacitance, C_{OX} is the oxide capacitance, and D_{IT} is the interface trap density. The variation of SS for intrinsic WS_2, MoS_2 and the in-situ lateral HS FETs is displayed in **Fig. 5.12(d)**. The WS_2 and MoS_2 FETs have median SS values of 299 ± 74 mV/dec and 234 ± 86 meV, respectively. For the in-situ lateral HS, it remains in the similar range of 284 ± 80 meV. The SS is directly related to the semiconducting channel capacitance and defect capacitance as observed from the above equations, but for fully ultrathin body FETs, $C_S = 0$. Thus, for an ultraclean interface and defect free surface contact-semiconductor interface, $C_T \ll C_{ox}$, ensuring that m ~ 1 and hence SS = 60 mV/dec. Clearly, in our FETs, the SS values are manyfold higher than the ideal value of 60 mV/dec, indicating the presence of interface traps at the channel material with dielectric and contact interface. We have calculated the defect density using the above formula assuming $C_S = 0$, thus

$$D_T = \frac{C_{ox}}{q} \times \left(\frac{SS \times q}{k_BT \times \ln(10)} - 1\right)$$

Using the above formula, we have calculated the interface trap/defect densities for 1L-MoS_2 and its variations with contact materials. The median values for the trap/defect densities were found be in the order of 10^{12} /(eV.cm^2).

Output variations:

We have plotted the output characteristics for all the device configurations with nine devices each. The statistical output variation with devices for intrinsic WS_2, MoS_2, and in-situ WS_2-MoS_2 lateral HS are displayed in Fig. 5.13, 5.14, and 5.15, respectively. The output plot clearly shows that the drain saturation voltage was reduced significantly for the HS. Thus, the lateral HS shows much better device characteristics for optoelectronic applications.

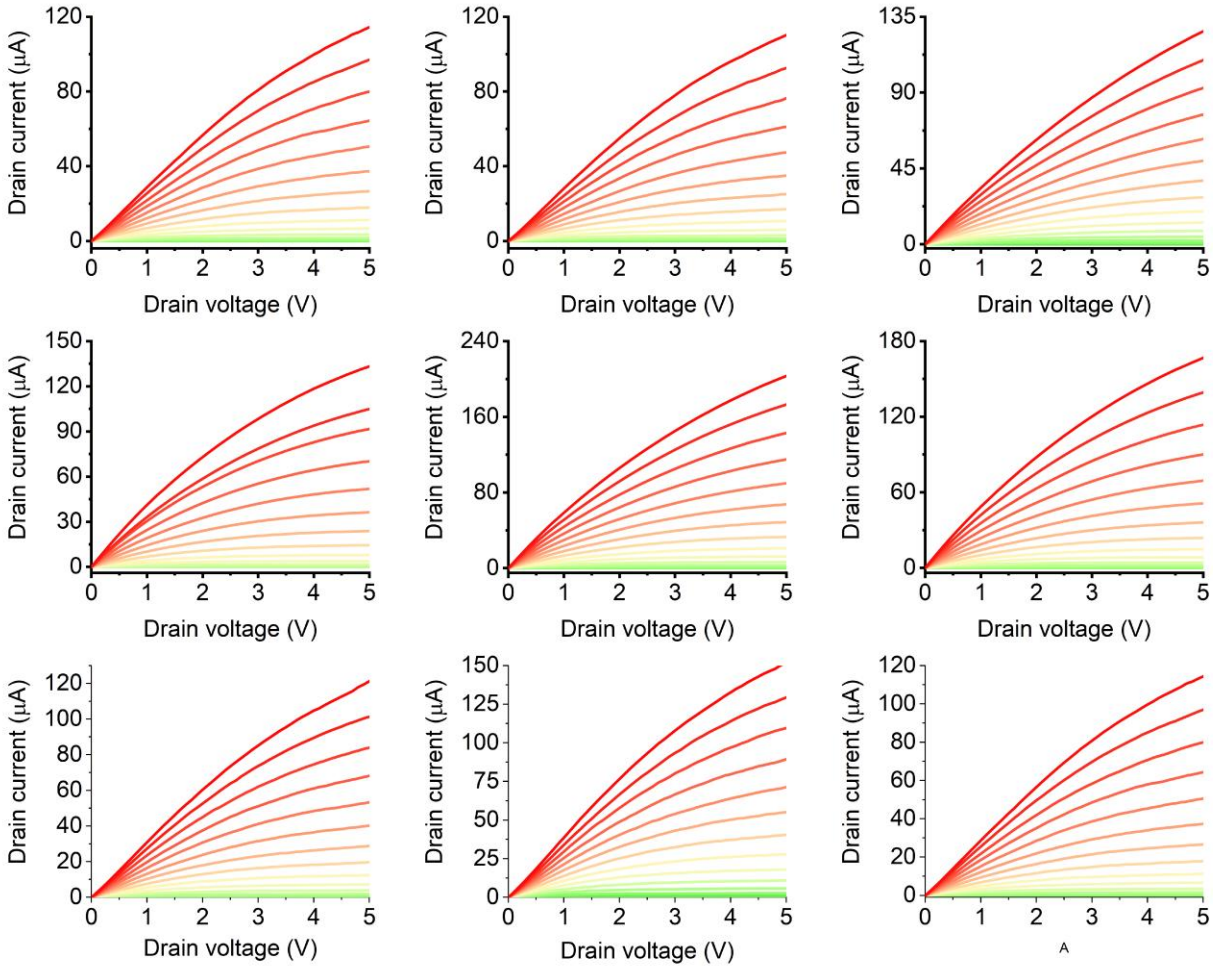

Figure 5.13: Statistical variation of device output characteristics for intrinsic WS_2.

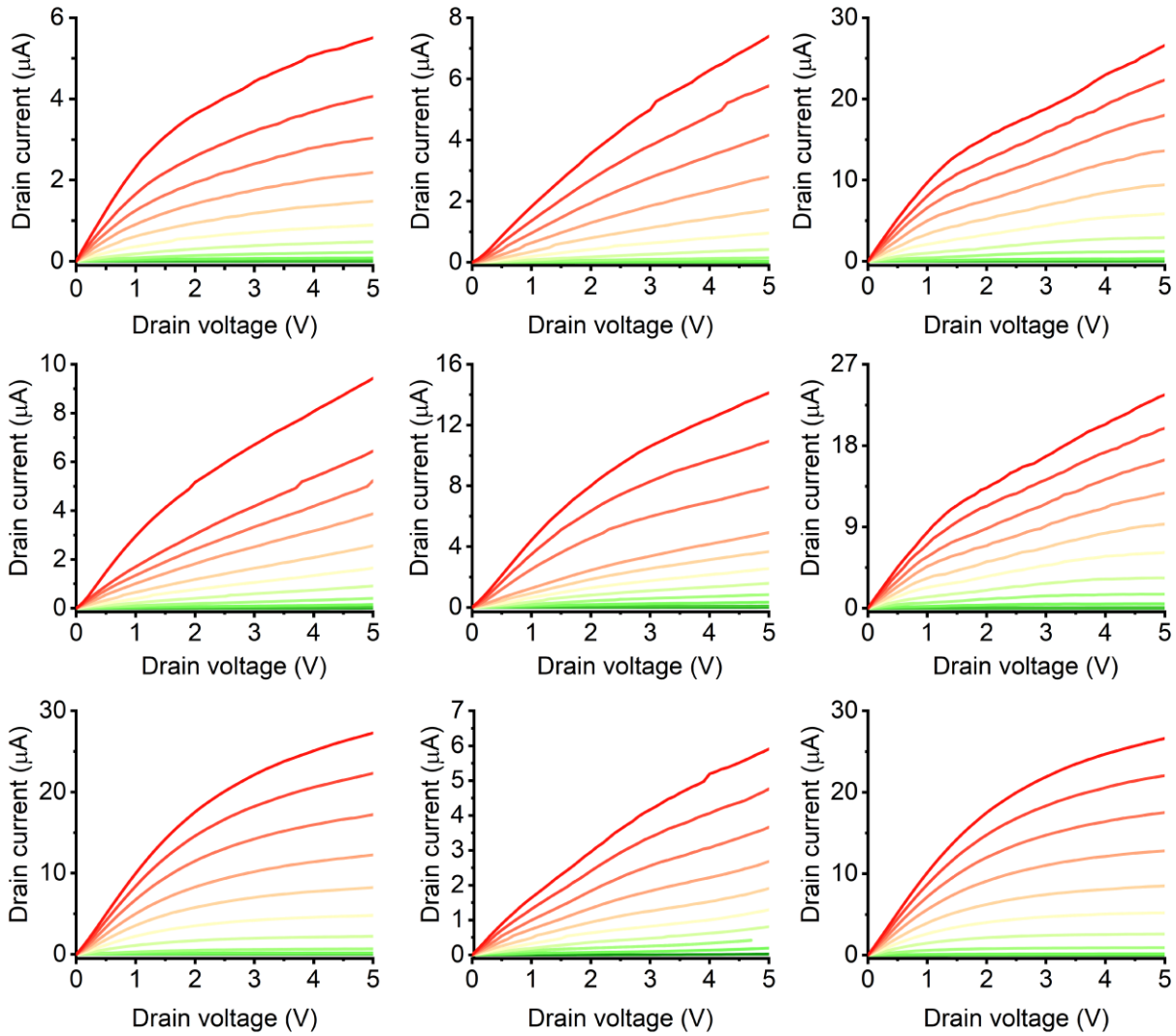

Figure 5.14: Statistical variation of device output characteristics for intrinsic MoS_2.

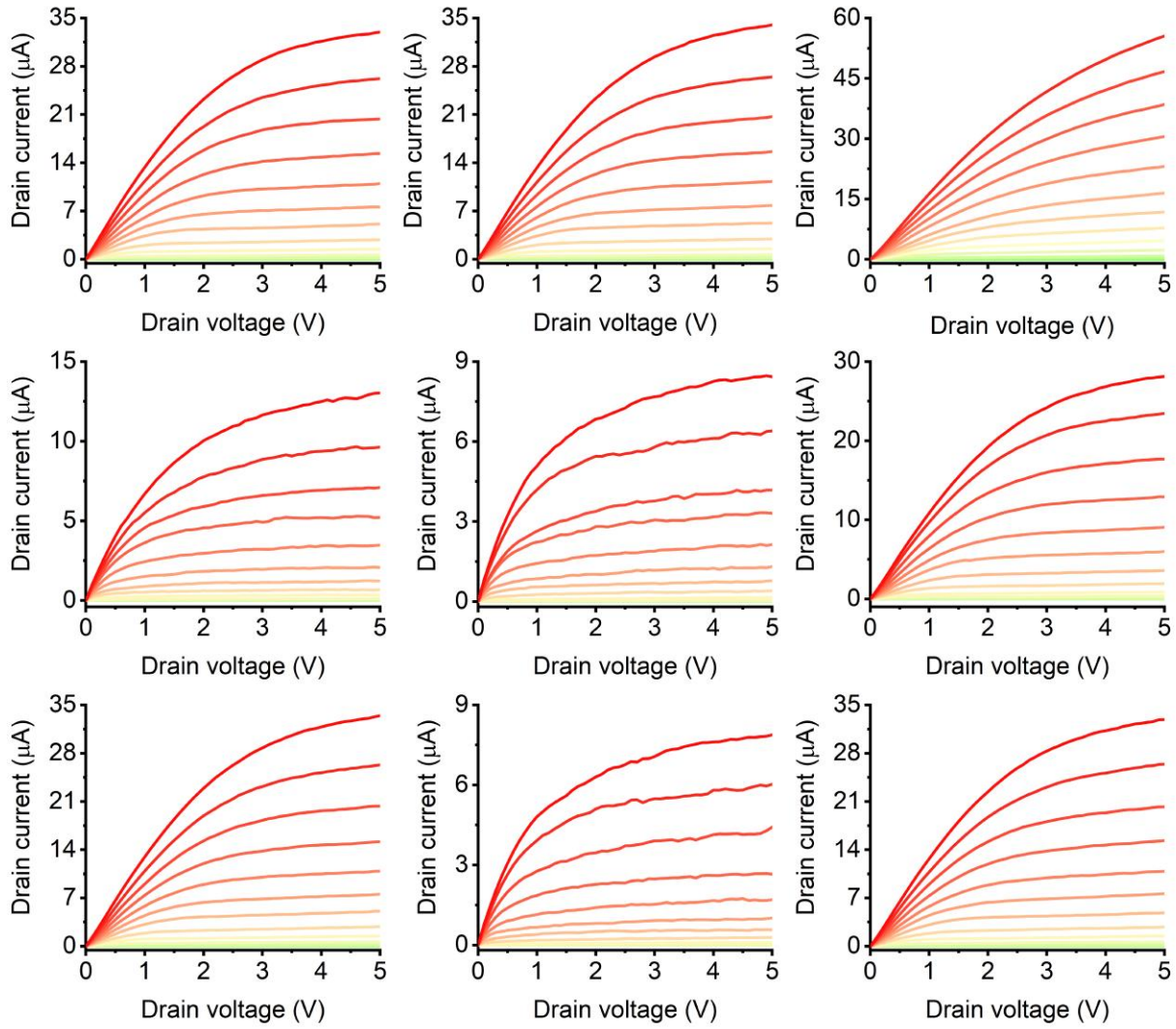

Figure 5.15: Statistical variation of device output characteristics for in-situ WS_2-MoS_2 lateral HS.

5.4 Conclusions

This chapter presents a novel single-step in-situ method for the growth of WS_2-MoS_2 lateral HSs using a CVD process. The proposed approach offers exceptional control over the growth process by fine-tuning the growth parameters. Characterization techniques such as spatial Raman and Auger mapping confirm the successful in-situ growth of the HS. Notably, the interface exhibits remarkable PL enhancement properties. Atomic-resolution HAADF-STEM imaging reveals a defect-free, high-quality growth achieved through the CVD technique. The in-situ synthesis results in an ultra-clean interface, enabling outstanding optoelectronic performance in FET applications. The lateral HS significantly reduces the off-state current by about two orders of magnitude while

maintaining nearly the same on-state current, leading to a tenfold improvement in the on/off current ratio. Furthermore, the HS exhibits a marked reduction in drain saturation voltage, making it a promising candidate for next-generation low-power electronic applications. These findings demonstrate an efficient, reduced-step synthesis of TMD HSs with enhanced optoelectronic properties, positioning them as suitable candidates for advanced optoelectronic and electronic applications.

References

(1) Mueller, T.; Malic, E. Exciton Physics and Device Application of Two-Dimensional Transition Metal Dichalcogenide Semiconductors. *Npj 2D Mater. Appl.* 2018, *2* (1), 1–12. https://doi.org/10.1038/s41699-018-0074-2.

(2) Lin, Y.-C.; Torsi, R.; Younas, R.; Hinkle, C. L.; Rigosi, A. F.; Hill, H. M.; Zhang, K.; Huang, S.; Shuck, C. E.; Chen, C.; Lin, Y.-H.; Maldonado-Lopez, D.; Mendoza-Cortes, J. L.; Ferrier, J.; Kar, S.; Nayir, N.; Rajabpour, S.; van Duin, A. C. T.; Liu, X.; Jariwala, D.; Jiang, J.; Shi, J.; Mortelmans, W.; Jaramillo, R.; Lopes, J. M. J.; Engel-Herbert, R.; Trofe, A.; Ignatova, T.; Lee, S. H.; Mao, Z.; Damian, L.; Wang, Y.; Steves, M. A.; Knappenberger, K. L. Jr.; Wang, Z.; Law, S.; Bepete, G.; Zhou, D.; Lin, J.-X.; Scheurer, M. S.; Li, J.; Wang, P.; Yu, G.; Wu, S.; Akinwande, D.; Redwing, J. M.; Terrones, M.; Robinson, J. A. Recent Advances in 2D Material Theory, Synthesis, Properties, and Applications. *ACS Nano* 2023, *17* (11), 9694–9747. https://doi.org/10.1021/acsnano.2c12759.

(3) Manzeli, S.; Ovchinnikov, D.; Pasquier, D.; Yazyev, O. V.; Kis, A. 2D Transition Metal Dichalcogenides. *Nat. Rev. Mater.* 2017, *2* (8), 1–15. https://doi.org/10.1038/natrevmats.2017.33.

(4) Sebastian, A.; Pendurthi, R.; Choudhury, T. H.; Redwing, J. M.; Das, S. Benchmarking Monolayer MoS_2 and WS_2 Field-Effect Transistors. *Nat. Commun.* 2021, *12* (1), 693. https://doi.org/10.1038/s41467-020-20732-w.

(5) Jayachandran, D.; Sakib, N. U.; Das, S. 3D Integration of 2D Electronics. *Nat. Rev. Electr. Eng.* 2024, *1* (5), 300–316. https://doi.org/10.1038/s44287-024-00038-5.

(6) Wu, R.; Zhang, H.; Ma, H.; Zhao, B.; Li, W.; Chen, Y.; Liu, J.; Liang, J.; Qin, Q.; Qi, W.; Chen, L.; Li, J.; Li, B.; Duan, X. Synthesis, Modulation, and Application of Two-Dimensional TMD Heterostructures. *Chem. Rev.* 2024, *124* (17), 10112–10191. https://doi.org/10.1021/acs.chemrev.4c00174.

(7) Chen, Y.; Sun, M. Two-Dimensional WS_2/MoS_2 Heterostructures: Properties and Applications. *Nanoscale* 2021, *13* (11), 5594–5619. https://doi.org/10.1039/D1NR00455G.

(8) Chen, K.; Wan, X.; Wen, J.; Xie, W.; Kang, Z.; Zeng, X.; Chen, H.; Xu, J.-B. Electronic Properties of MoS_2–WS_2 Heterostructures Synthesized with Two-Step Lateral Epitaxial Strategy. *ACS Nano* 2015, *9* (10), 9868–9876. https://doi.org/10.1021/acsnano.5b03188.

(9) Zhang, J.; Wang, J.; Chen, P.; Sun, Y.; Wu, S.; Jia, Z.; Lu, X.; Yu, H.; Chen, W.; Zhu, J.; Xie, G.; Yang, R.; Shi, D.; Xu, X.; Xiang, J.; Liu, K.; Zhang, G. Observation of Strong Interlayer Coupling in MoS_2/WS_2 Heterostructures. *Adv. Mater.* 2016, *28* (10), 1950–1956. https://doi.org/10.1002/adma.201504631.

(10) Chuang, H.-J.; Chamlagain, B.; Koehler, M.; Perera, M. M.; Yan, J.; Mandrus, D.; Tománek, D.; Zhou, Z. Low-Resistance 2D/2D Ohmic Contacts: A Universal Approach to High-Performance WSe_2, MoS_2, and $MoSe_2$ Transistors. *Nano Lett.* 2016, *16* (3), 1896–1902. https://doi.org/10.1021/acs.nanolett.5b05066.

(11) Ciarrocchi, A.; Tagarelli, F.; Avsar, A.; Kis, A. Excitonic Devices with van Der Waals Heterostructures: Valleytronics Meets Twistronics. *Nat. Rev. Mater.* 2022, *7* (6), 449–464. https://doi.org/10.1038/s41578-021-00408-7.

(12) Yelgel, C.; Yelgel, Ö. C.; Gülseren, O. Structural and Electronic Properties of MoS_2, WS_2, and WS_2/MoS_2 Heterostructures Encapsulated with Hexagonal Boron Nitride Monolayers. *J. Appl. Phys.* 2017, *122* (6), 065303. https://doi.org/10.1063/1.4998522.

(13) Ye, K.; Liu, L.; Liu, Y.; Nie, A.; Zhai, K.; Xiang, J.; Wang, B.; Wen, F.; Mu, C.; Zhao, Z.; Gong, Y.; Liu, Z.; Tian, Y. Lateral Bilayer MoS_2–WS_2 Heterostructure Photodetectors with High Responsivity and Detectivity. *Adv. Opt. Mater.* 2019, *7* (20), 1900815. https://doi.org/10.1002/adom.201900815.

(14) Zhou, J.; Tang, B.; Lin, J.; Lv, D.; Shi, J.; Sun, L.; Zeng, Q.; Niu, L.; Liu, F.; Wang, X.; Liu, X.; Suenaga, K.; Jin, C.; Liu, Z. Morphology Engineering in Monolayer MoS_2-WS_2 Lateral Heterostructures. *Adv. Funct. Mater.* 2018, *28* (31), 1801568. https://doi.org/10.1002/adfm.201801568.

(15) Zhou, J.; Zhang, W.; Lin, Y.-C.; Cao, J.; Zhou, Y.; Jiang, W.; Du, H.; Tang, B.; Shi, J.; Jiang, B.; Cao, X.; Lin, B.; Fu, Q.; Zhu, C.; Guo, W.; Huang, Y.; Yao, Y.; Parkin, S. S. P.; Zhou, J.; Gao, Y.; Wang, Y.; Hou, Y.; Yao, Y.; Suenaga, K.; Wu, X.; Liu, Z. Heterodimensional Superlattice with In-Plane Anomalous Hall Effect. *Nature* 2022, *609* (7925), 46–51. https://doi.org/10.1038/s41586-022-05031-2.

(16) Qiao, Y.; Wang, F.; Guo, W.; Wang, Y.; Wang, F. Multi-Wavelength Optoelectronic Synapse Based on MoS_2/WS_2 van Der Waals Heterostructures. *J. Phys. Appl. Phys.* 2024, *57* (49), 495104. https://doi.org/10.1088/1361-6463/ad77df.

(17) Gong, C.; Zhang, H.; Wang, W.; Colombo, L.; Wallace, R. M.; Cho, K. Band Alignment of Two-Dimensional Transition Metal Dichalcogenides: Application in Tunnel Field Effect Transistors. *Appl. Phys. Lett.* 2013, *103* (5), 053513. https://doi.org/10.1063/1.4817409.

(18) Mia, A. K.; Meyyappan, M.; Giri, P. K. Asymmetric Contact-Induced Selective Doping of CVD-Grown Bilayer WS_2 and Its Application in High-Performance Photodetection with an Ultralow Dark Current. *Nanoscale* 2024, *16* (17), 8583–8596. https://doi.org/10.1039/D3NR06118C.

(19) Mawlong, L. P. L.; Bora, A.; Giri, P. K. Coupled Charge Transfer Dynamics and Photoluminescence Quenching in Monolayer MoS_2 Decorated with WS_2 Quantum Dots. *Sci. Rep.* 2019, *9* (1), 19414. https://doi.org/10.1038/s41598-019-55776-6.

(20) Kim, H.; Kim, J.; Uddin, I.; Phan, N. A. N.; Whang, D.; Kim, G.-H. Dual-Channel WS_2/WSe_2 Heterostructure with Tunable Graphene Electrodes. *ACS Appl. Electron. Mater.* 2023, *5* (2), 913–919. https://doi.org/10.1021/acsaelm.2c01465.

(21) Jiang, Y.; Chen, S.; Zheng, W.; Zheng, B.; Pan, A. Interlayer Exciton Formation, Relaxation, and Transport in TMD van Der Waals Heterostructures. *Light Sci. Appl.* 2021, *10* (1), 72. https://doi.org/10.1038/s41377-021-00500-1.

(22) Sahoo, P. K.; Memaran, S.; Xin, Y.; Balicas, L.; Gutiérrez, H. R. One-Pot Growth of Two-Dimensional Lateral Heterostructures via Sequential Edge-Epitaxy. *Nature* 2018, *553* (7686), 63–67. https://doi.org/10.1038/nature25155.

(23) Gong, Y.; Lei, S.; Ye, G.; Li, B.; He, Y.; Keyshar, K.; Zhang, X.; Wang, Q.; Lou, J.; Liu, Z.; Vajtai, R.; Zhou, W.; Ajayan, P. M. Two-Step Growth of Two-Dimensional WSe_2/$MoSe_2$ Heterostructures. *Nano Lett.* 2015, *15* (9), 6135–6141. https://doi.org/10.1021/acs.nanolett.5b02423.

(24) Zhang, S.; Liu, H.; Zhang, F.; Zheng, X.; Zhang, X.; Zhang, B.; Zhang, T.; Ao, Z.; Zhang, X.; Lan, X.; Yang, X.; Zhong, M.; Li, J.; Li, B.; Ma, H.; Duan, X.; He, J.; Zhang, Z. Controllable Synthesis of WSe_2–WS_2 Lateral Heterostructures via Atomic Substitution. *ACS Nano* 2024. https://doi.org/10.1021/acsnano.4c06597.

(25) Wang, Z.; Xu, W.; Li, B.; Hao, Q.; Wu, D.; Qi, D.; Gan, H.; Xie, J.; Hong, G.; Zhang, W. Selective Chemical Vapor Deposition Growth of WS_2/MoS_2 Vertical and Lateral Heterostructures on Gold Foils. *Nanomaterials* 2022, *12* (10), 1696. https://doi.org/10.3390/nano12101696.

(26) Chen, C.; Yang, Y.; Zhou, X.; Xu, W.; Cui, Q.; Lu, J.; Jing, H.; Tian, D.; Xu, C.; Zhai, T.; Xu, H. Synthesis of Large-Area Uniform MoS_2–WS_2 Lateral Heterojunction Nanosheets for Photodetectors. *ACS Appl. Nano Mater.* 2021, *4* (5), 5522–5530. https://doi.org/10.1021/acsanm.1c00890.

(27) Thakur, D.; Sato, Y.; Sabarigresan, M.; Ramadurai, R.; Balakrishnan, V. Enhanced Optical Emission at MoS_2-WS_2 Heterostructure Interface with n-N Junction. *Appl. Surf. Sci.* 2022, *606*, 154923. https://doi.org/10.1016/j.apsusc.2022.154923.

(28) Sahoo, P. K.; Memaran, S.; Nugera, F. A.; Xin, Y.; Díaz Márquez, T.; Lu, Z.; Zheng, W.; Zhigadlo, N. D.; Smirnov, D.; Balicas, L.; Gutiérrez, H. R. Bilayer Lateral Heterostructures of Transition-Metal Dichalcogenides and Their Optoelectronic Response. *ACS Nano* 2019, *13* (11), 12372–12384. https://doi.org/10.1021/acsnano.9b04957.

(29) Vu, V. T.; Phan, T. L.; Vu, T. T. H.; Park, M. H.; Do, V. D.; Bui, V. Q.; Kim, K.; Lee, Y. H.; Yu, W. J. Synthesis of a Selectively Nb-Doped WS_2–MoS_2 Lateral Heterostructure for a High-Detectivity PN Photodiode. *ACS Nano* 2022, *16* (8), 12073–12082. https://doi.org/10.1021/acsnano.2c02242.

(30) Wang, Z.; Tripathi, M.; Golsanamlou, Z.; Kumari, P.; Lovarelli, G.; Mazziotti, F.; Logoteta, D.; Fiori, G.; Sementa, L.; Marega, G. M.; Ji, H. G.; Zhao, Y.; Radenovic, A.; Iannaccone, G.; Fortunelli, A.; Kis, A. Substitutional P-Type Doping in NbS_2–MoS_2 Lateral Heterostructures Grown by MOCVD. *Adv. Mater.* 2023, *35* (14), 2209371. https://doi.org/10.1002/adma.202209371.

(31) Berkdemir, A.; Gutiérrez, H. R.; Botello-Méndez, A. R.; Perea-López, N.; Elías, A. L.; Chia, C.-I.; Wang, B.; Crespi, V. H.; López-Urías, F.; Charlier, J.-C.; Terrones, H.; Terrones, M. Identification of Individual and Few Layers of WS_2 Using Raman Spectroscopy. *Sci. Rep.* 2013, *3* (1), 1755. https://doi.org/10.1038/srep01755.

(32) Gutiérrez, H. R.; Perea-López, N.; Elías, A. L.; Berkdemir, A.; Wang, B.; Lv, R.; López-Urías, F.; Crespi, V. H.; Terrones, H.; Terrones, M. Extraordinary Room-Temperature

Photoluminescence in Triangular WS_2 Monolayers. *Nano Lett.* 2013, *13* (8), 3447–3454. https://doi.org/10.1021/nl3026357.

(33) Huang, S.; Ling, X.; Liang, L.; Kong, J.; Terrones, H.; Meunier, V.; Dresselhaus, M. S. Probing the Interlayer Coupling of Twisted Bilayer MoS_2 Using Photoluminescence Spectroscopy. *Nano Lett.* 2014, *14* (10), 5500–5508. https://doi.org/10.1021/nl5014597.

(34) Roy, S.; Yang, X.; Gao, J. Biaxial Strain Tuned Upconversion Photoluminescence of Monolayer WS_2. *Sci. Rep.* 2024, *14* (1), 3860. https://doi.org/10.1038/s41598-024-54185-8.

(35) Paras; Yadav, K.; Kumar, P.; Teja, D. R.; Chakraborty, S.; Chakraborty, M.; Mohapatra, S. S.; Sahoo, A.; Chou, M. M. C.; Liang, C.-T.; Hang, D.-R. A Review on Low-Dimensional Nanomaterials: Nanofabrication, Characterization and Applications. *Nanomaterials* 2023, *13* (1), 160. https://doi.org/10.3390/nano13010160.

(36) Xu, M.; Fujita, D.; Gao, J.; Hanagata, N. Auger Electron Spectroscopy: A Rational Method for Determining Thickness of Graphene Films. *ACS Nano* 2010, *4* (5), 2937–2945. https://doi.org/10.1021/nn100276w.

(37) Biroju, R. K.; Maity, D.; Vretenár, V.; Vančo, Ľ.; Sharma, R.; Sahoo, M. R.; Kumar, J.; Gayathri, G.; Narayanan, T. N.; Nayak, S. K. Quantification of Alloy Atomic Composition Sites in 2D Ternary $MoS_{2(1-x)}Se_{2x}$ and Their Role in Persistent Photoconductivity, Enhanced Photoresponse and Photo-Electrocatalysis. *Mater. Today Adv.* 2024, *22*, 100504. https://doi.org/10.1016/j.mtadv.2024.100504.

(38) McCreary, K. M.; Hanbicki, A. T.; Jernigan, G. G.; Culbertson, J. C.; Jonker, B. T. Synthesis of Large-Area WS_2 Monolayers with Exceptional Photoluminescence. *Sci. Rep.* 2016, *6* (1), 19159. https://doi.org/10.1038/srep19159.

(39) Dodda, A.; Jayachandran, D.; Pannone, A.; Trainor, N.; Stepanoff, S. P.; Steves, M. A.; Radhakrishnan, S. S.; Bachu, S.; Ordonez, C. W.; Shallenberger, J. R.; Redwing, J. M.; Knappenberger, K. L.; Wolfe, D. E.; Das, S. Active Pixel Sensor Matrix Based on Monolayer MoS_2 Phototransistor Array. *Nat. Mater.* 2022, *21* (12), 1379–1387. https://doi.org/10.1038/s41563-022-01398-9.

(40) Duraisamy, S.; Ganguly, A.; Sharma, P. K.; Benson, J.; Davis, J.; Papakonstantinou, P. One-Step Hydrothermal Synthesis of Phase-Engineered MoS_2/MoO_3 Electrocatalysts for Hydrogen Evolution Reaction. *ACS Appl. Nano Mater.* 2021, *4* (3), 2642–2656. https://doi.org/10.1021/acsanm.0c03274.

(41) Smithe, K. K. H.; Suryavanshi, S. V.; Muñoz Rojo, M.; Tedjarati, A. D.; Pop, E. Low Variability in Synthetic Monolayer MoS_2 Devices. *ACS Nano* 2017, *11* (8), 8456–8463. https://doi.org/10.1021/acsnano.7b04100.

Chapter 6

Highly Sensitive and Selective Optical Detection of Staphylococcus aureus using Thiol Functionalized Monolayer Tungsten Disulfide Grown by Chemical Vapor Deposition

This chapter explores the potential application of CVD-grown 1L-WS_2 as biosensors using its excellent PL emission at room temperature. The extraordinary PL emission at room temperature from CVD-grown 1L-WS_2 was utilized for the first time here as a recognition tool for detecting *S. aureus* bacteria with high sensitivity and selectivity. The 1L-WS_2 possesses sulfur vacancy and is utilized for ssDNA aptamer immobilization to the sulfur vacancy sites of 1L-WS_2 via the thiol functional group. The small-sized, highly selective ssDNA aptamers identify and selectively interact with targeted *S. aureus*, enabling selective detection. Interestingly, the PL emission of 1L-WS_2 is strongly influenced by external charge doping. The shape of the PL emission peak for 1L-WS_2 undergoes significant changes in the presence of targeted *S. aureus* as a result of charge transfer originating from selective interactions of the ssDNA aptamer with *S. aureus*, while it remains unaffected for non-targeted *Escherichia coli*. The ratio of the integrated intensities of trion to neutral exciton peak was used as a calibration parameter for the quantification of *S. aureus* concentrations. The PL analysis of 1L-WS_2 with increasing concentration of *S. aureus* exhibits a linear response over 10^2 CFU/mL to 10^7 CFU/ml with a lower detection limit of 2.0 CFU/mL. The proposed sensing system can identify an unknown concentration of *S. aureus* in human urine with 78% accuracy at a concentration of 10^5 CFU/mL. These results demonstrate the potential future application of monolayer transition metal dichalcogenides in the optical biosensing of pathogenic species using suitable receptors.

6.1. Introduction

For decades, pathogenic bacterial infection has remained a significant threat to public health, persisting as the foremost cause of disease and mortality in many developing and underdeveloped countries.[1] Identifying and quantifying pathogenic bacteria species in the early stage of infections can prevent the outbreak of pathogenic diseases. Among those pathogenic bacterial species, *Staphylococcus aureus* (*S. aureus*) is one the most common gram-positive pathogens in the human

body. It is responsible for various diseases such as gastroenteritis, meningitis, toxic shock syndrome, osteomyelitis, skin and soft tissue infections, and many more.[2] During the pre-antibiotic era, diseases associated with *S. aureus* had the highest mortality rates[3], even surpassing the combined number of deaths caused by AIDS, tuberculosis, and viral hepatitis.[4] Currently, the increasing antibiotic resistance of *S. aureus* is a significant concern[5], and the scientific community fears a return to the pre-antibiotic era where antibiotics will no longer be effective in treating bacterial infections.[6] The excess usage of non-targeted antibiotics is one of the major causes of antibiotic resistance among pathogenic bacteria.[7] Therefore, selective and sensitive detection of *S. aureus* is crucial for the targeted use of antibiotics and as well as preventing a global outbreak.

Polymerase chain reaction (PCR), culture methods, and enzyme-linked immunosorbent assay (ELISA) are the gold standard for detecting *S. aureus*, but they require a significant amount of time and specialized trained personnel, limiting their applications in remote areas.[8–11] In addition to PCR, other detection mechanisms such as electrochemical[12,13], optical fiber[14], colorimetric[15], and photoluminescence (PL)[16–18] are also used for faster detection of *S. aureus* at low concentrations. However, these methods require hours for detection and hence there is an increasing demand for real-time detection of *S. aureus*. Among all sensing mechanisms, optical biosensors based on PL are capable of detecting analytes with high sensitivity in real-time.[19] Recently, ultrathin 2D transition metal dichalcogenides (TMDs) have gained significant interest in biosensing applications owing to their excellent optoelectronic properties.[20,21] 2D tungsten diselenide (WS_2), a member of the TMD family, is a promising material for next-generation optoelectronic and sensing applications. It features an ultrathin planar structure with a finite bandgap, high on-off ratio, interesting light emissions, absorption properties, and good stability in ambient environments.[22–25] The transition from indirect to direct band structure in monolayer WS_2 (1L-WS_2) gives rise to strong PL emission at room temperature.[26] There are very few reports of WS_2 in biosensing, and available reports are primarily based on Forster resonance energy transfer (FRET) methods, which are synthesized by chemical routes used for DNA detection.[27–29] To the best of our knowledge, there is no report of using 1L-WS_2-based optical biosensors. For the first time, we have explored the potential applications of CVD-grown 1L-WS_2 in PL-based optical biosensors for the detection of *S. aureus* with high sensitivity and selectivity.

The receptors play a crucial role in enhancing the specificity of any biosensor in detecting specific analytes in complex environments[30]. Conventionally, proteins and antibodies have been utilized as receptors in biosensing. However, recently, small-sized ssDNA aptamers are emerging as alternative receptors in biosensing[13,31]. The affordable cost, remarkable thermal stability, ease of modification with exceptional specificity, and compact size make aptamers suitable as bioreceptors[32].

Herein, we have taken advantage of the excellent PL emission of 1L-WS_2 at room temperature in developing an optical biosensor for the ultrasensitive detection of *S. aureus*. The high-temperature CVD technique was utilized to synthesize a uniform, large-area 1L-WS_2 on SiO_2/Si substrate. The as-synthesized 1L-WS_2 possesses inherent sulfur vacancy sites, and those have strong covalent interaction with thiol functional groups.[33,34] To utilize this strong interaction, the thiol functional group was added to the 5' terminal of the ssDNA aptamer probe, enabling the covalent functionalization of the 1L-WS_2 with the ssDNA aptamer via sulfur vacancy. The PL emission spectra show distinct features in the presence of targeted *S. aureus* and non-targeted *E. coli,* which enables selectivity in sensing. It is shown that the increasing concentration of *S. aureus* systematically alters the PL emission spectrum by shifting the neutral exciton peak due to increasing trion populations as compared to the neutral excitons. The enhanced trion contributions with increasing bacteria concentrations are attributed to the charge transfer from *S. aureus* to 1L-WS_2, which enables a quantitative assessment of the bacteria sensing.

6.2 Experimental Details

6.2.1 Synthesis of Monolayer WS_2 Flakes

The 1L-WS_2 flakes were synthesized using CVD employing a two-zone horizontal tubular furnace and WO_3 and sulfur powders as precursors. Detailed information regarding the synthesis process can be found in **section 2.1** of chapter 2. Briefly, 10 mg of WO_3 powder was placed at the center of a high-temperature heating zone. At the same time, a few pieces of SiO_2/Si substrates were kept just above the WO_3 powder, with their polished surfaces facing downward. Simultaneously, 200 mg of the S precursor was placed in the middle of the low-temperature heating zone within a mini quartz boat. The temperature of the first zone was adjusted to reach 150°C simultaneously with the high-temperature zone reaching 940°C. The system was then allowed to stabilize at this temperature for 15 minutes with Ar flowing at a rate of 100 sccm as carrier gas. Once the growth

process is complete, the system naturally cools down to ambient temperature. This resulted in the growth of uniform 1L-WS_2 flakes on the SiO_2/Si substrate.

6.2.2 The ssDNA Aptamer Selection

The ssDNA Aptamer specifically identifying and binding to *S. aureus* was developed by using the Cell-SELEX (Systematic Evolution of Ligands by EXponential enrichment) technology. Briefly, 1.5µM ssDNA aptamer library was incubated with 10^8 CFU/mL (Colony Formation Unit/mL) of *S. aureus* suspended in 1-X phosphate-buffered saline (PBS) at room temperature. After 45 min, cells were centrifuged for 5 min at 8000 rpm, and the unbound ssDNA aptamers in the aqueous phase were discarded, and the cell-bound aptamers were re-suspended in 250 µl nuclease-free deionized water. The cell-bound selected aptamers were recovered by heating the suspension at 95ºC for 10 min followed by centrifugation at 12,000 rpm for 15 min. The selected aptamer pool was enriched by Polymerase Chain reaction (PCR) being carried out for 10 cycles using 0.15 µM of Forward primer [5'-GGCTGGATGGGGCGTGT-3'] and 0.15 µM 5'-Biotin-labeled reverse primer [5'-CGCTGTCCGCACCGTTG-3']. The PCR program used was: pre-denaturation at 95ºC, 5 min followed by cycling step; 95ºC for 20s, annealing at 55ºC for 5s and extension at 72ºC for 10s. Amplified 2 µg of dsDNA pool was immobilized on activated streptavidin magnetic beads (NEB) in 200 µl of binding buffer (10mM Tris-HCl pH8.0, 1mM EDTA pH8.0, 2M NaCl). The selected ssDNA aptamer strand was separated from biotinylated strand by alkaline denaturation using 500 µl of 10 mM NaOH followed by purification by NAP-5 (Cytiva) desalting column according to manufactures' instructions. Before using the purified ssDNA for the next round, the ssDNA pool was concentrated to the volume of ~150µl. The SELEX was carried out for 10 rounds. For specificity to target S. aureus, after SELEX rounds 4, 6 and 8, negative selection was carried out using non-target bacterial: *E. coli, E.faecalis, K. pneumoniae, Pseudomonas sp. and Proteus sp.* During negative selection rounds, bound ssDNA aptamer pool was incubated with non-target bacteria pool for 30 min and unbound ssDNA pool was recovered by centrifugation and immediately incubated with target S. aureus. After the last round of selection, the ssDNA aptamer pool was PCR amplified using unlabeled forward and reverse primers, purified and cloned into the TA-cloning vector using pGEM-T® easy vector systems (Promega), transformed in JM109 competent cells and plated on IPTG-Xgal-Amp-LB Agar plates. Positive bacterial colonies (white colonies) were inoculated in 5 ml of Luria Bertani (LB) media and grown overnight at 37ºC at 220

rpm. Plasmids were isolated and individual cloned DNA aptamers were DNA sequenced using Sangers dideoxy chain termination method (1st Base, Axil Scientific, Singapore facility). The 20 selected DNA Aptamers that were sequenced, 3 of them were repeated and thus these 3 Aptamers were individually synthesized commercially with FAM label at 5'-end (IDT DNA Technologies, USA). Flow cytometry was used to assess the binding of the individual aptamer to target S. aureus and determination of dissociation constants (K_d) of individual selected aptamers with target S. aureus. The aptamer used in the present work exhibited highest specificity to the target S. aureus with K_d value of 40.96nM. The evaluated *S. aureus* Aptamer was commercially synthesized (IDT DNA Technologies, USA) with thiol group modification at the 5'-end of the DNA molecule; 5´-ThioMC6-D-GGC TGG ATG GGG CGT GTT GAT TCG AGT CGG AGA CGG CAT CCT GCA CAA ATG CCA ACG GTG CGG ACA GCG-3´.

6.2.3 ssDNA Aptamer Reduction and Functionalization with 1L-WS_2.

The thiol-modified ssDNA aptamers (IDT Technologies, USA) were reduced to have covalent bonding with sulfur vacancy site in 1L-WS_2. For reduction, 10 mM of tris-HCl buffer solution at pH 8 was prepared in NF water, and subsequently, 10 mM TECP solution was prepared using that same Tris-HCl buffer. Finally, 50 μM of ssDNA aptamers was added to 10 mM TECP solution by equal volume and kept it at room temperature for 3.0 hours as per protocol by IDT. This solution was drop cast on 1L-WS_2 and kept at 4ºC overnight in order to achieve the covalent bonding with the sulfur vacancy sites. The functionalized WS_2 was ultimately rinsed with the same Tris-HCl buffer to eliminate any unbound aptamers from the surface, ensuring that only strongly bound aptamers remained with the WS_2 surface. Finally, for the PL emission measurements, 5.0 μL solutions of *S. aureus* with different concentrations were drop cast on the ssDNA functionalized 1L-WS_2, washed in PBS solution after 30 minutes, and dried in nitrogen gas.

6.3. Results and Discussion

6.3.1 Optical, Raman and PL Analysis

The 1L-WS_2 grown via CVD exhibit a range of flake sizes, varying from tens to a few hundred micrometers, with an average size of approximately 100 μm, as shown in **Fig. 2.7 in section 2.4.5 of Chapter 2.** Raman spectroscopy is one of the most powerful techniques for characterizing 2D

materials[35] like WS_2 and was used to assess the uniformity within individual flakes as well as among multiple flakes. The uniformity of optical properties across the flakes was estimated via spatial Raman mapping as displayed in **Fig.6.1**. The **Fig.6.1(a)** shows optical image of a set of two 1L-WS_2 flakes across which spatial Raman mapping was performed to understand the spatial uniformity. The spatial Raman mapping was performed with a spatial resolution of 1 μm. The color mapping of the out-of-plane A_{1g} (red) mode and the strong 2LA mode summed with in plane E_{2g} (green) mode of 1L-WS_2 is presented in **Fig.6.1 (b) and 6.1(c)**, respectively. The excellent uniform color contrast for both flakes confirms the outstanding uniformity of the CVD-grown 1L-WS_2. The fitted Raman spectra of a CVD-grown and ssDNA aptamer functionalized single 1L-

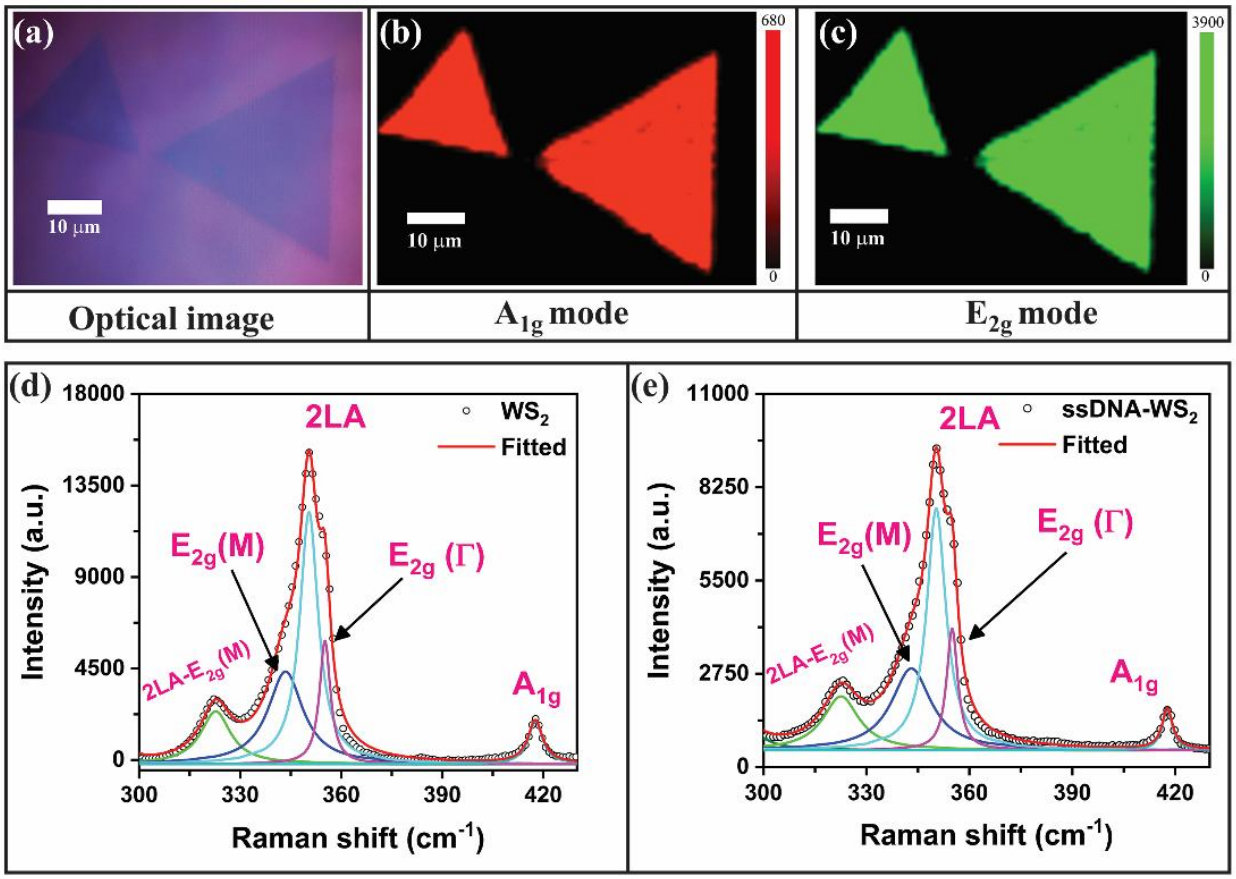

Figure. 6.1: (a) Optical image of two CVD grown 1L-WS_2 corresponding to spatial Raman mapping (b) Spatial color profile corresponding to intensity profile of the out of plane A_{1g} mode. (c) Spatial colour mapping corresponding to the intensity of 2LA+ E_{2g} Raman mode. (d) Deconvoluted Raman spectra of monolayer WS_2 before functionalization. (e) Deconvoluted Raman spectrum after functionalization with ssDNA.

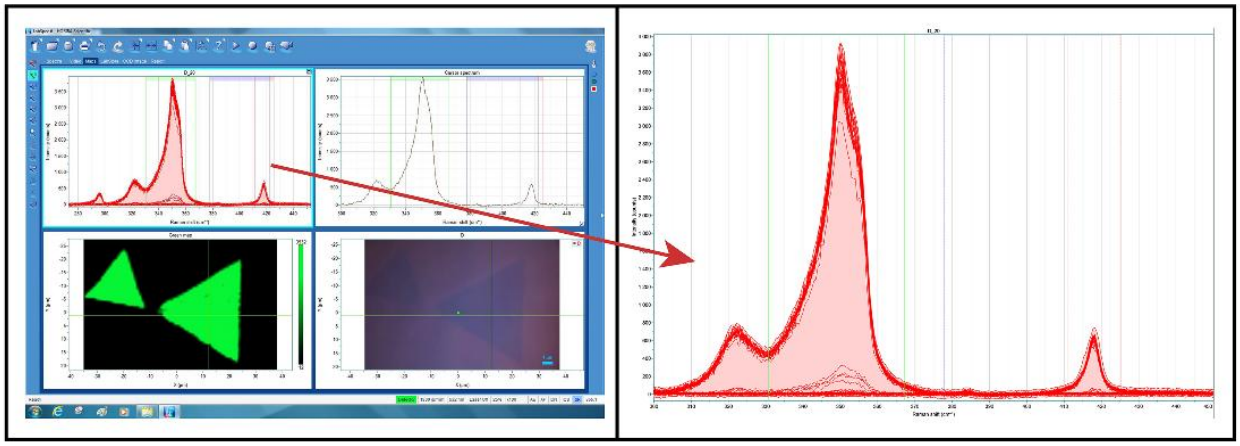

Figure 6.2: Raman mapping screen recorded spectrum for the 1L-WS_2 flakes with magnified Raman spectrum

WS_2 flake are shown in **Fig. 6.1(d)** and **6.1(e)** respectively. The Raman spectrum was fitted with the Lorentz function for further understanding the effect of functionalization. The characteristic, A_{1g} and E_{2g} Raman modes corresponding to out-of-plane and in-plane vibrations of S and W atoms, were observed at 417.6 and 455.2 cm^{-1}, respectively. When excited with a 532 nm laser, in addition to characteristic phonon modes, other modes are also observed[26], as labeled in **Fig.6.1(d).** For the Raman mapping, the complete spectrum record is shown in **Fig.6.2** which displays uniform spectrum intensity across all points for both flakes of 1L-WS_2. To further understand the uniformity among different flakes, we plotted the Raman spectra of 1L-WS_2 across ten different flakes, as depicted in **Fig. 6.3(a)**. The spectra exhibit good uniformity across all ten flakes, with minor variations in intensity. This small variation in intensity across the flakes is attributed to flake size distribution and focusing during measurements. Any surface treatment of 2D WS_2 flake, such as biofunctionalization, plasma exposure, or external doping, will affect the out-of-plane A_{1g} mode, as it strongly depends on the charge density[36], while E_{2g} modes change with strain.[37] The fundamental Raman mode intensity ratio and full width at half maximum (FWHM) are sensitive to electron density, as they strongly affect the electron-phonon coupling.[38] The variation of A_{1g} modes FWHM and the spectral weight ratio of A_{1g} to E_{2g} mode over the ten flakes is displayed in **Fig. 6.3(c)**. The graph indicates that the FWHM value remains almost constant for all ten flakes with a mean value of 5.07±0.2 cm^{-1}, while the ratio of area under the A_{1g} to E_{2g} peak is 0.45 ±0.01, indicating excellent uniformity across different flakes. The Raman spectra across ten different

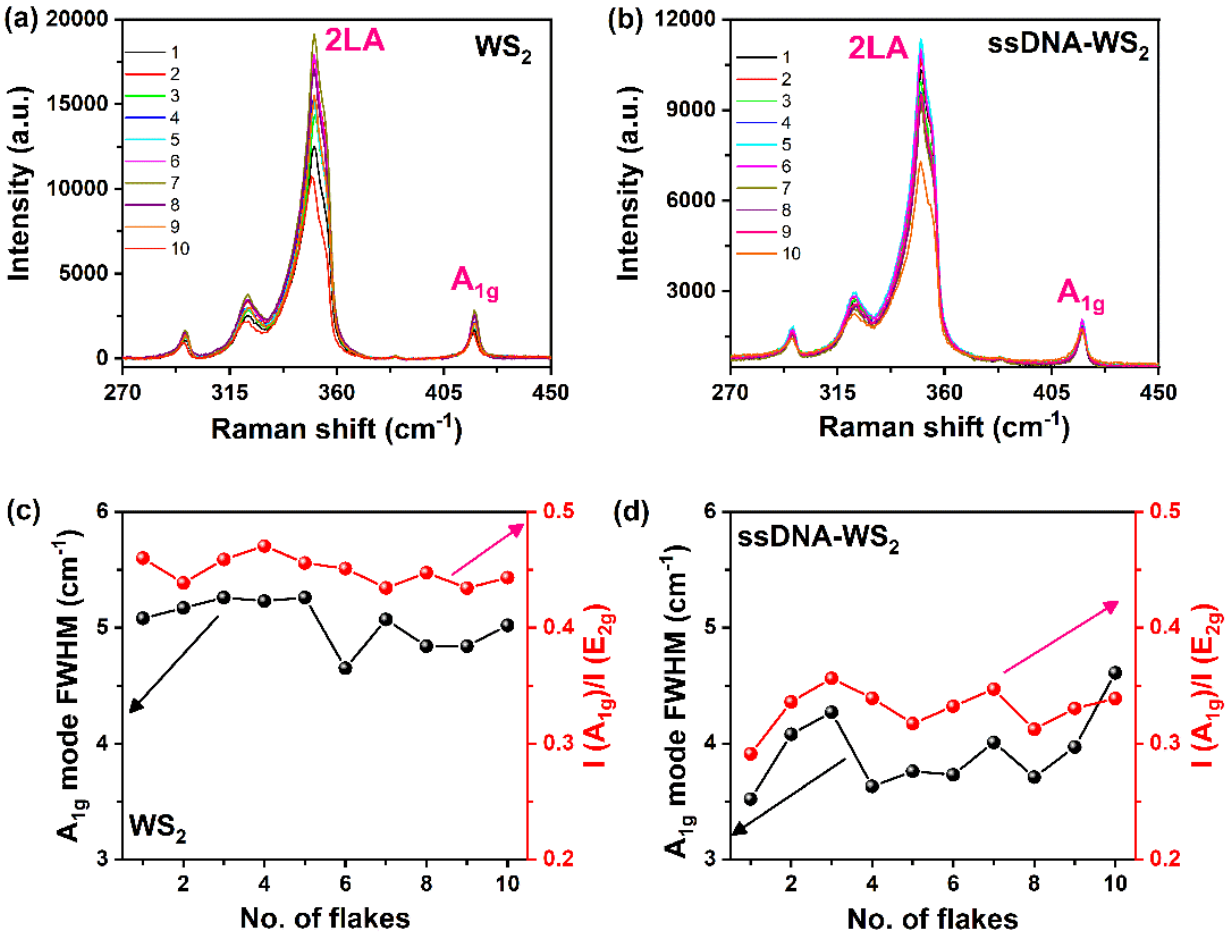

Figure 6.3: (a) Raman spectra of ten different 1L-WS_2 flakes. (b) Raman spectra of ssDNA aptamer functionalized 1L-WS_2 for ten different flakes. The variation of A_{1g} mode FWHM and integral spectral weight ratio between A_{1g} and E_{2g} of 1L-WS_2 (c) before ssDNA functionalization, and (d) after ssDNA functionalization.

flakes after ssDNA aptamer functionalization are displayed in **Fig. 6.3(b).** The excellent Raman intensity and uniformity indicate that the quality of the WS_2 flakes remains intact after functionalization. The peak parameters before and after functionalization across ten flakes are tabulated in **Table (6.1)**. The variation of A_{1g} mode FWHM with different flakes, along with the spectral weight ratio of A_{1g} and E_{2g} modes after functionalization, is displayed in **Fig. 6.3(d)**. The FWHM of the A_{1g} mode decreases significantly after functionalization, while there is no significant change in the FWHM of the E_{2g} mode. The decrease in FWHM of the A_{1g} mode implies

Table 6.1: Fitted Raman peak parameters of 1L-WS_2 before and after functionalization with ssDNA.

Flake number	Before functionalization			After functionalization		
	FWHM (A_{1g}:cm^{-1})	FWHM (E_{2g}:cm^{-1})	Area ratio (A_{1g}/E_{2g})	FWHM (A_{1g}:cm^{-1})	FWHM (E_{2g}:cm^{-1})	Area ratio (A_{1g}/E_{2g})
1	5.08	3.85	0.46	3.52	3.81	0.29
2	5.17	3.78	0.44	4.08	3.81	0.33
3	5.26	3.84	0.46	4.27	3.69	0.35
4	5.23	3.91	0.47	3.63	3.84	0.34
5	5.26	3.93	0.45	3.76	3.81	0.32
6	4.65	3.8	0.45	3.73	3.75	0.33
7	5.07	3.8	0.43	4.01	3.73	0.35
8	4.84	3.99	0.45	3.71	3.93	0.31
9	4.84	3.84	0.43	3.97	3.85	0.33
10	5.02	3.63	0.44	4.61	3.71	0.34

reduced electron-phonon coupling resulting from lowered electron density after functionalization.[36,38] The average FWHM value of the A_{1g} mode decreases by 24%, from 5.07 cm^{-1} to 3.85 cm^{-1}, due to the reduced electron density aligned by the ratio of A_{1g} to E_{2g} mode spectral weight, which also decreased from 0.45 to 0.33. The inherent sulfur vacancy sites in 1L-WS_2 act as electron donor site[39] and this decrease in electron density in the functionalized WS_2 can be attributed to the passivation of sulfur vacancy sites by the thiol functional group present in ssDNA aptamers.[34,40] The extraordinarily strong PL emission is an intrinsic characteristic of 1L-WS_2, as the PL emission is nearly quenched by 99% for bilayers and diminishes further for higher-layered WS_2 flakes.[26,41] The PL emission of 1L-WS_2 is strongly affected by charge doping. To understand the spatial charge uniformity, we have performed PL mapping on a 1L-WS_2 with a spatial resolution of 1 μm, which is displayed in **Fig. 6.4. Fig. 6.4(b)** shows the color PL spatial mapping corresponding to PL emission intensity of a 1L-WS_2, and **Fig. 6.4(a)** shows the corresponding optical image of that 1L-WS_2. The spatial PL intensity distribution indicates uniform intensity except for the edges which arises from defect sites.[42] A thorough examination of the PL spectrum reveals deviations from Gaussian symmetry, indicating the presence of multiple contributions. The fitted PL spectra of 1L-WS_2 are depicted in **Fig.6.4(c)**, revealing the presence of three Gaussian peaks contributing to the PL emission: neutral excitons (A^0), negatively charged trions (A^-), and defect-bound excitons (X^d).[43] The PL spectra for 1L-WS_2 is mainly dominated by neutral excitons with a spectral weight of approximately 80%. In the presence of external charge doping, the charged excitons, i.e., trion contribution is highly influenced[44], and hence, the ratio of the integrated intensities of trion to neutral excitons is an important parameter. The deconvoluted

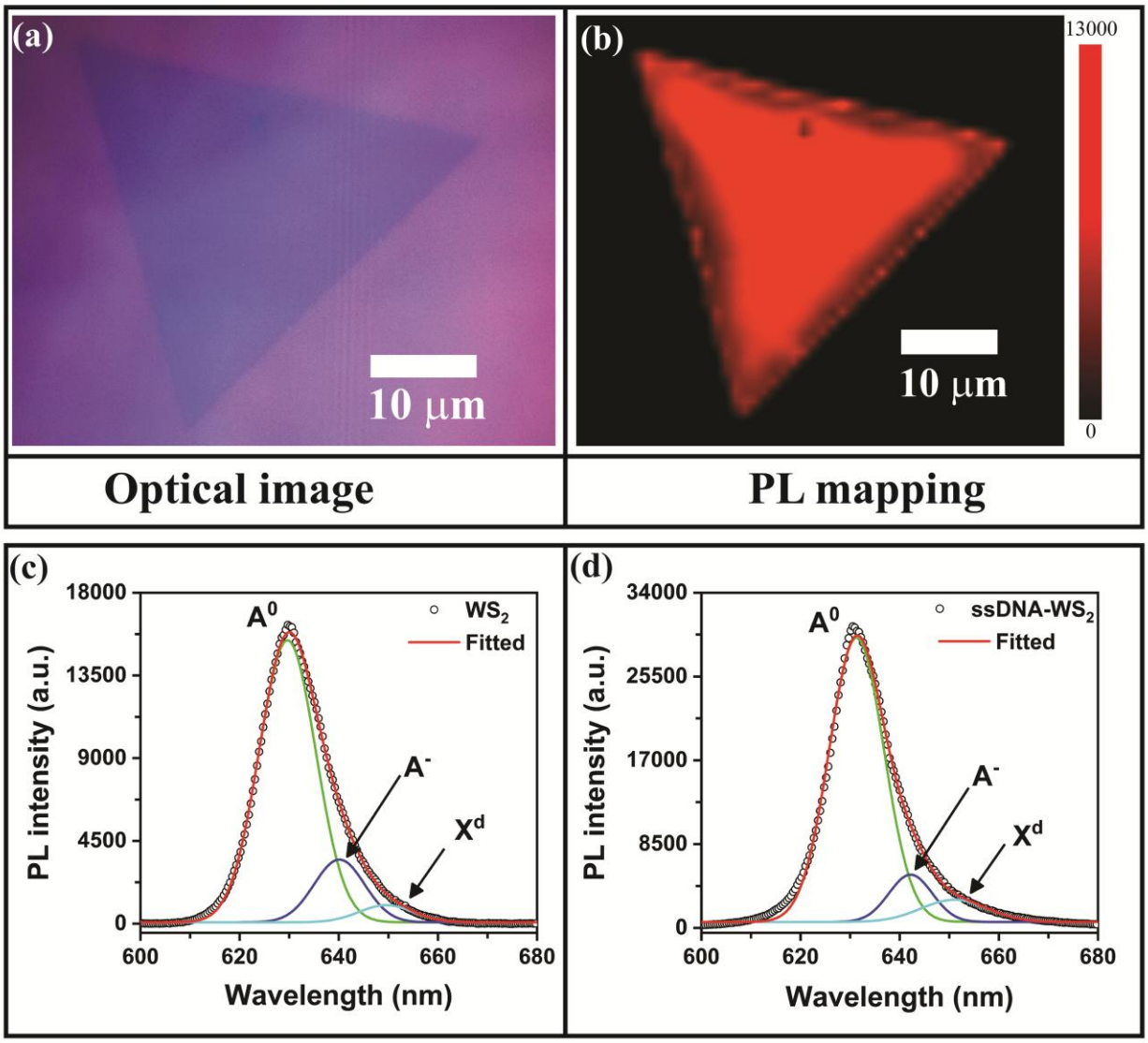

Figure 6.4: (a) Optical image of a 1L-WS_2 corresponding to spatial PL emission mapping. (b) The spatial PL color mapping of a 1L-WS_2 PL emission spectrum of monolayer WS_2 (c) Deconvoluted PL emission spectrum of 1L-WS_2. (d) Deconvoluted PL emission spectrum after ssDNA functionalization of 1L-WS_2.

PL emission spectrum of the thiol-modified ssDNA aptamer functionalized 1L-WS_2 is shown in **Fig. 6.4(d).** The PL emission of aptamer functionalized 1L-WS_2 exhibits an average 80% enhancement when compared to non-functionalized WS_2. This enhancement originated from the interaction between the thiol-modified ssDNA aptamers and 1L-WS_2. To further confirm the uniformity of PL emission across various flakes, we conducted PL emission measurements on ten different 1L-WS_2 flakes before and after ssDNA functionalization. The PL emission spectra of ten

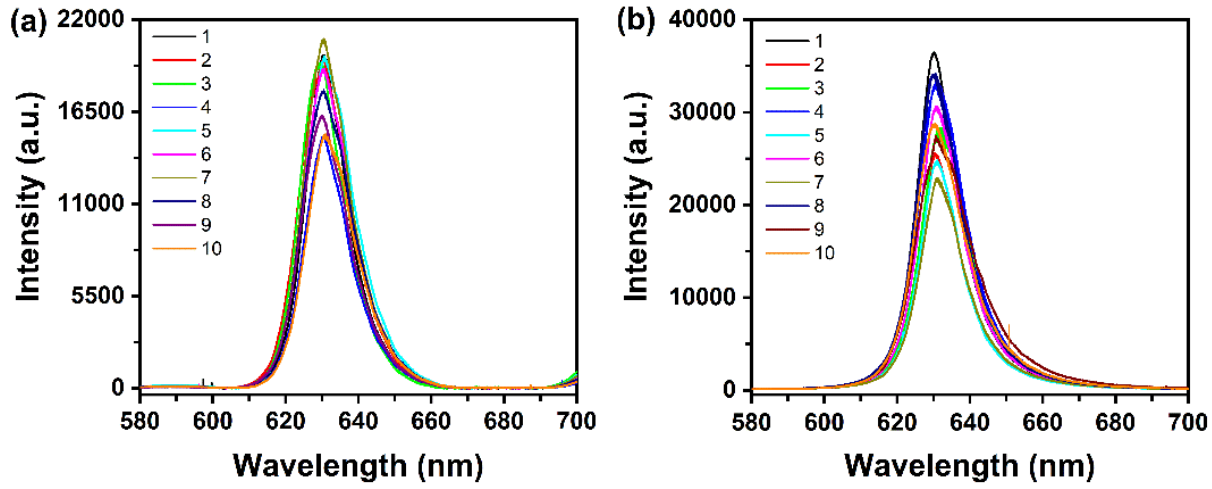

Figure 6.5: The PL emission spectra of 1L-WS_2 over ten different flakes. (a) Before ssDNA aptamer functionalization and (b) After ssDNA aptamer functionalization.

different 1L- WS_2 flakes before and after functionalization are displayed in **Fig. 6.5**. From the PL emission spectra, we observed a slight variation in intensity similar to Raman spectra, while the position of maximum intensity remains unchanged, further confirming the uniformity among different flakes, consistent with Raman analysis. For the 1L-WS_2, the ratio of the integrated intensities of trion to neutral excitons of the ten flakes is plotted (after fitting) in **Fig.6.10 (c)**. This shows an almost constant intensity ratio of trion to neutral exciton with a mean value of 0.19 ±0.02. To investigate the impact of electron-hole pair generation in PL emission of 1L-WS_2, we have studied the power dependent PL emission from the monolayer WS_2 as displayed in **Fig. 6.6.** The emission spectrum did not reveal any defect-bound excitons at low powers (sub-μW), suggesting that the formation of defect-bound excitons is induced by high-power laser heating. Interestingly, the intensity of the trion peak increases with excitation power, but the ratio of trions to neutral excitons remains almost constant, as shown in **Fig. 6.7**. Thus, the intensity ratio of trion to neutral exciton peaks provides a more significant means of identifying external doping. To understand the effect of thiol modified ssDNA aptamer interaction with the 1L-WS_2, we have plotted the ratio of the integrated intensities of trions to neutral excitons for the ssDNA functionalized 1L-WS_2 in **Fig. 6.10(c)**, where it decreases from 0.19 to 0.13 for the functionalized 1L-WS_2 indicating reduced electron density after functionalization and is consistent with the Raman spectral analyses, which resulted from the passivation of sulfur vacancy sites in 1L-WS_2 by thiol functional group in ssDNA

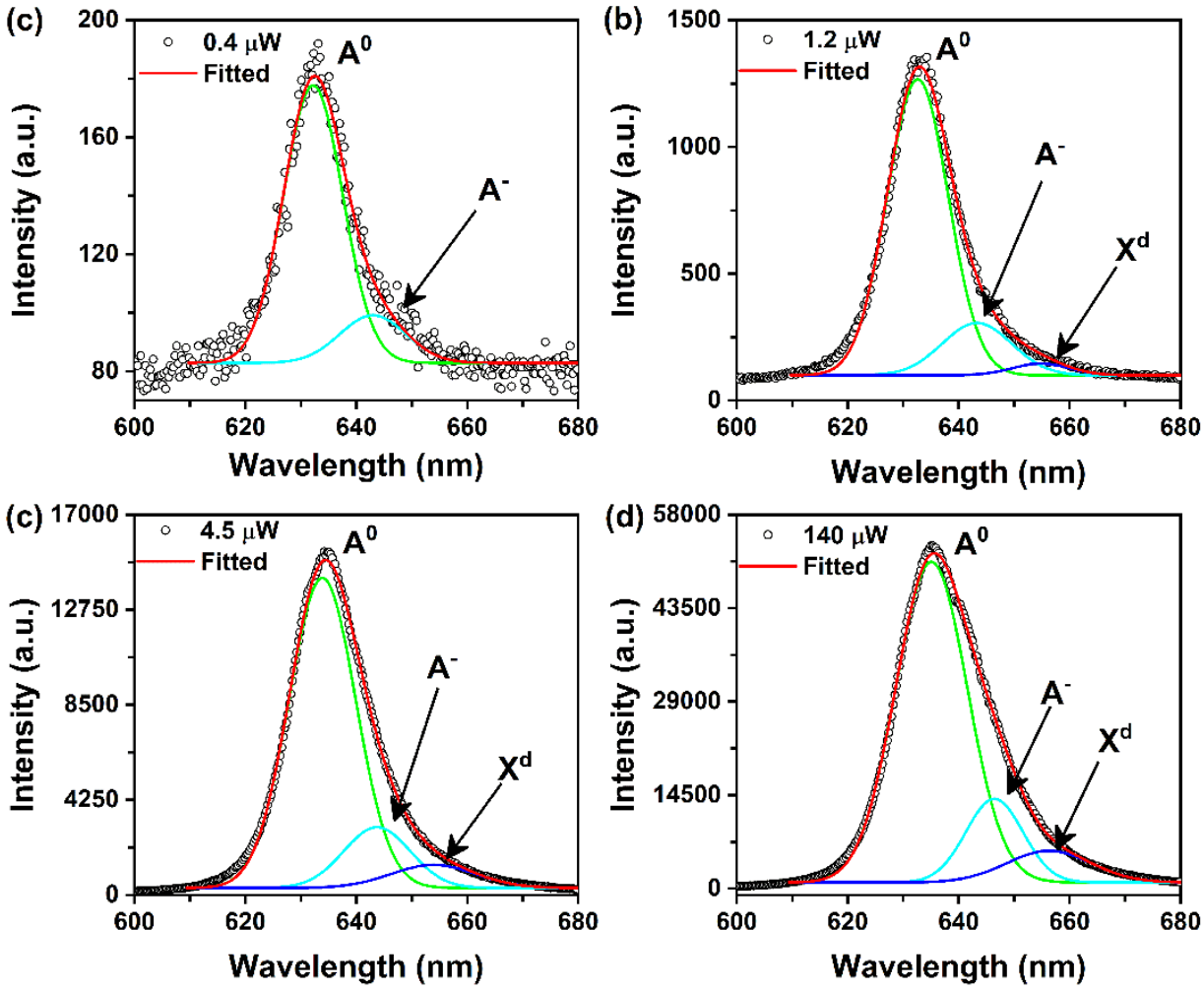

Figure 6.6: Power dependent PL emission of 1L-WS_2 under 532 nm laser excitation: (a) 0.4 μW, (b) 1.2 μW, (c) 4.5 μW, (d) 140 μW.

aptamer.[33,45] The decrease in electron density within the functionalized 1L-WS_2 is also reflected in the integral trion spectral weight, which decreases by 31% from 15.5 to 10.6 as the lower electron density will form a smaller fraction of trions. Thus, the sulfur vacancy sites are passivated via the thiol functional group present in the ssDNA aptamer.

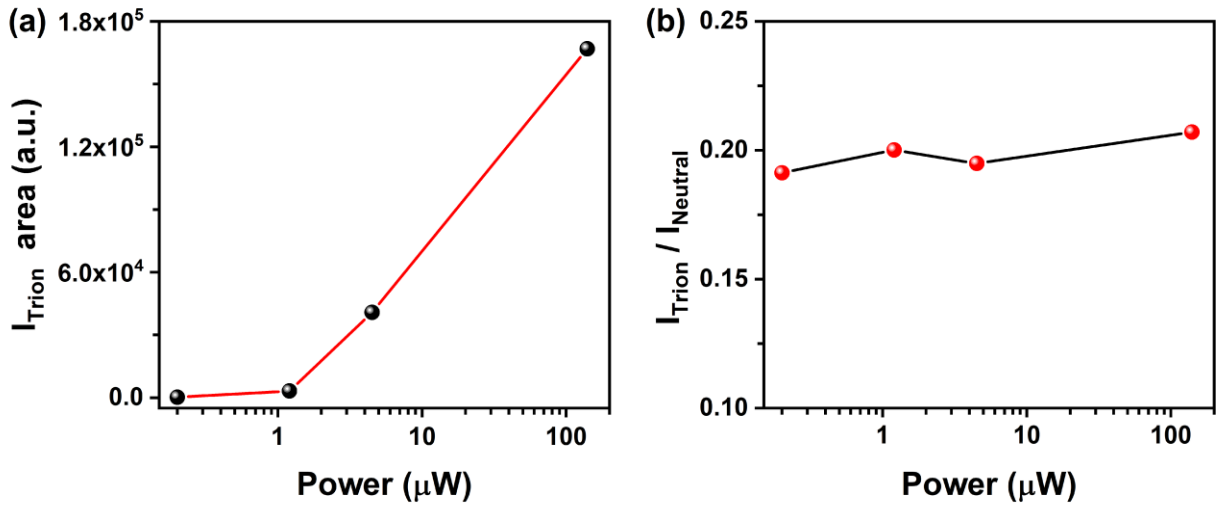

Figure 6.7: (a) Excitation power-dependence of the integrated intensity of trions in 1L-WS_2. (b) Excitation power-dependence of ratio of trion to neutral exciton intensity (integrated).

6.3.2 Chemical Analysis

The chemical characteristics of the 1L-WS_2 before and after ssDNA functionalization were examined using XPS. All XPS peak positions were referenced to the C-C peak at 284.7 eV. The XPS survey spectra of 1L-WS_2 before and after functionalization are presented in **Fig. 6.8**, and the high-resolution XPS spectra corresponding to individual elements are depicted in **Fig. 6.9**. The high-resolution C_{1s} spectra reveal a predominant C-C peak at 284.7 eV (accounting for 84.7% of

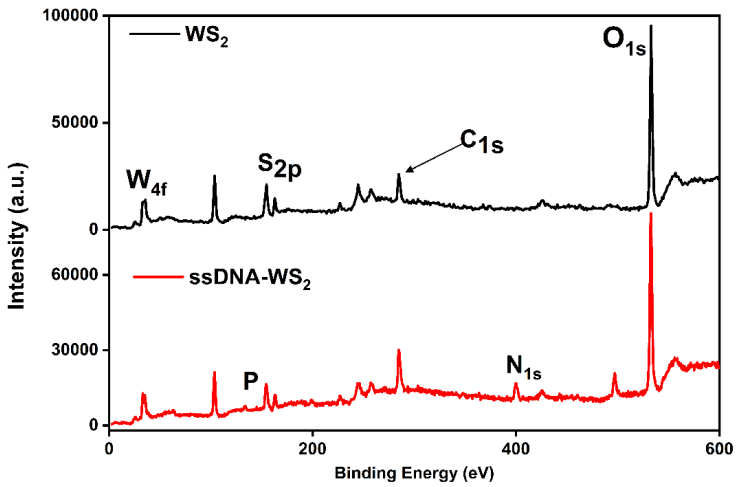

Figure 6.8: XPS survey spectrum of monolayer WS_2 before and after ssDNA aptamer functionalization.

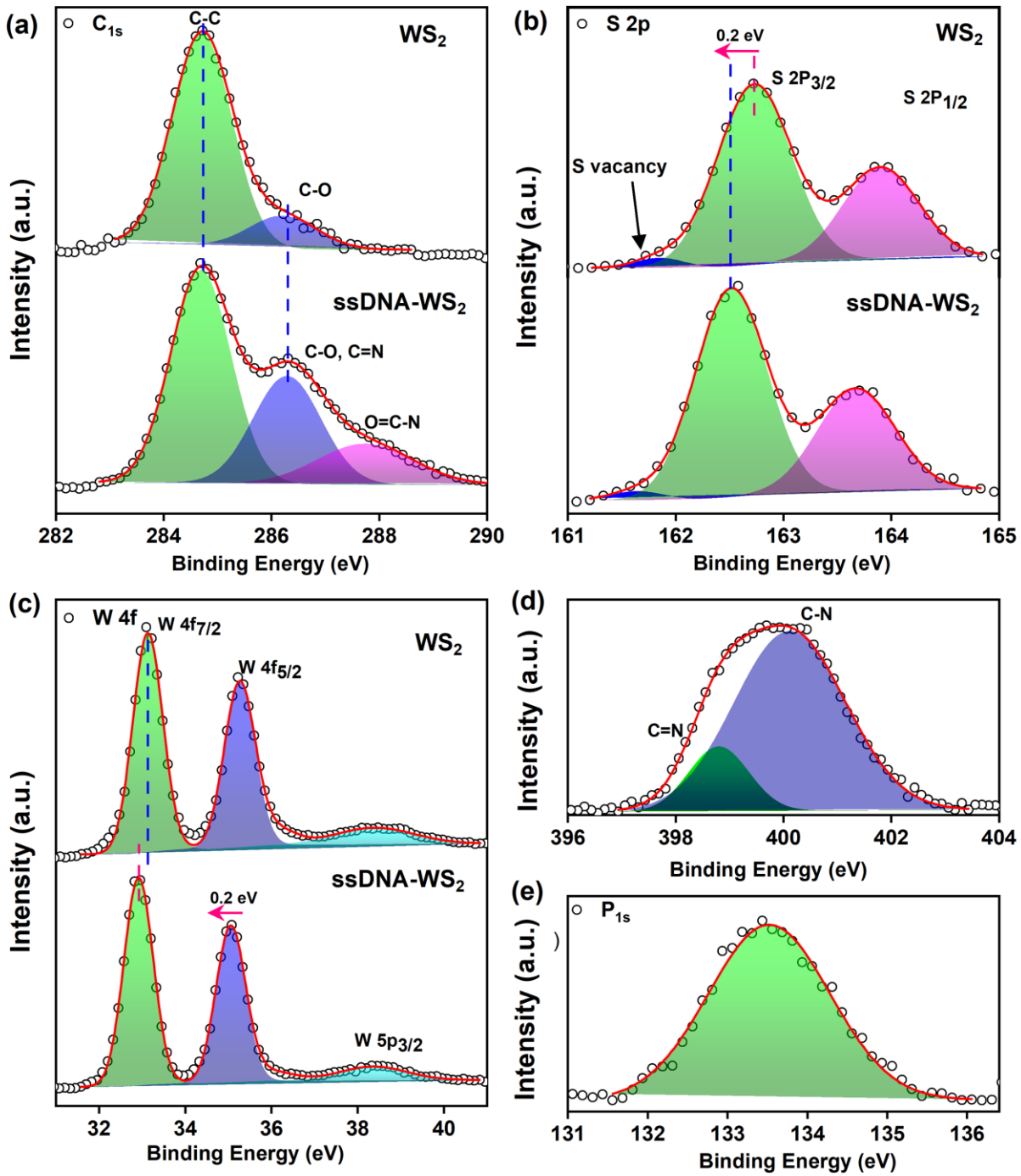

Figure 6.9: High-resolution XPS core binding energy spectra of (a) Carbon C_{1s}, (b) Sulfur S_{2p}, (c) Tungsten W_{4f}, (d) Nitrogen N_{1S}, and (e) Phosphorus $P_{1s.}$

spectral weight) and a shoulder hump at 286.2 eV (representing 15.3% of spectral weight), indicative of C-O binding energy.[46] For the ssDNA aptamer functionalized 1L-WS_2, the prominent C-C peak spectral weight decreased to 53.2%, with an increase in the spectral intensity of the 286.2 eV peak from 15.3% to 30.5%. Additionally, a new broad peak emerges at 287.7 eV with a spectral weight of 16.3%, as illustrated in **Fig. 6.9(a)**. This is because of oxygen and nitrogen being inherently present in ssDNA aptamers. Consequently, the bonding of ssDNA with sulfur vacancy sites leads to an increase in oxygen species, resulting in a heightened spectral weight of the C-O peak and the emergence of an additional peak corresponding to the energy of the O=C−N bond.[19] Therefore, the high-resolution C_{1s} binding energy spectrum confirms the functionalization of 1L-WS_2 with thiol-modified ssDNA aptamers. The high-resolution core binding energy levels of sulfur 2p are shown in **Fig. 6.9(b)**. The high-resolution deconvoluted sulfur 2p binding energy spectra reveal a prominent doublet with a 1.2 eV separation, appearing at 162.7 eV and 163.9 eV, attributed to S $2p_{3/2}$ and S $2p_{1/2}$, respectively.[47] These peaks are associated with the S^{2-} reduction state, confirming the formation of hexagonal 2H phase WS_2. The presence of inherent sulfur vacancies on the WS_2 surface is linked to an additional lower energy peak at 161.6 eV, accounting for 3.2% of the spectral weight, which reduced to 1.8% for the thiol-modified ssDNA aptamer functionalized WS_2[48,49]. Employing the passivation of sulfur vacancy sites using thiol functional groups results in a 0.2 eV red shift in the sulfur 2p doublet, as depicted in **Fig. 6.9(b).** This is equivalent to a shift in the Fermi energy position by 0.2 eV towards the valence band due to the decrease in electron density through sulfur vacancy passivation, consistent with the Raman and PL analyses.[50,51] The two prominent peaks of W 4f are observed at 33.1 eV and 35.2 eV, respectively, corresponding to the $4f_{7/2}$ and $4f_{5/2}$ orbitals, indicative of the W^{4+} oxidation state, as depicted in **Fig. 6.9(c).** The presence of the W^{4+} oxidation peak verifies the synthesis of semiconducting 2H-phase WS_2.[52] Additionally, two other low-intensity peaks at higher energy levels, observed at 35.3 eV and 37.7 eV, respectively, correspond to the oxide $4f_{7/2}$ and $4f_{5/2}$ orbitals associated with the W^{6+} oxidation state. The presence of W^{6+} originated from the unreacted WO_3 precursor powder present on the substrate. After functionalization, there is a similar shift in the binding energies for W 4f, The symbols are experimental data, and the solid lines are fitted spectra. approximately 0.2 eV, towards lower energy, as observed in S 2p. The stoichiometry of W and S in1L-WS_2 before and after functionalization is determined using the fitted XPS curves. The presence of sulfur vacancies in the 1L-WS_2 results in an S/W ratio of 1.85, which is lower than the expected/ideal

value of 2.0. This ratio subsequently increases to 1.95 after vacancy passivation by thiol functional groups, confirming the covalent attachment of ssDNA aptamers to the sulfur vacancy sites. Further confirmation was established by the presence of nitrogen and phosphorus in ssDNA functionalized 1L-WS_2, as shown in **Fig. 6.9(d) and 6.9(e),** respectively. These two elements are integral parts of ssDNA and were not present in bare 1L-WS_2.

6.3.3. Surface Functionalization

Functionalizing sensing surfaces with suitable probes enhances the selective detection of analytes, particularly in the presence of other similar analytes. Monolayer WS_2 without sulfur vacancies and defect sites are very stable and can only be weakly functionalized by weak van der Waals forces between the probes and basal plane of 1L-WS_2.[40] The presence of sulfur vacancies and defect sites can be utilized for the covalent functionalization of 1L-WS_2 flakes with suitable functional groups, especially thiols.[33,34] Hence, the ssDNA aptamer was modified with thiol functional groups to achieve covalent functionalization with WS_2 via sulfur vacancy sites.[33] The thiol attachments to the vacancy sites were analyzed using Raman, PL, and XPS spectroscopies. In the Raman spectroscopy analysis, we observed a decreased FWHM in the A_{1g} mode, which is a doping-sensitive out-of-plane vibration mode, indicating a reduction in electron density in WS_2 after functionalization.[36] This reduction in electron density could have originated from p-type doping in WS_2 by ssDNA aptamers or the passivation of electron-donating sulfur vacancies in WS_2 via thiol functional groups.[39] Furthermore, the enhancement in neutral excitons and the reduction in trions observed in the PL emission spectra after functionalization (as shown in **Fig. 6.4**) further support the assertion of sulfur vacancy passivation.[33] The final confirmation of the thiol attachments to the sulfur vacancy sites and ssDNA functionalization of 1L-WS_2 was obtained via XPS spectroscopy. The presence of nitrogen and phosphorus in the survey spectra shown in **Fig. 6.8** confirms the covalent binding of thiol functional groups to the sulfur vacancy sites, as both of these elements are inherently present only in thiol-modified ssDNA. The high-resolution spectra for N_{1s} and P_{1s} are shown in **Fig. 6.9 (d) and (e),** respectively. The effect of ssDNA functionalization on the WS_2 surface significantly affects the C_{1s} orbital binding energy spectrum, as depicted in **Fig. 6.9 (a).** The origin of additional oxygen species in the ssDNA aptamers enhances the spectral weight of the second peak at 286.2 eV from 15.3% to 30.5%. The additional peak at 287.7 eV is only observable in functionalized WS_2, arising from O-C=N bonding, with a spectral weight of 16.2%.

These changes in the C_{1s} spectrum are clearly attributed to thiol attachments to 1L-WS_2. Now, the intensity of the sulfur vacancy peak at 161.8 eV decreases from 2.5 % to 1.6 %, with no significant changes in the S^{2-} reduction and W^{4+} oxidation peaks, indicating the passivation of vacancy sites via the thiol functional group. The sulfur vacancy sites in WS_2 increase the electron density as they behave like electron donors, and the passivation of these vacancy sites decreases the electron density[39]. In the case of ssDNA-functionalized WS_2, both peaks exhibit a redshift of 0.2 eV compared to non-functionalized WS_2, indicating a corresponding shift of the Fermi energy level by 0.2 eV towards the valence band edge.[50,51] This shift is equivalent to p-type doping in 1L-WS_2, resulting from the attachment of thiol-modified ssDNA aptamers to the sulfur vacancy sites. Thus, the thiol-modified ssDNA aptamers were efficiently attached to the sulfur vacancy sites.

6.3.4. Sensing of *S. aureus* via 1L-WS_2

The PL emission spectrum of 1L-WS_2 is significantly affected by external charged doping. Using this phenomenon, *S. aureus* bacteria were detected through the modification of the PL emission spectrum of 1L-WS_2. **Fig. 6.10(a)** illustrates the PL spectra of 1L-WS_2 in the presence of various concentrations of *S. aureus*. We have noticed a significant blueshift (towards shorter wavelengths) by 53 meV in the neutral exciton peak, with the peak maxima shifting from 630 nm to 613 nm. The change in the spectrum is ascribed to the interaction between 1L-WS_2 and *S.aureus*. Alongside the shift in the neutral excitation peak, there is an increased trion contribution resulting from charge

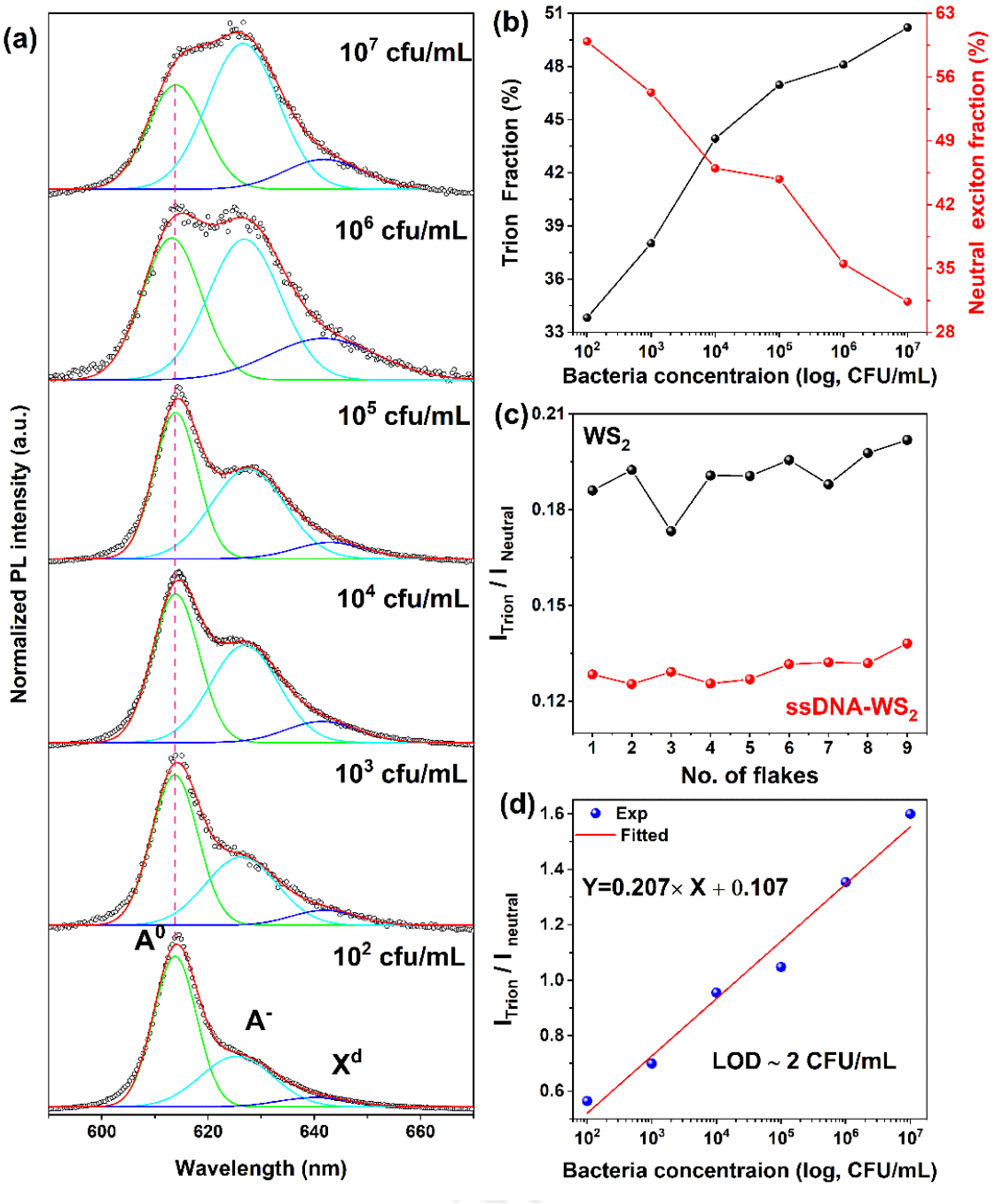

Figure 6.10: (a) Fitted PL emission spectra of ssDNA aptamer functionalized monolayer WS_2 in the presence of different concentrations of S. aureus. (b) Integral trion and neutral exciton spectral weight of the PL emission of functionalized monolayer WS_2 in the presence of different concentration S. aureus. (c) The spectral weight ratio of trion to neutral exciton in 1L-WS_2 before and after aptamer functionalization. (d) Calibration curve between S. aureus concentrations and ratio of integral trion to neutral exciton intensities.

transfer to WS_2 from *S. aureus.* The trion contribution increases with increasing concentrations of bacteria, surpassing the neutral exciton contribution at higher concentrations of bacteria. This occurs due to a more significant transfer of charges to WS_2 from a larger quantity of *S. aureus* bacteria at higher concentrations. The variation of the integral peak intensity of trions and neutral excitons is shown in **Fig. 6.10 (b).** At low concentrations, the integral trion to exciton spectral weight increases systematically with the increasing concentration of *S. aureus*, but it slows down at higher concentrations due to a lack of sufficient sites for interactions and, thus, limited charge transfer. As a result of this charge transfer, the integral spectral weight of the neutral exciton decreases due to its conversion into a charged trion. **Fig. 6.10 (d)** illustrates the variation of the ratio of trion to neutral exciton spectral weight with *S. aureus* concentration. We plotted the ratio of spectral weight between trion to neutral excitons against the logarithm of *S. aureus* concentrations to establish the calibration curve, as we vary the concentration over several orders

Table 6.2: Comparison of our 1L-WS_2 sensing platform with previous reports for S. aureus sensing.

Material	Methods	Linear range CFU/mL	Lower detection limit (CFU/mL)	Response Time (minutes)	Reference
Carbon Nanotubes	Electrochemical	8×10^2 - 1×10^3	800	02	Reference [13]
Au and Magnetic NPs	Colorimetric	1.5×10^2 - 1.5×10^6	1500	40	Reference [15]
Vancocin and pig immunoglobulin G (IgG) complex	Fluorimetric Assay	1×10^3 - 1×10^9	2900	130	Reference [17]
Polyelectrolyte	Long-period fiber gratings	1×10^4 - 1×10^8	224	30	Reference [3]
IgG functionalized fiber coupler	Fiber biosensor	7×10^1 - 7×10^4	3.1	40	Reference [14]
Multi-Walled CNT	Electrochemical	3×10^0 - 3×10^7	3.0	30	Reference [12]
RNA complex	Fluorescence	10^0 - 10^7	1	240	Reference [18]
Polydimethylsiloxane	Fluorescence	10^1 - 10^7	11.12	120	Reference [16]
Poly-l-Lysine-Functionalized Magnetic Beads	Polymerase chain reaction	1.8×10^1 - 1.8×10^6	18	240	Reference [9]
WS_2 QDs	Fluorescence	10^3 - 10^7	850	15	Reference [19]
1L-WS_2	Photoluminescence	10^2 - 10^7	2	15	*This work*

of magnitude. The strong correlation observed between the trion-to-neutral exciton intensity ratio (y) and *S. aureus* concentration (x) follows a linear equation: $y = 0.207x + 0.107$ (with an R^2 value of 0.98) within the wide range of 10^2 to 10^7 CFU/mL. Hence, utilizing the trion-to-neutral excitation peak intensity ratio from the calibration curve enables the identification and quantification of unknown concentrations of *S. aureus*. The linearly fitted calibration curve was utilized to find out the lower detection limit using the formula, $LOD = \frac{3.3 \times S_{dy}}{S}$, where S_{dy} represents the standard deviation of the y-intercept and S denotes the slope of the curve. This yields a very low detection limit of approximately 2 CFU/mL, which is outstanding. The performance of the proposed sensing system was compared with previously reported detections of *S. aureus*, as summarized in **Table 6.2**, showing the superiority of our sensing approach.

6.3.5. Sensitivity and Selectivity

Selectively detecting bacteria is essential to using specific anti-bacterial drugs to treat bacterial infections. To check the specific detection of *S. aureus* in the presence of other bacteria, we have studied the PL emission of 1L-WS_2 in the presence of *S. aureus* and *E. coli* under the same experimental conditions at 10^5 CFU/mL, as shown in **Fig. 6.11**. As we can see, in the presence of the targeted *S. aureus*, there is a noticeable shift in the PL spectrum. The neutral exciton peak shows a 17 nm blue shift in the PL spectra (from 630 nm to 613 nm) with an enhanced integral

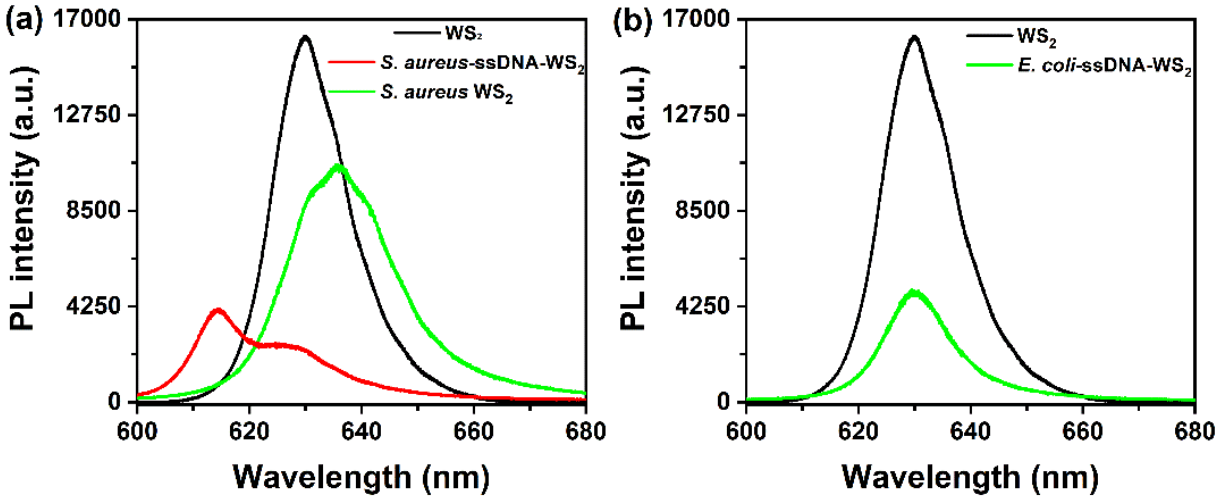

Figure 6.11: PL emission of spectra of monolayer WS_2 in the presence of 10^5 CFU/mL concentration of (a) targeted *S. aureus*, and (b) non-targeted *E. coli*.

trion spectral weight with the peak maxima at 624 nm, as shown in **Fig. 6.11(a).** In contrast, there is no shift in the PL emission peak position (630 nm) in the presence of non-targeted *E. coli*. This indicates that the selective capture of *S. aureus* by the probe ssDNA introduces negative charges to the WS_2 surface, resulting in PL quenching due to the enhanced trion contribution. In contrast, when *E. coli* is added, the probe ssDNA is unable to capture; hence, no charge transfer occurs between *E. coli* and 1L-WS_2. The marginal change in the PL intensity can be attributed to the ions present on the PBS solution adsorption on the WS_2 surface. Thus, our experimental findings imply that the 1L-WS_2-based biosensor exhibits excellent selectivity for its targeted bacteria. Additionally, the PL emission of 1L-WS_2 in the presence of *S. aureus* without an ssDNA aptamer probe does not exhibit any shift in the PL maxima, as shown in **Fig.6.11(a).** This is because *S. aureus* is not able to bind to 1L-WS_2. As a result, they are washed out during washing with PBS solution and nitrogen drying. However, there is a quenching of PL as well as slightly increased trion concentration because of the presence of various ions in the PBS solutions. The fitted PL emission curve of 1L-WS_2 in presence of 10^5 CFU/mL is shown in **Fig. 6.12.** Even though the trion fraction increases as compared to pristine WS_2 but much lower than that of aptamer functionalized 1L-WS_2. Thus, there is a need for functionalization for selectively capturing the targeted *S. aureus*.

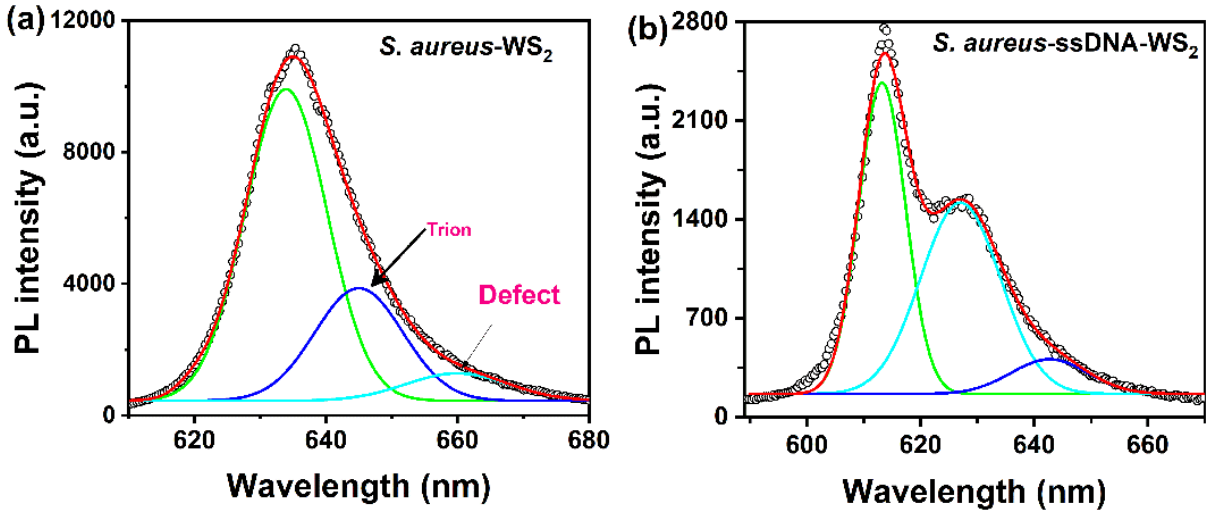

Figure 6.12: (a) PL emission of 1L-WS_2 in the presence of 10^5 CFU/mL *S.aureus* concentration without ssDNA functionalization; (b) PL emission of 1L-WS_2 in the presence of 10^5 CFU/mL *S.aureus* concentration with ssDNA functionalization.

6.3.6. Repeatability and sensing in a human urine sample

To check the reproducibility, we have studied the PL emission of three different samples of 1L-WS_2 in the presence of 10^5 CFU/mL concentration of *S. aureus*, as shown in **Fig. 6.13(a).** There is a marginal variation in the trion-to-neutral exciton ratio, though the shape of the curve remains unchanged. Thus, the reproducibility of the results is ensured. To evaluate the applicability of the proposed sensing system in detecting *S. aureus* in biological fluids, sensing of *S. aureus* in human urine was conducted. For that, we have added S. aureus in healthy human urine and recorded the PL emission of 1L-WS_2 in the presence of S. aureus in urine, as shown in **Fig. 6.13(b).** We observed an expected shift in the PL emission spectra with an enhanced trion- to neutral spectral ratio. For a concentration of 10^5 CFU/mL of *S. aureus* in urine, the trion-to-neutral excitation ratio was found to be 1.40, which is close to the expected value of 1.15 according to the calibration curve. Thus, the sensing system can identify a concentration of 10^5 CFU/mL of *S. aureus* with ~78% accuracy in healthy human urine. The increased trion-to-neutral exciton spectral ratio, as compared to the expected value of 1.15, can be attributed to the presence of other ions in human urine. The proposed sensor is capable of sensing complex real-world samples for practical application

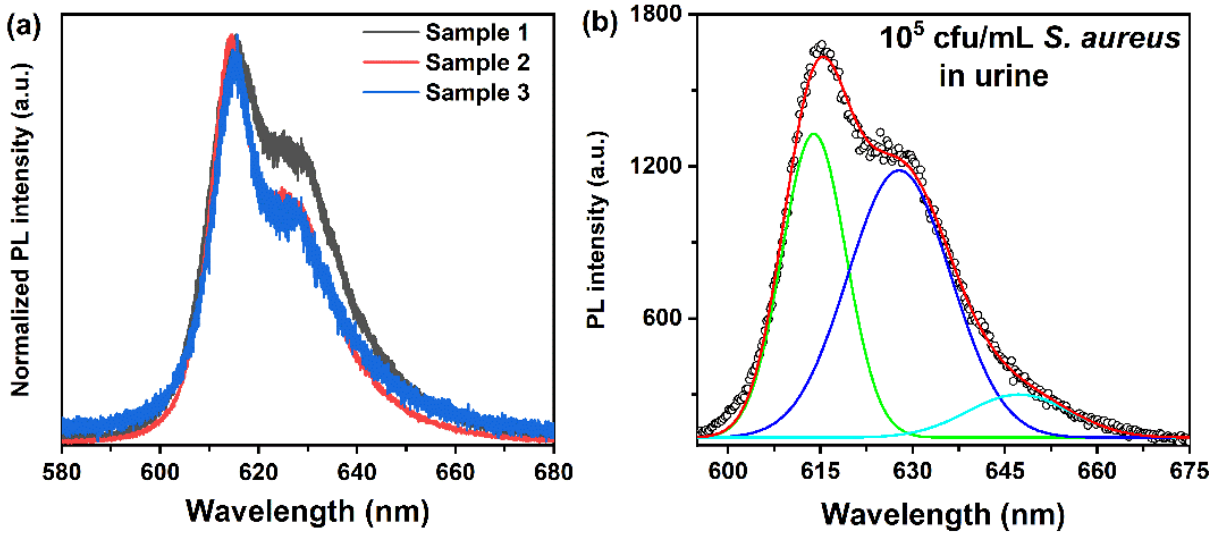

Figure 6.13: (a) The PL emission of three different monolayer WS_2 in presence of 10^5 CFU/mL concentration of S. aureus. (b) The PL emission of 1L-WS_2 in presence of S. aureus in human urine.

6.3.7. Sensing mechanism

The underlying sensing mechanism behind the above results is depicted schematically in **figure 6.14**. The critical ingredients for the sensing are the sulfur vacancies in 1L-WS_2 and its interaction

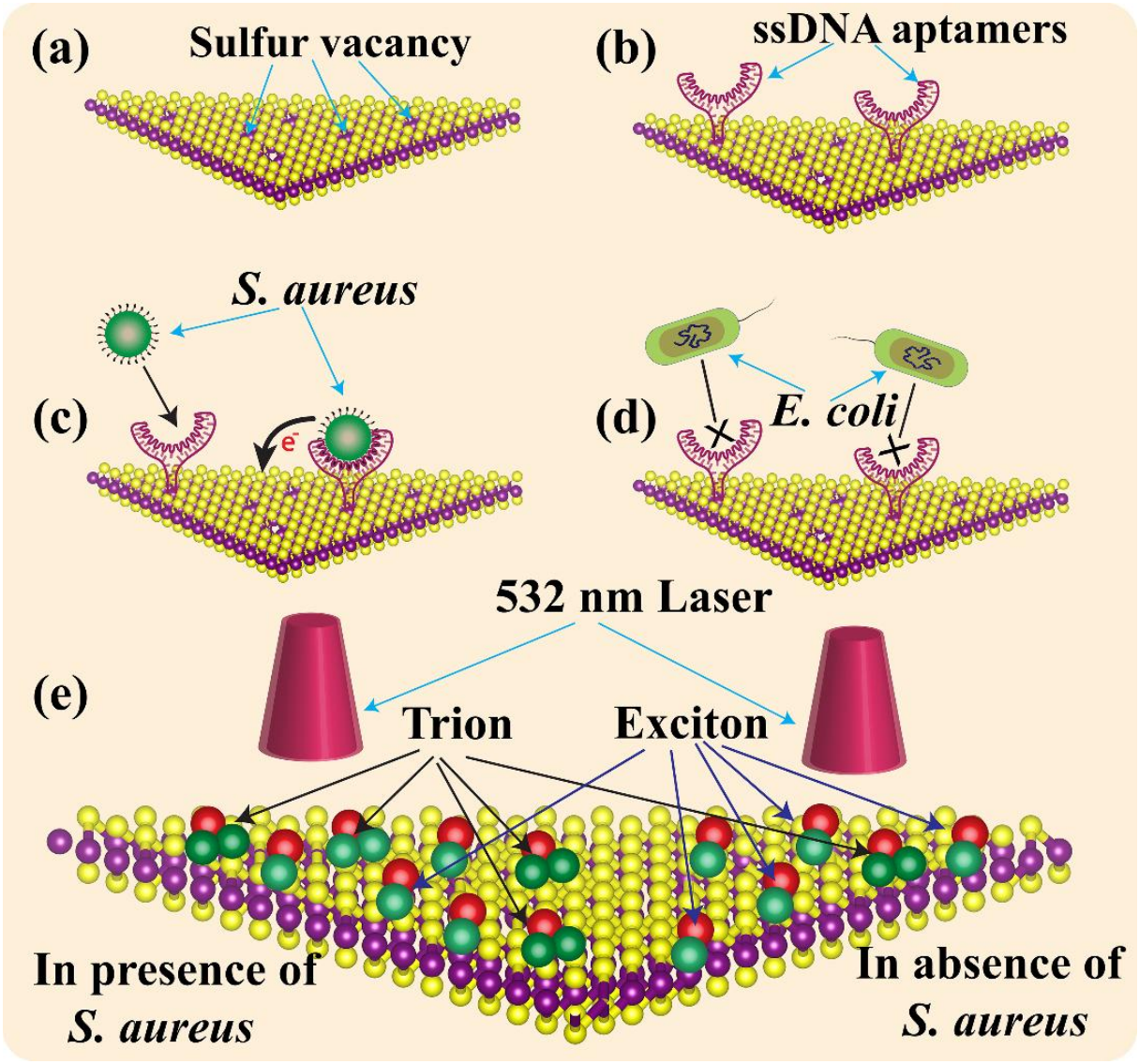

Figure 6.14: Schematic of the sensing mechanism of the proposed biosensor: (a) CVD-grown monolayer WS_2 with sulfur vacancies, (b) Thiol-modified ssDNA aptamer attached to the sulfur vacancy sites, (c) Targeted S. aureus are attached to the binding sides of ssDNA aptamer resulting in charge (electron) transfer to 1L-WS_2, (d) Non-targeted E. coli is not able to bind with ssDNA aptamers and hence negligible charge

transfer, (e) Schematics representation of trion and exciton formation dynamics in monolayer WS_2 in presence and absence of S. aureus.

with bacteria through the thiol functional groups. The presence of sulfur vacancies in the CVD-grown1L-WS_2, confirmed by XPS and PL spectroscopies, is illustrated in **Fig. 6.14 (a)**. The covalent interaction between sulfur vacancy sites and thiol functional groups facilitates bonding between thiol-modified ssDNA aptamers and 1L-WS_2, as depicted in **Fig. 6.14 (b)**. This bonding of ssDNA aptamers with 1L-WS_2 reduces the sulfur vacancy sites, as confirmed by PL, Raman, and XPS spectroscopy, resulting in lower electron-phonon coupling. The ssDNA aptamers exhibit high selectivity towards targeted analytes; hence, in the presence of targeted *S. aureus*, ssDNA aptamers identify and capture the target analyte, as shown in **Fig. 6.14 (c)**. This capture of analyte results in the charge transfer from *S. aureus* to the 1L-WS_2, thereby enhancing trion (negatively charged exciton) concentration and inducing a resulting shift in the PL emission peak due to relative change of spectral weights. In contrast, the ssDNA probe hinders the interaction between non-targeted E. coli and 1L-WS_2, leading to no alteration in the PL emission spectrum, as illustrated in **Fig. 6.14 (d)**. Consequently, the suggested sensing system offers highly selective detection of *S. aureus* at ultralow levels as monitored in terms of the relative population of trions in the system and paves the way for exploring other biomarkers through the use of appropriate probes and immobilization chemistry. **Fig. 6.14 (e)** illustrates that due to the electron transfer, there is a higher density of trions than neutral excitons in the presence of S. aureus, while this is absent in the presence of non-targeted bacteria.

6.4. Conclusions

In conclusion, we utilized the exceptionally high PL emission of 1L-WS_2 at room temperature, along with its intrinsic vacancy sites, for the label-free detection of *S. aureus* by a label-free, non-destructive optical technique. The 1L-WS_2 grown on SiO_2/Si substrates via the CVD method contains sulfur vacancy sites, as evidenced by XPS and PL spectroscopy, which form covalent bonds with thiol functional groups. Subsequently, a thiol functional group was added to the 5′ terminal of highly selective ssDNA aptamers targeting *S. aureus*. These thiol-modified ssDNA aptamers covalently bond with the sulfur vacancy sites in 1L-WS_2, resulting in enhanced PL emissions and reduced trion contributions. The passivation of sulfur vacancy sites also improves the S/W (sulfur to tungsten) ratio from 1.85 to 1.94 while shifting the Fermi position by 0.2 eV

towards the valence band. Furthermore, the binding of ssDNA aptamers with *S. aureus* alters the PL spectral shape of 1L-WS_2, with a blueshift of 54 meV. With increasing concentrations of *S. aureus*, PL quenches systematically due to the trion contribution surpassing that of neutral excitons at high concentrations. In contrast, for non-targeted *E. coli*, no change/shift in the PL emission spectrum is observed. Therefore, we have successfully detected *S. aureus* with very high sensitivity and selectivity by utilizing the systematic change in the intensity ratio of trion to neutral exciton peaks in the PL spectrum as quantification methods.

References

(1) Revelas, A. Healthcare – Associated Infections: A Public Health Problem. *Niger. Med. J.* 2012, *53* (2), 59. https://doi.org/10.4103/0300-1652.103543.

(2) Tong, S. Y. C.; Davis, J. S.; Eichenberger, E.; Holland, T. L.; Fowler, V. G. Staphylococcus Aureus Infections: Epidemiology, Pathophysiology, Clinical Manifestations, and Management. *Clin. Microbiol. Rev.* 2015, *28* (3), 603–661. https://doi.org/10.1128/CMR.00134-14.

(3) Yang, F.; Chang, T.-L.; Liu, T.; Wu, D.; Du, H.; Liang, J.; Tian, F. Label-Free Detection of Staphylococcus Aureus Bacteria Using Long-Period Fiber Gratings with Functional Polyelectrolyte Coatings. *Biosens. Bioelectron.* 2019, *133*, 147–153. https://doi.org/10.1016/j.bios.2019.03.024.

(4) van Hal, S. J.; Jensen, S. O.; Vaska, V. L.; Espedido, B. A.; Paterson, D. L.; Gosbell, I. B. Predictors of Mortality in Staphylococcus Aureus Bacteremia. *Clin. Microbiol. Rev.* 2012, *25* (2), 362–386. https://doi.org/10.1128/CMR.05022-11.

(5) Foster, T. J. Antibiotic Resistance in Staphylococcus Aureus. Current Status and Future Prospects. *FEMS Microbiol. Rev.* 2017, *41* (3), 430–449. https://doi.org/10.1093/femsre/fux007.

(6) Reardon, S. WHO Warns against "post-Antibiotic" Era. *Nature* 2014. https://doi.org/10.1038/nature.2014.15135.

(7) Adedeji, W. A. THE TREASURE CALLED ANTIBIOTICS. *Ann. Ib. Postgrad. Med.* 2016, *14* (2), 56–57.

(8) Brakstad, O. G.; Aasbakk, K.; Maeland, J. A. Detection of Staphylococcus Aureus by Polymerase Chain Reaction Amplification of the Nuc Gene. *J. Clin. Microbiol.* 1992, *30* (7), 1654–1660. https://doi.org/10.1128/jcm.30.7.1654-1660.1992.

(9) Deng, M.; Wang, Y.; Chen, G.; Liu, J.; Wang, Z.; Xu, H. Poly-l-Lysine-Functionalized Magnetic Beads Combined with Polymerase Chain Reaction for the Detection of Staphylococcus Aureus and Escherichia Coli O157:H7 in Milk. *J. Dairy Sci.* 2021, *104* (12), 12342–12352. https://doi.org/10.3168/jds.2021-20612.

(10) Trnčíková, T.; Hrušková, V.; Oravcová, K.; Pangallo, D.; Kaclíková, E. Rapid and Sensitive Detection of Staphylococcus Aureus in Food Using Selective Enrichment and Real-Time PCR Targeting a New Gene Marker. *Food Anal. Methods* 2008, *2* (4), 241. https://doi.org/10.1007/s12161-008-9056-x.

(11) Safdar, N.; Narans, L.; Gordon, B.; Maki, D. G. Comparison of Culture Screening Methods for Detection of Nasal Carriage of Methicillin-Resistant Staphylococcus Aureus: A Prospective Study Comparing 32 Methods. *J. Clin. Microbiol.* 2003, *41* (7), 3163–3166. https://doi.org/10.1128/JCM.41.7.3163-3166.2003.

(12) Farooq, U.; Ullah, M. W.; Yang, Q.; Aziz, A.; Xu, J.; Zhou, L.; Wang, S. High-Density Phage Particles Immobilization in Surface-Modified Bacterial Cellulose for Ultra-Sensitive and Selective Electrochemical Detection of Staphylococcus Aureus. *Biosens. Bioelectron.* 2020, *157*, 112163. https://doi.org/10.1016/j.bios.2020.112163.

(13) Zelada-Guillén, G. A.; Sebastián-Avila, J. L.; Blondeau, P.; Riu, J.; Rius, F. X. Label-Free Detection of Staphylococcus Aureus in Skin Using Real-Time Potentiometric Biosensors Based on Carbon Nanotubes and Aptamers. *Biosens. Bioelectron.* 2012, *31* (1), 226–232. https://doi.org/10.1016/j.bios.2011.10.021.

(14) Chen, L.; Leng, Y.-K.; Liu, B.; Liu, J.; Wan, S.-P.; Wu, T.; Yuan, J.; Shao, L.; Gu, G.; Fu, Y. Q.; Xu, H.; Xiong, Y.; He, X.-D.; Wu, Q. Ultrahigh-Sensitivity Label-Free Optical Fiber Biosensor Based on a Tapered Singlemode- No Core-Singlemode Coupler for Staphylococcus Aureus Detection. *Sens. Actuators B Chem.* 2020, *320*, 128283. https://doi.org/10.1016/j.snb.2020.128283.

(15) Sung, Y. J.; Suk, H.-J.; Sung, H. Y.; Li, T.; Poo, H.; Kim, M.-G. Novel Antibody/Gold Nanoparticle/Magnetic Nanoparticle Nanocomposites for Immunomagnetic Separation and Rapid Colorimetric Detection of Staphylococcus Aureus in Milk. *Biosens. Bioelectron.* 2013, *43*, 432–439. https://doi.org/10.1016/j.bios.2012.12.052.

(16) Guo, Y.; Li, J.; Song, X.; Xu, K.; Wang, J.; Zhao, C. Label-Free Detection of Staphylococcus Aureus Based on Bacteria-Imprinted Polymer and Turn-on Fluorescence Probes. *ACS Appl. Bio Mater.* 2021, *4* (1), 420–427. https://doi.org/10.1021/acsabm.0c00897.

(17) Kong, W.; Xiong, J.; Yue, H.; Fu, Z. Sandwich Fluorimetric Method for Specific Detection of Staphylococcus Aureus Based on Antibiotic-Affinity Strategy. *Anal. Chem.* **2015**, *87* (19), 9864–9868. https://doi.org/10.1021/acs.analchem.5b02301.

(18) Zhou, J.; Yin, L.; Dong, Y.; Peng, L.; Liu, G.; Man, S.; Ma, L. CRISPR-Cas13a Based Bacterial Detection Platform: Sensing Pathogen Staphylococcus Aureus in Food Samples. *Anal. Chim. Acta* 2020, *1127*, 225–233. https://doi.org/10.1016/j.aca.2020.06.041.

(19) Mia, A. K.; Bora, A.; Hossain, M. T.; Sinha, S.; Giri, P. K. Fast Detection of Staphylococcus Aureus Using Thiol-Functionalized WS_2 Quantum Dots and Bi2O2Se Nanosheets Hybrid Through Fluorescence Recovery Mechanism. *J. Mater. Chem. B* 2023. https://doi.org/10.1039/D3TB01465G.

(20) Mia, A. K.; Meyyappan, M.; Giri, P. K. Two-Dimensional Transition Metal Dichalcogenide Based Biosensors: From Fundamentals to Healthcare Applications. *Biosensors* 2023, *13* (2), 169. https://doi.org/10.3390/bios13020169.

(21) Mia, A. kaium; Bora, A.; Giri, P. K. Aptamer Functionalized CVD Grown Monolayer WS_2 Based FETs for Real-Time Detection of E. Coli. In *The Physics of Semiconductor Devices*; Singh, R., Singh, M., Kapoor, A., Eds.; Springer Nature: Singapore, 2024; pp 285–291. https://doi.org/10.1007/978-981-97-1571-8_33.

(22) Lan, C.; Li, C.; Ho, J. C.; Liu, Y. 2D WS_2: From Vapor Phase Synthesis to Device Applications. *Adv. Electron. Mater.* 2021, *7* (7), 2000688. https://doi.org/10.1002/aelm.202000688.

(23) Iqbal, M. W.; Iqbal, M. Z.; Khan, M. F.; Shehzad, M. A.; Seo, Y.; Park, J. H.; Hwang, C.; Eom, J. High-Mobility and Air-Stable Single-Layer WS_2 Field-Effect Transistors

Sandwiched between Chemical Vapor Deposition-Grown Hexagonal BN Films. *Sci. Rep.* 2015, *5* (1), 10699. https://doi.org/10.1038/srep10699.

(24) Ovchinnikov, D.; Allain, A.; Huang, Y.-S.; Dumcenco, D.; Kis, A. Electrical Transport Properties of Single-Layer WS_2. *ACS Nano* 2014, *8* (8), 8174–8181. https://doi.org/10.1021/nn502362b.

(25) Epstein, I.; Terrés, B.; Chaves, A. J.; Pusapati, V.-V.; Rhodes, D. A.; Frank, B.; Zimmermann, V.; Qin, Y.; Watanabe, K.; Taniguchi, T.; Giessen, H.; Tongay, S.; Hone, J. C.; Peres, N. M. R.; Koppens, F. H. L. Near-Unity Light Absorption in a Monolayer WS_2 Van Der Waals Heterostructure Cavity. *Nano Lett.* 2020, *20* (5), 3545–3552. https://doi.org/10.1021/acs.nanolett.0c00492.

(26) Mia, A. K.; Meyyappan, M.; Giri, P. K. Asymmetric Contact-Induced Selective Doping of CVD-Grown Bilayer WS_2 and Its Application in High-Performance Photodetection with Ultralow Dark Current. *Nanoscale* 2024. https://doi.org/10.1039/D3NR06118C.

(27) Wang, S.; Zhang, Y.; Ning, Y.; Zhang, G.-J. A WS 2 Nanosheet-Based Platform for Fluorescent DNA Detection via PNA–DNA Hybridization. *Analyst* 2015, *140* (2), 434–439. https://doi.org/10.1039/C4AN01738B.

(28) Xi, Q.; Zhou, D.-M.; Kan, Y.-Y.; Ge, J.; Wu, Z.-K.; Yu, R.-Q.; Jiang, J.-H. Highly Sensitive and Selective Strategy for MicroRNA Detection Based on WS_2 Nanosheet Mediated Fluorescence Quenching and Duplex-Specific Nuclease Signal Amplification. *Anal. Chem.* 2014, *86* (3), 1361–1365. https://doi.org/10.1021/ac403944c.

(29) Wang, P.; Wang, A.; Hassan, M. M.; Ouyang, Q.; Li, H.; Chen, Q. A Highly Sensitive Upconversion Nanoparticles-WS_2 Nanosheet Sensing Platform for Escherichia Coli Detection. *Sens. Actuators B Chem.* 2020, *320*, 128434. https://doi.org/10.1016/j.snb.2020.128434.

(30) Kong, R.-M.; Ding, L.; Wang, Z.; You, J.; Qu, F. A Novel Aptamer-Functionalized MoS_2 Nanosheet Fluorescent Biosensor for Sensitive Detection of Prostate Specific Antigen. *Anal. Bioanal. Chem.* 2015, *407* (2), 369–377. https://doi.org/10.1007/s00216-014-8267-9.

(31) Thakur, B.; Zhou, G.; Chang, J.; Pu, H.; Jin, B.; Sui, X.; Yuan, X.; Yang, C.-H.; Magruder, M.; Chen, J. Rapid Detection of Single E. Coli Bacteria Using a Graphene-Based Field-Effect Transistor Device. *Biosens. Bioelectron.* 2018, *110*, 16–22. https://doi.org/10.1016/j.bios.2018.03.014.

(32) Song, K.-M.; Lee, S.; Ban, C. Aptamers and Their Biological Applications. *Sensors* 2012, *12* (1), 612–631. https://doi.org/10.3390/s120100612.

(33) Bretscher, H.; Li, Z.; Xiao, J.; Qiu, D. Y.; Refaely-Abramson, S.; Alexander-Webber, J. A.; Tanoh, A.; Fan, Y.; Delport, G.; Williams, C. A.; Stranks, S. D.; Hofmann, S.; Neaton, J. B.; Louie, S. G.; Rao, A. Rational Passivation of Sulfur Vacancy Defects in Two-Dimensional Transition Metal Dichalcogenides. *ACS Nano* 2021, *15* (5), 8780–8789. https://doi.org/10.1021/acsnano.1c01220.

(34) Zhang, M.; Lihter, M.; Chen, T.-H.; Macha, M.; Rayabharam, A.; Banjac, K.; Zhao, Y.; Wang, Z.; Zhang, J.; Comtet, J.; Aluru, N. R.; Lingenfelder, M.; Kis, A.; Radenovic, A. Super-Resolved Optical Mapping of Reactive Sulfur-Vacancies in Two-Dimensional Transition Metal Dichalcogenides. *ACS Nano* 2021, *15* (4), 7168–7178. https://doi.org/10.1021/acsnano.1c00373.

(35) Berkdemir, A.; Gutiérrez, H. R.; Botello-Méndez, A. R.; Perea-López, N.; Elías, A. L.; Chia, C.-I.; Wang, B.; Crespi, V. H.; López-Urías, F.; Charlier, J.-C.; Terrones, H.; Terrones, M.

Identification of Individual and Few Layers of WS_2 Using Raman Spectroscopy. *Sci. Rep.* 2013, *3* (1), 1755. https://doi.org/10.1038/srep01755.

(36) Iqbal, M. W.; Shahzad, K.; Hussain, G.; Arshad, M. K.; Akbar, R.; Azam, S.; Aftab, S.; Alharbi, T.; Majid, A. Gate Dependent Phonon Shift in Tungsten Disulfide (WS_2) Field Effect Transistor. *Mater. Res. Express* 2019, *6* (11), 115909. https://doi.org/10.1088/2053-1591/ab485a.

(37) Wang, F.; Li, S.; Bissett, M. A.; Kinloch, I. A.; Li, Z.; Young, R. J. Strain Engineering in Monolayer WS_2 and WS_2 Nanocomposites. *2D Mater.* 2020, *7* (4), 045022. https://doi.org/10.1088/2053-1583/ababf1.

(38) Lu, X.; Utama, M. I. B.; Wang, X.; Xu, W.; Zhao, W.; Owen, M. H. S.; Xiong, Q. Gate-Tunable Resonant Raman Spectroscopy of Bilayer MoS_2. *Small* 2017, *13* (35), 1701039. https://doi.org/10.1002/smll.201701039.

(39) Yang, J.; Bussolotti, F.; Kawai, H.; Goh, K. E. J. Tuning the Conductivity Type in Monolayer WS_2 and MoS_2 by Sulfur Vacancies. *Phys. Status Solidi RRL – Rapid Res. Lett.* 2020, *14* (9), 2000248. https://doi.org/10.1002/pssr.202000248.

(40) Makarova, M.; Okawa, Y.; Aono, M. Selective Adsorption of Thiol Molecules at Sulfur Vacancies on MoS_2(0001), Followed by Vacancy Repair via S–C Dissociation. *J. Phys. Chem. C* 2012, *116* (42), 22411–22416. https://doi.org/10.1021/jp307267h.

(41) Xu, Z.; Lv, Y.; Li, J.; Huang, F.; Nie, P.; Zhang, S.; Zhao, S.; Zhao, S.; Wei, G. CVD Controlled Growth of Large-Scale WS_2 Monolayers. *RSC Adv.* 2019, *9* (51), 29628–29635. https://doi.org/10.1039/C9RA06219J.

(42) Gutiérrez, H. R.; Perea-López, N.; Elías, A. L.; Berkdemir, A.; Wang, B.; Lv, R.; López-Urías, F.; Crespi, V. H.; Terrones, H.; Terrones, M. Extraordinary Room-Temperature Photoluminescence in Triangular WS_2 Monolayers. *Nano Lett.* 2013, *13* (8), 3447–3454. https://doi.org/10.1021/nl3026357.

(43) Cao, Y.; Wood, S.; Richheimer, F.; Blakesley, J.; Young, R. J.; Castro, F. A. Enhancing and Quantifying Spatial Homogeneity in Monolayer WS_2. *Sci. Rep.* 2021, *11* (1), 14831. https://doi.org/10.1038/s41598-021-94263-9.

(44) Bora, A.; Mawlong, L. P. L.; Mia, A. K.; Giri, P. K. Manipulating Trion and Biexciton Emissions in Monolayer WS_2 by Sandwiching with Ultrathin ZnO Layers for Excitonic Light Emission Applications. *ACS Appl. Nano Mater.* 2024, *7* (8), 8612–8623. https://doi.org/10.1021/acsanm.3c06043.

(45) Catalán-Gómez, S.; Briones, M.; Cortijo-Campos, S.; García-Mendiola, T.; de Andrés, A.; Garg, S.; Kung, P.; Lorenzo, E.; Pau, J. L.; Redondo-Cubero, A. Breast Cancer Biomarker Detection through the Photoluminescence of Epitaxial Monolayer MoS_2 Flakes. *Sci. Rep.* 2020, *10* (1), 16039. https://doi.org/10.1038/s41598-020-73029-9.

(46) Ma, X.; Gao, F.; Liu, G.; Xie, Y.; Tu, X.; Li, Y.; Dai, R.; Qu, F.; Wang, W.; Lu, L. Sensitive Determination of Nitrite by Using an Electrode Modified with Hierarchical Three-Dimensional Tungsten Disulfide and Reduced Graphene Oxide Aerogel. *Microchim. Acta* 2019, *186* (5), 291. https://doi.org/10.1007/s00604-019-3379-8.

(47) Bora, A.; Mawlong, L. P.; Giri, P. K. Highly Suppressed Dark Current and Fast Photoresponse from Au Nanoparticle-Embedded, Si/Au/WS_2 Quantum-Dot-Based, Self-Biased Schottky Photodetectors. *ACS Appl. Electron. Mater.* 2021, *3* (11), 4891–4904.

(48) Donarelli, M.; Bisti, F.; Perrozzi, F.; Ottaviano, L. Tunable Sulfur Desorption in Exfoliated MoS_2 by Means of Thermal Annealing in Ultra-High Vacuum. *Chem. Phys. Lett.* 2013, *588*, 198–202. https://doi.org/10.1016/j.cplett.2013.10.034.

(49) Donarelli, M.; Prezioso, S.; Perrozzi, F.; Bisti, F.; Nardone, M.; Giancaterini, L.; Cantalini, C.; Ottaviano, L. Response to NO2 and Other Gases of Resistive Chemically Exfoliated MoS_2-Based Gas Sensors. *Sens. Actuators B Chem.* 2015, *207*, 602–613. https://doi.org/10.1016/j.snb.2014.10.099.

(50) Qin, Z.; Loh, L.; Wang, J.; Xu, X.; Zhang, Q.; Haas, B.; Alvarez, C.; Okuno, H.; Yong, J. Z.; Schultz, T.; Koch, N.; Dan, J.; Pennycook, S. J.; Zeng, D.; Bosman, M.; Eda, G. Growth of Nb-Doped Monolayer WS_2 by Liquid-Phase Precursor Mixing. *ACS Nano* 2019, *13* (9), 10768–10775. https://doi.org/10.1021/acsnano.9b05574.

(51) Rathod, U. P.; Egede, J.; Voevodin, A. A.; Shepherd, N. D. Extrinsic P-Type Doping of Few Layered WS_2 Films with Niobium by Pulsed Laser Deposition. *Appl. Phys. Lett.* 2018, *113* (6), 062106. https://doi.org/10.1063/1.5040119.

(52) McCreary, K. M.; Hanbicki, A. T.; Jernigan, G. G.; Culbertson, J. C.; Jonker, B. T. Synthesis of Large-Area WS_2 Monolayers with Exceptional Photoluminescence. *Sci. Rep.* 2016, *6* (1), 19159. https://doi.org/10.1038/srep19159.

Chapter 7

Fast Detection of *Staphylococcus aureus* using thiol-functionalized WS_2 Quantum Dots and Bi_2O_2Se Nanosheets Hybrid Through Photoluminescence Recovery Mechanism

This chapter presents a simple method for the detection of *S. aureus*, a harmful gram-positive human pathogenic bacterium using strong PL emission of WS_2 QDs. The WS_2 QDs of a mean diameter of 2.5 nm were synthesized by liquid exfoliation of bulk WS_2. Due to the quantum confinement effect, WS_2 QDs exhibit high PL emission under UV excitation. The addition of Bi_2O_2Se NSs resulted in the adsorption of WS_2 QDs on their surface, resulting in quenching of its PL emission through static quenching complex formation between WS_2 QDs and Bi_2O_2Se NSs. A specific sequencing ssDNA aptamer, which identifies and explicitly binds with *S. aureus*, was attached to the defect sites of WS_2 QDs for selective detection. The thiol-modified ssDNA aptamers attach covalently to the WS_2 QDs defect sites, which was confirmed by Raman and XPS. The interaction of *S. aureus* with aptamer functionalized WS_2 QDs weakens the van der Waals interaction between WS_2 QDs and Bi_2O_2Se nanosheets, which results in the detachment of WS_2 QDs from the Bi_2O_2Se nanosheet surface and restores PL intensity of WS_2 QDs. Similar measurements with non-targeted bacteria show that the system is selective towards *S. aureus*. Our PL-based biosensor has a linear response in the range 10^3-10^7 CFU/mL with a detection limit of 580 CFU/mL. We have observed a fast response time of 15 minutes for sensing, which is much faster than the previous reports. This proposed system was tested in human urine and can detect *S. aureus* in human urine sample selectively, proving its potential in real-life applications. The reported approach is versatile enough to sense other biomolecules and metal ions by choosing suitable receptors.

7.1. Introduction

The discovery of antibiotics that enabled treatments for various bacterial infections was a significant breakthrough in medical science[1,2]. However, antibiotic resistance has lately become one of the major challenges in global healthcare, as described by WHO. There is a fear among scientists of entering a post-antibiotic era where antibiotics will no longer be effective. Numerous reports suggest that excess and non-targeted usage of antibiotics has led to a surge in antibiotic

resistance[3,4]. Thus, the selective detection of bacteria is crucial for targeted antibiotic usage. The increasing antibiotic resistance in *S. aureus* is a matter of grave concern[5–7]. *S. aureus* is a gram-positive, spherical-shaped, human pathogenic bacterium commonly associated with various clinical infections such as septic arthritis[8–10]. The human body is a natural source of *S. aureus*. According to an estimation, almost 20 to 40 percent of the world population is colonized by *S. aureus*[11,12]. There is a higher risk of colonization among surgical patients, type 1 diabetes patients, and patients undergoing hemodialysis[13]. A wide range of bacterial infections, from simple skin diseases to life threatening conditions such as osteomyelitis, prosthetic device infections, pulmonary infections, and toxic shock syndrome, are caused by *S. aureus*[14,6]. *S. aureus*-related diseases are more likely when the skin's protective barrier or the mucosal barrier is compromised, allowing access to adjoining tissues or bloodstream[15]. *S. aureus* is also one of the most common food pathogens causing severe illnesses like diarrhoea[16,17]. UTIs are among the most common bacterial infections for women, with approximately 150 million cases reported yearly[18,19]. Although *S. aureus*-related UTIs are not so common in general, but for patients with urinary catheter devices, *S. aureus*-related UTIs are very common[7,20,21]. There is a high mortality rate due to infections caused by *S. aureus* bacteria, almost 20–30 percent of infected patients, even after effective antimicrobial treatments[22]. Thus, selective detection of *S. aureus* is essential for targeted therapies and misuse of antibiotics.

There are many methods for the detection of *S. aureus*, such as culture methods, PCR, and ELISA[23–26]. All these detection methods are time-consuming and require laboratory infrastructure and trained personnel. In comparison, the simple optical sensing of bioanalytes is very sensitive and can detect at significantly lower concentrations without the help of state-of-the-art detection systems[27,28]. The FRET is one such simple optical detection mechanism, where emission energy from a donor probe is transferred to the acceptor, that can help detect bioanalytes at low concentrations[29]. There have been many reports of FRET mechanism-based detection of bioanalytes but very few reports on bacterial detection[30–32]. Because of their highly photoluminescent characteristics, semiconducting QDs have recently been used in various applications, such as metal ion sensing, biomarker detection, and DNA hybridization using PL spectroscopy.[33,34] Due to their excellent properties, 2D WS_2 QDs are also utilized in sensing applications, but their utilization in the detection of bacteria has not yet been explored[35,36]. In the mechanism of FRET sensing, a photoluminescence quencher is required, which absorbs emissions

from the probe and quenches the probe's PL emission intensity[37]. Traditionally, TMDs nanosheets are used as quenchers in FRET-based biosensing applications[37–40], but Bi_2O_2Se can also quench the PL intensity by almost 90%, opening up a new sensing opportunity[41]. To our knowledge, there has been no report of potential biosensing applications of WS_2 QDs and Bi_2O_2Se NSs and WS_2 QDs/Bi_2O_2Se NSs composite. TMDs such as WS_2, MoS_2 etc., as well as Bi_2O_2Se have been known to exhibit excellent biocompatible and low toxicity[42–45]. They can be grown easily via simple synthesis strategies and are highly environmentally stable. Moreover, fascinating optical properties exhibited by highly photoluminescent WS_2 QDs and the quencher Bi_2O_2Se NSs are ideal for bacterial sensing mechanisms by FRET. Herein, we have explored the potential application of WS_2 QDs and Bi_2O_2Se NSs and WS_2 QDs/Bi_2O_2Se NSs composite in the detection of bacteria. The detector molecule plays an essential role in improving the selectivity of any biosensor in identifying the targeted analytes in complex environments[46]. Traditionally, antibodies are used as capture/detector molecules for biosensing applications, but ssDNA aptamers have recently emerged as alternative receptors in biosensing[47]. The aptamers are used for *S. aureus* detection through various highly sensitive and selective mechanisms [48]. The low cost, high thermal stability, easier modifications with excellent specificity, and smaller sizes make aptamers suitable as bioreceptors[49].

Herein, we have demonstrated *S. aureus* detection using aptamer functionalized WS_2 QDs and Bi_2O_2Se NSs with PL spectroscopy for the first time. We have synthesized the WS_2 QDs from bulk WS_2 using a probe sonicator and covalently functionalized them with thiol-modified ssDNA aptamer specific to *S. aureus*. The thiol-modified ssDNA aptamer functionalization of WS_2 QDs was verified by Raman and X-ray photoelectron spectroscopy (XPS) studies. It is shown that the excellent PL emission of WS_2 QDs was quenched by ~67% with Bi_2O_2Se NSs through the FRET mechanism. The FETEM images confirm the adsorption of WS_2 QDs on the Bi_2O_2Se NSs surface, resulting in PL quenching. The binding of *S. aureus* with the aptamer weakens the van der Waals interaction force between WS_2 QDs and Bi_2O_2Se NSs, resulting in detachment of WS_2 QDs, hence PL restoration. The higher bacteria concentration draws a greater number of WS_2 QDs from the Bi_2O_2Se NS surface, resulting higher PL enhancement. The specific aptamers do not bind to non-targeted bacteria, resulting in highly selective PL enhancement only for targeted *S. aureus*.

7.2. Experimental Details

7.2.1 Preparation of WS_2 QDs

A simple top-down chemical exfoliation technique was employed to synthesize the WS_2 QDs. Bulk WS_2 powder was dissolved in 30 mL of NMP at a concentration of 1 mg/mL. The solution in a glass beaker was sonicated in an ice-surrounded medium using an ultrasonic homogenizer (Sonic Ruptor 250, Omni International) with 40% output power and a frequency output of 20,000 cycles per second for 5 hours. High-energy pulses from a tip sonicator breaks the WS_2 sheets and forms small QDs during probe sonication. The functional groups in NMP help in layer intercalation and dispersion of QDs. The final solution containing NSs and QDs was heated at 120 °C using a magnetic stirrer at 400 rpm until the solvent dried out. The final product with known mass was centrifuged in ethanol at 12000 rpm at 4°C for 30 minutes to segregate the WS_2 QDs from few-layered nanosheets and residual bulk WS_2. The detailed schematic for the synthesis process is presented in **Fig. 7.1.**

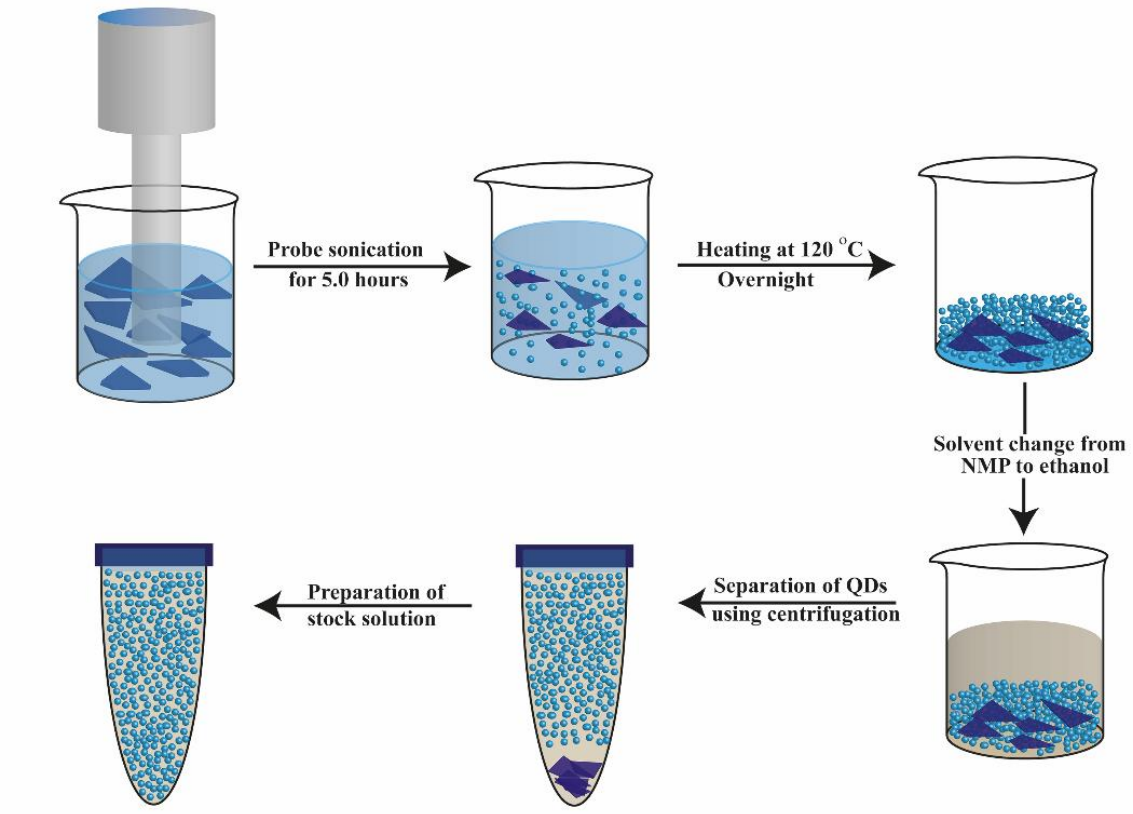

Figure 7.1: Schematic illustration of the synthesis of WS_2 QDs from bulk WS_2 powder

7.2.2 Synthesis of Bi_2O_2Se NSs

100 mg of $Bi(NO_3)_3 \cdot 5H_2O$ was mixed in 20 mL deionized (DI) water with the help of a magnetic stirrer at a temperature of 150°C at 550 rpm for 10 minutes. Subsequently, 13 mg of selenouria was added during this process, and 307 mg of EDTA after 10 minutes. Finally, 120 mg of KOH and 320 mg of NaOH were added to the solution and kept as it was for another 15 minutes. The final solution was centrifuged at 9000 rpm at 4 °C for 20 minutes in ethanol to remove residual impurities. The precipitate containing 2D Bi_2O_2Se NSs was then collected and centrifuged in DI water following similar conditions. The residue was then collected and kept at 80 ℃ inside a hot air oven for 24 hours, and thus, the Bi_2O_2Se NSs were obtained.

7.2.3 Aptamer Reduction and Functionalization with WS_2 QDs

The attached thiol functional group comes with disulfide bonds; for the functionalization of ssDNA aptamers with WS_2 QDSs, the disulfide bond was reduced by using TECP. For reduction, 10 mM of tris-HCl buffer solution at pH 8 was prepared in NF (nuclease-free) water, and subsequently, 10 mM TECP solution was prepared using that same Tris-HCl buffer. Finally, 50 µM of ssDNA aptamers was added to 10 mM TECP solution by equal volume and kept it at room temperature for 3.0 hours as per protocol by IDT. For the functionalization, WS_2 QDs were mixed with reduced aptamer solution and kept at 4°C for 24 hours before use.

7.2.4 Bacteria Culture and Aptamer Selection

All the bacterial strains: *Streptococcus aureus* (MTCC-9542), *Escherichia coli* (MTCC- 42), and *Klebsiella pneumoniae* (MTCC-7028) used in the present work were Indian isolates procured from MTCC (Microbial Type Culture Collection), Chandigarh, India**.** The aptamer selection process is discussed in section **6.2.2 of Chapter 6.**

7.2.5 Method of Detection

For the study of *S. aureus* sensing performance, serial dilution of *S. aureus* from 10^7 to 10^3 CFU/mL were prepared in 1X PBS solution. For sensing measurements,100 µL of bacteria solution with various concentrations was added to the 900 µL solutions containing aptamer functionalized WS_2 QDs and Bi_2O_2Se NSs solution. PL measurements were made after 15 minutes as we found a response time of around 15 minutes at optimum conditions. PL intensity is very low (at a minimum near the background) due to the quenching before adding bacterial solutions. To

minimize the effect of various ions present on the buffer solution, we measured the PL intensity with 100 µL of PBS without any bacteria and used it as background PL intensity. The biological medium samples were prepared in urine, and different concentrations of *S. aureus* were added to healthy human urine. For selectivity test, *E. coli* and *K. Pneumoniae* with 10^6 CFU/mL were prepared in same urine.

7.3 Results and Discussion

7.3.1 Structural and Chemical Analysis

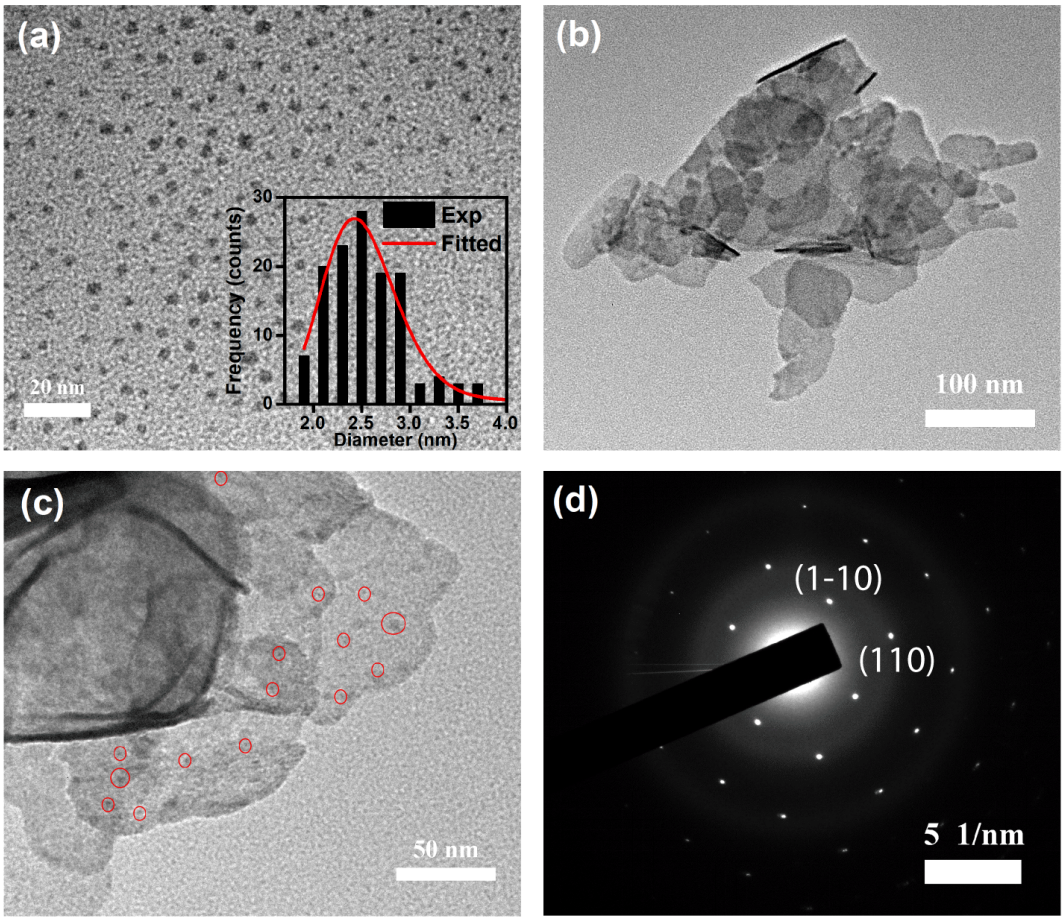

Figure 7.2: (a) FETEM image of as-synthesized WS_2 QDs; the inset shows the size distribution of WS_2 QDs with a log-normal fit. (b) FETEM image of Bi_2O_2Se NSs showing free-standing nanosheets of lateral size ~100 nm. (c) FETEM image of WS_2 QDs/Bi_2O_2Se NSs composite. The WS_2 QDs are adsorbed on the Bi_2O_2Se NS surface, as marked by the red circles. (d) SAED pattern of Bi_2O_2Se NSs showing high crystallinity.

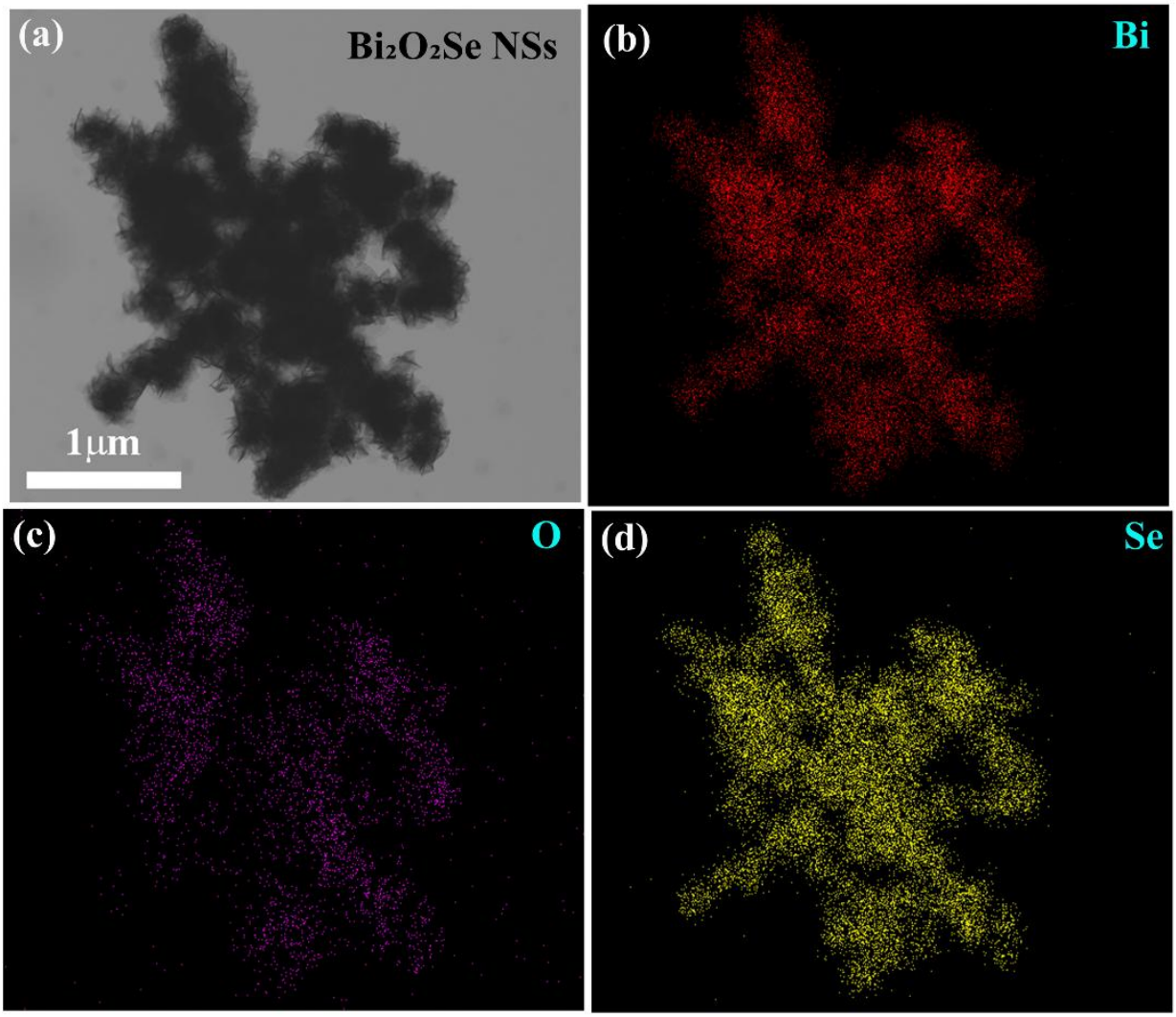

Figure 7.3: (a) Bright-field TEM image of Bi_2O_2Se NS. (b-d) The corresponding TEM elemental mapping of Bi, O, and Se

The uniform synthesis of WS_2 QDs was confirmed by field emission transmission electron microscopy (FETEM), as shown in **Fig. 7.2(a).** We have used the ImageJ software to determine the size distribution, which ranges from 1.9 to 3.6 nm. The size distribution was fitted with the log-normal function, which indicates the WS_2 QDs had a narrow size distribution with a mean diameter of 2.5 nm, as shown in the inset of **Fig. 7.2(a).** The FETEM image of chemically synthesized free-standing Bi_2O_2Se NSs is shown in **Fig. 7.2(b),** which reveals the size of the NSs are ~100 nm. When the NSs solutions are added to the WS_2 QDs solution, the ultra-small WS_2 QDs are adsorbed on the surface of Bi_2O_2Se NSs by week van der Waals force, which is evident from **Fig. 7.2(c).** The adsorbed WS_2 QDs are marked with red circles. The selected area electron

diffraction (SAED) pattern shown in **Fig.7.2(d)** reveals the tetragonal phase of Bi_2O_2Se NSs[50]. The chemical compositions were analyzed with elemental mapping using ener-rgy-dispersive X-ray spectroscopy (EDS) from the FETEM, as shown in **Fig. 7.3.** The elemental mapping shows atomic percentages of Bi, O and Se amounts to ~48.9%, ~17.6% and 33.5%, respectively. This amounts to an approximate composition of ~$Bi_2O_{0.7}Se_{1.4}$, which implies low oxygen content as compared to the desired atomic ratio of Bi:O:Se:2:2:1 for a stoichiometric Bi_2O_2Se. Thus, there are oxygen vacancy sites and excess selenium. The presence of O vacancy sites and excess selenium in chemically synthesized free-standing Bi_2O_2Se has been well explained by Hossain et al. [50].

The compositional information of samples was obtained by XPS. The survey scans XPS spectra of WS_2 QDs, aptamer functionalized WS_2 QDs, Bi_2O_2Se NSs, and WS_2 QDs/Bi_2O_2Se composite is shown in the stacked plot in **Fig. 7.4**. Since the WS_2 QDs were synthesized from commercial WS_2 bulk powder, the signature of tungsten and sulfur in the survey is as expected, as shown in **Fig. 7.4.** In the survey scan, in addition to the presence of carbon and oxygen, there is an intense peak at 400 eV corresponding to nitrogen, which arises because of the nitrogen content in the solvent N-Methyl-2-pyrrolidone (NMP). All the high-resolution XPS spectra plotted correspond to carbon C_{1s} at 284.8 eV, as shown in **Fig. 7.5(a).** The deconvoluted carbon spectrum for WS_2 QDs shows an intense peak at 284.8 eV corresponding to C-H binding energy (spectral weight 65%), as shown in **Fig. 7.5.** Two smaller humps at 286.1 eV and 288.1 eV correspond to the binding energy of C-N (spectral weight 24.5 %) and O=C-N (spectral weight 10.6%) bonds [51]. These two low-intensity peaks are due to nitrogen present in the solvent. The nitrogen functional groups present in NMP solvent help in the chemical exfoliation of bulk WS_2, and the high-power probe sonication breaks them into ultrathin and ultra-small WS_2 QDs[52]. For the WS_2 QDs/Bi_2O_2Se NSs composite, carbon C_{1s} spectra in **Fig. 7.5(a),** we have observed a significant decrease in spectral weight of the C-N bond from 24.5% to 5.5% and an increase for O=C-N bond from 10.6% to 15.5%, which are because of the oxygen present in Bi_2O_2Se NSs. The WS_2 QDs possess a large number of sulfur vacancies and defect sites. These sites aid in the binding of biomolecules, i.e., biofunctionalization. Detection of specific analytes in the presence of other analytes is an essential criterion for sensing applications. In this work, aptamers were covalently attached to the sulfur vacancy sites of WS_2 QD surface for specific detection of *S. aureus*. Thiol functional groups are known to form covalent bonds at sulfur vacancy sites of MoS_2 and WS_2[53–55]. As such, for the

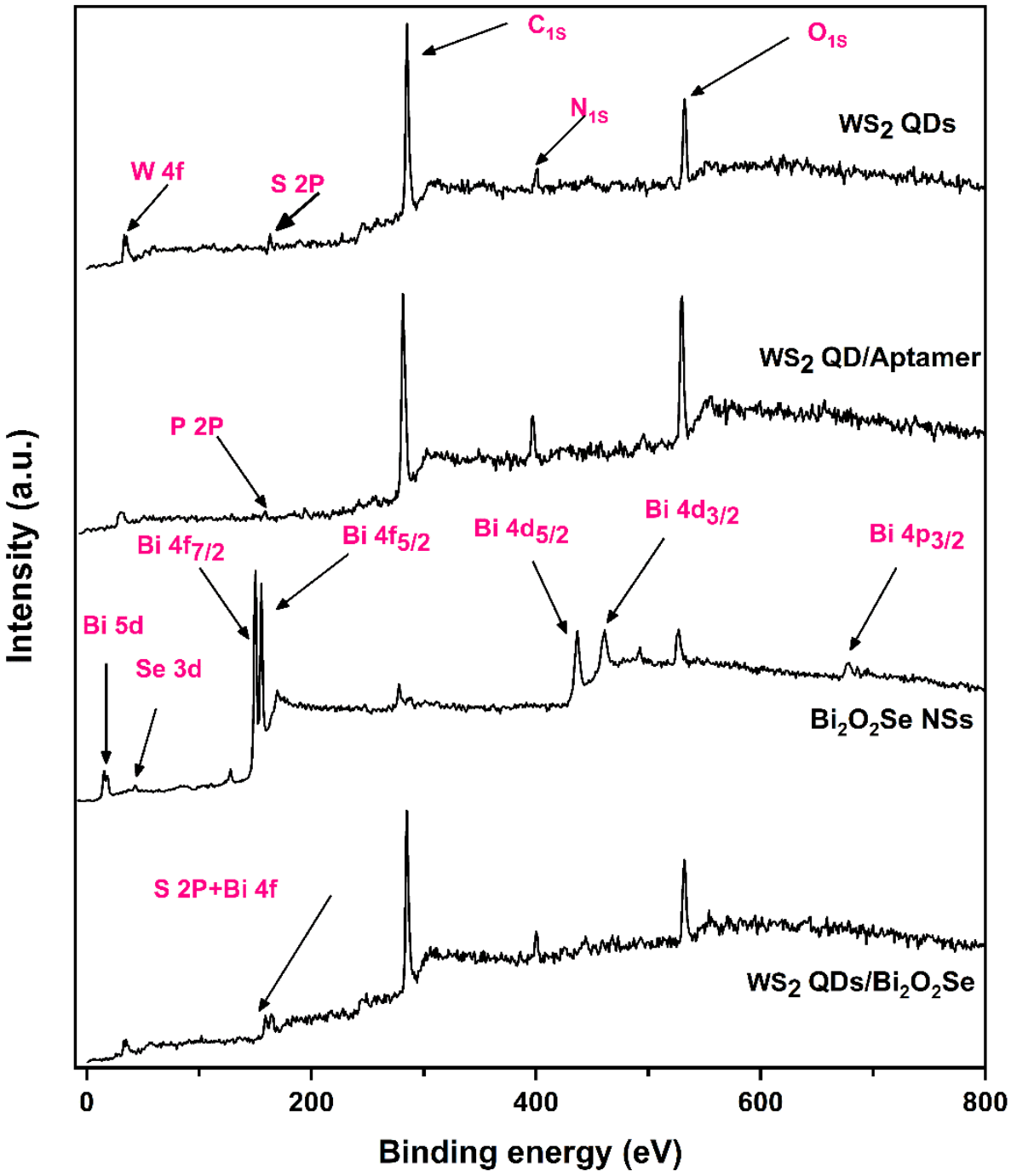

Figure 7.4: The XPS survey scan spectra of WS_2 QDs, aptamer functionalized WS_2 QDs, Bi_2O_2Se NS and the WS_2 QDs/Bi_2O_2Se NSs composite

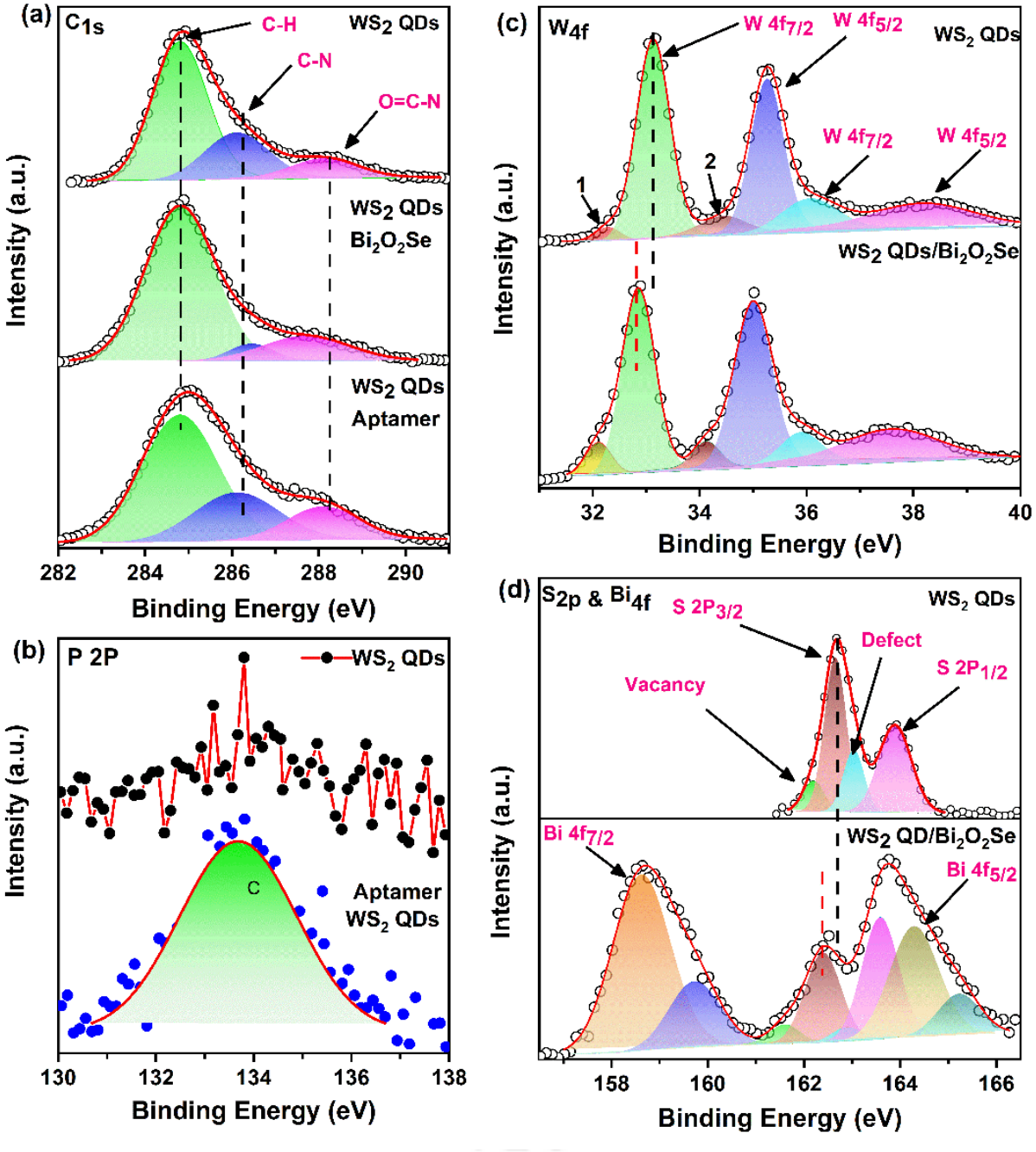

Figure 7.5: (a) XPS spectra of C1s for WS_2 QDs along with WS_2 QDs/Bi_2O_2Se NSs composite and aptamer functionalized WS_2 QDs from top to down. (b) Core binding energy spectrum for phosporus 2P for WS_2 QDs and the aptamer functionalized WS_2 QDs. Only presence for aptamer functionalized WS_2 QDs. (c) Binding energy spectra of W4f for WS_2 QDs and WS_2 QDs/Bi_2O_2Se NSs composite from top to bottom. (d) S 2p and Bi 4f binding energy spectrum. There are sharp peaks corresponding to Bi4f in addition to S2p for the composite

attachments of aptamers to the sulfur vacancies of WS_2 QDs surface, the 5´ terminal of the aptamer was modified with the thiol functional group. For the thiol-modified ssDNA aptamer attached WS_2 QDs, C_{1s} binding energy spectra is shown in **Fig. 7.5(a).** From the deconvoluted C_{1s} spectra, we can see that the C-N binding peak spectral weight is increased from 24 % to 26%, and the O=C-N bond has increased from 11 % to 13.7 %. The enhancement of this spectral weight can be attributed to the nitrogen and oxygen species present in the aptamers. To check the attachment of the aptamers to the WS_2 QDs, we have acquired the core level spectra corresponding to phosphorus 2p from the WS_2 QDs and WS_2 QDs/aptamer composite sample as shown in **Fig. 7.5(b)**. The aptamer-functionalized WS_2 QDs shows the P 2P at 133.6 eV, but there is no phosphorus signature in WS_2 QDs. The presence of phosphorus in the functionalized WS_2 QDs originated from the phosphate in ssDNA aptamer, confirming the attachments of aptamers on the WS_2 QDs surface[56]. Phosphorus originated from phosphate, one of the backbones for DNA aptamers. Comparative high-resolution core level spectra of tungsten for WS_2 QDs andWS_2/Bi_2O_2Se hybrid are shown in **Fig. 7.5 (c)**. The two prominent peaks with high intensity at 33.1 eV and 35.2 eV, separated by 2.1 eV, corresponding to the W $4f_{7/2}$ and W $4f_{5/2}$, respectively, and is associated with the W^{4+} oxidation state, which confirms the semiconducting 2H-phase of WS_2 QDs [57]. Along with the semiconducting 2H-phase, we have [58]. In addition, we observed two high energy peaks at 36.0 eV and 38.2 eV, corresponding 6^+ oxidation state of tungsten, indicating the presence of surface oxidized WS_2 QDs[59]. The high-resolution spectra of the core binding energy levels of sulfur for WS_2 QDs and WS_2/Bi_2O_2Se show two low energy peaks at 32.2 eV and 34.4 eV, corresponding to the metallic 1T-phase hybrid as shown in **Fig. 7.5 (d)**. The deconvoluted high-resolution spectra show a dominant sulfur doublet separated by 1.2 eV at 162.6 eV and 163.8 eV, corresponding to S $2p_{3/2}$ and S $2p_{1/2}$, respectively. The two prominent peaks are associated with the S^{2-} oxidation states, confirming the hexagonal 2H phase of semiconducting WS_2 QDs[60]. NMP-assisted chemical exfoliation in the presence of high-power probe sonication creates sulfur vacancies and defect sites on the WS_2 QDs surface. The deconvolution of S $2P_{3/2}$ peaks shows two low-intensity peaks at 262.2 eV and 263.0 eV having a spectral weight of 7.8% and 15.8%, respectively, which are related to the defects/impurity in WS_2 QDs[60–62]. The vacancies and defect sites are essential to modulate the material properties by attaching different functional groups for desired applications[63–65]. The sulfur to tungsten ratio calculated from the XPS is 1.46, implying the

presence of many sulfur vacancy sites. These sites are very important for the attachments of functional groups.

For the composite, the binding energy of tungsten and sulfur is downshifted by 0.3 eV, as shown in **Fig. 7.5(c) & (d)**. This is an indication of Fermi energy level shifting towards the valance band by the same amount, which equivalent to p-doping[66,67]. The electron transfer from WS_2 QDs to Bi_2O_2Se NSs may be due to surface defect passivation by oxygen present in NSs, causing the p-doping in WS_2 QDs. The composite material shows two sharp peaks at 158.6 eV and 164.0 eV, corresponding to Bi $4f_{7/2}$ and Bi $4f_{5/2,}$ respectively (Fig. 7.5(d))[68]. In addition to those sharp peaks, we have observed two additional low-intensity peaks at 159.7 eV and 165.2 eV due to Bi_2Se_3 bonding[69]. The binding energy spectra corresponding to the Sulfur of aptamer-modified WS_2 QDs was up shifted by 0.3 eV. The upshift of the binding energy indicates that the Fermi energy has moved by 0.3 eV towards conduction band, increasing the electron charge density[66]. The increase in electronic charge density is attributed to electron transfer from negatively charged aptamers to WS_2 QDs[70]. In addition to the shift, the spectral weight of the defect peak at 163.4 eV decreased to 3.0 % from 15.8 %, confirming the defect passivation of WS_2 QDs by thiol-modified aptamers. The passivation of defect sites by thiol-modified aptamers increases the Sulfur to tungsten ratio from 1.46 to 1.65.

The micro-Raman spectra of as-synthesized WS_2 QDs and WS_2 bulk powder were recorded using 532 nm laser excitation, as shown in **Fig. 7.6(a).** The two characteristic Raman modes for the bulk powder were observed at 355 cm^{-1} (E_{2g}) and 420.1 cm^{-1} (A_{1g}), corresponding to in-plane and out-of-plane vibrational modes of WS_2, respectively[71]. The fitted Raman spectra are shown in **Fig.3.5 (b).** The high-intensity Raman mode at 350.4 cm^{-1} corresponds to the 2LA phonon mode. It has been reported that the A_{1g} mode is sensitive to charge doping, while the E_{2g} mode is sensitive to induced strain[72]. For WS_2 QDs, there is no significant change in the peak positions as compared to bulk WS_2 powder, but the ratio of area under A_{1g} to E_{2g} mode increases significantly from 1.5 to 2.75 when bulk WS_2 were converted to WS_2 QDs. The enhanced A_{1g} mode intensity is attributed to the higher electron density caused by the sulfur vacancy and defect sites, which enhances electron-phonon coupling.[72,73] For the aptamer functionalized WS_2 QDs, the smaller size and negatively charged aptamers upon binding with the WS_2 QDs make WS_2 QDs more negatively charged via electron transfer from aptamer to WS_2 QDs[70]. From Raman analysis, we observed that

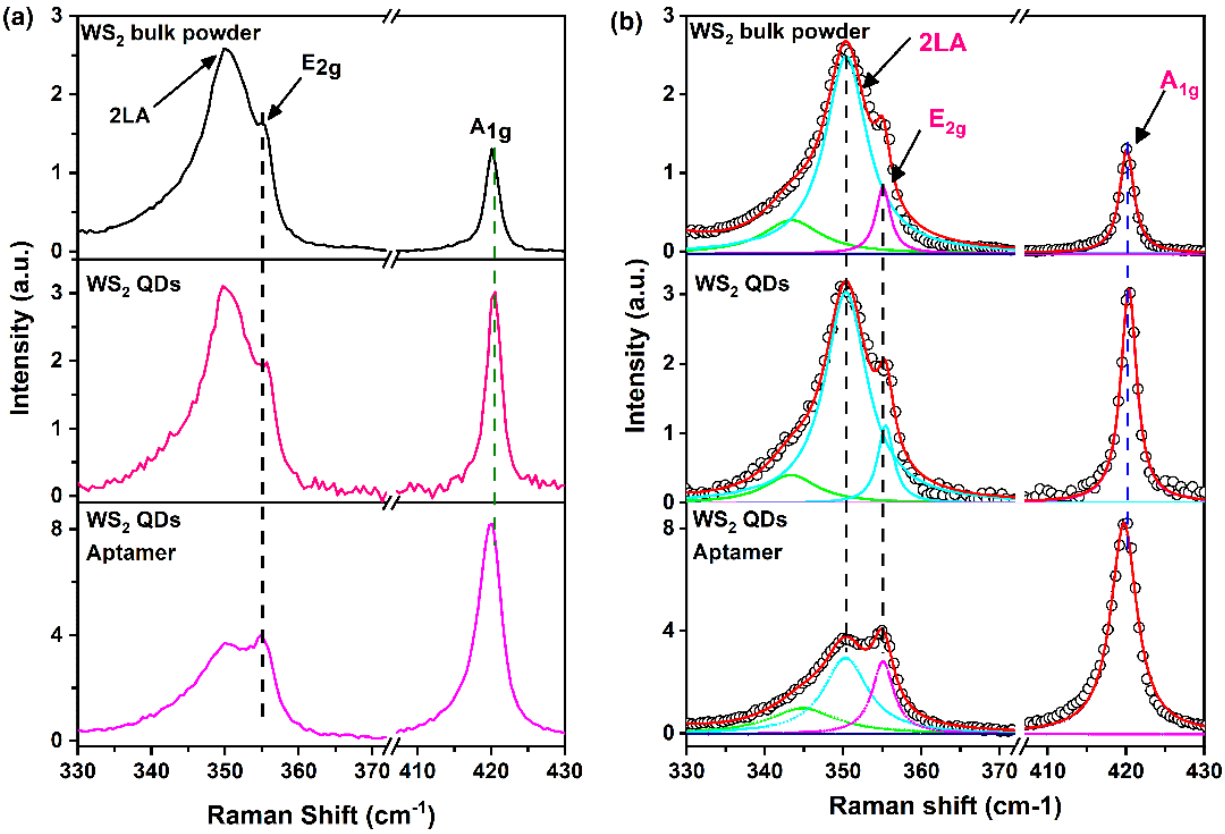

Figure 7.6: (a) Raman spectrum of WS_2 source powder, WS_2 QDs, Aptamer functionalized WS_2 QDs. (b) Fitted Raman spectrum of WS_2 source powder, WS_2 QDs, and Aptamer functionalized WS_2 QDs.

the A_{1g} mode is downshifted by 0.6 cm^{-1} from 420.4 cm^{-1} to 419.7 cm^{-1} as shown in **Fig.3.5(b)**, which confirms the electron enhancement due to aptamer functionalization[72]. The carrier enhancement was also observed in the FWHM for A_{1g} mode. The FWHM increased significantly from 2.5 cm^{-1} to 4.0 cm^{-1}, as well as the ratio of area under A_{1g} mode to E_{2g} mode also increased from 2.75 to 3.50, aiding the enhancement in overall electron density in the system[72–74]. The attachment of the thiol functional group to the vacancy and defect sites introduces a tensile strain in the WS_2 QDs. The broadening of E_{2g} mode and a minute blueshift of 0.4 cm^{-1} is a clear indication of strain resulting from aptamer attachment [75]. The peak parameters after fitting the Raman spectra are tabulated in **Table 7.1.** The UV-Vis absorbance spectra of WS_2 QDs dispersed in ethanol, recorded in the range of 250 to 800 nm range, is shown in **Fig. 7.7(a)**. We observe a strong absorption peak from the absorbance spectrum at ~293 nm, with a broad absorption tail up to ~500 nm. Since the QDs were synthesized via chemical exfoliation of bulk WS_2, there is a

Table 7.1 *Summary of the Raman modes of WS_2 source powder, WS_2 QDs, Aptamer functionalized WS_2 QDs.*

Samples	E_{2g} mode position (cm^{-1})	A_{1g} mode position (cm^{-1})	A_{1g} mode FWHM (cm^{-1})
Bulk WS_2 powder	355.1	420.1	2.23
WS_2 QDs	355.4	420.3	2.48
Aptamer/WS_2 QDs	355.1	419.7	4.05

possibility that WS_2 NSs are present along with the WS_2 QDs. An earlier study observed that 2D WS_2 NSs have two distinct absorption peaks in the visible region at around 530 nm and 640 nm, corresponding to direct excitonic band transition at the K point of the Brillouin zone[76]. The absence of those signatures in the absorption spectra for our WS_2 QDs confirms the successful separation of WS_2 QDs and NSs by centrifugation. The strong absorption in the deep UV region at 293 nm is attributed to the direct excitonic transition from the deep valance band to the conduction band edge. The broader absorption spectrum from 280 nm to 500 nm indicates a distribution of WS_2 QDs size, as seen from FETEM[77]. The bandgap of the as-synthesized WS_2 QDs was estimated at ~ 3.56 eV, using the Tauc plot as shown in the inset of **Fig. 7.7(a),** which is much higher than the 2D monolayer WS_2 [78]. This is due to the quantum confinement effect.

The quantum confinement in WS_2 QDs gives rise to high PL emission under UV illumination. The PL emission spectrum of the WS_2 QDs at 20 μg/mL under different excitation wavelengths ranging from 340 nm to 480 nm is shown in **Fig. 7.7(b)**. From the excitation-dependent PL emission, we observed a gradual shift of the spectra maximum along with the change in intensity. The emission spectrum at a low excitation wavelength of 340 nm and high excitation wavelength of 460 nm were fitted with Gaussian curves, as shown in **Fig. 7.8(a)**. The PL emission spectrum under low excitation wavelength consists of contributions from B exciton, neutral exciton, as well as surface and deep defect excitons. However, at the excitation wavelength of 460 nm, theemission contributions are only from defect-bound excitons. Hence, the wavelength-dependent emission

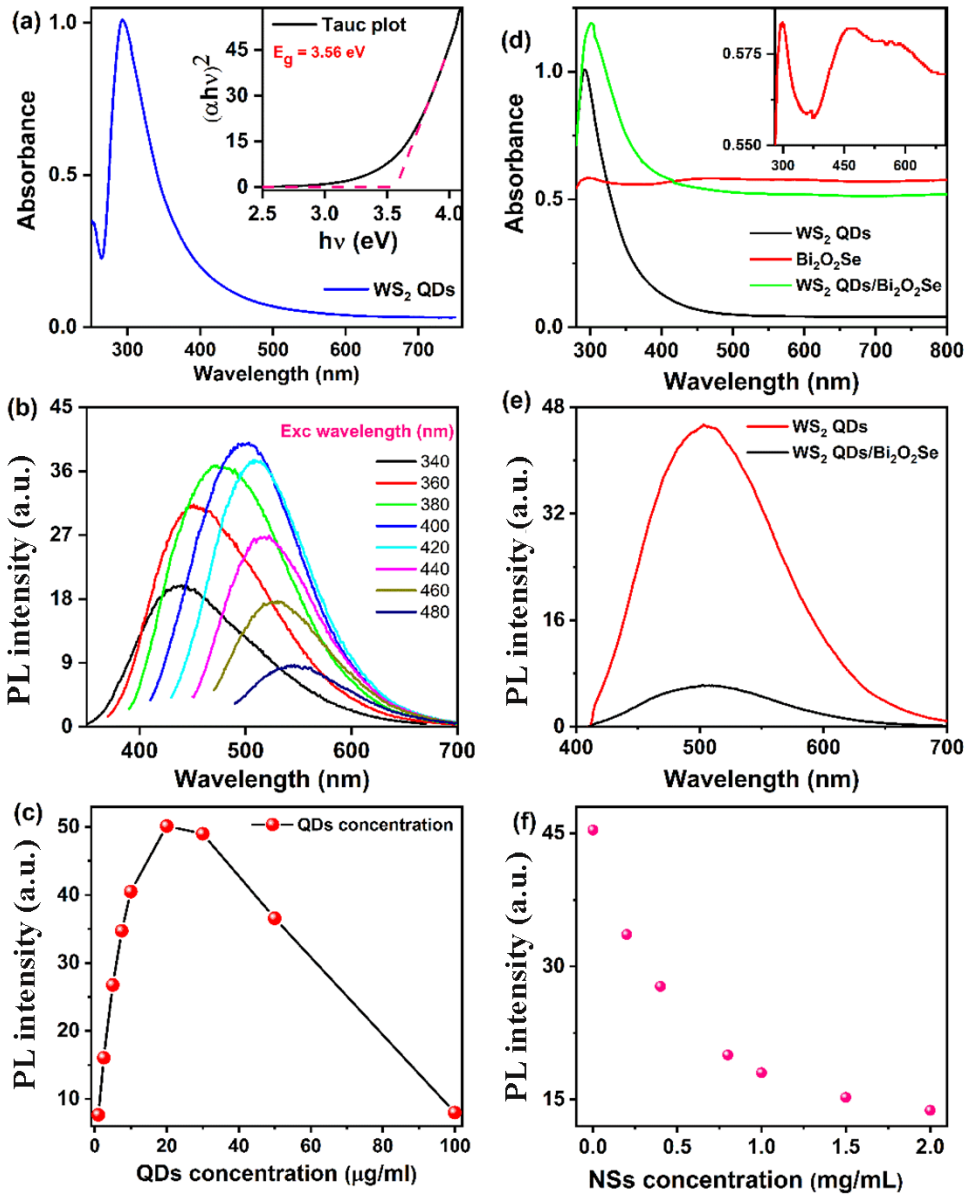

Figure 7.7: (a) The UV-visible absorption spectrum of WS_2 QDs dispersed in ethanol, the inset shows the Tauc plot from the absorption data for bandgap calculation (b) Wavelength-dependent PL emission spectrum with excitation wavelength from 340 nm to 480 nm with the interval of 20 nm (c) Concentration-dependent PL emission of WS_2 QDs under 405 nm laser excitation (d) The UV-visible absorption spectrum for Bi_2O_2Se and WS_2 QDs/Bi_2O_2Se NSs composite. Inset shown the magnified view of the peak absorbance (e) The PL emission spectra of WS_2 QDs under 405 nm laser excitation and its emission with 2 mg/mL Bi_2O_2Se NSs solution (f)The variation of PL intensity of WS_2 QDs in the presence of different concentrations of Bi_2O_2Se NSs.

intensity was attributed to the selective excitation and recombination of neutral excitons and defect-bound excitons at different excitation wavelengths as well as to the QD size distribution [60,79]. We have found the maximum intensity for an excitation wavelength of 400 nm, and hence we have used a 405 nm laser excitation for further PL measurements. Quantum yield (QY) of synthesized WS_2 QDs was measured with 330 nm excitation at a low concentration of 1μg/mL and the obtained QY was 52.1 %, the highest reported to date [60,80]. The high QY can be attributed to the confinement effect arising from narrow size distribution. The density of WS_2 QDs strongly affects the PL intensity. A laser excitation of 405 nm with an incident power of 2.0 mW was used for the concentration-dependent PL emission spectrum. We have diluted the WS_2 QDs in concentrations varying from 100.0 μg/mL to 1.0 μg/mL. The variation of PL intensity with the concentration of the WS_2 QDs is shown in **Fig.7.7(c).** We observed low PL emission at lower as well as higher WS_2 QDs concentrations. The variation of PL emission intensity with WS_2 QDs concentration can be explained as follows. The PL emission intensity highly depends upon the number of absorbed photons. Since fewer WS_2 QDs are present per unit volume at lower concentrations, it leads to less photon absorption. A higher fraction of incident photons is transmitted through the solvent at a lower concentration leading to low PL emission. With the increasing concentration of WS_2 QDs, photon absorption increases, hence the PL emission intensity. However, agglomeration of WS_2 QDs starts at higher concentrations, and the PL

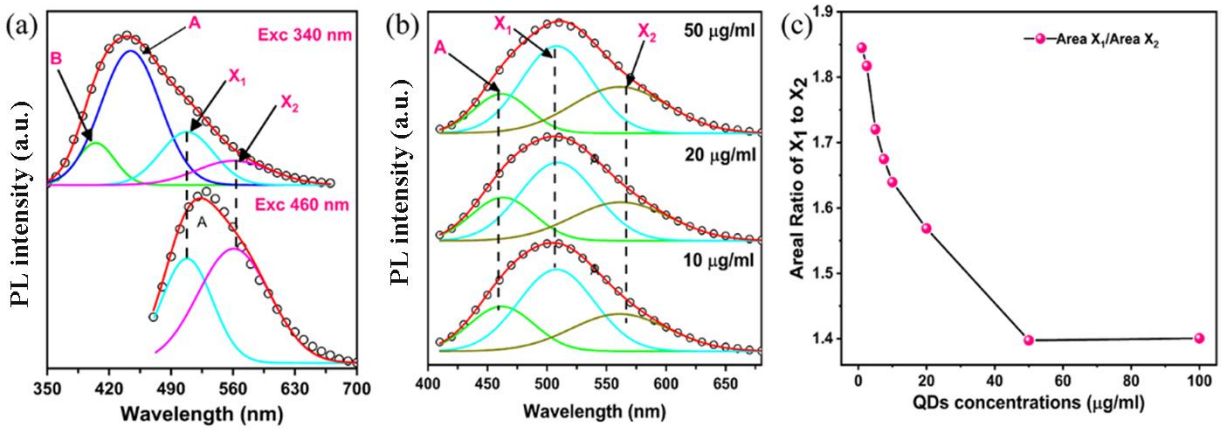

Figure 7.8: (a) The exciton wavelength-dependent PL emission spectra of WS_2 QDs and its fitting; (b) Concentration-dependent PL emission spectra and its fitting for WS_2 QDs; at higher concentration, the defect bound exciton peak (X_2) is dominant; (c) Areal intensity ratio of X_1 to X_2 as a function of QD concentrations

intensity subsequently decreases. We have fitted the emission spectrum with three peaks, neutral exciton (A), surface defect exciton (X_1), and deep defect exciton (X_2), as shown in **Fig. 7.8 (b)**. From the fitted curve, we have observed a relative increase in the intensity of deep defect excitons with increasing concentration, as the agglomeration may lead to surface defect passivation. Thus, we can conclude that 20 μg/mL is the optimum WS_2 QDs, concentration- for efficient PL which is used for further experiments. The areal ratio between the X_1 to X_2 is shown in **Fig. 7.8(c)**. We observe that this ratio decreases rapidly initially with increase in the concentration of WS_2 QDs and finally gets saturated at a high concentration. This indicates the passivation of surface defect states at higher concentrations.

7.3.2 Composite material for static PL quenching via complex formation

The UV-Vis absorbance spectra of Bi_2O_2Se NSs and it composite with WS_2 QDs is shown in **Fig. 7.7(d).** The Bi_2O_2Se NSs have high absorption in the range of 280 to 800 nm, with a broad absorption peak from 400 to 600 nm. For better observation, magnified view of the Bi_2O_2Se NSs absorbance is shown in the inset of **Fig. 7.7 (d)**. The WS_2 QDs/Bi_2O_2Se NSs composite have high absorption in the 280 to 800 nm range with an absorbance peak at 303 nm. The upshift of absorbance peak by 11 nm (from 292 nm to 303 nm) for the composite material is clearly due to the van der Waals interaction between the WS_2 QDs and Bi_2O_2Se NSs and charge/energy transfer from WS_2 QDs to Bi_2O_2Se NSs. Bi_2O_2Se NSs were used to quench the PL emission of the WS_2

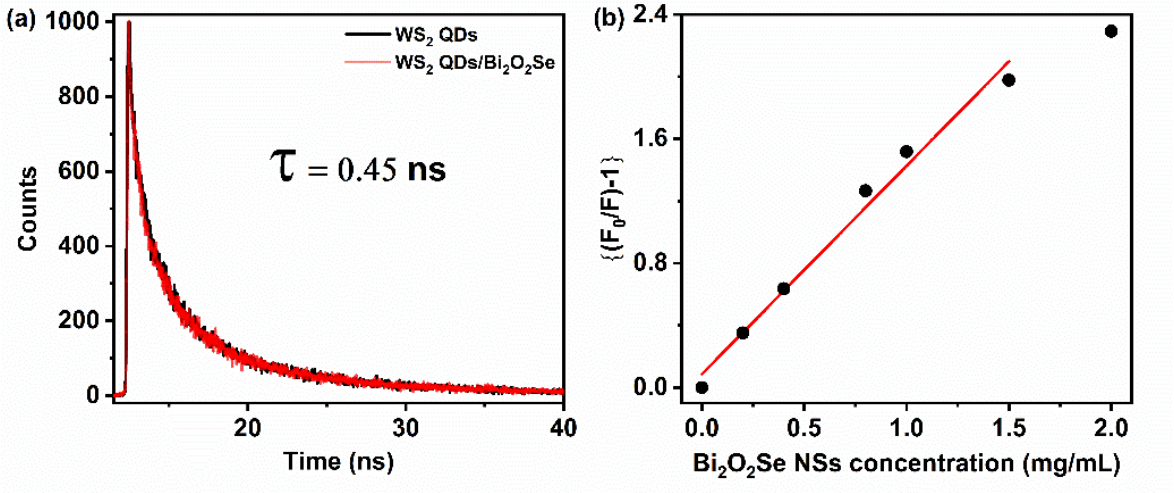

Figure 7.9: (a)TRPL spectra of WS_2 QDs and WS_2/Bi_2O_2Se NSs composite (b) Stern–Volmer plot for PL quenching.

QDs. Bi_2O_2Se is a non-van der Waals layered material having a tunable bandgap between 0.8 to 1.35 eV[81]. The WS_2 QDs PL emission with and without Bi_2O_2Se NSs under 405 nm laser excitation is shown in **Fig. 7.7(e)**. The addition of Bi_2O_2Se NSs quenches the PL emission of WS_2 QDs. The presence of sulfur vacancy in WS_2 QDs, helps in its attachments to Bi_2O_2Se NSs surface. For understanding the PL quenching dynamics, we studied the TRPL spectra of, WS_2 QDs and WS_2 QDs/Bi_2O_2Se NSs composite, which shown in **Fig. 7.9 (a)**. Even though the PL of WS_2 QDs quenches in the presence of Bi_2O_2Se but the TRPL spectra overlap with each other implicating the statics quenching through formation of dark complex[82]. Further, the Stern-Volmer plot between $\left(\frac{I_0}{I} - 1\right) vs$ Bi_2O_2Se concentration is shown in **Fig. 7.9 (b).** Where I_0 is the PL emission intensity of WS_2 QDs and I is the PL intensity at a given Bi_2O_2Se NSs concentration. Which shows at lower concentration, it follows linear behavior with Stern-Volmer constant of 1.34 mL^{-1}, confirming the statics quenching mechanism[83]. The PL emission quenching of WS_2 QDs in the presence of Bi_2O_2Se can be explained as follows. The emission peak of WS_2 QDs under 405 nm laser excitation clearly matches with the absorption band of Bi_2O_2Se NSs, as shown in **Fig.7.7 (d)**. The adsorption of WS_2 QDs on Bi_2O_2Se NSs result dark complex formation via charge transfer from WS_2 QDs to Bi_2O_2Se NSs as confirmed by Raman and XPS spectroscopy. With the increasing concentration of Bi_2O_2Se NSs, more WS_2 QDs are adsorbed on the NSs surface, hence lower PL emission intensity. The variation of WS_2 QDs PL emission with Bi_2O_2Se concentrations is shown in **Fig. 7.7(f)**. The PL emission intensity decreases rapidly initially with the increasing concentration of Bi_2O_2Se NS and finally gets saturated at higher concentration (>1.5 mg/mL).

7.3.3 Optimum sensing environment

An optimum sensing environment is essential for any sensing device, including proper sample preparation, buffer pH, response times, etc. Firstly, we optimized the WS_2 QDs concentration from the concentration-dependent PL spectrum, as shown in **Fig. 7.7 (c)**. We found the optimum concentration as 20 μg/mL, which gives the highest PL emission intensity. Secondly, the quenching of PL intensity depends strongly upon the concentration of Bi_2O_2Se NS solution, as more adsorption sites are available for the WS_2 QDs to attach with increasing Bi_2O_2Se NSs concentration, as shown in the inset of **Fig. 7.7(f)**. The PL intensity almost saturates after 1.5 mg/mL concentration of Bi_2O_2Se NSs. Thus, the concentration of 1.5 mg/mL for Bi_2O_2Se NSs was selected as the optimum concentration. The PL emission spectra of WS_2 QDs in presence of

Bi_2O_2Se NSs and WS_2 QDs/Bi_2O_2Se NSs/ *S. aureus* is shown in **Fig. 7.10 (a)**. Interestingly, the PL intensity of WS_2 QDs quenched by Bi_2O_2Se NSs is restored in presence of *S. aureus*, but requires a certain time, called response time. The response time is an essential parameter for a sensor, and it is the time required to respond after interaction with an analyte. We measured the PL intensity over time after adding 10^6 CFu/mL concentration of *S. aureus* bacteria solution in the composite solution. The variation of PL intensity after *S. aureus* addition is shown in **Fig. 7.10-(b)**. From the graph, it is observed that the PL intensity does not show any significant change initially. However, after 5 minutes, there is an exponential enhancement in the intensity, which finally saturates within 15 minutes. This can be understood as follows. Initially, it takes time to bind *S. aureus* bacteria with aptamers. Once the bacteria are attached to the WS_2 QDs via aptamers, bigger size *S. aureus* weakens the van der force between WS_2 QDs and Bi_2O_2Se NSs. Since the aptamers are attached to the WS_2 QDs by strong covalent bonds, while detaching WS_2 QDs also separates with S. aureus. Hence WS_2 QDs slowly start detaching from Bi_2O_2Se NSs. This detachment of WS_2 QDs from Bi_2O_2Se NSs surface interestingly leads to the restoration of the PL intensity, as shown in **Fig.7.10 (a)**. Finally, no further change in the PL intensity leads to saturation when the maximum number of bacteria is attached to the WS_2 QDs, and the WS_2 QDs are detached from Bi_2O_2Se NSs. Hence, the sensing environment has an optimum response time of 15 minutes. Our method has a much faster response (time of 15 minutes) with a simple synthesis and detection mechanism see **Table 7.2**. We have studied the PL intensity of the WS_2 QDs/Bi_2O_2Se NSs composite over 30 minutes. This confirms that the PL restoration is not due to the interaction between WS_2 QDs and Bi_2O_2Se NSs. The binding of the bacteria with aptamers helps in the detachment of WS_2 QDs from Bi_2O_2Se NSs and the restoration of the PL, which is exploited for the detection of the bacteria.

7.3.4 Sensing of *S. aureus* by using WS_2 QDs-Bi_2O_2Se complex

Before adding various concentrations of *S. aureus*, we measured the PL intensity of the sensing system with the addition of PBS without any bacteria, which shows an enhancement of PL emission. This enhancement originates from various factors such as decrease in the effective concentration of Bi_2O_2Se NSs and WS_2 QDs as well as from the different ions present in the buffer solution. This ensures that any further enhancement in the PL emission is due to *S. aureus* effects.

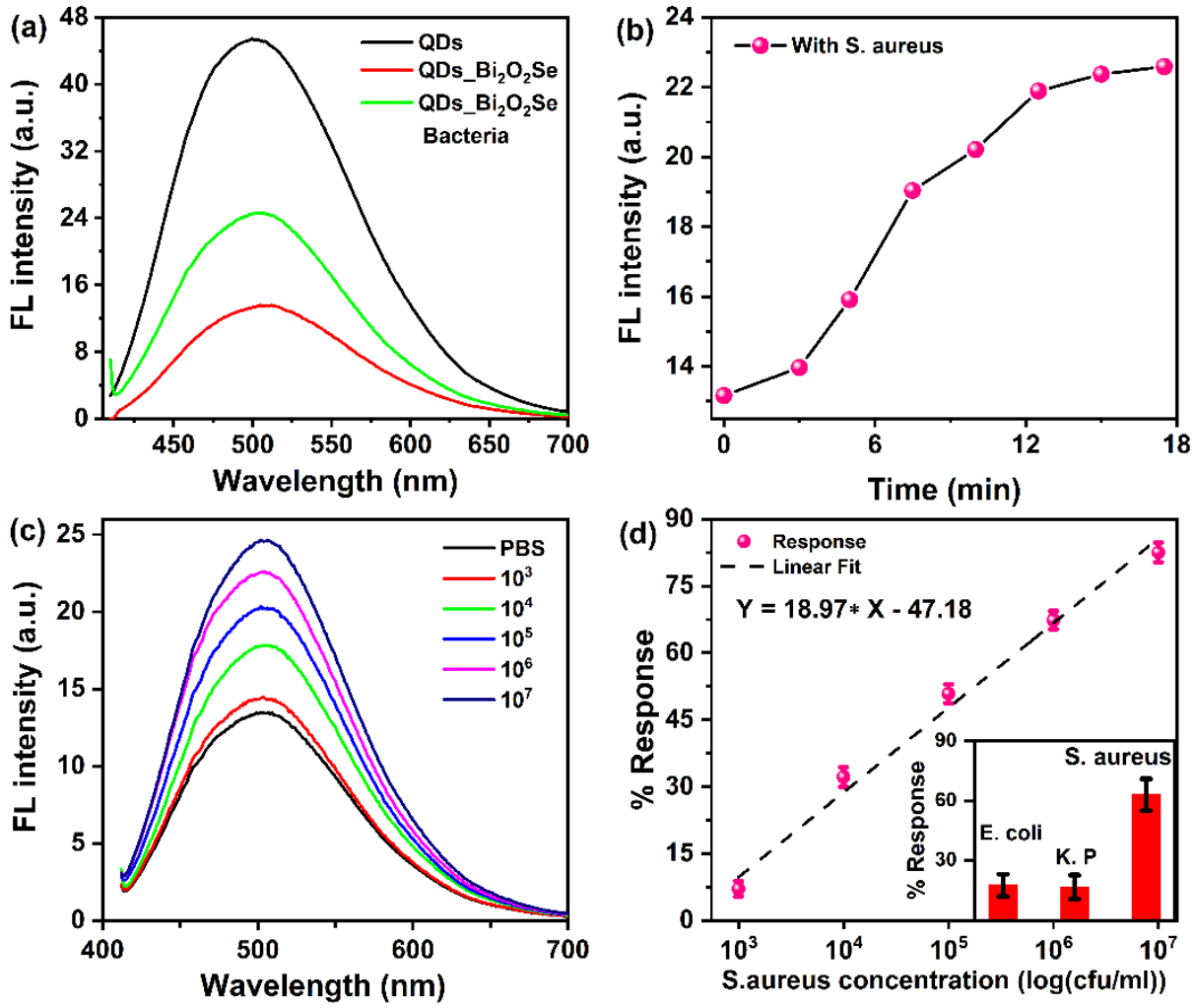

Figure 7.10: (a) PL emission spectra of WS_2 QDs along with WS_2 QDs/Bi_2O_2Se NS composite and composite in presence of 10^7 CFu/mL concentration of S.aureus bacteria. (b) Temporal response behavior, the restoration of PL intensity with time after addition of 10^6 CFu/ mL concentration of S. aureus bacteria, (c) concentration-dependent PL emission, (d) calibration of response curve. The inset in Figure 7.10 (d) shows the response of our system in presence of non-targeted E. coli and K. pneumoniae bacteria and targeted S. aureus bacteria all with 10^6 CFu/mL concentration.

With the addition of the solution bacteria, the PL intensity systematically rises. The variation of PL intensity with PBS and various bacteria concentrations is shown in **Fig. 7.10(c)**. The ssDNA aptamers identify the presence of *S. aureus* and bind with it. After binding with the bacteria, the WS_2 QDs complex detaches from the surface of NSs, and as the WS_2 QDs are now free-standing,

the PL intensity (F) restoration occurs. The presence of WS_2 QDs outside the Bi_2O_2Se NSs after bacteria addition confirms the same. The calibration curve between the change in PL intensity with respect to the concentration is shown in **Fig. 7.10(d)**. For the calibration curve, we have plotted the % of Response ($\Delta F=\frac{F-F_0}{F_0}\times 100$) against the logarithm of bacteria concentrations (log(cfu/mL)). Here, F_0 is the PL intensity with only PBS solution without any *S. aureus* and F is the PL in presence of *S. aureus*. A strong correlation between the bacteria concentration against Response follows the linear equation as $y = 18.97x - 47.18$ ($R^2 = 0.98$) over the range of 10^3 to 10^7 cfu/mL under 405 nm laser excitation. For comparison, we have summarized the sensing performances of previously reported sensors for the detection of *S. aureus* in Table 7.2, which shows our system has fastest response among the previous reports. To know the selectivity of our proposed system, we have carried out the PL measurement of some non-target bacteria, e.g., *Escherichia coli (E. coli)*, and *Klebsiella pneumoniae (KP)* with 10^6 cfu/mL concentration. The ssDNA aptamers specifically binding to *S. aureus* were developed

Table 7.2 Summary of the performance of different sensors for detecting S. Aureus.

Material and methods	Linear range CFu/ml	Lower detection limt (CFu/ml)	Response Time (minutes)	Reference
Electrochemical	8×10^2 to 1×10^3	800	6-11	Reference [84]
Colorimetric	1.5×10^2 to 1.5×10^6	1.500	40	Reference [85]
Fluorimetric Assay	1×10^3 to 1×10^9	2.900	130	Reference [86]
Long-period fiber gratings	1×10^4 to 1×10^8	224	30	Reference [87]
Fiber biosensor	7×10^1 to 7×10^4	3.1	40	Reference [88]
Electrochemical	3×10^0 to 3×10^7	3.0	30	Reference [89]
Photoluminescence	10^0 to 10^7	1	240	Reference [90]
Photoluminescence	10^1 to 10^7	11.12	120	Reference [91]
Polymerase chain reaction	1.8×10^1 to 1.8×10^6	18	240	Reference [92]
Photoluminescence	10^3 to 10^7	850	15	*This work*

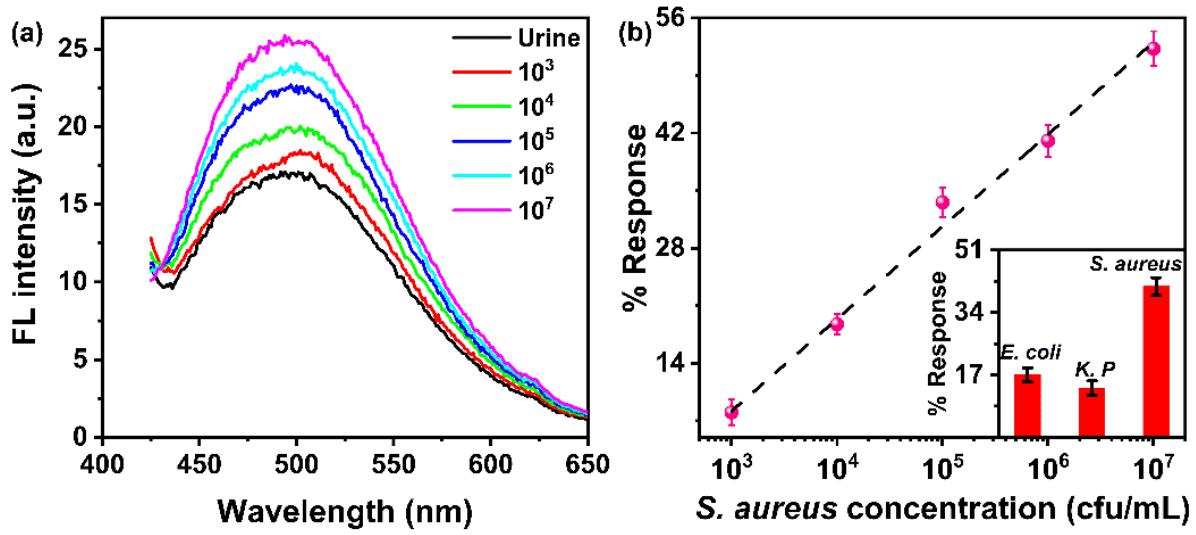

Figure 7.11: (a) PL emission of the system at different concentrations of *S. aureus* in urine medium. (b) Calibration curve for urine medium with *S. aureus* concentration, the inset shows the selectivity data in urine medium.

using the Cell-SELEX to have highly selective detection. The % response with targeted and non-targeted bacteria is shown in the inset of **Fig. 7.10 (d)**. For non-targeted bacteria (E. coli & K. pneumoniae), the response is only about 16 to 17 %, while for the targeted bacteria *S. aureus*, it is about 63% for the same 10^6 cfu/mL concentration. Thus, the use of the highly selective ssDNA aptamer probe gives highly selective response toward targeted *S. aureus*. The response of our sensor is relatively much lower for other bacteria as compared to *S. aureus* implying a highly selective detection system.

Next, we check the feasibility of utilizing the proposed sensing system in real-life biological fluids such as urine and blood serum. For the UTI related diseases, the patient urine is the ideal pathological sample. We have studied the sensing response in urine and the PL emission intensity at various concentrations is shown in **Fig. 7.11(a)**. It shows a systematic increase in the PL emission intensity with increasing *S. aureus* concentration indicating its ability to detect *S. aureus* in complex biofuild urine. In **Fig. 7.11 (b)**, we have shown the calibration curve, which shows a linear response with a slope of 11.22 units/cfu with a strong correlation of $y = 11.22x - 25.48$ (R^2=0.99). Although the slope of the response curve is decreased from 18.97 to 11.22, still it can detect *S. aureus* selectively as employed by the selective PL response only in presence of *S.*

aureus. The system response in presence of various other non-targeted bacteria is shown inset of **Fig. 7.11 (b)**. Thus, present method can be employed real-time detection of S. *aureus* using the urine sample.

7.3.5 Sensing Mechanism

The working mechanism of the present sensor is schematically shown in **Fig. 7.12** The WS_2 QDs are highly photoluminescent under UV illumination, as shown by the excitation-dependent PL emission curves in **Fig. 7.7 (b)**. Under 405 nm laser excitation, WS_2 QDs have emission maxima at around 500 nm as shown in **Fig. 7.7 (e)**. From the absorption spectrum of Bi_2O_2Se NSs, there is a broad absorption from 300 nm to 800 nm as shown in **Fig. 7.7 (d)** with a broad peak in the range 450 nm to 650 nm, as shown in the inset of **Fig. 7.7** (d). When Bi_2O_2Se is added to WS_2 QDs solution, WS_2 QDs are adsorbed on the Bi_2O_2Se NSs surface as confirmed by FETEM (in Figure 7.2(c)) via weak van der Waals interactions which results in quenching the PL emission of WS_2 QDs via dark complex as discussed earlier. The quenching of PL intensity occurs due to the absorption of WS_2 QDs emission by Bi_2O_2Se NSs. The maximum quenching of around 70 % was observed with 1.5 mg/mL Bi_2O_2Se concentration, as shown in **Fig. 7.7** (f). When aptamer solution was introduced in WS_2 QDs, aptamers were covalently attached to the WS_2 QDs surface on the sulfur vacancy and defect sites of WS_2. When the targeted *S. aureus* bacteria are added, they bind to the aptamers, which are already attached to the of WS_2 QDs surface by strong covalent bonds. The larger size bacteria weakens the interaction force between WS_2 QDs and Bi_2O_2Se NSs and aid in the detachment of the WS_2 QDs from Bi_2O_2Se NSs surface. At higher concentrations of *S. aureus*, a larger number of *S. aureus* will bind with aptamers leading to more WS_2 QDs detachments and hence further increase in the PL intensity. Instead of targeted *S. aureus*, the non-targeted bacteria were unable to bind with the specific aptamer, hence negligible change in the interaction between WS_2 QDs and Bi_2O_2Se NSs resulting no detachment of WS_2 QDs from Bi_2O_2Se NSs surface. Thus, one can detect targeted bacteria by using PL intensity restoration of WS_2 QDs as a recognition tool. This technique can also be implemented for other biomolecules detection by changing the probe molecule.

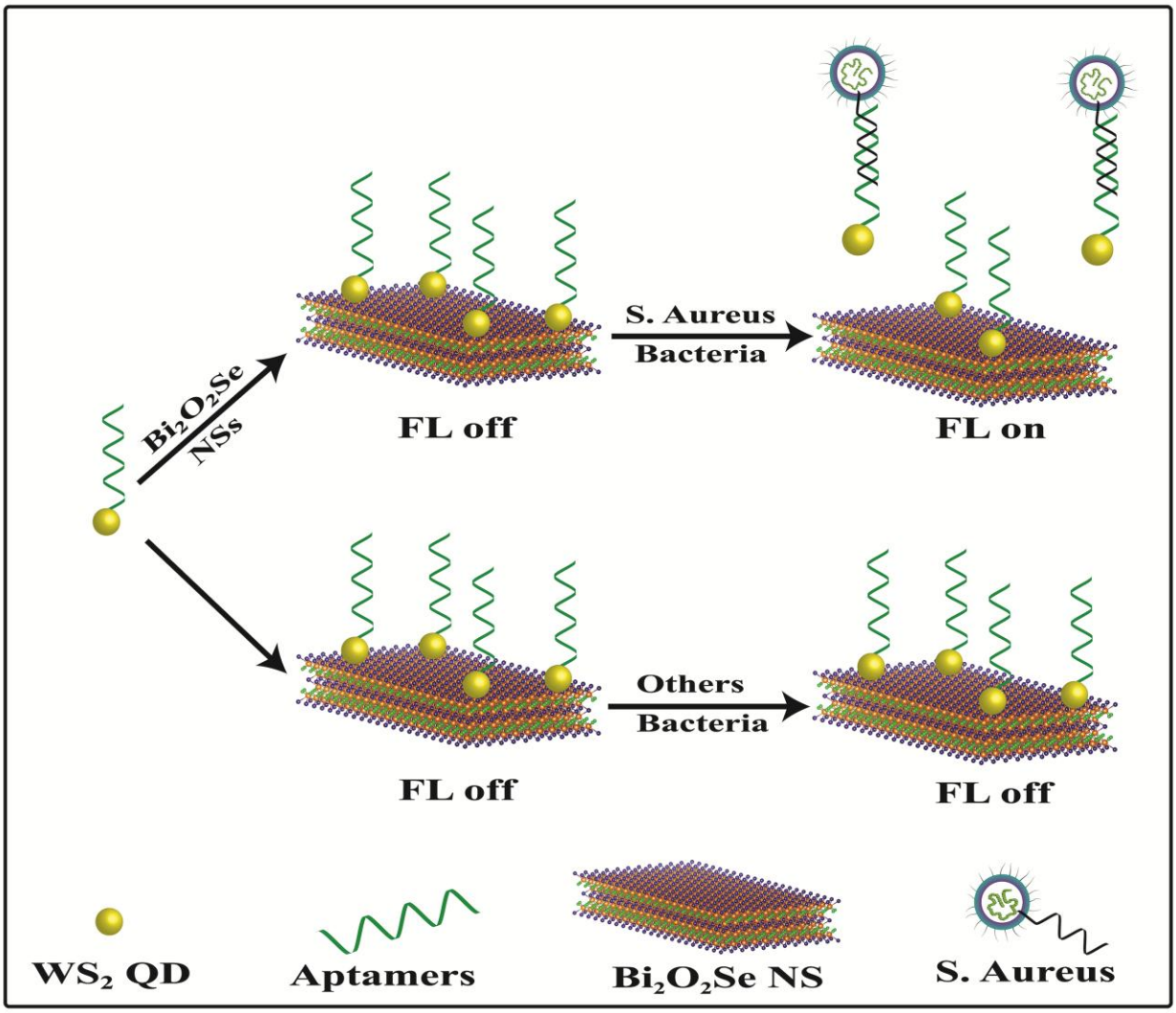

Figure 7.12: Schematic of the working principle of the proposed biosensors. The attachment of aptamer modified WS_2 QDs on the Bi_2O_2Se surface quenches PL as a result of non-rediative energy transfer. The attachment of targeted bacteria (e.g., S. aureus) causes the detachment of WS_2 QDs from Bi_2O_2Se NSs surface and restoration of PL intensity.

7.4 Conclusion

Herein, we demonstrated the fast detection of *S. aureus* bacteria using thiol-functionalized WS_2 QDs and 2D Bi_2O_2Se nanosheets using simple PL spectroscopy. We first synthesized a uniform distribution of WS_2 QDs by simple liquid exfoliation of bulk WS_2 sheets via a simple probe

sonication technique. The semiconducting WS_2 QDs with bandgap of 3.56 eV exhibit highest PL emission intensity under the 405 nm laser excitation at the optimum concentration of 20 µg/mL and possess an PL quantum yield of 52.1% for 1µg/mL concentration at 330 nm excitation. The as-synthesized WS_2 QDs have a high density of Sulfur vacancy sites, which aid in the attachment of the thiol functional group for aptamer immobilization. The reduction of sulfur vacancies and the signature of phosphorus in the XPS spectra confirmed the attachment of aptamer to WS_2 QDs. Finally, we have shown the *S. aureus* sensing using aptamer functionalized WS_2 QDs. The optimized sensing environment of this biosensor can detect *S. aureus* in PBS solution within 15 minutes, which is reasonably fast compared to previous reports. The concentration-dependent calibration curve shows a linear response over the range of 10^3 to 10^7 CFu/mL and a lower detection limit of 580 CFu/mL, which are significant. Further, the system can detect *S. aureus* in urine samples displaying its potential application for real time detection. This technique can also be used for detection of other biomolecules and metal ions by choosing suitable receptors.

References

(1) Adedeji, W. A. THE TREASURE CALLED ANTIBIOTICS. *Ann. Ib. Postgrad. Med.* 2016, *14* (2), 56–57.

(2) Hutchings, M. I.; Truman, A. W.; Wilkinson, B. Antibiotics: Past, Present and Future. *Curr. Opin. Microbiol.* 2019, *51*, 72–80. https://doi.org/10.1016/j.mib.2019.10.008.

(3) Ventola, C. L. The Antibiotic Resistance Crisis. *Pharm. Ther.* 2015, *40* (4), 277–283.

(4) Mancuso, G.; Midiri, A.; Gerace, E.; Biondo, C. Bacterial Antibiotic Resistance: The Most Critical Pathogens. *Pathogens* 2021, *10* (10), 1310. https://doi.org/10.3390/pathogens10101310.

(5) Foster, T. J. Antibiotic Resistance in Staphylococcus Aureus. Current Status and Future Prospects. *FEMS Microbiol. Rev.* 2017, *41* (3), 430–449. https://doi.org/10.1093/femsre/fux007.

(6) Haaber, J.; Penadés, J. R.; Ingmer, H. Transfer of Antibiotic Resistance in Staphylococcus Aureus. *Trends Microbiol.* 2017, *25* (11), 893–905. https://doi.org/10.1016/j.tim.2017.05.011.

(7) Barrett, S. P.; Savage, M. A.; Rebec, M. P.; Guyot, A.; Andrews, N.; Shrimpton, S. B. Antibiotic Sensitivity of Bacteria Associated with Community-Acquired Urinary Tract Infection in Britain. *J. Antimicrob. Chemother.* 1999, *44* (3), 359–365. https://doi.org/10.1093/jac/44.3.359.

(8) Lowy, F. D. Staphylococcus Aureus Infections. *N. Engl. J. Med.* 1998, *339* (8), 520–532. https://doi.org/10.1056/NEJM199808203390806.

(9) Skov, R. L.; Jensen, K. S. Community-Associated Meticillin-Resistant Staphylococcus Aureus as a Cause of Hospital-Acquired Infections. *J. Hosp. Infect.* 2009, *73* (4), 364–370. https://doi.org/10.1016/j.jhin.2009.07.004.

(10) DeLeo, F. R.; Otto, M.; Kreiswirth, B. N.; Chambers, H. F. Community-Associated Meticillin-Resistant Staphylococcus Aureus. *Lancet Lond. Engl.* 2010, *375* (9725), 1557–1568. https://doi.org/10.1016/S0140-6736(09)61999-1.

(11) Wertheim, H. F.; Melles, D. C.; Vos, M. C.; van Leeuwen, W.; van Belkum, A.; Verbrugh, H. A.; Nouwen, J. L. The Role of Nasal Carriage in Staphylococcus Aureus Infections. *Lancet Infect. Dis.* 2005, *5* (12), 751–762. https://doi.org/10.1016/S1473-3099(05)70295-4.

(12) Noble, W. C.; Valkenburg, H. A.; Wolters, C. H. L. Carriage of Staphylococcus Aureus in Random Samples of a Normal Population*. *Epidemiol. Infect.* 1967, *65* (4), 567–573. https://doi.org/10.1017/S002217240004609X.

(13) Safdar, N.; Bradley, E. A. The Risk of Infection after Nasal Colonization with Staphylococcus Aureus. *Am. J. Med.* 2008, *121* (4), 310–315. https://doi.org/10.1016/j.amjmed.2007.07.034.

(14) Tong, S. Y. C.; Davis, J. S.; Eichenberger, E.; Holland, T. L.; Fowler, V. G. Staphylococcus Aureus Infections: Epidemiology, Pathophysiology, Clinical Manifestations, and Management. *Clin. Microbiol. Rev.* 2015, *28* (3), 603–661. https://doi.org/10.1128/CMR.00134-14.

(15) Weems, J. J. The Many Faces of Staphylococcus Aureus Infection. *Postgrad. Med.* 2001, *110* (4), 24–36. https://doi.org/10.3810/pgm.2001.10.1042.

(16) Fratamico, P. M.; Bhunia, A. K.; Smith, J. L. Foodborne Pathogens: Microbiology and Molecular Biology. *Foodborne Pathog. Microbiol. Mol. Biol.* 2005.

(17) Argudín, M. Á.; Mendoza, M. C.; Rodicio, M. R. Food Poisoning and Staphylococcus Aureus Enterotoxins. *Toxins* 2010, *2* (7), 1751–1773. https://doi.org/10.3390/toxins2071751.

(18) Stamm, W. E.; Norrby, S. R. Urinary Tract Infections: Disease Panorama and Challenges. *J. Infect. Dis.* 2001, *183* (Supplement_1), S1–S4. https://doi.org/10.1086/318850.

(19) Flores-Mireles, A. L.; Walker, J. N.; Caparon, M.; Hultgren, S. J. Urinary Tract Infections: Epidemiology, Mechanisms of Infection and Treatment Options. *Nat. Rev. Microbiol.* 2015, *13* (5), 269–284. https://doi.org/10.1038/nrmicro3432.

(20) Demuth, P. J.; Gerding, D. N.; Crossley, K. Staphylococcus Aureus Bacteriuria. *Arch. Intern. Med.* 1979, *139* (1), 78–80. https://doi.org/10.1001/archinte.1979.03630380056019.

(21) Muder, R. R.; Brennen, C.; Rihs, J. D.; Wagener, M. M.; Obman, A.; Obman, A.; Stout, J. E.; Yu, V. L. Isolation of Staphylococcus Aureus from the Urinary Tract: Association of Isolation with Symptomatic Urinary Tract Infection and Subsequent Staphylococcal Bacteremia. *Clin. Infect. Dis.* 2006, *42* (1), 46–50. https://doi.org/10.1086/498518.

(22) van Hal, S. J.; Jensen, S. O.; Vaska, V. L.; Espedido, B. A.; Paterson, D. L.; Gosbell, I. B. Predictors of Mortality in Staphylococcus Aureus Bacteremia. *Clin. Microbiol. Rev.* 2012, *25* (2), 362–386. https://doi.org/10.1128/CMR.05022-11.

(23) Wang, J.; Wu, X.; Wang, C.; Shao, N.; Dong, P.; Xiao, R.; Wang, S. Magnetically Assisted Surface-Enhanced Raman Spectroscopy for the Detection of Staphylococcus Aureus Based on Aptamer Recognition. *ACS Appl. Mater. Interfaces* 2015, *7* (37), 20919–20929. https://doi.org/10.1021/acsami.5b06446.

(24) Brakstad, O. G.; Aasbakk, K.; Maeland, J. A. Detection of Staphylococcus Aureus by Polymerase Chain Reaction Amplification of the Nuc Gene. *J. Clin. Microbiol.* 1992, *30* (7), 1654–1660. https://doi.org/10.1128/jcm.30.7.1654-1660.1992.

(25) Trnčíková, T.; Hrušková, V.; Oravcová, K.; Pangallo, D.; Kaclíková, E. Rapid and Sensitive Detection of Staphylococcus Aureus in Food Using Selective Enrichment and Real-Time PCR Targeting a New Gene Marker. *Food Anal. Methods* 2008, *2* (4), 241. https://doi.org/10.1007/s12161-008-9056-x.

(26) BENNETT, R. W. Staphylococcal Enterotoxin and Its Rapid Identification in Foods by Enzyme-Linked Immunosorbent Assay–Based Methodology. *J. Food Prot.* 2005, *68* (6), 1264–1270. https://doi.org/10.4315/0362-028X-68.6.1264.

(27) Damborský, P.; Švitel, J.; Katrlík, J. Optical Biosensors. *Essays Biochem.* 2016, *60* (1), 91–100. https://doi.org/10.1042/EBC20150010.

(28) Chen, C.; Wang, J. Optical Biosensors: An Exhaustive and Comprehensive Review. *Analyst* 2020, *145* (5), 1605–1628. https://doi.org/10.1039/C9AN01998G.

(29) Liu, L.; He, F.; Yu, Y.; Wang, Y. Application of FRET Biosensors in Mechanobiology and Mechanopharmacological Screening. *Front. Bioeng. Biotechnol.* 2020, *8*.

(30) Mia, A. K.; Meyyappan, M.; Giri, P. K. Two-Dimensional Transition Metal Dichalcogenide Based Biosensors: From Fundamentals to Healthcare Applications. *Biosensors* 2023, *13* (2), 169. https://doi.org/10.3390/bios13020169.

(31) Wang, S.; Zhang, Y.; Ning, Y.; Zhang, G.-J. A WS 2 Nanosheet-Based Platform for Fluorescent DNA Detection via PNA–DNA Hybridization. *Analyst* 2015, *140* (2), 434–439. https://doi.org/10.1039/C4AN01738B.

(32) Xi, Q.; Zhou, D.-M.; Kan, Y.-Y.; Ge, J.; Wu, Z.-K.; Yu, R.-Q.; Jiang, J.-H. Highly Sensitive and Selective Strategy for MicroRNA Detection Based on WS_2 Nanosheet Mediated Fluorescence Quenching and Duplex-Specific Nuclease Signal Amplification. *Anal. Chem.* **2014**, *86* (3), 1361–1365. https://doi.org/10.1021/ac403944c.

(33) Das, R.; Parveen, S.; Bora, A.; Giri, P. K. Origin of High Photoluminescence Yield and High SERS Sensitivity of Nitrogen-Doped Graphene Quantum Dots. *Carbon* 2020, *160*, 273–286. https://doi.org/10.1016/j.carbon.2020.01.030.

(34) Hildebrandt, N.; Spillmann, C. M.; Algar, W. R.; Pons, T.; Stewart, M. H.; Oh, E.; Susumu, K.; Díaz, S. A.; Delehanty, J. B.; Medintz, I. L. Energy Transfer with Semiconductor Quantum Dot Bioconjugates: A Versatile Platform for Biosensing, Energy Harvesting, and Other Developing Applications. *Chem. Rev.* 2017, *117* (2), 536–711. https://doi.org/10.1021/acs.chemrev.6b00030.

(35) Yan, Y.; Zhang, C.; Gu, W.; Ding, C.; Li, X.; Xian, Y. Facile Synthesis of Water-Soluble WS_2 Quantum Dots for Turn-On Fluorescent Measurement of Lipoic Acid. *J. Phys. Chem. C* 2016, *120* (22), 12170–12177. https://doi.org/10.1021/acs.jpcc.6b01868.

(36) Kim, M.-J.; Jeon, S.-J.; Kang, T. W.; Ju, J.-M.; Yim, D.; Kim, H.-I.; Park, J. H.; Kim, J.-H. 2H-WS_2 Quantum Dots Produced by Modulating the Dimension and Phase of 1T-Nanosheets for Antibody-Free Optical Sensing of Neurotransmitters. *ACS Appl. Mater. Interfaces* 2017, *9* (14), 12316–12323. https://doi.org/10.1021/acsami.7b01644.

(37) Wang, P.; Wang, A.; Hassan, M. M.; Ouyang, Q.; Li, H.; Chen, Q. A Highly Sensitive Upconversion Nanoparticles-WS_2 Nanosheet Sensing Platform for Escherichia Coli

Detection. *Sens. Actuators B Chem.* **2020**, *320*, 128434. https://doi.org/10.1016/j.snb.2020.128434.

(38) Geldert, A.; Kenry; Lim, C. T. Paper-Based MoS_2 Nanosheet-Mediated FRET Aptasensor for Rapid Malaria Diagnosis. *Sci. Rep.* 2017, *7* (1), 17510. https://doi.org/10.1038/s41598-017-17616-3.

(39) Singh, P.; Gupta, R.; Sinha, M.; Kumar, R.; Bhalla, V. MoS_2 Based Digital Response Platform for Aptamer Based Fluorescent Detection of Pathogens. *Microchim. Acta* 2016, *183* (4), 1501–1506. https://doi.org/10.1007/s00604-016-1762-2.

(40) Han, J.; Xia, H.; Wu, Y.; Nie Kong, S.; Deivasigamani, A.; Xu, R.; M. Hui, K.; Kang, Y. Single-Layer MoS 2 Nanosheet Grafted Upconversion Nanoparticles for near-Infrared Fluorescence Imaging-Guided Deep Tissue Cancer Phototherapy. *Nanoscale* 2016, *8* (15), 7861–7865. https://doi.org/10.1039/C6NR00150E.

(41) Tarik Hossain, M.; Das, M.; Ghosh, J.; Ghosh, S.; K. Giri, P. Understanding the Interfacial Charge Transfer in the CVD Grown Bi 2 O 2 Se/CsPbBr 3 Nanocrystal Heterostructure and Its Exploitation in Superior Photodetection: Experiment vs. Theory. *Nanoscale* 2021, *13* (35), 14945–14959. https://doi.org/10.1039/D1NR04470B.

(42) Appel, J. H.; Li, D. O.; Podlevsky, J. D.; Debnath, A.; Green, A. A.; Wang, Q. H.; Chae, J. Low Cytotoxicity and Genotoxicity of Two-Dimensional MoS_2 and WS_2. *ACS Biomater. Sci. Eng.* 2016, *2* (3), 361–367. https://doi.org/10.1021/acsbiomaterials.5b00467.

(43) Zhou, X.; Sun, H.; Bai, X. Two-Dimensional Transition Metal Dichalcogenides: Synthesis, Biomedical Applications and Biosafety Evaluation. *Front. Bioeng. Biotechnol.* 2020, *8*.

(44) Mu, X.; Li, C.; Wang, L.; Zhang, R.; Huang, Y.; Yu, X.; Wong, P. K.; Ye, L. Biosafe Bi_2O_2Se Ultrathin Nanosheet for Water Disinfection via Solar-Induced Photothermal Synergistic Effect. *J. Hazard. Mater.* 2022, *440*, 129808. https://doi.org/10.1016/j.jhazmat.2022.129808.

(45) Xie, H.; Liu, M.; You, B.; Luo, G.; Chen, Y.; Liu, B.; Jiang, Z.; Chu, P. K.; Shao, J.; Yu, X.-F. Biodegradable Bi_2O_2Se Quantum Dots for Photoacoustic Imaging-Guided Cancer Photothermal Therapy. *Small* 2020, *16* (1), 1905208. https://doi.org/10.1002/smll.201905208.

(46) Kong, R.-M.; Ding, L.; Wang, Z.; You, J.; Qu, F. A Novel Aptamer-Functionalized MoS_2 Nanosheet Fluorescent Biosensor for Sensitive Detection of Prostate Specific Antigen. *Anal. Bioanal. Chem.* 2015, *407* (2), 369–377. https://doi.org/10.1007/s00216-014-8267-9.

(47) Thakur, B.; Zhou, G.; Chang, J.; Pu, H.; Jin, B.; Sui, X.; Yuan, X.; Yang, C.-H.; Magruder, M.; Chen, J. Rapid Detection of Single E. Coli Bacteria Using a Graphene-Based Field-Effect Transistor Device. *Biosens. Bioelectron.* 2018, *110*, 16–22. https://doi.org/10.1016/j.bios.2018.03.014.

(48) Shahdordizadeh, M.; Taghdisi, S. M.; Ansari, N.; Alebooye Langroodi, F.; Abnous, K.; Ramezani, M. Aptamer Based Biosensors for Detection of Staphylococcus Aureus. *Sens. Actuators B Chem.* 2017, *241*, 619–635. https://doi.org/10.1016/j.snb.2016.10.088.

(49) Song, K.-M.; Lee, S.; Ban, C. Aptamers and Their Biological Applications. *Sensors* 2012, *12* (1), 612–631. https://doi.org/10.3390/s120100612.

(50) Tarik Hossain, M.; Jena, T.; Debnath, S.; K. Giri, P. Defect-Induced Photogating Effect and Its Modulation in Ultrathin Free-Standing Bi_2O_2Se Nanosheets with Visible to Near-Infrared Photoresponse. *J. Mater. Chem. C* 2023. https://doi.org/10.1039/D3TC01129A.

(51) Liu, M.; Li, W.; Rong, J.; Zhou, C. Novel Polymer Nanocomposite Hydrogel with Natural Clay Nanotubes. *Colloid Polym. Sci.* 2012, *290* (10), 895–905. https://doi.org/10.1007/s00396-012-2588-z.

(52) Coleman, J. N.; Lotya, M.; O'Neill, A.; Bergin, S. D.; King, P. J.; Khan, U.; Young, K.; Gaucher, A.; De, S.; Smith, R. J.; Shvets, I. V.; Arora, S. K.; Stanton, G.; Kim, H.-Y.; Lee, K.; Kim, G. T.; Duesberg, G. S.; Hallam, T.; Boland, J. J.; Wang, J. J.; Donegan, J. F.; Grunlan, J. C.; Moriarty, G.; Shmeliov, A.; Nicholls, R. J.; Perkins, J. M.; Grieveson, E. M.; Theuwissen, K.; McComb, D. W.; Nellist, P. D.; Nicolosi, V. Two-Dimensional Nanosheets Produced by Liquid Exfoliation of Layered Materials. *Science* 2011, *331* (6017), 568–571. https://doi.org/10.1126/science.1194975.

(53) Makarova, M.; Okawa, Y.; Aono, M. Selective Adsorption of Thiol Molecules at Sulfur Vacancies on MoS_2(0001), Followed by Vacancy Repair via S–C Dissociation. *J. Phys. Chem. C* 2012, *116* (42), 22411–22416. https://doi.org/10.1021/jp307267h.

(54) Chou, S. S.; De, M.; Kim, J.; Byun, S.; Dykstra, C.; Yu, J.; Huang, J.; Dravid, V. P. Ligand Conjugation of Chemically Exfoliated MoS_2. *J. Am. Chem. Soc.* 2013, *135* (12), 4584–4587. https://doi.org/10.1021/ja310929s.

(55) Ratwani, C. R.; Zhao, S.; Huang, Y.; Hadfield, M.; Kamali, A. R.; Abdelkader, A. M. Surface Modification of Transition Metal Dichalcogenide Nanosheets for Intrinsically Self-Healing Hydrogels with Enhanced Mechanical Properties. *Small n/a* (n/a), 2207081. https://doi.org/10.1002/smll.202207081.

(56) Petrovykh, D. Y.; Kimura-Suda, H.; Whitman, L. J.; Tarlov, M. J. Quantitative Analysis and Characterization of DNA Immobilized on Gold. *J. Am. Chem. Soc.* 2003, *125* (17), 5219–5226. https://doi.org/10.1021/ja029450c.

(57) Bora, A.; Mawlong, L. P.; Giri, P. K. Highly Suppressed Dark Current and Fast Photoresponse from Au Nanoparticle-Embedded, Si/Au/WS_2 Quantum-Dot-Based, Self-Biased Schottky Photodetectors. *ACS Appl. Electron. Mater.* 2021, *3* (11), 4891–4904.

(58) Mahler, B.; Hoepfner, V.; Liao, K.; Ozin, G. A. Colloidal Synthesis of 1T-WS_2 and 2H-WS_2 Nanosheets: Applications for Photocatalytic Hydrogen Evolution. *J. Am. Chem. Soc.* 2014, *136* (40), 14121–14127. https://doi.org/10.1021/ja506261t.

(59) Singh, V. K.; Mishra, H.; Ali, R.; Umrao, S.; Srivastava, R.; Abraham, S.; Misra, A.; Singh, V. N.; Mishra, H.; Tiwari, R. S.; Srivastava, A. In Situ Functionalized Fluorescent WS_2 -QDs as Sensitive and Selective Probe for Fe^{3+} and a Detailed Study of Its Fluorescence Quenching. *ACS Appl. Nano Mater.* 2019, *2* (1), 566–576. https://doi.org/10.1021/acsanm.8b02162.

(60) Bora, A.; Mawlong, L. P. L.; Das, R.; Giri, P. K. Understanding the Excitation Wavelength Dependent Spectral Shift and Large Exciton Binding Energy of Tungsten Disulfide Quantum Dots and Its Interaction with Single-Walled Carbon Nanotubes. *J. Colloid Interface Sci.* 2020, *561*, 519–532. https://doi.org/10.1016/j.jcis.2019.11.027.

(61) Donarelli, M.; Bisti, F.; Perrozzi, F.; Ottaviano, L. Tunable Sulfur Desorption in Exfoliated MoS_2 by Means of Thermal Annealing in Ultra-High Vacuum. *Chem. Phys. Lett.* 2013, *588*, 198–202. https://doi.org/10.1016/j.cplett.2013.10.034.

(62) Donarelli, M.; Prezioso, S.; Perrozzi, F.; Bisti, F.; Nardone, M.; Giancaterini, L.; Cantalini, C.; Ottaviano, L. Response to NO2 and Other Gases of Resistive Chemically Exfoliated MoS_2-Based Gas Sensors. *Sens. Actuators B Chem.* 2015, *207*, 602–613. https://doi.org/10.1016/j.snb.2014.10.099.

(63) Mitterreiter, E.; Schuler, B.; Micevic, A.; Hernangómez-Pérez, D.; Barthelmi, K.; Cochrane, K. A.; Kiemle, J.; Sigger, F.; Klein, J.; Wong, E.; Barnard, E. S.; Watanabe, K.; Taniguchi, T.; Lorke, M.; Jahnke, F.; Finley, J. J.; Schwartzberg, A. M.; Qiu, D. Y.; Refaely-Abramson, S.; Holleitner, A. W.; Weber-Bargioni, A.; Kastl, C. The Role of Chalcogen Vacancies for Atomic Defect Emission in MoS_2. *Nat. Commun.* 2021, *12* (1), 3822. https://doi.org/10.1038/s41467-021-24102-y.

(64) Zhang, M.; Lihter, M.; Chen, T.-H.; Macha, M.; Rayabharam, A.; Banjac, K.; Zhao, Y.; Wang, Z.; Zhang, J.; Comtet, J.; Aluru, N. R.; Lingenfelder, M.; Kis, A.; Radenovic, A. Super-Resolved Optical Mapping of Reactive Sulfur-Vacancies in Two-Dimensional Transition Metal Dichalcogenides. *ACS Nano* 2021, *15* (4), 7168–7178. https://doi.org/10.1021/acsnano.1c00373.

(65) Bretscher, H.; Li, Z.; Xiao, J.; Qiu, D. Y.; Refaely-Abramson, S.; Alexander-Webber, J. A.; Tanoh, A.; Fan, Y.; Delport, G.; Williams, C. A.; Stranks, S. D.; Hofmann, S.; Neaton, J. B.; Louie, S. G.; Rao, A. Rational Passivation of Sulfur Vacancy Defects in Two-Dimensional Transition Metal Dichalcogenides. *ACS Nano* 2021, *15* (5), 8780–8789. https://doi.org/10.1021/acsnano.1c01220.

(66) Qin, Z.; Loh, L.; Wang, J.; Xu, X.; Zhang, Q.; Haas, B.; Alvarez, C.; Okuno, H.; Yong, J. Z.; Schultz, T.; Koch, N.; Dan, J.; Pennycook, S. J.; Zeng, D.; Bosman, M.; Eda, G. Growth of Nb-Doped Monolayer WS_2 by Liquid-Phase Precursor Mixing. *ACS Nano* 2019, *13* (9), 10768–10775. https://doi.org/10.1021/acsnano.9b05574.

(67) Rathod, U. P.; Egede, J.; Voevodin, A. A.; Shepherd, N. D. Extrinsic P-Type Doping of Few Layered WS_2 Films with Niobium by Pulsed Laser Deposition. *Appl. Phys. Lett.* 2018, *113* (6), 062106. https://doi.org/10.1063/1.5040119.

(68) Khan, U.; Tang, L.; Ding, B.; Yuting, L.; Feng, S.; Chen, W.; Khan, M. J.; Liu, B.; Cheng, H.-M. Catalyst-Free Growth of Atomically Thin Bi_2O_2Se Nanoribbons for High-Performance Electronics and Optoelectronics. *Adv. Funct. Mater.* 2021, *31* (31), 2101170. https://doi.org/10.1002/adfm.202101170.

(69) Park, J.-C.; Kim, S.; Choi, H.; Jung, Y.; Oh, I.; Hwang, J. B.; Lee, S. Growth of Multilayer WSe_2/Bi_2O_2Se Heterostructures for Photodetection without Lithography. *Cryst. Growth Des.* 2023, *23* (4), 2092–2098. https://doi.org/10.1021/acs.cgd.2c01029.

(70) Froehlich, C. E.; He, J.; Haynes, C. L. Investigation of Charged Small Molecule–Aptamer Interactions with Surface Plasmon Resonance. *Anal. Chem.* 2023, *95* (5), 2639–2644. https://doi.org/10.1021/acs.analchem.2c04192.

(71) Berkdemir, A.; Gutiérrez, H. R.; Botello-Méndez, A. R.; Perea-López, N.; Elías, A. L.; Chia, C.-I.; Wang, B.; Crespi, V. H.; López-Urías, F.; Charlier, J.-C.; Terrones, H.; Terrones, M. Identification of Individual and Few Layers of WS_2 Using Raman Spectroscopy. *Sci. Rep.* 2013, *3* (1), 1755. https://doi.org/10.1038/srep01755.

(72) Iqbal, M. W.; Shahzad, K.; Hussain, G.; Arshad, M. K.; Akbar, R.; Azam, S.; Aftab, S.; Alharbi, T.; Majid, A. Gate Dependent Phonon Shift in Tungsten Disulfide (WS_2) Field Effect Transistor. *Mater. Res. Express* 2019, *6* (11), 115909. https://doi.org/10.1088/2053-1591/ab485a.

(73) Chakraborty, B.; Bera, A.; Muthu, D. V. S.; Bhowmick, S.; Waghmare, U. V.; Sood, A. K. Symmetry-Dependent Phonon Renormalization in Monolayer MoS${}_{2}$ Transistor. *Phys. Rev. B* 2012, *85* (16), 161403. https://doi.org/10.1103/PhysRevB.85.161403.

(74) Li, Y.; Zhang, X.; Wang, J.; Ma, X.; Shi, J.-A.; Guo, X.; Zuo, Y.; Li, R.; Hong, H.; Li, N.; Xu, K.; Huang, X.; Tian, H.; Yang, Y.; Yao, Z.; Liao, P.; Li, X.; Guo, J.; Huang, Y.; Gao, P.; Wang, L.; Yang, X.; Dai, Q.; Wang, E.; Liu, K.; Zhou, W.; Yu, X.; Liang, L.; Jiang, Y.; Li, X.-Z.; Liu, L. Engineering Interlayer Electron–Phonon Coupling in WS_2/BN Heterostructures. *Nano Lett.* 2022, *22* (7), 2725–2733. https://doi.org/10.1021/acs.nanolett.1c04598.

(75) Wang, F.; Li, S.; Bissett, M. A.; Kinloch, I. A.; Li, Z.; Young, R. J. Strain Engineering in Monolayer WS_2 and WS_2 Nanocomposites. *2D Mater.* 2020, *7* (4), 045022. https://doi.org/10.1088/2053-1583/ababf1.

(76) Mishra, A. K.; Lakshmi, K. V.; Huang, L. Eco-Friendly Synthesis of Metal Dichalcogenides Nanosheets and Their Environmental Remediation Potential Driven by Visible Light. *Sci. Rep.* 2015, *5* (1), 15718. https://doi.org/10.1038/srep15718.

(77) Toufanian, R.; Zhong, X.; Kays, J. C.; Saeboe, A. M.; Dennis, A. M. Correlating ZnSe Quantum Dot Absorption with Particle Size and Concentration. *Chem. Mater.* 2021, *33* (18), 7527–7536. https://doi.org/10.1021/acs.chemmater.1c02501.

(78) Gutiérrez, H. R.; Perea-López, N.; Elías, A. L.; Berkdemir, A.; Wang, B.; Lv, R.; López-Urías, F.; Crespi, V. H.; Terrones, H.; Terrones, M. Extraordinary Room-Temperature Photoluminescence in Triangular WS_2 Monolayers. *Nano Lett.* 2013, *13* (8), 3447–3454. https://doi.org/10.1021/nl3026357.

(79) Fu, W.; Yin, J.; Cao, H.; Zhou, Z.; Zhang, J.; Fu, J.; Warner, J. H.; Wang, C.; Jia, X.; Greaves, G. N.; Cheetham, A. K. Non-Blinking Luminescence from Charged Single Graphene Quantum Dots. *Adv. Mater. n/a* (n/a), 2304074. https://doi.org/10.1002/adma.202304074.

(80) Yin, W.; Bai, X.; Chen, P.; Zhang, X.; Su, L.; Ji, C.; Gao, H.; Song, H.; Yu, W. W. Rational Control of Size and Photoluminescence of WS_2 Quantum Dots for White Light-Emitting Diodes. *ACS Appl. Mater. Interfaces* 2018, *10* (50), 43824–43830. https://doi.org/10.1021/acsami.8b17966.

(81) Ghosh, T.; Samanta, M.; Vasdev, A.; Dolui, K.; Ghatak, J.; Das, T.; Sheet, G.; Biswas, K. Ultrathin Free-Standing Nanosheets of Bi_2O_2Se: Room Temperature Ferroelectricity in Self-Assembled Charged Layered Heterostructure. *Nano Lett.* 2019, *19* (8), 5703–5709. https://doi.org/10.1021/acs.nanolett.9b02312.

(82) Mátyus, L.; Szöllősi, J.; Jenei, A. Steady-State Fluorescence Quenching Applications for Studying Protein Structure and Dynamics. *J. Photochem. Photobiol. B* 2006, *83* (3), 223–236. https://doi.org/10.1016/j.jphotobiol.2005.12.017.

(83) Tanwar, A. S.; Parui, R.; Garai, R.; Chanu, M. A.; Iyer, P. K. Dual "Static and Dynamic" Fluorescence Quenching Mechanisms Based Detection of TNT via a Cationic Conjugated Polymer. *ACS Meas. Sci. Au* 2022, *2* (1), 23–30. https://doi.org/10.1021/acsmeasuresciau.1c00023.

(84) Zelada-Guillén, G. A.; Sebastián-Avila, J. L.; Blondeau, P.; Riu, J.; Rius, F. X. Label-Free Detection of Staphylococcus Aureus in Skin Using Real-Time Potentiometric Biosensors Based on Carbon Nanotubes and Aptamers. *Biosens. Bioelectron.* 2012, *31* (1), 226–232. https://doi.org/10.1016/j.bios.2011.10.021.

(85) Sung, Y. J.; Suk, H.-J.; Sung, H. Y.; Li, T.; Poo, H.; Kim, M.-G. Novel Antibody/Gold Nanoparticle/Magnetic Nanoparticle Nanocomposites for Immunomagnetic Separation and Rapid Colorimetric Detection of Staphylococcus Aureus in Milk. *Biosens. Bioelectron.* 2013, *43*, 432–439. https://doi.org/10.1016/j.bios.2012.12.052.

(86) Kong, W.; Xiong, J.; Yue, H.; Fu, Z. Sandwich Fluorimetric Method for Specific Detection of Staphylococcus Aureus Based on Antibiotic-Affinity Strategy. *Anal. Chem.* 2015, *87* (19), 9864–9868. https://doi.org/10.1021/acs.analchem.5b02301.

(87) Yang, F.; Chang, T.-L.; Liu, T.; Wu, D.; Du, H.; Liang, J.; Tian, F. Label-Free Detection of Staphylococcus Aureus Bacteria Using Long-Period Fiber Gratings with Functional Polyelectrolyte Coatings. *Biosens. Bioelectron.* 2019, *133*, 147–153. https://doi.org/10.1016/j.bios.2019.03.024.

(88) Chen, L.; Leng, Y.-K.; Liu, B.; Liu, J.; Wan, S.-P.; Wu, T.; Yuan, J.; Shao, L.; Gu, G.; Fu, Y. Q.; Xu, H.; Xiong, Y.; He, X.-D.; Wu, Q. Ultrahigh-Sensitivity Label-Free Optical Fiber Biosensor Based on a Tapered Singlemode- No Core-Singlemode Coupler for Staphylococcus Aureus Detection. *Sens. Actuators B Chem.* 2020, *320*, 128283. https://doi.org/10.1016/j.snb.2020.128283.

(89) Farooq, U.; Ullah, M. W.; Yang, Q.; Aziz, A.; Xu, J.; Zhou, L.; Wang, S. High-Density Phage Particles Immobilization in Surface-Modified Bacterial Cellulose for Ultra-Sensitive and Selective Electrochemical Detection of Staphylococcus Aureus. *Biosens. Bioelectron.* 2020, *157*, 112163. https://doi.org/10.1016/j.bios.2020.112163.

(90) Zhou, J.; Yin, L.; Dong, Y.; Peng, L.; Liu, G.; Man, S.; Ma, L. CRISPR-Cas13a Based Bacterial Detection Platform: Sensing Pathogen Staphylococcus Aureus in Food Samples. *Anal. Chim. Acta* 2020, *1127*, 225–233. https://doi.org/10.1016/j.aca.2020.06.041.

(91) Guo, Y.; Li, J.; Song, X.; Xu, K.; Wang, J.; Zhao, C. Label-Free Detection of Staphylococcus Aureus Based on Bacteria-Imprinted Polymer and Turn-on Fluorescence Probes. *ACS Appl. Bio Mater.* 2021, *4* (1), 420–427. https://doi.org/10.1021/acsabm.0c00897.

(92) Deng, M.; Wang, Y.; Chen, G.; Liu, J.; Wang, Z.; Xu, H. Poly-l-Lysine-Functionalized Magnetic Beads Combined with Polymerase Chain Reaction for the Detection of Staphylococcus Aureus and Escherichia Coli O157:H7 in Milk. *J. Dairy Sci.* 2021, *104* (12), 12342–12352. https://doi.org/10.3168/jds.2021-20612.

Chapter 8

Summary and Outlook

This chapter summarizes the key contributions of this thesis and highlights novel findings related to the synthesis of 1L and 2L WS_2, its lateral heterostructure with MoS_2 using CVD technique, and WS_2 QDs via liquid phase exfoliation from bulk WS_2. It also summarizes their applications in high-performance photodetection, field-effect transistors, and biosensing. Finally, the chapter presents the future outlook and potential directions for further research.

8.1. Summary and Highlights of the Thesis Contribution

In this dissertation, we have demonstrated the controlled growth of 1L and 2L WS_2 using a CVD method. We optimized various growth parameters, including carrier gas flow, growth temperature, precursors, growth pressure, and growth duration to achieve high-quality and large-area growth of 1L and 2L WS_2 on SiO_2/Si substrates (Chapter 2).

Subsequently, we developed a high-performance photodetector using CVD-grown 2L WS_2 through contact engineering. By employing metal electrodes with higher and lower work functions relative to bilayer WS_2, we achieved asymmetric lateral doping in WS_2 flakes, as verified by photoluminescence spectral profiles and Raman mapping. This doping asymmetry created two depletion regions, enabling unidirectional electron flow, which reduced dark current under reverse bias and improved overall device performance (Chapter 3) with on-off ratio ~10^5 and a peak responsivity of 1.2A/W.

We further analyzed the effect of metal (Au) and non-metal (Bi_2Se_3) contacts on 1L-MoS_2 for high-performance FETs. The use of non-metal contacts enhanced the on/off ratio by two orders of magnitude and increased mobility, attributed to the reduction of defects at the contact interface. In comparison to metal contacts, the non-metal contacts in MoS_2-based flexible photodetectors significantly improved detection performance (Chapter 4). The FETs on-off ratio improved by two orders of magnitude and there was a two fold enhancement in the mobility.

Additionally, we investigated a single-step CVD growth of bilayer WS_2-MoS_2 LHS with excellent control over the relative areas of WS_2 and MoS_2. We observed significant photoluminescence enhancement at the junction interface in the LHS due to presence of local 1L-WS_2 and induced strain. Finally, we fabricated FETs based on WS_2, MoS_2, and WS_2-MoS_2 heterostructures, which exhibited improved on/off ratios and lower saturation voltages. These enhancements were attributed to the cleaner interface and faster charge transfer between WS_2 and MoS_2 (Chapter 5).

The 1L-WS_2 exhibits excellent PL emission at room temperature, which has been utilized for the first time as a recognition tool for detecting *S. aureus* bacteria with high sensitivity and selectivity. The PL emission peak of 1L-WS_2 undergoes significant changes in the presence of targeted *S. aureus* due to charge transfer resulting from the selective interaction of the ssDNA aptamer with *S. aureus*, while it remains unchanged for non-targeted *E.coli*. PL analysis of 1L-WS_2 with increasing *S. aureus* concentration exhibits a linear response from 10^2 CFU/mL to 10^7 CFU/mL, with a lower detection limit of 2.0 CFU/mL (Chapter 6).

Finally, we synthesized WS_2 QDs with a mean diameter of 2.5 nm via liquid exfoliation of bulk WS_2. These QDs are highly fluorescent under UV illumination, but their fluorescence is quenched upon absorption on the surface of Bi_2O_2Se NSs. Interestingly, the PL intensity of the WS_2 QDs is restored after interaction with targeted *S. aureus* in the presence of ssDNA aptamers, with the intensity increasing as the *S. aureus* concentration rises. Similar experiments with non-target bacteria confirm the systems selectivity for *S. aureus*. Our fluorescence-based biosensor exhibits a linear response in the range of 10^3–10^7 CFU/mL, with a detection limit of 580 CFU/mL (Chapter 7)

8.2. Scope of Future Work

In this thesis, we have demonstrated the controlled growth of high-quality, large-area monolayer and bilayer WS_2, along with its lateral heterostructure with MoS_2, using a single-step CVD technique. These materials have been explored for their applications in devices ranging from optoelectronics to biosensing. Silicon-based semiconductors have dominated commercial systems for decades, but 2D materials, especially TMDs, represent a promising alternative. However, extensive research is needed from growth and device fabrication to characterization, before they can replace commercial silicon. TMDs, especially for specific applications like biosensing, hold

great potential for next-generation technologies. Overall, there is significant scope to expand this work to a broader range of applications, as discussed below.

1. This study can be applied to achieve controlled large-area growth of other 2D TMDs, inducing anisotropic 2D materials.
2. Ultrathin 2D TMD-based devices can be stacked layer by layer in a multi-stack device architecture, significantly increasing device density beyond Moore's limit.
3. The single-step grown lateral heterostructure of WS_2-MoS_2 has demonstrated excellent device characteristics, with the potential for high-performance electronic applications. This can be used with other 2D TMD heterostructure.
4. The remarkable PL enhancement at the WS_2-MoS_2 interface can be further explored for surface-enhanced Raman scattering (SERS) and tip-enhanced Raman scattering (TERS)-based optical biosensing.
5. Individual devices can be integrated for memory and storage applications in electronic data systems.
6. TMDs exhibit excellent on-off ratios, yet their potential in FET-based biosensing remains underexplored. They hold promise for real-time, ultra-low detection of bio-analytes.
7. Strain engineering in 2D TMDs can be applied to improve device performance.